



Skolkovo Institute of Science and Technology

**MEMORY COMPRESSION OF THE GALERKIN VOLUME INTEGRAL EQUATIONS  
AND COIL MODELING FOR THE ELECTRICAL PROPERTY MAPPING OF  
BIOLOGICAL TISSUE**

Doctoral Thesis

by

ILIAS I. GIANNAKOPOULOS





Skolkovo Institute of Science and Technology

Skolkovo Institute of Science and Technology

MEMORY COMPRESSION OF THE GALERKIN VOLUME INTEGRAL EQUATIONS  
AND COIL MODELING FOR THE ELECTRICAL PROPERTY MAPPING OF  
BIOLOGICAL TISSUE

*Doctoral Thesis*

by

ILIAS I. GIANNAKOPOULOS

DOCTORAL PROGRAM IN COMPUTATIONAL AND DATA SCIENCE AND  
ENGINEERING

Supervisor  
Prof. Maxim Fedorov

Moscow 2020

©Ilias I. Giannakopoulos 2020



The presented doctoral dissertation was funded by the Skoltech-MIT Next Generation Program, “Next Generation Fast Methods for Medical and Nanoscale Technology” and the National Science Foundation-Career 1453675, “Interactions of Radiofrequency Electromagnetic Fields with Biological Tissue: New Tools to Address Challenges and Exploit Opportunities”. The author with this declares that the work presented in this thesis was carried out by himself at the Skolkovo Institute of Science and Technology, Moscow, except where due acknowledgment is made and has not been submitted for any other degree.

Ilias I. Giannakopoulos

Maxim Fedorov



*To my family, Marianna, Ioannis, and Stefanos.  
Στην οικογένειά μου, Μαριάννα, Ιωάννη, και Στέφανο.  
Моей семье Марианне, Иоаннису, и Стефаносу.*



## ABSTRACT

---

The scope of this doctoral dissertation is to study the interactions of electromagnetic (EM) waves and biological tissue in the presence of a strong magnetic field, and demonstrate the utility of novel methods via their application to simulations for the Magnetic Resonance Imaging (MRI) of realistic human head models. In problems related to MRI, the maximum use of the single operating frequency allows the careful design and optimization of fast and robust algorithms of computational electromagnetics (CEM), based on integral equations (IE). Specifically, surface integral equations (SIE) are employed to analyze the radio-frequency (RF) transmit-receive coils of the magnetic resonance (MR) scanner, while volume integral equations (VIE) model the EM interactions of human tissues with finite electrical properties (EP). The fast and accurate estimation of the interactions above is of paramount importance since a poor design of an RF coil might lead to detrimental effects in the quality of the MR image and the safety of the patient, especially in modern ultra-high-field (UHF) scanners.

Specifically, in the first part of this thesis, we present a method of memory footprint reduction for FFT-based, EM VIE formulations. The arising Green's function tensors have low multilinear rank properties, which allows the employment of tensor decompositions (Tucker, Canonical decompositions, and Tensor Train) for their compression, thereby significantly reducing the required memory storage for numerical simulations. Consequently, the compressed components can fit inside a graphical processing unit (GPU) on which highly parallelized computations can vastly accelerate the iterative solution of the arising linear system. Besides, we provide a variety of novel and efficient matrix-vector product methods that maintain the linear complexity of the traditional element-wise product of FFT-based VIE and can provide up to an order of magnitude of acceleration. For the second part, we turn our interest to the non-invasive cross-sectional mapping of the electrical property (EP) distributions of realistic human head models using MR measurements, and the recently introduced Global Maxwell Tomography (GMT). Previous work evaluated GMT using ideal radiofrequency (RF) excitations, while this dissertation aims to assess GMT's performance in simulation, using a realistic RF coil. The designed coil is a transmit-receive array with eight decoupled channels for 7 Tesla head imaging. We calculated the RF transmit field inside inhomogeneous head models for different RF shimming approaches, and used them as input for GMT to reconstruct brain EP. The coil tuning/decoupling remained relatively stable when the coil was load with different head models. The mean error in EP es-

timization changed from 7.5% to 9.5% and from 4.84% to 7.2% for the relative permittivity and conductivity, respectively, when changing head models without re-tuning the coil. When an SVD-based RF shimming algorithm is applied, in place of excitation with one coil channel at a time, we observed that the reconstruction slightly improves. Despite errors in EP, the prediction of the RF transmit field, and the voxel-wise absorbed power have less than 0.5% mean error over the entire head. Also, GMT could accurately detect a numerically inserted tumor. The results summarized above show that GMT can reliably reconstruct EP in realistic simulated scenarios using a tailored 8-channel RF coil design at 7 Tesla, thus, enabling future in-vivo GMT experiments. The significance of this work is that GMT could provide accurate estimations of tissue EP, which could be used as biomarkers and could enable patient-specific estimation of RF power deposition, which is an unsolved problem for UHF MRI. Finally, there is a costly trade-off between accuracy and time footprint for GMT, and regrettably, the reconstruction requires days to converge, especially for fine resolutions. Thus we investigate deep learning architectures that can vastly accelerate the reconstruction and overcome such impasses. The proposed approach is to train a tensor-to-tensor convolutional neural network that maps the MR measurements to the corresponding EP of tissue-mimicking phantoms.

The novel RF coil designs can aid GMT to provide accurate estimations of tissue EP, which could be used as biomarkers and could enable patient-specific estimation of RF power deposition, which is an unsolved problem for UHF MRI. Moreover, the novel accelerated through GPU programming, tensor decomposition-based methods, will offer more precise and faster biomedical analysis. As a result, both contributions of this thesis could help to exploit the full potential of UHF MRI.

This page is intentionally left blank.



## LIST OF PUBLICATIONS

---

### Journal Publications

1. **Giannakopoulos, Ilias I**, M. S. Litsarev, and A. G. Polimeridis, “Memory footprint reduction for the FFT-based volume integral equation method via tensor decompositions,” *IEEE Transactions on Antennas and Propagation*, vol. 67, no. 12, pp. 7476–7486, 2019.
2. **Giannakopoulos, Ilias**, J. E. Serrallés, L. Daniel *et al.*, “Magnetic-resonance-based electrical property mapping using global maxwell tomography with an 8-channel head coil at 7 tesla: a simulation study,” *IEEE Transactions on Biomedical Engineering*, 2020.
3. J. E. Serralles, **Giannakopoulos, Ilias**, B. Zhang *et al.*, “Noninvasive estimation of electrical properties from magnetic resonance measurements via Global Maxwell Tomography and match regularization,” *IEEE Transactions on Biomedical Engineering*, vol. 67, no. 1, pp. 3–15, 2019.
4. I. P. Georgakis, **Giannakopoulos, Ilias I**, M. S. Litsarev, and A. G. Polimeridis, “A fast volume integral equation solver with linear basis functions for the accurate computation of electromagnetic fields in MRI,” *arXiv preprint arXiv:1902.02196*, under review in *IEEE Transactions on Antennas and Propagation*, 2019.

### Conference Publications

1. **Giannakopoulos, Ilias I**, M. S. Litsarev, and A. G. Polimeridis, “3D cross-Tucker approximation in FFT-based volume integral equation methods,” in *2018 IEEE International Symposium on Antennas and Propagation & USNC/URSI National Radio Science Meeting*. IEEE, 2018, pp. 2507–2508. **Honorable Mention Award**
2. **Giannakopoulos, Ilias I**, J. E. Serralles, B. Zhange *et al.*, “Electrical properties mapping in a tissue-mimicking phantom using Global Maxwell Tomography with a realistic coil model at 7 Tesla,” in *2nd International Workshop on MR-based Electrical Properties Tomography*. IMEP, 2019, pp. 82–83.
3. **Giannakopoulos, Ilias I**, J. E. Serrallés, B. Zhang *et al.*, “Global Maxwell Tomography using an 8-channel radiofrequency coil: simulation results for a tissue-mimicking phantom at

7T” in *2019 IEEE International Symposium on Antennas and Propagation and USNC-URSI Radio Science Meeting*. IEEE, 2019, pp. 823–824.

4. **Giannakopoulos, Ilias I, J. E. Serrallés, G. Guryev *et al.***, “On the usage of deep neural networks as a tensor-to-tensor translation between MR measurements and electrical properties,” in *Proc. ISMRM*, 2020, p. 3193.

This page is intentionally left blank.



## ACKNOWLEDGEMENTS

---

The presented doctoral dissertation was prepared between August 2016 and May 2020 in the Skoltech Center for the Computational Data-Intensive Science and Engineering of the Skolkovo Institute of Science and Technology, Moscow, Russian Federation and in the research laboratory of electronics, Computational Prototyping Group of the Massachusetts Institute of Technology, Cambridge, MA, United States of America.

Upon completion, I would like to thank my Ph.D. advisor Professor Maxim Fedorov for his excellent collaboration and for his reliable support in this work. Besides, I would also like to thank my Ph.D. co-advisors, Professor Jacob White, Professor Riccardo Lattanzi, and Dr. Athanasios Polimeridis for their incomparable passion and dedication towards the most challenging concepts in the accounting dissertation. Their patience, motivation, immense knowledge and guidance helped me in all the time of research and writing of this thesis. I could not have imagined having better advisors and mentors for my Ph.D. study.

I feel the need also to thank prof. Stamatios Lefkimmiatis, prof. Luca Daniel, prof. Daniel Sodickson, prof. Lawrence Wald, prof. Elfar Adalsteinsson, prof. Ivan Oseledets, prof. Alexander Shapeev, prof. Maxim Panov, prof. Marwan Charara and prof. Dimitrios Chrisoulidis for the knowledge and support that they kindly provided over the years, as well as the interest that caused me on the problems of electromagnetics, magnetic resonance imaging, and numerical mathematics. I can not help mentioning the assistance that my colleagues and friends, Dr. Mikhail Litsarev, Dr. Samuel Groth, Dr. Bei Zhang, Dr. Ioannis Georgakis, Dr. Alexandra Tambova, Jose Seralles, and Georgy Guryev, kindly offered me. Without their precious support, it would not be possible to conduct this research.

Exceptional gratitude goes out to the research grants providers, namely the Skoltech-MIT Next-Generation Program, “*Next Generation Fast Methods for Medical and Nanoscale Technology*” and the National Science Foundation-Career 1453675, “*Interactions of Radiofrequency Electromagnetic Fields with Biological Tissue: New Tools to Address Challenges and Exploit Opportunities*”. Moreover, I would like to thank the Institute of Electrical and Electronics Engineers for awarding my work with an honorable mention in the 2018 IEEE AP-S Student Paper Competition. Furthermore, my sincere appreciation goes out to the Skoltech Center for Computational and Data-Intensive Science and Engineering and the Computational Prototyping Group of the Research Laboratory of Electronics in the Massachusetts Institute of Technology for their trust

and support these past years.

Here I feel obliged to quote the words of the Greek writer, Nikos Kazantzakis, which I believe express my personal benefit over the past four years of my Ph.D. studies, “Arrogance did not move us, nor the simple certainty that one day the peak would stand still and we would reach it; nor if we reached it, that we would find happiness, salvation and the Paradise there; we ascended, because happiness, salvation and Paradise for us was the ascent.”

Above all, I wholeheartedly thank my family, Marianna, Ioannis, and Stefanos, for the universal support of my efforts for this dissertation and in my life in general.

Moscow, September, 2020

Ilias I. Giannakopoulos

This page is intentionally left blank.



# CONTENTS

---

Abstract . . . . .	v
List of Publications . . . . .	ix
Acknowledgements . . . . .	xiii
Contents . . . . .	xvii
List of Abbreviations and Notation . . . . .	xxiii
List of Figures . . . . .	xxix
List of Tables . . . . .	.xxxvii
<b>1 Introduction . . . . .</b>	<b>1</b>
1.1 Historical and Literature Review . . . . .	2
1.2 Thesis Structure and Contribution . . . . .	9
<b>2 Electromagnetic Theory . . . . .</b>	<b>15</b>
2.1 Fundamental Theorems of Electromagnetism . . . . .	15
2.1.1 Maxwell's Equations and Boundary Conditions . . . . .	15
2.1.1.1 Integral form of Maxwell's Equations . . . . .	16
2.1.1.2 Time-harmonic form of Maxwell's Equations . . . . .	18
2.1.1.3 Boundary Conditions . . . . .	19
2.1.2 Superposition, Duality and Reciprocity Theorems . . . . .	20
2.1.3 Vector Wave Equations . . . . .	21
2.1.4 Green's function . . . . .	21
2.1.5 Surface Equivalence Principle . . . . .	22

2.1.6	Volume Equivalence Principle . . . . .	25
2.2	Computational Electromagnetism . . . . .	26
2.2.1	Differential and Integral Methods . . . . .	27
2.2.2	Method of Moments . . . . .	28
2.2.2.1	Collocation Method . . . . .	29
2.2.2.2	Nyström Method . . . . .	29
<b>3</b>	<b>Integral Equation Methods . . . . .</b>	<b>31</b>
3.1	Surface Integral Equations . . . . .	33
3.1.1	Surface Integral Equation for Impenetrable Scatterers . . . . .	33
3.1.2	Surface Integral Equation for Penetrable Scatterers . . . . .	36
3.1.3	Rao-Wilton-Glisson Basis Functions . . . . .	38
3.1.3.1	Singular Integrals . . . . .	41
3.1.4	Numerical Problems of EFIE . . . . .	41
3.1.4.1	Combined Field Integral Equation . . . . .	42
3.1.4.2	Low-Frequency Catastrophe of EFIE . . . . .	42
3.1.4.3	Calderón Preconditioner . . . . .	43
3.1.5	Far Field Measurements . . . . .	44
3.1.6	Computation of Power . . . . .	44
3.1.7	Lumped Elements . . . . .	51
3.1.8	Network Parameters . . . . .	53
3.2	Volume Integral Equations . . . . .	54
3.2.1	Current-Based Volume Integral Equation . . . . .	55
3.2.1.1	Galerkin Linear System . . . . .	56
3.2.2	Flux-Based Volume Integral Equation . . . . .	57
3.2.2.1	Galerkin Linear System . . . . .	58
3.2.2.2	CG-FFT Matrix-Vector Products . . . . .	61
3.2.3	Scattering from Homogeneous Spheres . . . . .	63
3.2.4	Scattering from Realistic Human Body Models . . . . .	65
3.3	Volume-Surface Integral Equations . . . . .	66
<b>4</b>	<b>Memory Footprint Reduction for the FFT-based VIE . . . . .</b>	<b>73</b>
4.1	Tensor Decompositions . . . . .	74
4.1.1	Tucker Decomposition . . . . .	76
4.1.2	Canonical Polyadic Decomposition . . . . .	77
4.1.3	Tensor Train Decomposition . . . . .	77
4.2	Compression Algorithms . . . . .	79
4.2.1	Higher-Order Singular Value Decomposition . . . . .	79

4.2.2	Tucker-Based Three-Dimensional Cross Approximation . . . . .	80
4.2.3	Tucker + Canonical Decomposition Method . . . . .	82
4.3	Matrix-Vector Product Implementation . . . . .	83
4.3.1	Circulant Embedding and Fourier Transform . . . . .	83
4.3.2	Matrix-Vector Product Cost . . . . .	84
4.3.3	Time Footprint of the Matrix-Vector Product . . . . .	85
4.4	Results . . . . .	87
4.4.1	Multilinear Rank . . . . .	87
4.4.2	Compression Factor . . . . .	89
4.4.3	EM Simulations for Realistic Human Body Models . . . . .	91
4.4.4	Scaling Properties of Memory Compressed Approaches . . . . .	97
4.5	Current Compression on the FFT-based VIE . . . . .	97
4.6	Summary . . . . .	101
<b>5</b>	<b>RF Coil Design for Global Maxwell Tomography . . . . .</b>	<b>103</b>
5.1	Theoretical background on Global Maxwell Tomography . . . . .	105
5.2	RF Coil Design for Global Maxwell Tomography . . . . .	107
5.2.1	Tuning, Matching and Decoupling Optimization . . . . .	110
5.2.2	Numerical Results . . . . .	112
5.2.2.1	Projected Electromagnetic Fields . . . . .	112
5.2.2.2	Voltage Calibration Patterns . . . . .	115
5.2.2.3	Tuning-Matching-Decoupling Sensitivity . . . . .	117
5.2.2.4	Electrical Properties Reconstruction . . . . .	118
5.2.2.5	Estimated Electromagnetic Field Distribution . . . . .	122
5.2.2.6	Brain Tumor Detection . . . . .	126
5.3	Electrical Properties Reconstruction Using Deep Convolutional Neural Networks . . . . .	128
5.3.1	Data Generation . . . . .	130
5.3.2	Convolutional Neural Network . . . . .	131
5.3.2.1	UNET Architecture . . . . .	133
5.3.3	Training and Testing . . . . .	136
5.4	Summary . . . . .	137
<b>6</b>	<b>Conclusion . . . . .</b>	<b>141</b>
6.1	Conclusions and Contributions . . . . .	141
6.2	Future Research . . . . .	144
	<b>References . . . . .</b>	<b>147</b>

Appendix A	Mie Scattering	I
A.1	Debye's Potentials	I
A.2	Spherical Wave Functions	IV
A.3	Incident Plane Wave	VI
A.4	Scattered Wave	VII
A.5	Impenetrable Sphere	VIII
A.6	Penetrable Sphere	IX
A.7	Extinction- and Scattering-Cross Sections	X
Appendix B	Wirtinger Calculus	XIII
B.1	Introduction to $\mathbb{C}\mathbb{R}$ -Calculus	XIII
B.2	$\mathbb{C}\mathbb{R}$ -Calculus of Multiple Variables	XIV
Appendix C	Numerical Linear Algebra	XIX
C.1	Definitions	XIX
C.2	Adaptive Cross Approximation	XX
C.3	Maxvol Algorithm	XXI
Appendix D	Integration Background	XXV
D.1	Simplex Coordinates	XXV
D.2	Gauss Quadrature Rules	XXVI
D.2.1	Gauss Quadrature Rule for Rectangles	XXVII
D.2.2	Gauss Quadrature Rule for Right-Angle Triangles	XXVII
D.2.3	Gauss Quadrature Rule for Cubes	XXVII
D.3	Spherical Mean	XXVIII
Appendix E	Gradient Calculation	XXXI

This page is intentionally left blank.



## LIST OF ABBREVIATIONS AND NOTATION

---

<i>Acronym</i>	<i>Definition</i>
1D	One Dimensional
2D	Two Dimensional
3D	Three Dimensional
4D	Four Dimensional
6D	Six Dimensional
ACA	Adaptive Cross Approximation
ALS	Alternating Least Squares
BC	Buffa-Christiansen
BCCB	Block Circulant - Circulant Blocks
BN	Batch Normalization
BTTB	Block Toeplitz - Toeplitz Blocks
CANDECOMP	Canonical Polyadic Decomposition
CEM	Computational Electromagnetics
CFIE	Combined Field Integral Equation
CG	Conjugate Gradient
CG-FFT	Conjugate Gradient - Fast Fourier Transform
CG-TT	Conjugate Gradient - Tensor Train
cGAN	Conditional Generative Adversarial Network
CNN	Convolutional Neural Network
CP	Canonical Decomposition
CPU	Central Processing Unit
$\mathbb{C}\mathbb{R}$	Complex - Real
CSI-EPT	Contrast Source Inversion - Electrical Properties Tomography
DE	Differential Equation
DEMCEM	Direct Evaluation Method in Computational Electromagnetics
DSEFIE	Dual - Surface Electric Field Integral Equation
DSI	Displaced Surface Integral

DSMFIE	Dual - Surface Magnetic Field Integral Equation
DVIE	Electric Flux Volume Integral Equation
EFIE	Electric Field Integral Equation
EIT	Electrical Impedance Tomography
EM	Electromagnetic
EP	Electrical Property
EPT	Electrical Property Tomography
EVIE	Electric Field Volume Integral Equation
FCN	Fully Connected Network
FD	Finite Difference
FDTD	Finite Difference Time Domain
FEM	Finite Element Method
FFT	Fast Fourier Transform
FFT-VIE	Fast Fourier Transform - Volume Integral Equation
FMM	Fast Multipole Method
GMRES	Generalized Minimal Residual Method
GMT	Global Maxwell Tomography
GPU	Graphical Processing Unit
HEI	Hall Effect Imaging
HOSVD	Higher-Order Singular Value Decomposition
IE	Integral Equation
JMVIE	Electromagnetic Current Volume Integral Equation
JVIE	Electric Current Volume Integral Equation
LMT	Local Maxwell Tomography
MARIE	Magnetic Resonance Integral Equation suite
MAT-MI	Magnetoacoustic Tomography - Magnetic Induction
MaxVol	Maximum Volume
MFIE	Magnetic Field Integral Equation
MIT	Magnetic Impedance Tomography
MLFMA	Multilevel Fast Multipole Method
MoM	Method of Moments
MR	Magnetic Resonance
MR-EPT	Magnetic Resonance - Electrical Property Tomography
MREIT	Magnetic Resonance Electrical Impedance Tomography
MRI	Magnetic Resonance Imaging

MSE	Mean Squared Error
NN	Neural Network
PARAFAC	Parallel Factor Analysis
PDE	Partial Differential Equation
PEC	Perfect Electric Conductor
pFFT	Precorrected Fast Fourier Transform
PFT	Power - Force - Torque
PMC	Perfect Magnetic Conductor
PNAE	Peak Normalized Absolute Error
PNAME	Peak Normalized Absolute Mean Error
PWC	Piecewise Constant
PWL	Piecewise Linear
RAM	Random Access Memory
ReLU	Rectified Linear Unit
RF	Radiofrequency
RWG	Rao - Wilton - Glisson
SAR	Specific Absorption Rate
SI	International System of Units
SIE	Surface Integral Equation
SNR	Signal to Noise Ratio
SVD	Singular Value Decomposition
TT	Tensor Train
TV	Total Variation
UHF	Ultra - High - Field
VIE	Volume Integral Equation
VSIE	Volume - Surface Integral Equation

<i>Notation</i>	<i>Description</i>
$i$	Imaginary unit $i^2 = -1$
$\mathbb{C}$	Set of complex numbers
$a$	Scalar in $\mathbb{C}$
$\mathfrak{a}$	Time varying scalar in $\mathbb{C}$
$\hat{a}$	Unit vector
$\mathbf{a}$	Vector in $\mathbb{C}^3$
$\mathfrak{A}$	Time varying vector in $\mathbb{C}^3$

$\mathbf{a}$	Vector in $\mathbb{C}^n$
$\mathcal{A}$	Operator acting on vectors in $\mathbb{C}^3$
$A$	Matrix in $\mathbb{C}^{n_1 \times n_2}$
$\mathcal{A}$	Tensor in $\mathbb{C}^{n_1 \times n_2 \times n_3}$
$\cdot_{i_1 i_2 i_3 \dots}$	Element of array
$\cdot_{:i_2 i_3}$	Row vector of tensor
$\cdot_{::i_3}$	Slice matrix of tensor
$A^{(\cdot)}$	Two-dimensional reshape of $\mathcal{A}$
$\mathcal{F}\{\cdot\}$	Fourier transform
$\mathcal{Re}\{\cdot\}$	Real part of complex
$\mathcal{Im}\{\cdot\}$	Imaginary part of complex
$\cdot^*$	Conjugate (transpose) operation
$\Sigma$	Summation operator
$\Pi$	Product operator
$\nabla$	Del operator
$\cdot^T$	Transpose operation
$\mathbb{A}$	Set
$P_{\mathbb{A}}\{\cdot\}$	Projection to $\mathbb{A}$
$\mathcal{A}$	Euclidean contour, surface, or volume
$[\cdot]$	Spherical mean
$\bar{A}$	Dyad
$\tilde{\cdot}$	Approximation
$\mathcal{O}(\cdot)$	Complexity
$\cdot$	Inner product in $\mathbb{C}^3$
$\langle \cdot \rangle$	Inner product in $\mathbb{C}^n$
$\times$	Outer product in $\mathbb{C}^3$
$\odot$	Outer product in $\mathbb{C}^n$
$\times_i$	n-mode product
$\circ$	Element-wise product
$\otimes$	Kronecker product
$\circledast$	Khatri-Rao product

This page is intentionally left blank.



## LIST OF FIGURES

---

2.1	(left) Open Euclidean surface $\mathcal{S}_1$ , terminated by a contour $\mathcal{C}$ , and their respective differential elements. (right) Euclidean surface $\mathcal{S}_2$ enclosing the volume $\mathcal{V}$ . . . . .	17
2.2	Boundary between two media 1 and 2 with different EP. . . . .	19
2.3	Surface equivalence principle and extinction theorem. . . . .	23
2.4	Volume equivalence principle. . . . .	25
3.1	Scattering by a PEC surface. . . . .	34
3.2	Local circular region . . . . .	35
3.3	Scattering by a surface with permittivity $\epsilon$ and permeability $\mu$ . . . . .	37
3.4	RWG functions defined on the common edge of two triangles. . . . .	39
3.5	Interaction between two triangles $\mathcal{T}_n$ and $\mathcal{T}_m$ . . . . .	40
3.6	Condition number of the MoM matrix of the (top) EFIE, MFIE and CFIE formulations for a PEC sphere, and the (bottom) PMCHWT and Müller formulations for a diamond sphere with $\epsilon_r = 5.68 - j0.0023/(\epsilon_0\omega)$ , of unit radiuses. . . . .	45
3.7	Radiation pattern of a PEC sphere with unit radius on the azimuthial cut $\phi = 0$ . The incident field is a linear polarized plane wave. The far-field is obtained with the Mie solution and the EFIE, MFIE, CFIE, for three different discretizations. . . . .	46
3.8	Radiation pattern of a diamond sphere with unit radius on the azimuthial cut $\phi = 0$ . The incident field is a linear polarized plane wave. The far-field is obtained with the Mie solution and the PMCHWT, Müller, for three different discretizations. . . . .	46
3.9	Radiation pattern of a concrete sphere with unit radius on the azimuthial cut $\phi = 0$ . The incident field is a linear polarized plane wave. The far-field is obtained with the Mie solution and the PMCHWT, Müller, for three different discretizations. . . . .	47
3.10	Radiation pattern of a titanium sphere with unit radius on the azimuthial cut $\phi = 0$ . The incident field is a linear polarized plane wave. The far-field is obtained with Mie solution and the PMCHWT, Müller, for three different discretizations. . . . .	47
3.11	$L_2$ relative error of the far-field of a (top) PEC and (bottom) a diamond sphere with unit radiuses on the azimuthial cut $\phi = 0$ , in respect to the wavelength, using the (top) EFIE, MFIE, CFIE and (bottom) PMCHWT, Müller, for three different discretizations and comparing with the Mie solution. . . . .	48

3.12	Absorbed and scattered power efficiencies for a gold nanoparticle, irradiated with a linearly polarized plane wave, for a wide range of frequencies. The image of the gold nanoparticle is obtained from the department of chemistry and molecular biology of the University of Gothenburg. . . . .	51
3.13	(left) Actual capacitive lumped element of an RF coil and (right) modelled element with the delta-gap method (red line). . . . .	52
3.14	Scattering by a volume with permittivity $\epsilon(\mathbf{r})$ and permeability $\mu(\mathbf{r})$ . . . . .	55
3.15	Total electric field on the $\hat{y}$ axis of homogeneous spheres irradiated with a linear polarized plane wave, articulated from biological material properties, corresponding to 0.5 (green), 1 (red), 1.5 (magenta), 3 (cyan), 7 (blue), 14 (black) Tesla MRI. Each color represents a different sphere, and each marker a different resolution, according to the legend. . . . .	64
3.16	Convergence properties of JVIE (-PWC, -PWL) and DVIE formulations for the highly inhomogeneous realistic human body model “Billie”. . . . .	65
3.17	(a) Relative permittivity and (b) conductivity of a sagittal cut of “Billie” head, corresponding to 7T MR measurements. (c,d,e) Magnitude of the total electric field for the same sagittal cut calculated with DVIE, JVIE-PWC and JVIE-PWL respectively. (From left to right) 5, 2 and 1 mm <sup>3</sup> resolution. . . . .	67
3.18	(a) Relative permittivity and (b) conductivity of an axial cut of “Billie” head, corresponding to 7T MR measurements. (c,d,e) Magnitude of the total electric field for the same axial cut calculated with DVIE, JVIE-PWC and JVIE-PWL respectively. (From left to right) 5, 2 and 1 mm <sup>3</sup> resolution. (From left to right) 5, 2 and 1 mm <sup>3</sup> resolution. . . . .	68
3.19	(a) Relative permittivity and (b) conductivity of a coronal cut of “Billie” head, corresponding to 7T MR measurements. (c,d,e) Magnitude of the total electric field for the same coronal cut calculated with DVIE, JVIE-PWC and JVIE-PWL respectively. (From left to right) 5, 2 and 1 mm <sup>3</sup> resolution. (From left to right) 5, 2 and 1 mm <sup>3</sup> resolution. . . . .	69
4.1	Tucker decomposition of a low multilinear rank tensor $\mathcal{A}$ . . . . .	76
4.2	Canonical polyadic decomposition of a tensor $\mathcal{A}$ . . . . .	77
4.3	Tensor Train of $\mathcal{A}$ in $d$ dimensions. . . . .	78
4.4	Unfoldings of $\mathcal{A}$ . . . . .	79
4.5	Visual representation of Tucker + CP method. . . . .	84
4.6	Visual representation of the tensor decomposition-based solvers. . . . .	86
4.7	The maximum ranks of Green’s function tensors. They scale almost linearly with respect to frequency. . . . .	89
4.8	(Left axis) Maximum rank of the triplet $\{r_1, r_2, r_3\}$ for the worst case scenario and (right axis) overall compression factor for all the unique components of $\mathcal{N}$ . Results are shown for various tolerances. . . . .	91

4.9	(Left axis) Maximum rank of the triplet $\{r_1, r_2, r_3\}$ for the worst case scenario and (right axis) overall compression factor for all the unique components of $\mathcal{K}$ . Results are shown for various tolerances. . . . .	92
4.10	Relative error of the absorbed power and $ b_1^+ $ , between the Tucker decomposition-based approaches and the traditional one. . . . .	94
4.11	(from left to right and top to bottom) Relative permittivity, absorbed power calculated with the FFT-JVIE traditional solver, the HOSVD-based solver, and the Tucker+CP solver, conductivity and $ b_1^+ $ calculated with the same solvers respectively for a (a) sagittal, coronal (b) and an axial (c) cut of “Duke” realistic human head model, corresponding to 7 Tesla MRI applications. . . . .	95
4.12	(from left to right and top to bottom) Relative permittivity and conductivity on a coronal cut of “Billie” body model, corresponding to 7 Tesla MR-measurements. Total electric field, total magnetic field, polarisation current, absorbed power, $ b_1^+ $ and $ b_1^- $ . . . . .	96
4.13	(Left axis) Convergence time of GMRES and (right axis) memory footprint for all the unique components of $\mathcal{N}$ . On the top right corner we zoom on the convergence time of finer resolutions for enhanced visualization. . . . .	98
4.14	The relative error of the scalar absorbed power between the traditional FFT-JVIE, HOSVD, Tucker+CP methods, and the Mie series. . . . .	99
4.15	Sparse FFTs on the tensor of the unknown currents (green array). The yellow arrows define the direction of the zero-padding and the 1D FFTs. (left) Implementation of 1D FFTs over $x$ and $y$ dimensions and (right) 1D FFTs on the $z$ direction for one cubic set of unknowns. . . . .	100
4.16	Local absorbed power on (top) a sagittal and (bottom) an axial cut of “Billie”. (left) Traditional FFT-JVIE and (right) memory-efficient MatVec approach. The field is masked outside the head for enhanced visualization. . . . .	101
5.1	(top) Cylindrical coil and (bottom) Stadium coil. (left) The 8-channel triangular loop array loaded with the 4-compartment tissue-mimicking phantom (the relative permittivity and conductivity of each compartment are indicated in the legend) and the head model. (right) The locations of the lumped elements are shown for a representative array element. . . . .	108
5.2	The $S$ parameters of the cylindrical coil, while loaded with the 4-compartment phantom, after optimizing for the values of the variable capacitors. . . . .	113
5.3	The $S$ parameters of the stadium coil, while loaded with the “Duke” head model, after optimizing for the values of the variable capacitors. . . . .	114
5.4	(from left to right and top to bottom) The scattered electric and magnetic fields from each channel of the cylindrical coil, used as incident fields for GMT. . . .	114

5.5	(from left to right and top to bottom) Synthetic noisy MR measurements ( $ b_1^+ $ ) for each of the eight transmit coils, inside the central axial section of the tissue mimicking phantom. Peak SNR was set to 100. . . . .	115
5.6	(from left to right and top to bottom) The scattered electric and magnetic fields from each channel of the stadium coil, used as incident fields for GMT. . . . .	115
5.7	(from left to right and top to bottom) Synthetic noisy MR measurements ( $ b_1^+ $ ) for each of the eight transmit coils, inside an axial section of the head model. Peak SNR was set to 200. The field is masked outside the head for enhanced visualization. . . . .	116
5.8	Relative phase between the $b_1^+$ produced from the first channel and the rest in the interior structure of the head model with the stadium coil (port 1 to 8, from left to right and top to bottom). . . . .	117
5.9	(top) The stadium triangular coil loaded with the realistic human head model “Ella”. (bottom) The new $S_m$ parameters of the RF coil while loaded with “Ella” head model. The coil was tuned, matched and decoupled with “Duke” head model as a load. . . . .	119
5.10	Reconstructed EP using GMT with a homogeneous initial guess for the middle axial section of the phantom. Both EP were estimated with negligible error. . .	120
5.11	Reconstructed relative permittivity (top) and conductivity (bottom) for an axial, a sagittal and a coronal slice of “Duke” head model, using three different excitation patterns. From left to right, ground truth EP are compared with results for “SVD shimming”, “one port at a time”, and “all but one” voltage calibration patterns. . . . .	121
5.12	Reconstructed relative permittivity (left sub-figure) and conductivity (right sub-figure) are compared with ground truth EP, for an axial, a sagittal and a coronal plane of “Ella”, using the “one port at a time” excitation pattern. . . . .	122
5.13	The overlapping coil loaded with a cropped realistic human head model “Billie”. The coil was tuned, matched and decoupled with the same cropped head model as a load. . . . .	123
5.14	Reconstructed relative permittivity (left sub-figure) and conductivity (right sub-figure) are compared with ground truth EP, for an axial, a sagittal and a coronal plane of “Billie”, using the “one port at a time” excitation pattern and an overlapping RF coil desing. . . . .	123
5.15	Histograms of the PNAE for all voxels in the “Duke” head model. The error distribution is shown for (top) relative permittivity and (bottom) conductivity. Zoomed view of two regions of the histograms are also shown to highlight differences among the three excitation patterns. . . . .	124

5.16	(top) Absorbed power and (bottom) $ b_1^+ $ for an axial, a sagittal and a coronal planes of the “Duke” head model. Maps were calculated for a circularly polarized mode excitation using the ground truth EP (left) and the EP reconstructed with the “one port at a time” excitation pattern (middle). A map of the absolute difference is shown for each estimated measurement (right). . . . .	125
5.17	Histogram of the peak normalized absolute error for the (left) absorbed power and the (right) $ b_1^+ $ calculated using the EP reconstructed with the “one port at a time” approach for the “Duke” head model and the stadium triangular coil. . .	126
5.18	Relative permittivity (left) and conductivity (right) maps of “Duke” head model with a numerically inserted tumor. Ground Truth EP (top) and GMT reconstructions (bottom) are compared for the central axial plane of the tumor. . . .	127
5.19	The numerically inserted tumor is compared with the tumor segmented from the reconstructed conductivity map (top). The histogram of the reconstructed conductivity for the tumor voxels (bottom), showing that values were clustered around the actual value of 1.1 S/m. . . . .	129
5.20	Domain of interest that encloses all possible scatterers of choice (homogeneous cylinders, ellipsoids, and cuboids with random dimensions, where 3 to 12 spherical features with different EP were placed in their interior). The scatterers load the 8 channel radiofrequency cylindrical, triangular coil. The working frequency was 297.2 MHz, corresponding to 7 Tesla MRI. . . . .	131
5.21	Four randomly generated data-point geometries from a 10900 long dataset. Different colors indicate different spherical features. Each individual feature has different tissue-mimicking EPs. . . . .	132
5.22	Measurable MR quantities and EPs of four characteristic tissue-mimicking phantoms. (top) $ b_1^+ $ and (middle) relative phase between the first and the remaining seven channels (the orientation of the channels is left to right and top to bottom). (bottom, left) Relative permittivity and (bottom, right) electric conductivity. . .	133
5.23	3D UNET. (top) The chosen architecture of the network. The number of channels is shown above each layer. Each operation is followed by appropriate padding and dilation sizes to keep the dimensions consistent. (bottom) The table denotes the operations through the hidden layers of the network. . . . .	135
5.24	(left) Sum of mean squared errors for all training examples. An error close to 2% indicates good training, without overfitting. (right) Histogram of the MSE for both the relative permittivity and the conductivity for all individual 900 testing examples. The error remains small between 0% and 10%. . . . .	136

5.25 EP reconstruction using the proposed convolutional 3D UNET. (top,left) Reconstruction on two testing examples. (top, right) Reconstruction in the presence of additive Gaussian noise to the  $b_1^+$  with peak SNR (second line) 200, (third) 150, and (fourth) 100. (bottom) Reconstruction using different regularizers: (first line) Ground Truth, (second) CNN trained for 400 epochs, using dropout on the second third and fourth step of analysis and synthesis with rate 0.1, 0.25 and 0.5 respectively, (third and fourth) CNN Trained for 400 and 1600 epochs using dropout on the fourth step with rate 0.5 and  $L_2$  regularizer with weight 0.0001. . . . . 137

This page is intentionally left blank.



## LIST OF TABLES

---

3.1	Simulation characteristics for various spheres . . . . .	63
3.2	Number of iterations of GMRES for tolerance $10^{-5}$ . . . . .	64
4.1	Complexity of Novel Matrix-Vector Products . . . . .	85
4.2	Time Footprint in ms of Matrix Vector Product . . . . .	88
4.3	Memory Requirements of discretized $\mathcal{N}$ with PWL functions . . . . .	90
4.4	Memory (in MB) for the decomposed $\mathcal{N}$ and $\mathcal{K}$ tensors . . . . .	90
4.5	Convergence time of GMRES . . . . .	93
4.6	Convergence time of GMRES . . . . .	100
5.1	Information on the cylindrical 8-channel RF coil . . . . .	109
5.2	Information on the stadium 8-channel RF coil . . . . .	109
5.3	PNAME for the EP reconstructions . . . . .	120
5.4	Comparison of estimated EM field quantities . . . . .	126



# Chapter 1

## INTRODUCTION

---

**M**AGNETIC Resonance Imaging (MRI) has become an indispensable tool for the non-invasive biomedical imaging of biological tissue, disease diagnosis, and pathology characterization. Magnetic resonance (MR) belongs to a family of medical imaging techniques of radiology, such as the well-known X-ray radiography, ultrasound, computed tomography, and the positron emission tomography, among others. MR is established as a powerful modality because it does not expose the human body to harmful radiations. Thus it is widely used in neuroimaging, angiography, cardiovascular, musculoskeletal, liver, and gastrointestinal imaging. Paul Lauterbur [9] introduced MRI in 1973 based on the work of Felix Bloch [10] and Edward Purcell [11] in nuclear magnetic resonance in 1946. In the following decades, MRI became available for clinical usage in hospitals and medical centers, and the biomedical imaging quality was enhanced. MRI is still developing to this day, through a vast number of applications and the introduction of higher quality clinical scanners.

The imaging process in MRI depends on a large number of variables, such as the main power of the magnet, the operating frequency, the resonating atoms, the transceive coils, and their respective voltage calibration patterns, the receive coils, the magnetic field encoding, among others. Depending on the application of interest, specific sets of parameters are used, i.e., in most applications, the nuclei of  $^1H$  are resonated, at a frequency proportional to the gyromagnetic ratio  $\gamma = 42.58 \text{ MHz/Tesla}$ , since the human body consists mostly of water. During the last years, MR scientists focused on increasing the power of the magnet from 1.5 to 7 Telsa [12] to retrieve detailed images of the interior anatomical structure of the human body, by exploiting the larger signal-to-noise ratio (SNR) available with this larger main magnetic field. Regrettably, the resonating frequency of hydrogen atoms (Larmor frequency) multiplies the strength of the field, thus resulting in an operating frequency of  $\sim 300 \text{ MHz}$ . The associated wavelength inside the biological tissue is short enough to result in dominating interactions between electromagnetic (EM) waves and the tissue itself. Consequently, these interactions might lead to detrimental effects in the medical images' quality and strong radiofrequency (RF) power deposition in local spots of the tissue.

To tackle the impasse mentioned above, the accurate modeling of the EM phenomena is crucial. Truthfully, in ultra-high-field (UHF) MR scanners ( $\geq 7$  Tesla), the precise design of RF transmit coils and their associated EM fields is pivotal for practical applications, without the risk of compromising patient safety [13–16]. Therefore, the employed EM simulations have to lead to the superior numerical accuracy needed, without relinquishing computational time, to ensure quick testing of multiple designs. The present dissertation aims to provide a technique for a significant speed-up of such EM simulations.

Nevertheless, one can only perform a small number of EM simulations, since the number of available electrical property (EP) maps of realistic human body models [17] is quite small. Thus, results in simulation, could easily lead to erroneous predictions of the EM field behavior in patients with significantly different anatomical structures [18]. Although numerous *ex vivo* or *in situ* animal measurements have been made over time, preliminary access to *in vivo* EP distributions of human tissue have remained extremely limited, and indeed fundamental questions regarding the origin and distribution of these properties have tantalized scientists for decades. However, a reliable method for the non-invasive cross-sectional mapping of tissue electrical properties, based on measurements obtained with MR imaging systems has been proposed [3]. The method, dubbed Global Maxwell Tomography (GMT), provides an insight on the distribution of EM fields in tissue, which can be used to improve the diagnostic power of MR imaging, but could also enable marked improvement in speed and accuracy over current probe-based EM field mapping approaches used to satisfy safety regulatory requirements for wireless devices. Furthermore, *in vivo* electrical properties, maps could be employed as biomarkers for cancer (and other pathologies), as well as to improve the effectiveness of existing therapeutic modalities, such as RF ablation, RF hyperthermia, and electrochemotherapy. A part of this thesis is devoted to the performance investigation of GMT using realistic RF coils, in simulation, thus pushing it one step closer to future *in-vivo* experiments.

## 1.1 Historical and Literature Review

The EM phenomena in the macroscopic scale can be described with the solution of Maxwell's equations [19]. In general cases and applications, the geometry under-study is arbitrary, and the electrical properties are inhomogeneous, e.g., a human head, thus the equations are impossible to solve analytically. This fact, in line with the ever-increasing computational power of modern central processing units (CPU), has been the principal cause for the development of various numerical techniques for the estimation of the solution of Maxwell's equations [20]. All these methods synthesize the subject matter of computational electromagnetics (CEM) [21], which, over the years, has become a centerpiece of the EM field theory. The particular method of choice between the copiousness of arithmetic techniques is crucial since their respective particularities assess their reliability and effectiveness in the application of interest.

A wide variety of broadly employed over the past years and well-entrenched CEM techniques

can model the interactions between EM waves and biological tissue. Nevertheless, in MRI, the single operating frequency allows the customization of fast algorithms, if methods, based on integral equation (IE) formulations, are used, i.e., the magnetic-resonance integral equation suite (MARIE) [22–24] and the MARIE 2.0 (soon to be released) [1, 4] can produce reasonable EM field estimations in minutes for the analysis of a realistic human head model of clinical voxel resolution ( $5\text{mm}^3$  up to  $2\text{mm}^3$ ). The expression of IE formulations begins with the imposition of the boundary conditions for the electric and magnetic fields. Precisely, the boundary conditions are replaced from unknown equivalent sources using the surface or volume equivalence principles [25]. For inhomogeneous bodies, volume sources are used, while the conductors are replaced with a surface equivalent current source<sup>1</sup>. Depending on the initial boundary condition that was used one can end up to different IE formulations (i.e., for surfaces we can derive the electric or magnetic field integral equations, EFIE, MFIE, and for volumes the current, electric field or electric flux volume integral equations, JVIE, EVIE, DVIE, among others). The resulting equations can be solved using a discretization technique like the method of moments (MoM) for the estimation of the unknowns [26].

In both surface and volume integral equation (SIE, VIE), the boundary conditions between the interfaces of the media and the radiation conditions in the infinite sphere are amalgamated in the Green's functions. Thus, we only need to discretize the surfaces or the volumes of interest, which results in a dense matrix. The arising 4D or 6D integrals can be computed with quadrature rules, such as the Gauss-Legendre, while the singular integrals that arise in the diagonal of the matrix are tackled with highly sophisticated semi-analytical integrations [27, 28]. In SIE formulations, these matrices are usually small, since only the surface is discretized, however, in VIE the resulting MoM matrices are vast in terms of memory, and it is only possible to store them for very coarse resolutions.

For the dimensions of a human head, using an MRI clinical resolution of  $2\text{mm}^3$ , the arising MoM matrix requires millions of GB of storage memory, unavailable in any commercial CPU. This impasse led to the employment of the Fast Multipole Method (FMM) [29] in 1990 from Rokhlin [30] for the solution of the vector wave equation. The multilevel FMM (MLFMA) [31–37] compress the off-diagonal blocks of the MoM matrix and reduces its memory complexity from  $\mathcal{O}(n^2)$  to  $\mathcal{O}(n \log n)$ . Besides, the matrix-vector product can be implemented with  $\mathcal{O}(n \log n)$  operations<sup>2</sup> with the aid of an iterative solver of choice, instead of the  $\mathcal{O}(n^3)$  complexity of the Gaussian elimination (LU decomposition). In the next years, other methods have been proposed for the memory compression of the MoM-IE (i.e., the impedance matrix localization [38], the matrix decomposition method [39] and the wavelet decomposition method [40–49]).

Alternatively, the translational invariance property of the Green's function can be exploited

---

<sup>1</sup>We note that for a homogeneous volume, surface currents can still be used. We refer the reader for additional information on Chapters 2 and 3.

<sup>2</sup>The actual complexity is  $\mathcal{O}(cn \log n)$ , where  $c$  is a relatively big multiplicative constant.

if the discretization grid is uniform (or projected to one) to enforce a Toeplitz structure on the MoM matrix. In this case, the matrix-vector product can be carried out just by using the Toeplitz defining tensor in  $\mathcal{O}(n \log n)$  complexity<sup>3</sup>. These techniques exploit the Fast Fourier Transform (FFT) [50] inside an iterative solver, e.g., the conjugate gradient (CG) method, thus are dubbed as CG-FFT. In contrast with the MLFMA, the CG-FFT are suitable mostly for VIE problems, since, their application on SIE requires significant preprocessing with methods such as the precorrected FFT (pFFT) [51]. The VIE methods that employ the CG-FFT technique are dubbed FFT-based VIE or simply FFT-VIE. Here is a non-exhaustive list [52–65] of the applications and techniques that arose due to the versatility of the method. Very recently, a preconditioning technique for the FFT-VIE, based on Tony Chan’s work [66], was proposed, where the number of iterations of CG is reduced [67]. Regrettably, the method requires homogeneous EP (or close to homogeneous) for significant acceleration; thus, for a human head simulation, it is not applicable efficiently.

FFT-based VIE is employed in the open-source software MARIE package, thus the swift convergence time of the solver. Specifically, polynomial basis functions are used to map the equivalent electric currents to the electromagnetic field and precisely simulate the EM interactions between biological tissue and RF coils. However, in [4], it was shown that the results obtained with piecewise constant basis functions (PWC) were not able to achieve the desired superior numerical accuracy in clinical resolutions. Thus higher-order polynomials have to be avoided, i.e., piecewise linear basis functions (PWL). The numerical results were excellent, and the solver stable and robust, but, regrettably, the required memory footprint of the discretized Green’s function operators, formulated as tensors, was excessive, forbidding the usage of heterogeneous computing techniques (using CPUs and graphical processing units, GPU, in tandem). The inability to use a GPU is a drawback towards real-time simulations since the usage of its highly parallel architecture can lead to significant accelerations for the FFT and element-wise products in the matrix-vector product routine of the FFT-VIE.

The need for new fast methods in VIE is necessary. Thankfully, in MRI frequencies, the dimensions of the human body are comparable with the operating wavelength. Thus, the Green’s function VIE tensors<sup>4</sup> present low-rank properties [5,68], and their required memory footprint vastly decreases from hundreds of GB to dozens of MB. In the first part of this dissertation, we exploit this remarkable compression, using Tucker and other tensor decomposition algorithms. As a result, we can use GPUs for the acceleration of the matrix-vector, with proposed novel and efficient methods, achieving an order of magnitude speed-up over the traditional methods that cannot fit in GPU [1]. Namely, problems of 84 million unknowns can fit in a 12 GB GPU, and the time footprint of the matrix-vector product is less than two hours, while the traditional methods need around twelve.

<sup>3</sup>In this case, the multiplicative constant is much smaller than the one appearing in MLFMA.

<sup>4</sup>The Toeplitz defining vectors of the MoM matrix are formulated as tensors since the geometries under study are 3D.

In parallel with the development of the methods presented herein, other EM scientists employed tensor decompositions for the memory compression of IE formulations. Specifically, the authors in [69, 70] employed the higher-order singular value decomposition (HOSVD) to compress the storage, of the translation operator tensors in FMM-FFT, accelerated SIE formulation [71], up to 90%. The authors in [72, 73] propose a new method dubbed conjugate gradient-tensor train (CG-TT). They reshape the MoM matrix of SIE and VIE formulations to a multi-dimensional array and compress it with the TT-cross approximation [74] algorithm to reduce the memory and operations complexity. However, CG-TT is only applicable for problems with homogeneous EP since the method compresses the whole MoM matrix and not just the Green's function tensors, as in our case.

The shrewd reader could argue that machine learning methods can be employed for the speed-up of VIE simulations. A safe way to apply machine learning is with the novel architectures of autoencoders [75] and UNETs [76]. Precisely, one could build a tensor-to-tensor translation network between pairs of EP distributions and incident fields and polarisation currents and then using these currents as an initial guess of the iterative solver used in FFT-based VIE. The better initial guess, used in tandem with the proposed tensor decomposition-based methods, could lead to even faster simulations, since the iteration count would be much smaller, comparing to the one obtained by initiating the solver with zeros everywhere. However, for human head simulations, the realistic and available data are ten [17], a number too small for robust neural network (NN) training. Variations, translations, and rotations [77] can be employed to such heads, but still, the resulting dataset will not be rich enough for generalization in entirely different testing head models.

The previous paragraph is just one small example of the usability of accurate EP tomography-mapping (EPT) for heads. The EP reconstruction concerns the second part of this thesis since their in-vivo access will lead to a series of applications, except the availability of machine learning datasets. The EPs, namely, relative electric permittivity and electric conductivity, can be used as additional biomarkers<sup>5</sup> for pathogenic processes, especially for the detection of malignant tumors. From ex-vivo experiments [78–80], we already know with confidence that the electric conductivity and relative permittivity of tumors, e.g., malignant tumor in the liver, infiltrating breast carcinoma, human glioma, change up to 30% comparing to the peripheral and surrounding tissues. Thus, not only the widely-known electrochemotherapy [81, 82] can be improved, but also the hyperthermia [83, 84], which is directly connected with the power deposition, thus the EP distributions of the tissue.

Moreover, the undeviating relation between the EP and the EM waves, through Maxwell's equations, make the EPT a versatile tool to address the safety concerns in UHF MRI. Concretely, the generated incident EM waves from the RF coils have short wavelengths in these frequencies, and the arising interactions between them and the biological tissue can lead to damages due

---

<sup>5</sup>There is already access to the relaxation times,  $T_1$  and  $T_2$ , and the proton density through the traditional MRI.

to high heating. However, prior knowledge of the EP distribution of the tissue can result in patient-specific simulations for various coil designs, thus ensure the safety prerequisites for efficient scanning. The main metric used to study these problems is the specific absorption rate (SAR) given from

$$\text{SAR} = \iiint_{\mathcal{V}} \frac{\sigma_e(\mathbf{r}) |\mathbf{e}(\mathbf{r})|^2}{\rho(\mathbf{r})} d\mathbf{r} \quad (1.1)$$

where  $\mathcal{V}$  is the volume of the tissue in study,  $\mathbf{r}$  is the vector of the position,  $\mathbf{e}(\mathbf{r})$  is the electric field intensity,  $\sigma_e(\mathbf{r})$  is the electric conductivity and  $\rho(\mathbf{r})$  is the proton density (additional details can be found in Chapter 2). SAR should be lower than a predefined upper bound to avoid tissue overheating. Unfortunately, the higher the frequency, the higher the magnitude of the electric field intensity, thus the higher the SAR. Therefore, to ensure that the upper bound of SAR is not reached, highly accurate, and patient-specific, simulations have to be used, for which EPT is a ubiquitous commodity.

Historically, the EPT has proven to be a by no means trivial task. In the following, we will briefly mention all the proposed methods developed and used over the years for the EPT. On the one hand, before the widespread use of magnetic resonance tomography, scientists used several antennas and sensors placed around the body that radiate incident electromagnetic fields to the biological tissue under study. The backscattering radiation was measured using receiver antennas on the surface of the body. The resulting inverse problem is heavily ill-posed, meaning that it is severely underdetermined since the receivers are much less than the number of unknowns (even in very coarse resolutions), and leads to non-unique solutions. On the other hand, the usage of MR measurements, that encode the spatial distributions and the anatomical structure of the tissue in the received signal, was proposed. According to Bloch's equations (the fundamental equations in MRI), the signals are related to the total magnetic field in the interior of the body; thus, the problem becomes significantly more well-posed. This unique advantage led to the naming of these methods as MR-based, while for the aforementioned to non-MR-based. In the following, we will briefly refer to some of the most well-known EPT methods, starting from the non-MR-based ones.

The oldest non-MR method is the electrical impedance tomography (EIT). This non-invasive technique aims to infer the EPs of the biological tissue, by employing the voltage measurements obtained from arrays of electrodes placed on the surface of the body [85–89]. The mechanics of the method start with the imposition of electric currents on the body, using an electrode pair. At the same instant, the voltages of the receiving electrode pairs are measured. The voltage measurement is repeated for every pair of electrodes and results in a cross-sectional image of the EP distributions. The speed and the simplicity of the method are quite evident from its mechanics, while the electromagnetic radiation appearing is not harmful to the human body (small magnitude of the electric currents, zero ionizing radiation). Regrettably, the method has three significant drawbacks. First, it only works for low spatial resolutions. Second, a finite number of

electrode pairs can be used, thus, resulting in a small number of measurements, and third, the SNR is low. The problem is inherently ill-posed; thus, the authors in [90] propose to use EIT for breast carcinoma detection by combining it with other cancer diagnosis methods.

The counterpart of the EIT is called magnetic induction tomography [91] (MIT). Here, the electrodes are replaced by coils, which operate as receive and transmit antennas. In EIT, the direct contact between body and electrodes led to small SNR due to the movements of the patient. In the case of MIT, SNR is higher, since both receive and transmit coils are placed away from the body. MIT can accurately determine the geometrical characteristics of the target [92]. However, the inverse problem to solve is still highly ill-posed, and only low spatial resolutions can be obtained.

Although MR measurements are used, the magnetic resonance electrical impedance tomography (MREIT) belongs to the same family of EIT and MIT. The induced by the electrodes, electric currents on the surface of the body scatter EM fields in the inner biological tissues. Thus, magnetic flux density arises (Maxwell's equations), which can be measured by employing an MR scanner. The usage of the MR measurements allows for EP cross-sectional images with very fine resolutions ( $\leq 1 \text{ mm}^2$ ) [93–95]. In [96], the first MREIT in-vivo experiment was performed. Nevertheless, the method is still not suitable for clinical usage: The image resolution substantially worsens, if the magnitude of the induced electric current is small enough to ensure the patient safety prerequisites. Higher magnitudes put the safety of the patient at risk.

Another technique, dubbed magnetoacoustic tomography with magnetic induction (MAT-MI), was developed by Yuan Xu et al. in 2005 [97]. The method starts with the positioning of the body in a magnetostatic and a magnetodynamic field. According to Faraday's law of induction, the magnetodynamic field induces eddy current on the body. Due to the magnetostatic field, this current produces mechanical vibrations, which results in the propagation of ultrasonic waves (Lorentz force). As in EIT and MIT, a set of receivers <sup>6</sup> outside the body collect the waves to perform the EP reconstruction. In [98], the authors discuss the limitations and potential clinical usage of MAT-MI.

The authors in [99] exploit the ordinary Hall effect for the reconstruction of the electric conductivity. Edwin Hall discovered ordinary Hall effect in 1879 [100] and is expressed as follows: If a magnetic field is applied to an electric conductor, perpendicular to an electric current on the conductor, then a voltage difference <sup>7</sup> is generated over the conductor and transverse to the current. The Hall effect imaging (HEI) employs an ultrasound pulse, and the resulting acoustic waves, which encode the spatial information of the voltage difference, are collected and used for conductivity reconstruction. The method has promising potential for the reconstruction of high-quality images. However, it is still in the prototype stage [101].

Microwave imaging is a promising method for the detection of abnormalities, such as breast carcinoma [102–104] and brain tumors [105, 106]. In the same manner, as in EIT and MIT,

---

<sup>6</sup>Detectors is a more appropriate term since the waves are ultrasonic.

<sup>7</sup>The so-called *Hall Voltage*

the idea is the usage of transceiving and receiving antennas in the microwave frequencies. The backscattered EM field is collected and recorded. Microwave imaging is very ill-posed; thus, the high-resolution images are vulnerable to noise and unwelcome reflections. However, the low cost of the modality makes it very useful in other applications, such as the quick detection of foreign bodies in food containers [107]. Since microwave imaging is suitable for abnormalities detection, the resulting images can be used as a fruitful classification dataset for a machine learning algorithm.

The methods described above can be used for abnormality detection, but are unable to produce high resolute images. Thus the EPT of a highly inhomogeneous biological brain is not feasible. To produce such images, methods that exploit the spatial information encoded in the MR signal are used. The first MR-based method was introduced in 1991 by Haacke et al. [108], where the reconstruction of multilayered phantoms was performed in simulations for 1 and 1.5 Tesla scanners. Even by exploiting the MR data, the problem is still ill-posed, and the reconstructions were not good. In 2003 Han Wen performed a non-invasive quantitative electric conductivity reconstruction in animal experiments [109]. In 2009 [110] an EPT mapping was performed using the complex transceive magnetic flux ( $b_1^+$ ). In this case, an assumption is made for the phase of  $b_1^+$ , which does not hold in UHF scanners [111]. The only truly measurable quantities in MR are the absolute values of the  $b_1^+$  and the relative phases between each excitation channel [112]. Later in 2012, Local Maxwell Tomography (LMT) was proposed, which is assumption-free but requires additional scanning time, which is not pleasant for the patient. Furthermore, the methods, as mentioned earlier, exploit the partial differential (PDE) forms of Maxwell's equations. Thus, the computation of the EP distributions leads to MRI noise amplifications<sup>8</sup>. To tackle the noise amplification impasse and to remove the boundary artifacts appearing between different tissues, gradient methods were proposed [114, 115]. In [116, 117], the authors formulate the problem as an optimization-minimization of a cost function between simulated (obtained from the solution of the forward model) and experimental MR measurements. These approaches are accompanied by a Total Variation (TV) regularizer to account for the noise. Deplorably, the methods require assumptions that are not true in UHF, and the EP distribution presents discontinuities between tissue boundaries. These approaches are tested both for simulation and in-vivo experiments. In 2015, the contrast source inversion-EPT (CSI-EPT) was proposed [118]. The method uses the IE form of Maxwell's equations, where the noise amplification of the  $b_1^+$  does not appear since its Laplacian is not calculated. Nevertheless, this method only works for symmetrical scatterers, and it was not generalized to 3D scatterers.

In the present thesis, GMT is employed for the EP reconstruction of brain tissue [3]. GMT is an assumption-free method and only employs measurable MR quantities for the formulation of an inverse problem. The goal is to minimize a cost-function between iteratively simulated MR measurements and experimental ones. For the solutions of the forward problem, the volume IE

---

<sup>8</sup>The EP distributions are proportional to the Laplacian of the  $b_1^+$  [113]

## 1.2. Thesis Structure and Contribution

---

representation of Maxwell's equations is employed. To make the inverse problem robust to noise, the so-called *match regularizer*, is used. The gradient of the cost function and the regularizer are calculated analytically, ensuring superior accuracy and a faster optimization algorithm. The method is 3D, and it is highly parallelizable to  $n$  independent problems, corresponding to each of the  $n$  excitations. GMT is tested in simulation for 7 Tesla MRI frequencies, where the  $b_1^+$  encodes additional anatomical information, in contrast to MR scanners with lower field strength, i.e., 3 and 1.5 Tesla. In our initial work, GMT [3] was verified using an ideal excitation, an ultimate EM basis with randomly excited and randomly oriented dipoles. This basis produced orthonormal excitations that proved to be favorable for the EP reconstruction. However, the excitations were ideal, and it is yet unknown how a traditional RF coil could generate the same current distributions as the basis.

Nevertheless, an experiment was performed for the EP reconstruction of a homogeneous cylinder in [3], using the excitations produced by a coil design presented in [119, 120]. The coil is an eight-channel transmit-receive array, and its construction allows for excellent decoupling between all channels. The resulting  $b_1^+$  maps differ for each channel, thus, producing an orthogonal set. In [6, 7] we attempted the reconstruction of more challenging inhomogeneous tissue-mimicking phantoms, and the results were excellent. Finally, in our currently under-review work [2], we are proposing the usage of a novel RF coil design, uniquely designed for brain tissue EP reconstruction.

With the recent rise of deep learning [121], it was only a matter of time until the EPT was attempted with a NN. In 2019 Stefano Mandija et al. attempted to reconstruct the EP of brain tissue by training an image-to-image translation network. The method is a brute-force network in 2D where the input is the  $b_1^+$  map and the spin-echo MR image, and the output the relative permittivity or the electric conductivity<sup>9</sup>. While the reconstruction for cases close to the training dataset is admirable, this approach deals with the problem more from the scope of image similarities and less from the underneath electrodynamic phenomena. We propose a more general approach, where we train a NN with input only the measurable  $b_1^+$  quantities, and output both EP, for the whole 3D volume of the scatterer. The proposed tensor-to-tensor translation network investigates on the feasibility of the EPT using NNs, for simple tissue-mimicking inhomogeneous scatterers [8].

## 1.2 Thesis Structure and Contribution

The subjects of the work presented herein are mainly motivated by the impasses described in the previous section. The thesis can be divided into two main parts. The first one aims to develop new memory-efficient methods for the execution of FFT-based VIE simulations in GPU, even for fine resolutions, thus providing a significant acceleration over traditional approaches. The second part of this thesis investigates the performance of GMT, using novel problem-dedicated RF coil

---

<sup>9</sup>Two networks are trained: One for the relative permittivity and one for the electric conductivity

designs, thus pushing it one step closer to in-vivo experiments and clinical usage. An attempt to perform the EPT using deep learning networks is proposed. Each chapter of the thesis furnishes the reader with a wide variety of results, showing the superior performance of the novel methods, mainly focusing on problems of MRI. In the following paragraphs, we describe the contents and the novel contributions of this dissertation.

The first introductory Chapter starts with the presentation of a literature review in the research activity related to memory compression techniques of integral equation formulations, in problems of electromagnetics. A variety of methods is referred, while a novel method, based on tensor decompositions, is proposed. With the aid of GPU, high-speed simulations can be carried efficiently even for fine resolutions. Subsequently, methods for the reconstruction of the electrical property distribution of biological tissue are presented. The difficulties of these methods are recorded, where, up to this day, none of them managed to be employed for clinical usage. The advantages and disadvantages of GMT are stated, while a problem-dedicated RF coil design is proposed to push GMT one step closer to future in vivo experiments. Finally, some light is shed on the usage of deep learning algorithms for the EP reconstruction problem. Both the tensor decomposition method for fast simulations, and the novel RF coil design, demonstrate - according to the writer - the critical parts of this dissertation, while they underline its necessity and importance.

In the second Chapter, fundamental theorems and elements of electromagnetism are presented. First, the general form of Maxwell's equations is written, followed by their integral and the time-harmonic form. A paragraph is devoted to the proof of boundary conditions between two media with different electromagnetic properties. Furthermore, the superposition, the duality, and the reciprocity theorems are introduced, followed by the definition of the dyadic Green's function and the vector wave equation. These fundamental aspects are essential for the derivation of the surface and volume equivalence theorems, which with their turn, are vital for the derivation of the SIE and VIE formulations, respectively, used later in the thesis. The Chapter is concluded with brief addressing of the MoM, a technique used for the efficient numerical solution of SIE and VIE.

A detailed presentation of the IE methods for the solution of scattering problems from conductive and homogeneous surfaces and inhomogeneous volumetric objects is the subject of the third Chapter. The Chapter is divided into two main sections. Specifically, the first section of the Chapter is devoted to -as far as possible- the best possible representation of all those steps required to numerically solve the state-of-the-art surface integral equations, with the help of the MoM, both for perfect electric conductors (PEC) and for homogeneous objects. In particular, the critical role of Rao-Wilton-Glisson (RWG) basis functions in the discretization of the SIE is highlighted, per the Galerkin equation. Answers are also given to all issues related to corresponding MoM matrix element calculations, as well as the system's solution. Multiple SIE formulations are studied, with the main focus of the EFIE for PEC, where its numerical problems are presented.

Results of the far-field and the power are shown for spherical scatterers, and the accuracy of SIE is verified via comparisons with the Mie series solution. The SIE section is concluded with two paragraphs on the lumped elements modeling on top of conducting surfaces, and the network parameters' calculation of PEC RF coils modeled with the EFIE. Even though none of the aforementioned results present any novelty, they aim to provide the reader with a deeper understanding of SIE and their versatility and usefulness on problems of EM radiation. The second section of the third Chapter focuses on VIE. A theoretical investigation of the performance of multiple VIE formulations is shown, and the superiority of JVIE is established. The JVIE discretization with polynomial basis functions is described, and the discretized Green's function operators, namely  $\mathcal{N}$  and  $\mathcal{K}$ , are shown. An assiduous analysis of the DVIE formulation follows, which is used by the MR community to study the EM phenomena that occur in the presence of human tissue. There, the precise details of the CG-FFT algorithm are shown. Subsequently, the superiority of JVIE over the DVIE formulation is presented by performing simulations on a realistic head model for multiple discretizations. Not only JVIE, expanded with PWL basis functions, converges faster to the solution, but it is also more accurate in the entire region of the head model. The Chapter closes by mentioning the so-called coupled VIE-SIE (VSIE) solvers.

The development of a series of methodologies for the memory footprint reduction of the tensors appearing in FFT-VIE methods, along with a set of novel matrix-vector product implementations, is the subject of the fourth Chapter. The usability of the new methods is verified by a plethora of results. In particular, the Tucker decomposition, the canonical polyadic model (CP), and the TT decomposition are employed through a varied set of numerical linear algebra algorithms, i.e., HOSVD, cross-Tucker, Tucker+CP, for the compression of the Green's function tensors appearing in the discretized FFT-VIE formulations. The immense memory compression enables the usage of GPUs, even for fine discretizations, and problems that bow to fate to CPU execution for hours can now be simulated in fifteen minutes. This speed-up corresponding to an order of magnitude of acceleration is achievable since novel matrix-vector product methods are proposed, where the linear complexity of the element-wise product (used in the traditional matrix-vector product) is preserved. The new methods are tested in EM simulations for the scattering of realistic human head and body models. Their accuracy, in some cases, is higher than the tolerance of the iterative solver, which results in zero error between them and the traditional technique. Finally, the Chapter is concluded by providing a mathematical trick in the implementation of the FFT in the tensor of the unknowns, which allows additional memory compression, so problems with up to 84 million unknowns can be solved in a 12 GB GPU fast.

In the fifth Chapter, a novel RF coil design is developed and used in tandem with the GMT algorithm for the EP reconstruction of biological head tissue in a simulated 7 Tesla MRI environment. The design is inspired by a smaller coil, used for the reconstruction of tissue-mimicking phantoms, also presented in the Chapter. The fundamental theory behind GMT is briefly mentioned, while the disadvantages of the ideal excitation used in earlier GMT reconstructions are

presented. Afterward, the EFIE for PEC scatterers, extensively described in the third Chapter, is employed for the modeling of the RF coils, while the effect of the lumped elements is included in the MoM using the delta-gap method. To perform RF coil, tuning, matching, and decoupling, a novel optimization process was developed, which optimizes the values of the variable capacitors, spread across the coil, to ensure power transfer from the feeding ports to the loading scatterer, and minimize reflections. A set of carefully designed experiments follows. Specifically, using different voltage calibration patterns, the EP reconstructions are presented, with small error over the ground truth. The reconstructed properties are enough to estimate the electromagnetic field intensities in the interior of the scatterer, with excellent accuracy. Finally, the superior performance of the coil is shown for the challenging case of a head model with a malignant tumor. GMT can detect the tumor's location, while its reconstructed EPs are precise. The last section of the fifth Chapter studies the performance of a convolutional neural network (CNN) for the translation of MR measurements to EP maps. The proposed network is the well-known UNET for 3D data. A dataset of simple geometrical objects with different shapes and EP is generated, while randomly, a random amount of spherical features (with random EP each), is inserted in every one of these objects. The network shows good performance for a vast number of testing examples that did not exist on the training set. However, it is noted that this network is just one particular example; thus, robust conclusions cannot be driven yet, regarding the usage of machine learning in the EP reconstruction problem.

Last but not least, in the Conclusion chapter, the contributions of the methods presented in the thesis are summarized, and future projects are suggested. After the bibliography section, five appendices are included for completeness. Correctly, in appendix A, the Mie series solution for spherical scatterers is presented. In B preliminary details on Wirtinger calculus are noted. In C, we summarize some numerical linear algebra definitions and algorithms, used extensively in the thesis. In D, the numerical integration techniques, employed for the computation of the integrals appearing in SIE and VIE, are shown. Finally, in appendix E, the computation of the gradient of a cost-function is described.

This page is intentionally left blank.



# Chapter 2

## ELECTROMAGNETIC THEORY

---

### 2.1 Fundamental Theorems of Electromagnetism

#### 2.1.1 Maxwell's Equations and Boundary Conditions

THE problems of electromagnetism can be described from the four Maxwell's equations [19] and all numerical forms for electromagnetic field calculations starts from them. The most known form of the equations is their differential time-domain form, which was presented in 1861 from James Clerk Maxwell as a combination of equations proposed by Gauss, Ampere, Faraday, and Henry.

$$\begin{aligned}\nabla \times \mathfrak{H} &= \mathbf{J} + \frac{\partial \mathbf{D}}{\partial t} && \text{Ampere-Maxwell law} \\ \nabla \times \mathfrak{E} &= -\mathfrak{M} - \frac{\partial \mathfrak{B}}{\partial t} && \text{Faraday's law} \\ \nabla \cdot \mathfrak{B} &= \rho_m && \text{Gauss' law for magnetic fields} \\ \nabla \cdot \mathbf{D} &= \rho_e && \text{Gauss' law.}\end{aligned}\tag{2.1}$$

In the above equations and for the rest of this dissertation  $t$  is time measured in seconds,  $\mathfrak{E}$  is the electric field intensity in V/m,  $\mathbf{D}$  is the electric flux density in C/m<sup>2</sup>,  $\mathfrak{H}$  is the magnetic field intensity in A/m,  $\mathfrak{B}$  is the magnetic field density in Wb/m<sup>2</sup> := T,  $\mathbf{J}$  is the electric current density in A/m<sup>2</sup>,  $\mathfrak{M}$  is the magnetic current density in V/m<sup>2</sup>,  $\rho_e$  is the electric charge density in C/m<sup>3</sup> and  $\rho_m$  is the magnetic charge density in Wb/m<sup>3</sup>.  $\mathfrak{M}$  and  $\rho_m$  are fictitious quantities and are employed only for mathematical utility in the equations. All units are derivatives from the *International System of Units* (SI).

We can derive additional equations by taking the divergence of Ampere-Maxwell law or Faraday's law and applying the Gauss' law for magnetic fields or Gauss' law, respectively. By making

use of calculus identities, one can find the following *continuity equations*

$$\begin{aligned}\nabla \times \mathfrak{H} &= \mathbf{J} + \frac{\partial \mathcal{D}}{\partial t} && \text{electric charges} \\ \nabla \times \mathfrak{E} &= \mathfrak{M} - \frac{\partial \mathcal{B}}{\partial t} && \text{magnetic charges.}\end{aligned}\tag{2.2}$$

The continuity equations can be used as fundamental ones instead of the Gauss' laws. Although, for this dissertation, the four Maxwell's equations are considered the fundamental equations. Additionally, a set of natural relationships between some terms appearing in Maxwell's equations is defined as follows.

$$\begin{aligned}\mathcal{D} &= \epsilon_0 \epsilon_r \mathfrak{E} \\ \mathcal{B} &= \mu_0 \mu_r \mathfrak{H} \\ \mathbf{J} &= \sigma_e \mathfrak{E} \\ \mathfrak{M} &= \sigma_m \mathfrak{H},\end{aligned}\tag{2.3}$$

where the scalar terms are the so-called *electrical properties*,  $\mu_0$  is the vacuum magnetic permeability, and it is equal to  $4\pi \cdot 10^{-7}$  (H/m).  $\epsilon_0$  is the vacuum electric permittivity, and it is equal to  $1/(\mu_0 c^2)$ , with  $c = 299792458$  m/s being the speed of light.  $\epsilon_r$  and  $\mu_r$  are the media's relative permittivity and permeability, respectively, while  $\sigma_e$  and  $\sigma_m$  are the electric and magnetic current conductivity measured in S/m and  $\Omega$ /m respectively.

These terms characterize the electrodynamic and electrostatic behavior of the media and play a fundamental role in the problems studied in this dissertation. The electrical properties  $\epsilon_r$ ,  $\mu_r$ ,  $\sigma_e$ , and  $\sigma_m$  can vary through the material's section where they are categorized as homogeneous if they are constant through the whole material or inhomogeneous if they are not. Moreover, they are called dispersive if their value changes along with the operating frequency. Finally, they are characterized as linear if they are independent of the field intensities and isotropic if they are independent of the field polarity. For example, a human head is dispersive, highly inhomogeneous, linear, and isotropic <sup>1</sup>.

Through this point, we have introduced the most fundamental concepts of electromagnetism. In the remaining of this Chapter we will introduce additional theorems of electromagnetism and work our way to a robust definition of an integral equation formulation that can be solved numerically and return the electromagnetic field measurements of a known media and excitation pattern <sup>2</sup>. Towards this direction, we will derive the integral form of Maxwell's Equations.

### 2.1.1.1 Integral form of Maxwell's Equations

Let us consider an open Euclidean surface  $\mathcal{S}_1$  terminated by a contour  $\mathcal{C}$  and a Euclidean surface  $\mathcal{S}_2$  enclosing a volume  $\mathcal{V}$ , shown in the left of 2.1 and right respectively.

<sup>1</sup>The EPs are anisotropic; however, the effect of the anisotropy is negligible in high-field, and UHF MRI related studies

<sup>2</sup>a wide variety of textbooks investigate deeply on these theories of electromagnetics [20, 26, 122–128], thus, we will keep the definitions brief

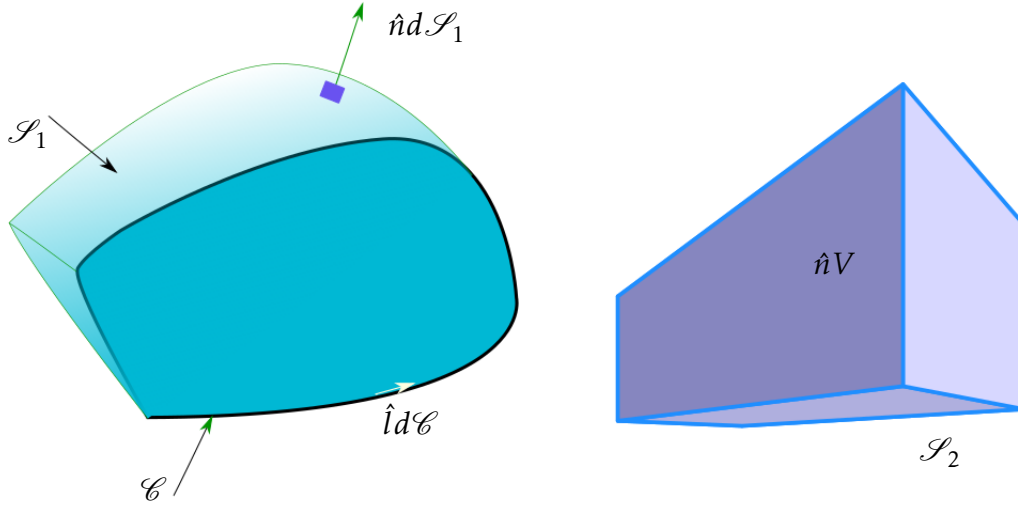


Figure 2.1: (left) Open Euclidean surface  $\mathcal{S}_1$ , terminated by a contour  $\mathcal{C}$ , and their respective differential elements. (right) Euclidean surface  $\mathcal{S}_2$  enclosing the volume  $\mathcal{V}$ .

By integrating the Ampere-Maxwell and the Faraday's law over the surface  $\mathcal{S}_1$  and applying Kelvin-Stokes theorem, we derive the following

$$\begin{aligned}
 \iint_{\mathcal{S}_1} (\nabla \times \mathfrak{H}) \cdot d\mathcal{S}_1 &= \iint_{\mathcal{S}_1} \mathbf{J} \cdot d\mathcal{S}_1 + \iint_{\mathcal{S}_1} \frac{\partial \mathfrak{D}}{\partial t} \cdot d\mathcal{S}_1 \Rightarrow \\
 \oint_{\mathcal{C}} \mathfrak{H} \cdot \hat{l}d\mathcal{C} &= \iint_{\mathcal{S}_1} \left( \mathbf{J} + \frac{\partial \mathfrak{D}}{\partial t} \right) \cdot d\mathcal{S}_1 \\
 \iint_{\mathcal{S}_1} (\nabla \times \mathfrak{E}) \cdot d\mathcal{S}_1 &= - \iint_{\mathcal{S}_1} \mathfrak{m} \cdot d\mathcal{S}_1 - \iint_{\mathcal{S}_1} \frac{\partial \mathfrak{B}}{\partial t} \cdot d\mathcal{S}_1 \Rightarrow \\
 \oint_{\mathcal{C}} \mathfrak{E} \cdot \hat{l}d\mathcal{C} &= - \iint_{\mathcal{S}_1} \left( \mathfrak{m} + \frac{\partial \mathfrak{B}}{\partial t} \right) \cdot d\mathcal{S}_1,
 \end{aligned} \tag{2.4}$$

where  $\hat{n}$  is the surface normal vector,  $d\mathcal{S}_1$  is the differential surface element and  $\hat{l}d\mathcal{C}$  is the differential contour element. Integrating Gauss' laws and applying Gauss' theorem (divergence theorem) we end up to the following equations

$$\begin{aligned}
 \iiint_{\mathcal{V}} (\nabla \cdot \mathfrak{D}) \cdot d\mathcal{V} &= \iiint_{\mathcal{V}} \rho_e d\mathcal{V} \Rightarrow \oiint_{\mathcal{S}_2} \mathfrak{D} \cdot d\mathcal{S}_2 = \iiint_{\mathcal{V}} \rho_e d\mathcal{V} \\
 \iiint_{\mathcal{V}} (\nabla \cdot \mathfrak{B}) \cdot d\mathcal{V} &= \iiint_{\mathcal{V}} \rho_m d\mathcal{V} \Rightarrow \oiint_{\mathcal{S}_2} \mathfrak{B} \cdot d\mathcal{S}_2 = \iiint_{\mathcal{V}} \rho_m d\mathcal{V},
 \end{aligned} \tag{2.5}$$

where  $d\mathcal{V}$  is the differential volume element and  $d\mathcal{S}_2$  the differential surface element.

### 2.1.1.2 Time-harmonic form of Maxwell's Equations

Plethora of electromagnetic related problems, and especially MRI applications which are the main interest of this thesis, use time-harmonically varying fields, at a working frequency (or frequencies)  $f$ , measured in Hz. In this case the following equation holds true for the electric field

$$\mathbf{E} = \mathcal{R}e\{\mathbf{e}e^{-i\omega t}\}, \quad (2.6)$$

where  $\omega$  is the angular frequency equal to  $2\pi f$ , measured in rad/s and the complex vector  $\mathbf{e} \in \mathbb{C}^3$  is called electric field phasor. Thus, for time-harmonic electromagnetic fields, using 2.1 and 2.6 one can rewrite Maxwell's equations in the following simplified form

$$\begin{aligned} \nabla \times \mathbf{h} &= \mathbf{j} - i\omega\epsilon_0\epsilon_r\mathbf{e} \\ \nabla \times \mathbf{e} &= -\mathbf{m} + i\omega\mu_0\mu_r\mathbf{h} \\ \nabla \cdot (\mu_0\mu_r\mathbf{h}) &= \rho_m \\ \nabla \cdot (\epsilon_0\epsilon_r\mathbf{e}) &= \rho_e. \end{aligned} \quad (2.7)$$

All of the equations as mentioned earlier can be redefined using this simpler representation for time-harmonic fields.

In general, in the problems of electromagnetism, the current densities can be separated into excitation and induced currents. By definition, this phenomenon is expressed as

$$\mathbf{j} = \mathbf{j}_{\text{exc}} + \sigma_e\mathbf{e}, \quad \mathbf{m} = \mathbf{m}_{\text{exc}} + \sigma_m\mathbf{h}. \quad (2.8)$$

The electric and magnetic conductivities can be expressed as the imaginary part of a complex relative permittivity and permeability given from the following

$$\epsilon = \epsilon_0 \left( \epsilon_r - i \frac{\sigma_e}{\omega\epsilon_0} \right), \quad \mu = \mu_0 \left( \mu_r - i \frac{\sigma_m}{\omega\mu_0} \right), \quad (2.9)$$

and they represent the material losses. Using the above one can rewrite Maxwell's equations (using the continuity equations 2.2 in their time-harmonic form), as follows

$$\begin{aligned} \nabla \times \mathbf{h} &= \mathbf{j}_{\text{exc}} - i\omega\epsilon\mathbf{e} \\ \nabla \times \mathbf{e} &= -\mathbf{m}_{\text{exc}} + i\omega\mu\mathbf{h} \\ \nabla \cdot (\mu\mathbf{h}) &= -\frac{\nabla \cdot \mathbf{m}_{\text{exc}}}{i\omega} \\ \nabla \cdot (\epsilon\mathbf{e}) &= -\frac{\nabla \cdot \mathbf{j}_{\text{exc}}}{i\omega}, \end{aligned} \quad (2.10)$$

or in their integral form as

$$\begin{aligned}
 \oint_{\mathcal{C}} \mathbf{h} \cdot \hat{l} d\mathcal{C} &= \iint_{\mathcal{S}_1} (\mathbf{j}_{\text{exc}} - i\omega\epsilon\mathbf{e}) \cdot d\mathcal{S}_1 \\
 \oint_{\mathcal{C}} \mathbf{e} \cdot \hat{l} d\mathcal{C} &= - \iint_{\mathcal{S}_1} (\mathbf{m}_{\text{exc}} - i\omega\mu\mathbf{h}) \cdot d\mathcal{S}_1 \\
 \oiint_{\mathcal{S}_2} \epsilon\mathbf{e} \cdot d\mathcal{S}_2 &= \iiint_{\mathcal{V}} \frac{\nabla \cdot \mathbf{j}_{\text{exc}}}{i\omega} d\mathcal{V} \\
 \oiint_{\mathcal{S}_2} \mu\mathbf{h} \cdot d\mathcal{S}_2 &= \iiint_{\mathcal{V}} \frac{\nabla \cdot \mathbf{m}_{\text{exc}}}{i\omega} d\mathcal{V}.
 \end{aligned} \tag{2.11}$$

### 2.1.1.3 Boundary Conditions

The electric and magnetic fields obey a set of boundary conditions between media with different EP, i.e., different brain tissues of a human body or boundary between a perfect electric conductive coil material and the air. In 2.2 we show the boundary between the medium 1 and 2 with EPs  $\epsilon_1, \mu_1$  and  $\epsilon_2, \mu_2$  respectively. The surface  $\mathcal{S}_1$  and its contour  $\mathcal{C}$  correspond to the infinitesimally small orthogonal shown on the left of 2.2, while the volume  $\mathcal{V}$  and the surface  $\mathcal{S}_2$  correspond to the infinitesimally small cylinder illustrated on the right. We assume that the height  $\Delta h$  is close to 0. Using the integral form of Maxwell's equations, the integrals are reduced to 1D (Ampere-Maxwell law, Faraday's law) and 2D (Gauss' laws).

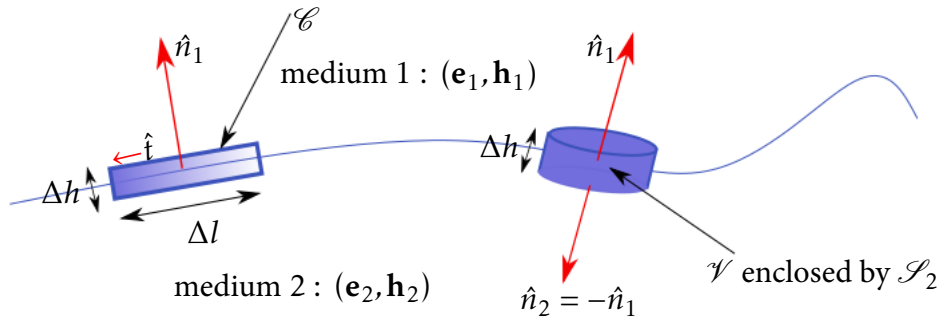


Figure 2.2: Boundary between two media 1 and 2 with different EP.

Since the quantities  $\epsilon\mathbf{e}$  and  $\mu\mathbf{h}$  are finite at the interface between the two media, one can derive the following equations

$$\begin{aligned}
 (\mathbf{h}_1 - \mathbf{h}_2) \cdot \hat{t} &= [\mathbf{j}_{\text{exc}} \cdot (\hat{n}_1 \times \hat{t})] \Delta h = \mathbf{j}_{\text{exc}} \Delta h = \mathbf{j}_d \\
 (\mathbf{e}_1 - \mathbf{e}_2) \cdot \hat{t} &= -[\mathbf{m}_{\text{exc}} \cdot (\hat{n}_1 \times \hat{t})] \Delta h = -\mathbf{m}_{\text{exc}} \Delta h = -\mathbf{m}_d,
 \end{aligned} \tag{2.12}$$

where  $\mathbf{j}_d$  and  $\mathbf{m}_d$  are called impressed electric and magnetic current densities at the interface, respectively.

Similarly, the Gauss' laws obtain the following form

$$\begin{aligned}\hat{n}_1 \cdot (\mu_1 \mathbf{h}_1 - \mu_2 \mathbf{h}_2) &= \rho_m \Delta h = \rho_{md} \\ \hat{n}_1 \cdot (\epsilon_1 \mathbf{e}_1 - \epsilon_2 \mathbf{e}_2) &= \rho_e \Delta h = \rho_{ed},\end{aligned}\tag{2.13}$$

where  $\rho_{md}$  and  $\rho_{ed}$  are called impressed electric and magnetic surface charge densities at the interface, respectively.

In the problems of interest in the presented dissertation, magnetic currents and charges do not exist, and the boundary conditions acquire the following elegant form

$$\begin{aligned}\hat{n}_1 \times (\mathbf{h}_1 - \mathbf{h}_2) &= \mathbf{j}_d \\ \hat{n}_1 \times (\mathbf{e}_1 - \mathbf{e}_2) &= 0 \\ \hat{n}_1 \cdot (\mu_1 \mathbf{h}_1 - \mu_2 \mathbf{h}_2) &= 0 \\ \hat{n}_1 \cdot (\epsilon_1 \mathbf{e}_1 - \epsilon_2 \mathbf{e}_2) &= \rho_{ed}.\end{aligned}\tag{2.14}$$

It is observed that the tangential electric field is continuous across the interface, while the tangential magnetic field is discontinuous due to the impressed electric current density. Finally, if one of the media is a perfect electric conductor (RF coils), then  $\mathbf{e}_2$  and  $\mathbf{h}_2$  are 0 everywhere, and the boundary conditions are simplified. These boundary conditions are crucial for the derivation of surface and volume integral equations, as will be seen later in the present and the next Chapter.

### 2.1.2 Superposition, Duality and Reciprocity Theorems

Using the fundamental Maxwell's equations and the boundary conditions, one can derive multiple vital theorems in electromagnetics. One of them is the *superposition theorem*, where for a linear medium, it is proven that the total electromagnetic field intensity due to multiple sources is the sum of the electromagnetic field intensities produced by each source independently. This theorem is extremely useful in modern 7 Tesla MRI problems, where the number of transmit coil channels is 8. In this case, one can consider each channel as a single excitation, solve all 8 of them with a numerical method (see in the next Chapters) and sum them with any weighting factor to derive any form of excitation (for example the excitation modes of birdcage coils) used for imaging.

Let us consider  $n$  excitation sources. In this case, Ampere-Maxwell law and Faraday's law are

$$\begin{aligned}\nabla \times \mathbf{h}_i &= \mathbf{j}_i^{\text{exc}} - i\omega \epsilon \mathbf{e}_i \\ \nabla \times \mathbf{e}_i &= -\mathbf{m}_i^{\text{exc}} + i\omega \mu \mathbf{h}_i,\end{aligned}\tag{2.15}$$

where  $i = 1, 2, \dots, n$ . By adding the  $n$  set of equations together, it is clear that

$$\mathbf{e} = \sum_{i=1}^n \mathbf{e}_i, \quad \mathbf{h} = \sum_{i=1}^n \mathbf{h}_i.\tag{2.16}$$

Another important theorem is the duality theorem, where it is stated and proven that the electric and magnetic field quantities are commutable. Specifically, Ampere-Maxwell law can be derived from Faraday's law if  $\mathbf{m} \rightarrow -\mathbf{j}$ ,  $\mathbf{e} \rightarrow \mathbf{h}$ ,  $\mathbf{h} \rightarrow -\mathbf{e}$  and  $\mu \rightarrow \epsilon$ , while Faraday's law is obtained through Ampere-Maxwell law if  $\mathbf{j} \rightarrow \mathbf{m}$ ,  $\mathbf{e} \rightarrow \mathbf{h}$ ,  $\mathbf{h} \rightarrow -\mathbf{e}$  and  $\epsilon \rightarrow \mu$ . The duality theorem can greatly reduce the computational time of electromagnetic simulations for specific applications.

A useful theorem in electromagnetic applications is the reciprocity theorem. The theorem states that the electromagnetic field and the electromagnetic sources are commutable, without affecting the systems' response. The proof of the reciprocity theorem can be found in multiple textbooks [127, 128]; thus, it is skipped.

### 2.1.3 Vector Wave Equations

Ampere-Maxwell law and Faraday's law are coupled in a sense that the unknown electric and magnetic field intensities appear in both of them. Alternatively, one can decouple these equations and derive one differential equation of higher order for each of the electric and magnetic field intensities. Even if the order is higher, the decoupled now system is a more elegant form for problems of computational electromagnetics. After some operations on Faraday's law, one can derive the following

$$\begin{aligned} \nabla \times \left( \frac{1}{\mu_r} \nabla \times \mathbf{e} \right) - k_0^2 \epsilon_r \mathbf{e} &= i\omega \mu_0 \mathbf{j}_{\text{exc}} - \nabla \times \left( \frac{1}{\mu_r} \times \mathbf{m}_{\text{exc}} \right) \Rightarrow \\ \nabla \times \nabla \times \mathbf{e} - k^2 \mathbf{e} + \mu_r \nabla \left( \frac{1}{\mu_r} \right) \times \nabla \times \mathbf{e} &= i\omega \mu \mathbf{j}_{\text{exc}} - \nabla \times \mathbf{m}_{\text{exc}} - \mu_r \nabla \left( \frac{1}{\mu_r} \times \right) \times \mathbf{m}_{\text{exc}}. \end{aligned} \quad (2.17)$$

Similarly, starting from Ampere-Maxwell law, one can derive the following

$$\begin{aligned} \nabla \times \left( \frac{1}{\epsilon_r} \nabla \times \mathbf{h} \right) - k_0^2 \mu_r \mathbf{h} &= i\omega \mu_0 \mathbf{m}_{\text{exc}} + \nabla \times \left( \frac{1}{\epsilon_r} \times \mathbf{j}_{\text{exc}} \right) \Rightarrow \\ \nabla \times \nabla \times \mathbf{h} - k^2 \mathbf{h} + \epsilon_r \nabla \left( \frac{1}{\epsilon_r} \right) \times \nabla \times \mathbf{h} &= i\omega \epsilon \mathbf{m}_{\text{exc}} + \nabla \times \mathbf{j}_{\text{exc}} + \epsilon_r \nabla \left( \frac{1}{\epsilon_r} \times \right) \times \mathbf{j}_{\text{exc}}. \end{aligned} \quad (2.18)$$

The 2.17 is the *electric field vector wave equation*, while the 2.18 is the *vector magnetic field wave equation*.  $k$  is the wavenumber of the medium and it is equal to  $k_0 \sqrt{\epsilon \mu}$ , where  $k_0$  is the wavenumber of vacuum and it is equal to  $2\pi f/c$ .

### 2.1.4 Green's function

One key aspect of the electromagnetic field theory is *Green's functions* and play a crucial role in the derivation, solution, and sophisticated algorithm application in the IE methods. Concretely, the vector wave equations can be solved with the help of Green's functions with a generalization of the method initially proposed by George Green, in 1828, for the solution of the electrostatic Poisson equation of the potential produced by a given charge distribution, in [129]. In general, Green's functions represent the response of an electrodynamic system in a delta function excitation. Thereunto, Green's function can be considered as a mathematical description of

the distant electromagnetic interactions between currents and loads. Finally, the electromagnetic field quantities can be obtained as transcendental integrals of the sources multiplied by the respective Green's functions.

In the present thesis, we are mostly interested in the Green's function of the electric field for electric sources, since the human body and the RF coils are non-magnetic objects. We will refer to this function as the *dyadic Green's function* [130–133], which is nothing else than a point source response of the electric field vector wave equation. We assume that the medium is homogeneous and non-magnetic, while magnetic sources do not exist. The fields are time-harmonic; thus, the quantity  $e^{-i\omega t}$  can be neglected. The equation, 2.17 becomes

$$\nabla \times \nabla \times \mathbf{e}(\mathbf{r}) - k^2 \mathbf{e}(\mathbf{r}) = i\omega\mu \mathbf{j}_{\text{exc}}, \quad (2.19)$$

where  $\mathbf{r}$  is the observation point. Given that the dyadic Green's function is the point source response of 2.19 one can express the observed electric field at a point  $\mathbf{r}$  as the following integral

$$\mathbf{e}(\mathbf{r}) = i\omega\mu \iiint_{\mathcal{V}} \bar{\mathbf{G}}(\mathbf{r}, \mathbf{r}') \cdot \mathbf{j}_{\text{exc}}(\mathbf{r}') d\mathcal{V}, \quad (2.20)$$

where  $\mathbf{r}'$  are the source points,  $\bar{\mathbf{G}}$  is the dyadic Green's function, and  $\mathcal{V}$  is the volume of the homogeneous domain of interest. The dyadic Green's function can be found from 2.19 as follows

$$\begin{aligned} \nabla \times \nabla \times \bar{\mathbf{G}}(\mathbf{r}, \mathbf{r}') - k^2 \bar{\mathbf{G}}(\mathbf{r}, \mathbf{r}') &= \bar{\mathbf{I}} \delta(\mathbf{r} - \mathbf{r}') \Rightarrow \\ \bar{\mathbf{G}}(\mathbf{r}, \mathbf{r}') &= \left( \bar{\mathbf{I}} + \frac{\nabla \nabla}{k^2} \right) \frac{e^{ik|\mathbf{r}-\mathbf{r}'|}}{4\pi|\mathbf{r}-\mathbf{r}'|}, \end{aligned} \quad (2.21)$$

with  $\bar{\mathbf{I}}$  being the unit dyad. Finally, the *free-space Green's function*, or the *fundamental Helmholtz solution* is defined as follows

$$g(\mathbf{r}, \mathbf{r}') = \frac{e^{ik|\mathbf{r}-\mathbf{r}'|}}{4\pi|\mathbf{r}-\mathbf{r}'|}. \quad (2.22)$$

### 2.1.5 Surface Equivalence Principle

To derive the integral equation formulations that will be used extensively in the present thesis, one has to apply the surface and volume equivalence principles. In this section, we will derive the so-called *surface equivalence principle and extinction theorem* [129, 134, 135] while in the next, we will focus on the volume equivalent one. The surface equivalence principle and extinction theorem is very similar to the well-known Huygens' principle: "Every point on a wave-front may be considered a source of secondary spherical wavelets which spread out in the forward direction at the speed of light. The new wave-front is the tangential surface to all of these secondary wavelets" [136].

In 2.3 we show a surface  $\mathcal{S}$ , with normal  $\hat{n}$ , bounding the volume  $\mathcal{V}_2$  while the rest of the space is the volume  $\mathcal{V}_1$ . In region 1 there is a current source  $\mathbf{j}_1$  (we dropped the subscript "exc"), while in region 2 a  $\mathbf{j}_2$ .

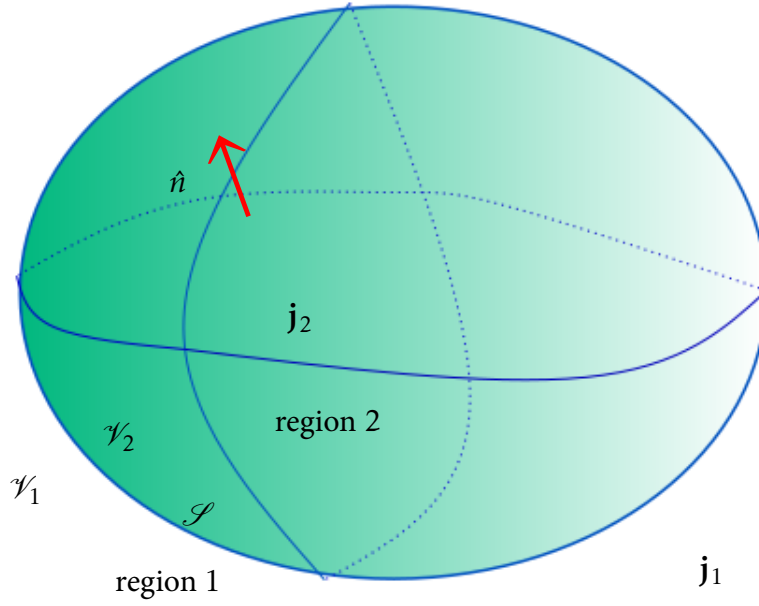


Figure 2.3: Surface equivalence principle and extinction theorem.

We consider the wavenumber to be constant, and multiply the electric field vector wave equation 2.19, for source  $\mathbf{j}(\mathbf{r})$ , with  $\bar{\mathbf{G}}(\mathbf{r}, \mathbf{r}')$  from the right. In addition, for point source response, with multiply 2.19 with  $\mathbf{e}(\mathbf{r})$  from the left. We subtract these equations and result to the following

$$\mathbf{e}(\mathbf{r}) \cdot \nabla \times \nabla \times \bar{\mathbf{G}}(\mathbf{r}, \mathbf{r}') - \nabla \times \nabla \times \mathbf{e}(\mathbf{r}) \cdot \bar{\mathbf{G}}(\mathbf{r}, \mathbf{r}') = \delta(\mathbf{r} - \mathbf{r}') \mathbf{e}(\mathbf{r}) - i\omega\mu \mathbf{j}(\mathbf{r}) \cdot \bar{\mathbf{G}}(\mathbf{r}, \mathbf{r}'). \quad (2.23)$$

If we integrate over  $\mathcal{V}_1$ , the equation takes the following form

$$\mathbf{e}(\mathbf{r}') - \mathbf{e}_1(\mathbf{r}') = \iiint_{\mathcal{V}_1} [\mathbf{e}(\mathbf{r}) \cdot \nabla \times \nabla \times \bar{\mathbf{G}}(\mathbf{r}, \mathbf{r}') - \nabla \times \nabla \times \mathbf{e}(\mathbf{r}) \cdot \bar{\mathbf{G}}(\mathbf{r}, \mathbf{r}')] d\mathcal{V}_1, \quad (2.24)$$

where

$$\mathbf{e}(\mathbf{r}') = \iiint_{\mathcal{V}_1} \delta(\mathbf{r} - \mathbf{r}') \mathbf{e}(\mathbf{r}) d\mathbf{r}, \quad \mathbf{e}_1(\mathbf{r}') = i\omega\mu \iiint_{\mathcal{V}_1} \mathbf{j}_1(\mathbf{r} - \mathbf{r}') \cdot \bar{\mathbf{G}}(\mathbf{r}, \mathbf{r}') d\mathbf{r}. \quad (2.25)$$

The second form represents the total electric field intensity in  $\mathcal{V}_1$  due to the source  $\mathbf{j}_1$ , since  $\mathbf{j}_2$  exists in  $\mathcal{V}_2$  only. Using

$$\begin{aligned} & -\nabla \cdot [\mathbf{e}(\mathbf{r}) \times \nabla \times \bar{\mathbf{G}}(\mathbf{r}, \mathbf{r}') + \nabla \times \mathbf{e}(\mathbf{r}) \times \bar{\mathbf{G}}(\mathbf{r}, \mathbf{r}')] = \\ & = \mathbf{e}(\mathbf{r}) \cdot \nabla \times \nabla \times \bar{\mathbf{G}}(\mathbf{r}, \mathbf{r}') - \nabla \times \nabla \times \mathbf{e}(\mathbf{r}) \cdot \bar{\mathbf{G}}(\mathbf{r}, \mathbf{r}'), \end{aligned} \quad (2.26)$$

the Gauss' divergence theorem and Faraday's law, the integral over  $\mathcal{V}_1$  becomes a closed integral between the bounding surface  $\mathcal{S}$  and the infinite sphere  $\mathcal{S}_\infty$  as follows

$$\mathbf{e}(\mathbf{r}') - \mathbf{e}_1(\mathbf{r}') = \oiint_{\mathcal{S} + \mathcal{S}_\infty} [\hat{\mathbf{n}} \times \mathbf{e}(\mathbf{r}) \cdot \nabla \times \bar{\mathbf{G}}(\mathbf{r}, \mathbf{r}') + i\omega\mu \hat{\mathbf{n}} \times \mathbf{h}(\mathbf{r}) \cdot \bar{\mathbf{G}}(\mathbf{r}, \mathbf{r}')] d\mathcal{S}, \quad (2.27)$$

or

$$\begin{cases} r' \in \mathcal{V}_1, & \mathbf{e}(\mathbf{r}') \\ r' \notin \mathcal{V}_1, & 0 \end{cases} = \mathbf{e}_1(\mathbf{r}') + \oint\!\!\!\!\!\oint_{\mathcal{S}} [\hat{\mathbf{n}} \times \mathbf{e}(\mathbf{r}') \cdot \nabla \times \bar{\mathbf{G}}(\mathbf{r}, \mathbf{r}') + i\omega\mu\hat{\mathbf{n}} \times \mathbf{h}(\mathbf{r}') \cdot \bar{\mathbf{G}}(\mathbf{r}, \mathbf{r}')] d\mathcal{S}, \quad (2.28)$$

because the electric field intensity  $\mathbf{e}(\mathbf{r}')$  vanishes in  $\mathcal{V}_2$  and the integral goes to zero at the infinite sphere. Also, we can shift  $\mathbf{r}$  and  $\mathbf{r}'$  in 2.28 and take its transpose to obtain the following form

$$\begin{cases} r \in \mathcal{V}_1, & \mathbf{e}(\mathbf{r}) \\ r \in \mathcal{V}_2, & 0 \end{cases} = \mathbf{e}_1(\mathbf{r}) + \oint\!\!\!\!\!\oint_{\mathcal{S}} [\nabla \times \bar{\mathbf{G}}(\mathbf{r}, \mathbf{r}') \cdot \hat{\mathbf{n}}' \times \mathbf{e}(\mathbf{r}') + i\omega\mu\bar{\mathbf{G}}(\mathbf{r}, \mathbf{r}') \cdot \hat{\mathbf{n}}' \times \mathbf{h}(\mathbf{r}')] d\mathcal{S}', \quad (2.29)$$

where the reciprocity theorem was used once again on the dyadic Green's function:

$$\nabla \times \bar{\mathbf{G}}(\mathbf{r}, \mathbf{r}') = [\nabla' \times \bar{\mathbf{G}}(\mathbf{r}', \mathbf{r})]^T, \quad \bar{\mathbf{G}}(\mathbf{r}, \mathbf{r}') = [\bar{\mathbf{G}}(\mathbf{r}', \mathbf{r})]^T. \quad (2.30)$$

Equation 2.29 is known as the *Stratton-Chu equation* for the electric field. With duality, one can derive the following Stratton-Chu equation for the magnetic field

$$\begin{cases} r \in \mathcal{V}_1, & \mathbf{h}(\mathbf{r}) \\ r \in \mathcal{V}_2, & 0 \end{cases} = \mathbf{h}_1(\mathbf{r}) + \oint\!\!\!\!\!\oint_{\mathcal{S}} [\nabla \times \bar{\mathbf{G}}(\mathbf{r}, \mathbf{r}') \cdot \hat{\mathbf{n}}' \times \mathbf{h}(\mathbf{r}') - i\omega\epsilon\bar{\mathbf{G}}(\mathbf{r}, \mathbf{r}') \cdot \hat{\mathbf{n}}' \times \mathbf{e}(\mathbf{r}')] d\mathcal{S}', \quad (2.31)$$

The cross products of the electric and magnetic field intensities with the normal of  $\mathcal{S}$  can be thought as surface quantities of  $\mathcal{S}$ . Specifically, we can define them as equivalent surface currents on  $\mathcal{S}$

$$\mathbf{m}_{\text{eq}}(\mathbf{r}') = -\hat{\mathbf{n}}' \times \mathbf{e}(\mathbf{r}'), \quad \mathbf{j}_{\text{eq}}(\mathbf{r}') = \hat{\mathbf{n}}' \times \mathbf{h}(\mathbf{r}'). \quad (2.32)$$

The electric field intensity yields surface magnetic currents, while the magnetic field intensity yields electric ones. The Stratton-Chu equation becomes

$$\begin{cases} r \in \mathcal{V}_1, & \mathbf{e}(\mathbf{r}) \\ r \in \mathcal{V}_2, & 0 \end{cases} = \mathbf{e}_1(\mathbf{r}) - \oint\!\!\!\!\!\oint_{\mathcal{S}} [\nabla \times \bar{\mathbf{G}}(\mathbf{r}, \mathbf{r}') \cdot \mathbf{m}_{\text{eq}}(\mathbf{r}') + i\omega\mu\bar{\mathbf{G}}(\mathbf{r}, \mathbf{r}') \cdot \mathbf{j}_{\text{eq}}(\mathbf{r}')] d\mathcal{S}'. \quad (2.33)$$

The equation 2.33 is the *surface equivalence principle* [137] and it means that the total electric field intensity  $\mathbf{e}(\mathbf{r})$  in a volume  $\mathcal{V}_1$  is generated by the sources in the interior of it ( $\mathbf{j}_1(\mathbf{r})$ ) and the ones in the exterior of it ( $\mathbf{j}_2(\mathbf{r})$ ). In addition, the total electric field intensity can be expressed as the sum of the electric field intensity in the interior of  $\mathcal{V}_1$ , generated by  $\mathbf{j}_1(\mathbf{r})$  and an electric field intensity generated by the radiation of the equivalent magnetic and electric surface currents on the bounding surface of  $\mathcal{V}_2$ . Furthermore, the impressed equivalent currents on  $\mathcal{S}$  generate equivalent electromagnetic field intensities with the sources in  $\mathcal{V}_2$  ( $\mathbf{j}_2(\mathbf{r})$ ).

The similarity with the Huygens' principle, or the *extinction theorem*, can be observed from the bottom part of 2.33. The radiation from the surface equivalent currents cancels out the electromagnetic field intensity in  $\mathcal{V}_2$ , produced by the sources in  $\mathcal{V}_1$ .

### 2.1.6 Volume Equivalence Principle

Similarly with the surface equivalence principle, the volume equivalence principle aims to use a set of equivalent polarisation currents to replace the electromagnetic field intensities generated in the presence of an inhomogeneous medium enclosed in a volume. Let us consider the volume (object) shown on the left of 2.4. The volume is inhomogeneous with  $\epsilon(\mathbf{r})$  and  $\mu(\mathbf{r})$ , surrounded by vacuum. An electromagnetic current source with  $\mathbf{j}(\mathbf{r})$  and  $\mathbf{m}(\mathbf{r})$ , away from the object, generates a set of the so-called incident fields  $\mathbf{e}_{\text{inc}}(\mathbf{r})$  and  $\mathbf{h}_{\text{inc}}(\mathbf{r})$  that excite it. As a result, scattered electromagnetic fields are created ( $\mathbf{e}_{\text{sca}}(\mathbf{r}), \mathbf{h}_{\text{sca}}(\mathbf{r})$ ), to satisfy the boundary conditions of the problem.

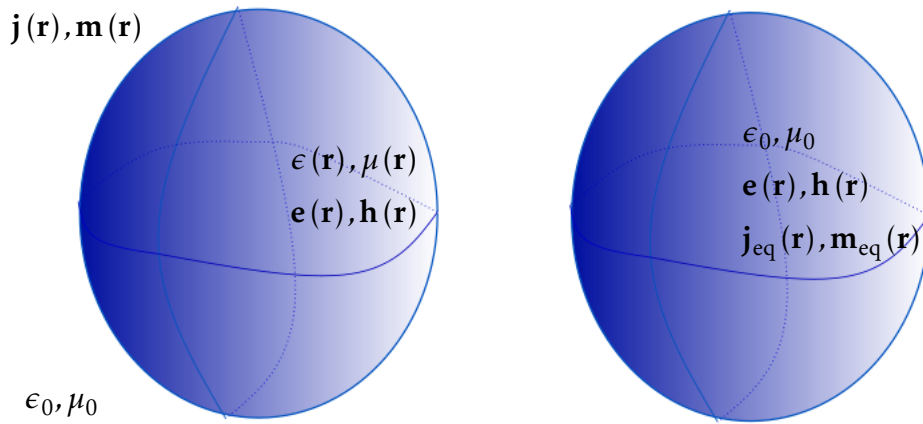


Figure 2.4: Volume equivalence principle.

The resulting total electromagnetic field intensities are nothing else than the sum of the incident and scattered fields:

$$\mathbf{e}(\mathbf{r}) = \mathbf{e}_{\text{inc}}(\mathbf{r}) + \mathbf{e}_{\text{sca}}(\mathbf{r}), \quad \mathbf{h}(\mathbf{r}) = \mathbf{h}_{\text{inc}}(\mathbf{r}) + \mathbf{h}_{\text{sca}}(\mathbf{r}). \quad (2.34)$$

The total and incident electromagnetic field intensities satisfy Ampere-Maxwell and Faraday's laws. By exploiting this fact, one ends up quickly to the following equations for the scattered electromagnetic field intensities:

$$\begin{aligned} \nabla \times \mathbf{h}_{\text{sca}}(\mathbf{r}) &= -i\omega [\epsilon(\mathbf{r}) - \epsilon_0] \mathbf{e}(\mathbf{r}) - i\omega \epsilon_0 \mathbf{e}_{\text{sca}}(\mathbf{r}) \\ \nabla \times \mathbf{e}_{\text{sca}}(\mathbf{r}) &= -i\omega [\mu(\mathbf{r}) - \mu_0] \mathbf{h}(\mathbf{r}) + i\omega \mu_0 \mathbf{h}_{\text{sca}}(\mathbf{r}). \end{aligned} \quad (2.35)$$

Additionally, the scattered electromagnetic field intensities should satisfy Ampere-Maxwell and Faraday's laws as well. Therefore, this means that a set of equivalent volumetric polarisation currents is responsible for the generation of these scattered fields and can be expressed as follows

$$\mathbf{j}_{\text{eq}}(\mathbf{r}) = i\omega \epsilon_0 [\epsilon_r(\mathbf{r}) - 1] \mathbf{e}(\mathbf{r}), \quad \mathbf{m}_{\text{eq}}(\mathbf{r}) = i\omega \mu_0 [\mu_r(\mathbf{r}) - 1] \mathbf{h}(\mathbf{r}). \quad (2.36)$$

Equation 2.36 is the volume equivalence principle and states that the new equivalent electromagnetic sources can replace the object with free-space.

## 2.2 Computational Electromagnetism

In the sections above, we have introduced the fundamental equations (Maxwell's equations) of the electromagnetic theory along with a set of boundary conditions between different media. If used in tandem, one can solve for unknown electromagnetic field quantities, such as the EM field intensities, the absorbed power, and multiple MR measurements. Towards this direction, one has to employ the surface and volume equivalence principle to define the so-called integral equations (more formal definitions are introduced in Chapter 3). Nevertheless, IEs are impossible to be solved fully analytically for arbitrary, real-world objects of electrical and biomedical engineering applications<sup>3</sup>. Regrettably, analytical solutions exist only for perfect spheres with stratified media layers and infinitely long cylinders, based on the Mie Series approach [138]. Therefore, numerical methods are mandatory for the efficient calculation of the electromagnetic field quantities.

Specifically, the scientific field for such methods that are applied in problems of electromagnetics is called computational electromagnetics and focuses on accurate, fast, and efficient numerical simulations of the EM scattering in an application of interest. Apart from MR imaging systems, and bioengineering, CEM is used in a wide variety of applications, such as photonics, sensors, remote sensing, telecommunications, radars, and antenna theory, among others. Most of the methods arising in this area can be applied to different applications without many alternations, thus the great versatility of CEM. This versatility is easily observed from the commercially available packages that are used for various applications in the last decades [22, 139–141]. Finally, all numerical techniques of CEM are divided into time-domain and frequency-domain methods and in differential and integral methods, depending on which form of Maxwell's equations is used.

In the first section of this Chapter, we mentioned that a wide variety of EM applications, and especially the ones that concern this dissertation, use harmonically time-varying fields; therefore, using the Fourier transform, the time variable is replaced with a phase shift. As expected, this led to multiple frequency domain methods (such as the integral equations and finite element method) that can estimate only the spatial variations of the electromagnetic field quantities. Nevertheless, the vastly increasing computational power and memory allowed the modeling of non-time harmonic EM problems. These time-domain methods (i.e., finite difference time domain method, FDTD [142–144]) mimic the spatio-temporal behavior of the EM fields. Specifically, the EM fields are computed and stored in the 3D space and the respective computational space should be terminated due to the limited capability of storage in the computer's memory. As a result, these methods are optimal by definition for closed problems, while for the case of open scattering problems, specific absorption boundary and radiation conditions should

---

<sup>3</sup>Such problem is the scattering from biological tissue in the presence of RF coils

be included. These methods can return results for multiple frequencies with one solution of the system, while the respective frequency methods require the inversion of a matrix for a single frequency solution. Finally, time-domain methods offer a more “natural” observation on the EM fields’ behavior since they study straight the 4D electrodynamic phenomena.

Nevertheless, MRI is a single-frequency and a time-harmonic problem, and as a result, frequency-domain methods are an excellent tool for such simulations. Besides, when the maximal use of a specific setting is possible (single frequency), frequency methods (and especially integral methods) provide an opportunity for customization of fast algorithms, such as the extreme memory compression method developed in Chapter 4, which is one of the main contributions of this thesis.

### 2.2.1 Differential and Integral Methods

Differential equation (DE, or PDE) methods arise straight from Maxwell’s equations or the vector wave equations without preprocessing. Thus, these methods can be utilized to solve problems of arbitrary geometries and inhomogeneous objects. Since the electromagnetic quantities are stored in 3D space, the methods are bounded by the memory footprint of the problem and computer’s available memory. Therefore, such an impasse states that these methods are optimal for closed problems, while for far-field scattering measurements, one has to employ appropriate boundary and radiation conditions. Usually, PDE methods lead to vast sparse matrices that model the local interactions between an electromagnetic field-related quantity. Finally, the most well-known PDE methods are the finite element method (FEM) [145–148] in the frequency domain and the previously mentioned FDTD in the time domain.

Instead of solving Maxwell’s equations directly in their PDE form, one can exploit the surface and volume equivalence principles and reform them as integral equations. In the case of homogeneous scatterers, the surface equivalence principle can be restricted in their boundary, thus hugely reducing the dimensionality of the problem. One needs to compute the equivalent currents only on the surface of the scatterer, thus, creating a dense but much smaller matrix than the PDE methods, which can be easily solved with classic direct approaches (Gaussian elimination). For inhomogeneous problems, one can employ the volume equivalence principle and utilize the free-space dyadic Green’s function for an efficient solution to the problem at hand. Regrettably, the number of unknowns vastly increases in contrast with the surface approach, and the arising matrix is almost impossible to be stored for fine resolutions even in modern servers.

Nevertheless, one can exploit the translational invariant property of the Green’s function if the discretization is uniform. In this case, the arising matrix acquires a Toeplitz structure, therefore only the Toeplitz defining vector needs to be computed for the implementation of the matrix-vector product with a CG-FFT method [53, 57, 149, 150]. Moreover, other methods that are not restricted to uniform grids are available in the literature, such as the precorrected FFT approach [51] the adaptive integral equation [56], and the well-known fast multipole methods [30, 32, 151–

154]. Finally, the discretization scheme for the integral equation methods is efficiently performed through their transformation to a system of equations via the Method of Moments [155], which is explained in the following subsection.

### 2.2.2 Method of Moments

Let us consider an unknown function  $f$  and an operator  $\mathcal{L}$ , where  $\mathcal{L}(f) = g$ . In fact, the operator is translated to a mapping between  $f \in \mathbb{D}(\mathcal{L})$  and  $g \in \mathbb{R}(\mathcal{L})$ .  $\mathbb{D}(\mathcal{L})$  is the domain of  $\mathcal{L}$  and it is an infinite dimension Hilbert space<sup>4</sup>, while  $\mathbb{R}(\mathcal{L})$  is the codomain of  $\mathcal{L}$  and it is a non-proper subset of  $\mathbb{D}(\mathcal{L})$ .

If  $f_i, i = 1, 2, \dots$  is an orthonormal basis of  $\mathbb{D}(\mathcal{L})$  then  $f$  can be expressed as an exact linear combination of  $f_n$  as follows

$$f = \sum_{i=1}^{\infty} a_i f_i, \quad \|a\|_{L_1} \geq 0. \quad (2.37)$$

To reduce the method to  $n$  dimensions instead of infinite, we define a linear subspace  $\mathbb{F}^n(\mathcal{L}) \subset \mathbb{D}(\mathcal{L})$  and an orthonormal basis  $f_i, i = 1, 2, \dots, n$ , from functions of the infinite space  $\mathbb{D}(\mathcal{L})$ . Any function  $q \in \mathbb{F}^n(\mathcal{L})$  can be approximated with the equation

$$q \approx \sum_{i=1}^n a_i f_i, \quad \|a\|_{L_1} \geq 0. \quad (2.38)$$

In addition, we define another linear subspace  $\mathbb{W}^n(\mathcal{L}) \subset \mathbb{D}(\mathcal{L})$  and an orthonormal basis of it  $w_i, i = 1, 2, \dots, n$ . Any function  $p \in \mathbb{D}(\mathcal{L})$  can be expressed, using the projection theorem, as

$$p = P_{\mathbb{W}^n(\mathcal{L})}\{p\} + h, \quad \langle h, w_i \rangle_{\mathbb{W}^n(\mathcal{L})} = 0, \quad \forall w_i \in \mathbb{W}^n(\mathcal{L}), \quad (2.39)$$

where  $P_{\mathbb{W}^n(\mathcal{L})}\{p\}$  is the projection of function  $p$  in  $\mathbb{W}^n(\mathcal{L})$ ,  $h$  is the minimum distance of  $p$  from  $\mathbb{W}^n(\mathcal{L})$ , and  $\langle \cdot, \cdot \rangle_{\mathbb{X}}$  is the inner product on  $\mathbb{X}$ .

Method of moments approximates the exact solution of 2.37 of the problem  $\mathcal{L}(f) = g$  with a function given from 2.38 in such a way that the projection of the function  $\mathcal{L}(f)$  and  $\mathcal{L}(q)$  on  $\mathbb{W}^n(\mathcal{L})$  are equal, or equivalently using 2.39

$$\mathcal{L}(f) - \mathcal{L}(q) = h_f - h_q \rightarrow \text{minimum}, \quad (2.40)$$

where  $h_f$  and  $h_q$  are the minimum distances of  $f$  and  $q$  from  $\mathbb{W}^n(\mathcal{L})$  respectively. To minimize the difference between these projections one has to enforce an equality between the projection of the infinite and the finite functions,  $f$  and  $q$  respectively, on the orthonormal basis of  $\mathbb{W}^n(\mathcal{L})$  or equivalently

$$\langle w_i, \mathcal{L}(q) \rangle_{\mathbb{W}^n(\mathcal{L})} = \langle w_i, \mathcal{L}(f) \rangle_{\mathbb{W}^n(\mathcal{L})}. \quad (2.41)$$

<sup>4</sup>A complete metric space, equipped with an inner product, defined in Appendix C

Using 2.41 and 2.38 in tandem we end up in an algebraic system of equations  $Z\mathbf{a} = \mathbf{b}$ , where

$$Z = \begin{bmatrix} \langle \mathbf{w}_1, \mathcal{L}(f_1) \rangle & \langle \mathbf{w}_1, \mathcal{L}(f_2) \rangle & \cdots & \langle \mathbf{w}_1, \mathcal{L}(f_n) \rangle \\ \langle \mathbf{w}_2, \mathcal{L}(f_1) \rangle & \langle \mathbf{w}_2, \mathcal{L}(f_2) \rangle & \cdots & \langle \mathbf{w}_2, \mathcal{L}(f_n) \rangle \\ \cdots & \cdots & \cdots & \cdots \\ \langle \mathbf{w}_n, \mathcal{L}(f_1) \rangle & \langle \mathbf{w}_n, \mathcal{L}(f_2) \rangle & \cdots & \langle \mathbf{w}_n, \mathcal{L}(f_n) \rangle \end{bmatrix}, \mathbf{a} = \begin{bmatrix} \mathbf{a}_1 \\ \mathbf{a}_2 \\ \cdots \\ \mathbf{a}_n \end{bmatrix}, \mathbf{b} = \begin{bmatrix} \langle \mathbf{w}_1, \mathcal{L}(g) \rangle \\ \langle \mathbf{w}_2, \mathcal{L}(g) \rangle \\ \cdots \\ \langle \mathbf{w}_n, \mathcal{L}(g) \rangle \end{bmatrix}. \quad (2.42)$$

Vector  $\mathbf{a}$  contains the unknown coefficients of the problem, which in integral equations are usually the equivalent currents, the electric flux density, or the electric field intensity. Finally the solution  $f$  is approximated as

$$f = [f_1 f_2 \cdots f_n] Z^{-1} \mathbf{b}. \quad (2.43)$$

Method of moments is often called the *Galerkin method* credited to the Russian mathematician Boris Grigoryevich Galerkin and the Swiss physicist Walther Ritz. Depending on the chosen basis and testing functions of choice, the method is called Bubnov-Galerkin or Ritz-Galerkin for the same set of functions, and Petrov-Galerkin for different sets of functions. The optimal sets of basis and testing functions are the ones that guarantee a solvable problem as long as we increase  $n$ , and the inverse operator of  $\mathcal{L}$  is bounded as  $n \rightarrow \infty$ . For the integral equation methods we usually use the Ritz-Galerkin method and consider  $\mathbb{W}^n(\mathcal{L}) \equiv \mathbb{F}^n(\mathcal{L})$  which yields accurate results, although for computational reasons, one can employ a simpler Petrov-Galerkin method, the *collocation method*. For the integral methods referred to in this thesis, we use the Galerkin approach; however, we include a brief description of the collocation method for completeness, below.

### 2.2.2.1 Collocation Method

The collocation method is one of the most simple Petrov-Galerkin methods, where the basis functions are evaluated over a set of collocation points  $x_i, i = 1, 2, \dots, n$  (i.e., piecewise-constant functions, with collocation point the center of the discretization element), and the testing functions are the Dirac delta functions  $\delta(x - x_i)$  in the same set of collocation points. Due to the usage of the Dirac delta functions, the Galerkin arising integrals of  $Z$  have a reduced dimension (in surface equations from 4D to 2D and in volume equations from 6D to 3D) which simplifies the calculation process but worsens the accuracy. Furthermore, if the number of the collocation points is  $> n$ , the system  $Z\mathbf{a} = \mathbf{b}$  is underdetermined. Thus, least squares approaches have to be employed for its accurate solution.

### 2.2.2.2 Nyström Method

The collocation method can be simplified even further by approximating the integral with a weighted sum over a set of  $n$  sampled points. However, this approach can lead to singularities if the sampled points exist on the same discretization element as the respective collocation points. Thus, advanced quadrature integration techniques are employed to evaluate the appearing singular integrals.



# Chapter 3

## INTEGRAL EQUATION METHODS

---

**T**HE fast, efficient and accurate modeling of the EM scattering by arbitrary isotropic objects is of paramount importance in a plethora of modern applications. After the implementation of the Mie series by Gustav Mie in 1908 [138], the only full analytical method to study the scattering of homogeneous spherical scatterers, the numerical methods became veritable workhorses for the analysis of the electromagnetic scattering. Specifically, over the last decades, CEM solvers are considered a ubiquitous commodity for various applications. Examples include telecommunications, antenna theory, photonics, nondestructive testing, target identification, and geophysical exploration. Besides, a variety of software is available for fast and accurate EM modeling and simulations. However, computational electromagnetics is still an open area of research since more competitive applications arise daily, i.e., interactions between biological tissue, RF coils, and EM waves in modern UHF MR ( $\geq 7$  Tesla) scanners. In these problems, the interactions between electromagnetic waves and human tissue becomes more dominant than in the traditionally used MR scanners (1.5, 3 Telsa), and can easily have detrimental effect to the quality of the images and the safety of the patients, if not modeled accurately while designing the scanner and the RF coils [13–16]. The wide variety of different tissues inside human heads makes them truly inhomogeneous scatterers; hence the computational accurate and fast analysis of such cases is by no means a trivial task.

When we are dealing with the scattering from objects of finite electrical properties, hence penetrable, we can use a wide variety of methods based on partial differential equations, such as the FDTD and the FE methods for Maxwell's and wave equations, respectively. For general applications, these methods are a panacea, since geometries with arbitrary spatially-varying and piecewise homogeneous electrical properties are handled without additional retooling [156–158]. Nevertheless, methods that are based on the integrodifferential form of Maxwell's equations (namely integral equations) offer an ideal platform for the customization of fast algorithms where the maximal use of a specific setting is possible, i.e., in nuclear magnetic resonance imaging where the operating frequency is constant and a multiple of the Larmor's frequency. Although, for a general-purpose solver, they might become prohibitively slow and complicated.

For linear problems, such as the scattering from an arbitrary object, the linear superposition principle allows us to find the fundamental solution of the system or the Green's function [129] of the respective PDE. The Green's function is an exact propagator of the electromagnetic field from a source point  $\mathbf{r}'$  to an observation point  $\mathbf{r}$ . Hence, the grid dispersion error that appears on PDE methods vanishes for IE [143, 159]. IE methods are divided into two families, surface and volume methods. In the case of surface equations, the unknowns reside on the surface of the scatterer [20]. Thus we do not need to solve for the whole 3D space around and interior of the scatterer like in PDE cases. However, VIE has to be solved for the whole 3D space, since it is used to model inhomogeneous objects; thus, a more significant number of unknowns than in the surface equation case is required.

Moreover, many advantages can be exploited in a simulation, based on IE. The arising Green's function operators do not depend on the characteristics of the scatterer, but only from the domain of the mesh, thus they can be precomputed before the simulation. Furthermore, due to the similar nature of SIE and VIE, a coupling between the MRI RF coil and the human tissue can be used [23]. SIE is optimal for perfect electrical conductors like the metal of the RF coil, while VIE can solve for the inhomogeneity of the human tissue inside the scanner. IEs are also handy for the efficient reconstruction of the electrical properties of human tissue [160] since they can form a fully 3D global problem. Furthermore, IEs have been used as a method for the construction of a so-called ultimate basis that allows the representation of a reduced-order model for the RF coil - human body interactions, or dielectric pad - human body interactions.

In terms of implementation complexity, A PDE-based software can be implemented simpler than an IE-based one, since IEs require the proper evaluation of arising singular integrals in their Green's function kernels. However, sophisticated packages are implemented and used, for this reason, such as [27, 28], even as a black-box solution. On the one hand, a PDE method solves a sparse matrix system with  $\mathcal{O}(n)$  complexity ( $n$  is the number of unknowns), which significantly reduces the computation and memory cost. On the other hand, the associated IE systems require the storage of a dense matrix with memory complexity  $\mathcal{O}(n^2)$ , and for many years IE could not be used for realistic problems. However, this impasse was tackled with the introduction of fast IE solvers [20,30,31,151,161–164] which allow us to perform the arising matrix-vector product with  $\mathcal{O}(n \log n)$  complexity either by exploiting the translational invariance property of the Green's function, by representing the unknown physical quantities on uniform tessellations (FFT-based VIEs), or by using the fast multipole method [165].

The present thesis introduces tensor decomposition techniques that can be used on FFT-based VIE and compress the arising Green's function tensors more than 3000 times [1, 5, 68], this compression allows us to fit and run simulations of huge problems inside GPU and thus, accelerate their solution by order of magnitude. These methods are described in Chapter 4. In the remainder of this Chapter, we will present the state-of-the-art SIE solvers and focus on the accelerated VIE methods based on FFT. Additionally, we will describe the lumped element modeling

for RF coils, which will be used extensively in Chapter 5 for the design of problem-dedicated RF coils for the EP reconstruction problem.

#### 3.1 Surface Integral Equations

Electromagnetic scattering problems are studied as radiation problems where incident sources generate the arising radiating currents on the surface of the scatterer. For instance, in antenna theory, the currents, as mentioned earlier, are created via a voltage source, and then they radiate a scattered field. To derive accurate representations of the current induced on the surface of the finite size object, we can exploit the surface equivalence principle. In this section, we will focus on surface integral equation methods, in which we solve a linear system for the induced current on the surface of a PEC or homogeneous scatterer. The integrodifferential operator is applied to the unknown current, thus, the name integral equation. Usually, the MoM is used to derive a linear system where the vector of the unknowns describes the components of the current on specific points of the in-study surface (determined by the discretization technique and the basis functions). After the solution of the arising dense linear system (either with a standard LU decomposition or an iterative solver), the electromagnetic fields inside and outside the scatterer can be calculated by solving the integrals of the equation mentioned above.

##### 3.1.1 Surface Integral Equation for Impenetrable Scatterers

In this section, we present two IE formulations for perfect electric conductors: the electric and magnetic field IE. The scatterers are termed as impenetrable objects since no electromagnetic energy can penetrate inside them, originating from a source in the exterior space. Similarly, impenetrable scatterers are the perfect magnetic conductors (PMC) in which the tangential magnetic field is zero on their interior. We consider an incident electromagnetic field  $\mathbf{e}_{\text{inc}}$  that impinges on a PEC. Thus, equivalent electric current will be induced on the surface  $\mathcal{S}$  of the object, and a scattered field will appear. Graphically this can be observed in figure 3.1.

Just outside surface  $\mathcal{S}$  we define another surface  $\mathcal{S}^+$ , approximately large enough to contain it, and we apply the *equivalence principle* and the *extinction theorem*. Equivalent electric and magnetic currents arise on  $\mathcal{S}^+$  as follows

$$\mathbf{j}_{\text{eq}} = \hat{n} \times \mathbf{h}, \text{ and } \mathbf{m}_{\text{eq}} = -\hat{n} \times \mathbf{e}. \quad (3.1)$$

However, since the object is a PEC, no magnetic currents will be imposed on its surface. Thus, the equivalence principle and the extinction theorem can be written as follows

$$\begin{cases} r \in \mathcal{V}_1, & \mathbf{e}(\mathbf{r}) \\ r \in \mathcal{V}_2, & 0 \end{cases} = \mathbf{e}_{\text{inc}}(\mathbf{r}) + \int_{\mathcal{S}^+} i\omega\mu\bar{G}(\mathbf{r},\mathbf{r}')\mathbf{j}_{\text{eq}}(\mathbf{r}')d\mathbf{r}', \quad (3.2)$$

where  $\mathbf{r}$  denotes the observation point,  $\mathbf{r}'$  the source point,  $\mathcal{V}_1$  the volume outside the surface

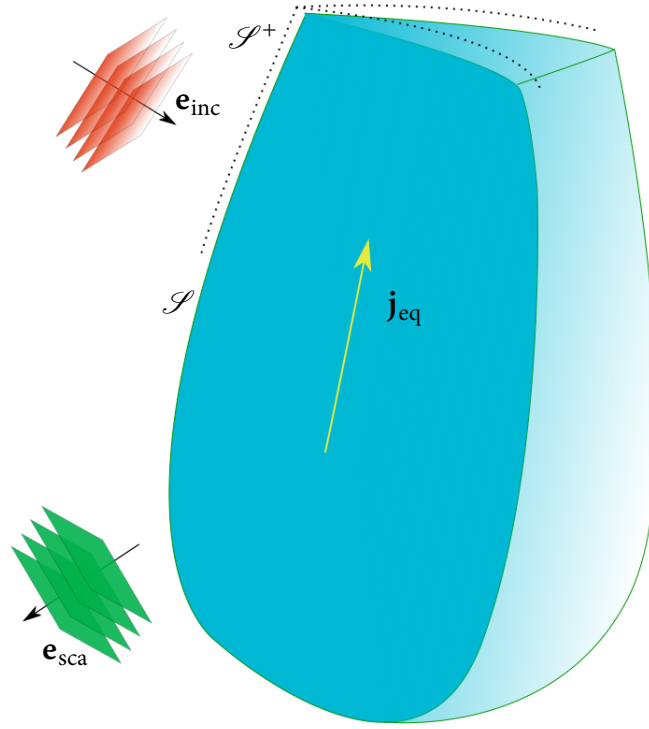


Figure 3.1: Scattering by a PEC surface.

$\mathcal{S}^+$  and  $\mathcal{V}_2$  the volume enclosed by it. For  $\mathbf{r} \in \mathcal{S}$  the theorem can be written as the following IE

$$\mathbf{e}_{\text{inc}}(\mathbf{r}) + \int_{\mathcal{S}^+} i\omega\mu\bar{G}(\mathbf{r},\mathbf{r}')\mathbf{j}_{\text{eq}}(\mathbf{r}')d\mathbf{r}' = 0. \quad (3.3)$$

A similar magnetic field-based IE can be derived by taking the curl of 3.3 (or its dual)

$$\mathbf{h}_{\text{inc}}(\mathbf{r}) + \nabla \times \int_{\mathcal{S}^+} i\omega\mu\bar{G}(\mathbf{r},\mathbf{r}')\mathbf{j}_{\text{eq}}(\mathbf{r}')d\mathbf{r}' = 0. \quad (3.4)$$

Since  $\mathcal{S}^+$  is infinitesimally close to  $\mathcal{S}$  the tangential component of the magnetic field,  $\hat{\mathbf{n}} \times \mathbf{h}$  is equal, for both surfaces. Thus the equivalent electric current on  $\mathcal{S}$  is equal to the equivalent current on  $\mathcal{S}^+$ . In addition, since  $\hat{\mathbf{n}} \times \mathbf{e} = 0$  on the surface it is sufficient to use only the tangential component of 3.3 and 3.4. Thus, the aforementioned equations become

$$\begin{aligned} \hat{\mathbf{n}} \times \mathbf{e}_{\text{inc}}(\mathbf{r}) + i\omega\mu\hat{\mathbf{n}} \times \int_{\mathcal{S}^+} \bar{G}(\mathbf{r},\mathbf{r}')\mathbf{j}_{\text{eq}}(\mathbf{r}')d\mathbf{r}' &= 0 \\ \hat{\mathbf{n}} \times \mathbf{h}_{\text{inc}}(\mathbf{r}) + \hat{\mathbf{n}} \times \nabla \times \int_{\mathcal{S}^+} i\omega\mu\bar{G}(\mathbf{r},\mathbf{r}')\mathbf{j}_{\text{eq}}(\mathbf{r}')d\mathbf{r}' &= 0. \end{aligned} \quad (3.5)$$

These equations are referred to in the literature as *Electric Field Integral Equation* and *Magnetic Field Integral Equation* and they find many applications, especially in antenna theory. To avoid

### 3.1. Surface Integral Equations

carrying the integral, we introduce the following operator notation

$$\begin{aligned}\mathcal{L}(\mathbf{j}) &= i\omega\mu \int_{\mathcal{S}^+} \bar{\mathbf{G}}(\mathbf{r}, \mathbf{r}') \mathbf{j} d\mathbf{r}' \\ \mathcal{K}(\mathbf{j}) &= \nabla \times \int_{\mathcal{S}^+} \bar{\mathbf{G}}(\mathbf{r}, \mathbf{r}') \mathbf{j} d\mathbf{r}'.\end{aligned}\tag{3.6}$$

The  $\mathcal{K}$  operator can be simplified by using the following property of the dyadic Green's function

$$\nabla \times \bar{\mathbf{G}}(\mathbf{r}, \mathbf{r}') = \nabla \times \left[ \bar{\mathbf{I}} + \left( \frac{1}{k^2} \nabla \cdot \nabla g(\mathbf{r}, \mathbf{r}') \right) \right].\tag{3.7}$$

Since,  $\nabla \times \nabla g(\mathbf{r}, \mathbf{r}') = 0$  we can write the 3.7 as follows

$$\nabla \times \bar{\mathbf{G}}(\mathbf{r}, \mathbf{r}') = \nabla g(\mathbf{r}, \mathbf{r}') \times \bar{\mathbf{I}}.\tag{3.8}$$

Thus, the  $\mathcal{K}$  operator becomes:

$$\mathcal{K}(\mathbf{j}) = \nabla \times \int_{\mathcal{S}^+} \nabla g(\mathbf{r}, \mathbf{r}') \times \mathbf{j} d\mathbf{r}'.\tag{3.9}$$

When  $\mathbf{r} = \mathbf{r}'$  the gradient of Green's function goes to infinity ( $\propto 1/|\mathbf{r} - \mathbf{r}'|^2$ ), thus, the integral of  $\mathcal{K}$  is strongly singular. To calculate it the Cauchy's principal value theorem is used as follows

$$\begin{aligned}\hat{n} \times \left[ \int_{\mathcal{S}^+} \mathbf{j}_{\text{eq}}(\mathbf{r}') \times \nabla' g(\mathbf{r}, \mathbf{r}') d\mathbf{r}' \right] &= \\ \hat{n} \times \left[ \int_{\mathcal{S}^+ - \delta\mathcal{S}^+} \mathbf{j}_{\text{eq}}(\mathbf{r}') \times \nabla' g(\mathbf{r}, \mathbf{r}') d\mathbf{r}' + \int_{\delta\mathcal{S}^+} \mathbf{j}_{\text{eq}}(\mathbf{r}') \times \nabla' g(\mathbf{r}, \mathbf{r}') d\mathbf{r}' \right],\end{aligned}\tag{3.10}$$

where  $\delta\mathcal{S}^+$  is a small circular region of radius  $\alpha$  in  $\mathcal{S}^+$  located close to  $\mathbf{r}$ , and it is portrayed in the following figure 3.2.

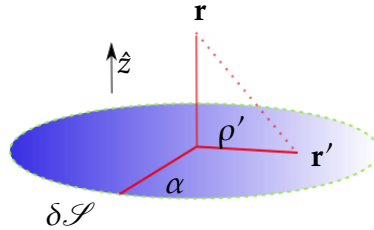


Figure 3.2: Local circular region

We will choose the center of  $\delta\mathcal{S}^+$  as the origin of a local cylindrical coordinate system in order to have  $|\mathbf{r} - \mathbf{r}'| = \sqrt{(\rho')^2 + (z - z')^2}$ , and we assume that  $\hat{n} = \hat{z}$  inside  $\delta\mathcal{S}^+$ . Therefore, the Green's function in the new local coordinate system can be approximated as follows

$$g(\mathbf{r}, \mathbf{r}') \approx \frac{1}{4\pi\sqrt{(\rho')^2 + (z - z')^2}}, \quad |\mathbf{r} - \mathbf{r}'| \ll 1.\tag{3.11}$$

Inside  $\delta\mathcal{S}^+$  the current  $\mathbf{j}_{\text{eq}}(\mathbf{r}')$  is everywhere tangential to the surface, since  $\hat{\mathbf{n}} = \hat{\mathbf{z}}$ . Moreover, since  $\delta\mathcal{S}^+$  is infinitely small, we can also assume that  $\mathbf{j}_{\text{eq}}(\mathbf{r}')$  is approximately equal to  $\mathbf{j}_{\text{eq}}(\mathbf{r})$  and constant. By exploiting the gradient form  $\nabla' = \frac{\partial}{\partial\rho'}\hat{\rho} + \frac{1}{\rho'}\frac{\partial}{\partial\phi'}\hat{\phi}' + \frac{\partial}{\partial z'}\hat{\mathbf{z}}$  we have

$$\begin{aligned} \hat{\mathbf{n}} \times \left[ \int_{\delta\mathcal{S}^+} \mathbf{j}_{\text{eq}}(\mathbf{r}') \times \nabla' g(\mathbf{r}, \mathbf{r}') d\mathbf{r}' \right] &= \int_{\delta\mathcal{S}^+} \hat{\mathbf{z}} \times \mathbf{j}_{\text{eq}}(\mathbf{r}') \times \nabla' g(\mathbf{r}, \mathbf{r}') d\mathbf{r}' = \int_{\delta\mathcal{S}^+} \mathbf{j}_{\text{eq}}(\mathbf{r}') \left[ \frac{\partial g(\mathbf{r}, \mathbf{r}')}{\partial z'} \right] d\mathbf{r}' \stackrel{z'=0}{=} \\ & \int_{\delta\mathcal{S}^+} \mathbf{j}_{\text{eq}}(\mathbf{r}') \frac{z}{4\pi[(\rho')^2 + (z-z')^2]^{\frac{3}{2}}} d\rho' = \frac{\mathbf{j}_{\text{eq}}(\mathbf{r}')}{2} \int_0^\alpha \frac{z\rho'}{4\pi[(\rho')^2 + (z)^2]^{\frac{3}{2}}} d\rho' = \frac{\mathbf{j}_{\text{eq}}(\mathbf{r}')}{2} \left[ \frac{z}{|z|} - \frac{z}{\alpha^2 + z^2} \right] \Rightarrow \quad (3.12) \\ \lim_{z \rightarrow 0^+} \frac{\mathbf{j}_{\text{eq}}(\mathbf{r}')}{2} \left[ \frac{z}{|z|} - \frac{z}{\alpha^2 + z^2} \right] &= \frac{\mathbf{j}_{\text{eq}}(\mathbf{r})}{2}. \end{aligned}$$

According to the above, the MFIE takes the following form

$$0 = \hat{\mathbf{n}} \times \mathbf{h}_{\text{inc}}(\mathbf{r}) - \frac{\mathbf{j}_{\text{eq}}(\mathbf{r})}{2} + \hat{\mathbf{n}} \times \left[ \int_{\mathcal{S}-\delta\mathcal{S}} \mathbf{j}_{\text{eq}}(\mathbf{r}') \times \nabla' g(\mathbf{r}, \mathbf{r}') d\mathbf{r}' \right]. \quad (3.13)$$

The equation holds when the circular area  $\delta\mathcal{S}^+$  is planar. In the case of geometry with sharp edges, like the apex of a cone, a correction in the approximation is required. According to [166] equation 3.12 results to  $\Omega_0/4\pi \cdot \mathbf{j}_{\text{eq}}(\mathbf{r})$ , where  $\Omega_0$  accounts to the exterior solid angle. MFIE becomes

$$0 = \hat{\mathbf{n}} \times \mathbf{h}_{\text{inc}}(\mathbf{r}) - \left(1 - \frac{\Omega_0}{4\pi}\right) \mathbf{j}_{\text{eq}}(\mathbf{r}) + \hat{\mathbf{n}} \times \left[ \int_{\mathcal{S}-\delta\mathcal{S}} \mathbf{j}_{\text{eq}}(\mathbf{r}') \times \nabla' g(\mathbf{r}, \mathbf{r}') d\mathbf{r}' \right]. \quad (3.14)$$

For smooth geometries,  $\Omega_0 = 2\pi$  and equation 3.14 becomes the 3.13. However, an adjustment on the solid angle, as it was done in [167], yields more accurate results. Finally, we note that MFIE is derived using a limiting argument for closed scatterers, and, in contrast with EFIE, it cannot be applied to open surfaces (RF coils with width = 0).

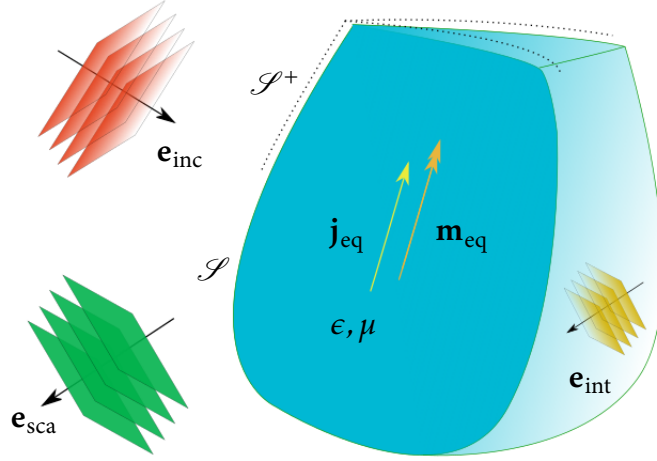
### 3.1.2 Surface Integral Equation for Penetrable Scatterers

While the IE formulations mentioned above for PEC objects are of paramount importance, since they can be used to model metallic antennas, it is also interesting to study the scattering of penetrable objects as well. Such problem tantalized scientists for years [146, 147, 168–173] and it was only after 1960 when IEs were used to study such problems [155, 174–177]. However, in [178], a comprehensive method was provided.

In the case of homogeneous dielectric objects, electromagnetic energy flows into the scatterer, and different boundary conditions (than in the PEC case) have to be satisfied. Similarly, as in SIE for PEC scatterers, one can derive the EFIE and MFIE for homogeneous scatterers with complex permittivity  $\epsilon$  and a permeability  $\mu$  like in 3.3.

In this case, the equivalent surface currents on  $S^+$  are

$$\mathbf{j}_{\text{eq}} = \hat{\mathbf{n}} \times \mathbf{h}, \quad \mathbf{m}_{\text{eq}} = \mathbf{e} \times \hat{\mathbf{n}}. \quad (3.15)$$


 Figure 3.3: Scattering by a surface with permittivity  $\epsilon$  and permeability  $\mu$ .

The equivalence principle and extinction theorem is written as

$$\begin{cases} r \in \mathcal{V}_1, & \mathbf{e}(\mathbf{r}) \\ r \in \mathcal{V}_2, & 0 \end{cases} = \mathbf{e}_{\text{inc}}(\mathbf{r}) + \int_{\mathcal{S}^+} i\omega\mu\bar{G}(\mathbf{r},\mathbf{r}')\mathbf{j}_{\text{eq}}(\mathbf{r}')d\mathbf{r}' - \nabla \times \int_{\mathcal{S}^+} \bar{G}(\mathbf{r},\mathbf{r}')\mathbf{m}_{\text{eq}}(\mathbf{r}')d\mathbf{r}'. \quad (3.16)$$

After the application of the extinction theorem we have

$$0 = \mathbf{e}_{\text{inc}}(\mathbf{r}) + \int_{\mathcal{S}^+} i\omega\mu\bar{G}(\mathbf{r},\mathbf{r}')\mathbf{j}_{\text{eq}}(\mathbf{r}')d\mathbf{r}' - \nabla \times \int_{\mathcal{S}^+} \bar{G}(\mathbf{r},\mathbf{r}')\mathbf{m}_{\text{eq}}(\mathbf{r}')d\mathbf{r}', \quad (3.17)$$

which is called *Electric Field Integral Equation for Penetrable Objects*. Another EFIE equation can be defined if we apply the extinction theorem on the surface of our object in an inside-out manner. Thus, both EFIEs can be written with the help of  $\mathcal{L}$  and  $\mathcal{K}$  operators as follows

$$\begin{aligned} -\mathbf{e}_{\text{inc}}(\mathbf{r}) &= \mathcal{L}_1(\mathbf{j}_{\text{eq}}(\mathbf{r}')) - \mathcal{K}_1(\mathbf{m}_{\text{eq}}(\mathbf{r}')) \\ 0 &= \mathcal{L}_2(\mathbf{j}_{\text{eq}}(\mathbf{r}')) - \mathcal{K}_2(\mathbf{m}_{\text{eq}}(\mathbf{r}')), \end{aligned} \quad (3.18)$$

where the subscripts 1, 2 denote the medium (either inside or outside the scatterer). The equivalent surface currents are the same across the surface  $\mathcal{S}^-$  (A surface just inside  $\mathcal{S}$ , used to derive the interior EFIE) and  $\mathcal{S}^+$ , since the continuity of the tangential electric and magnetic fields, must be preserved on  $\mathcal{S}$ . By invoking the duality principle on EFIE or by applying the curl operator, we can derive the *Magnetic Field Integral Equation for Penetrable Objects*.

$$\begin{aligned} -\mathbf{h}_{\text{inc}}(\mathbf{r}) &= \frac{\epsilon_1}{\mu_1}\mathcal{L}_1(\mathbf{m}_{\text{eq}}(\mathbf{r}')) - \mathcal{K}_1(\mathbf{j}_{\text{eq}}(\mathbf{r}')) \\ 0 &= \frac{\epsilon_2}{\mu_2}\mathcal{L}_2(\mathbf{m}_{\text{eq}}(\mathbf{r}')) - \mathcal{K}_2(\mathbf{j}_{\text{eq}}(\mathbf{r}')). \end{aligned} \quad (3.19)$$

However, even though we have two equations with two unknowns (for each set of equations), we cannot solve for the equivalent surface currents, since the continuity conditions that have to be

satisfied are

$$\begin{aligned}\mathbf{e}_{\text{int}}^{\text{tan}} &= \mathbf{e}_{\text{inc}}^{\text{tan}} + \mathbf{e}_{\text{scat}}^{\text{tan}} \\ \mathbf{h}_{\text{int}}^{\text{tan}} &= \mathbf{h}_{\text{inc}}^{\text{tan}} + \mathbf{h}_{\text{scat}}^{\text{tan}}.\end{aligned}\quad (3.20)$$

Thus, both EFIEs and MFIEs are equivalent. To tackle this problem, and solve for the unknown currents, a linear combination of the exterior equations and the interior equations of EFIE and MFIE is used. According to [179], the solution of such formulation is unique. The combination is modeled as the following weighted sum

$$\begin{aligned}-\alpha_1 \mathbf{e}_{\text{inc}}(\mathbf{r}) &= [\alpha_1 \mathcal{L}_1(\mathbf{j}_{\text{eq}}) + \alpha_2 \mathcal{L}_2(\mathbf{j}_{\text{eq}})] - [\alpha_1 \mathcal{K}_1(\mathbf{m}_{\text{eq}}) + \alpha_2 \mathcal{K}_2(\mathbf{m}_{\text{eq}})] \\ -\eta_1 \beta_1 \mathbf{h}_{\text{inc}}(\mathbf{r}) &= -\eta_1 [\beta_1 \mathcal{K}_1(\mathbf{j}_{\text{eq}}) + \beta_2 \mathcal{K}_2(\mathbf{j}_{\text{eq}})] + \eta_1 \left[ \beta_1 \frac{\epsilon_1}{\mu_1} \mathcal{L}_1(\mathbf{m}_{\text{eq}}) + \beta_2 \frac{\epsilon_2}{\mu_2} \mathcal{L}_2(\mathbf{m}_{\text{eq}}) \right],\end{aligned}\quad (3.21)$$

where  $\eta_1 = \frac{\mu_1}{\epsilon_1}$  is used, in the second equation, in order to ensure that both equations of the system are of the same units. Furthermore, it is proved that the product  $\alpha_i \beta_i^*$  should be real and positive, in order to have a unique solution. For  $\alpha_1 = \alpha_2 = \beta_1 = \beta_2 = 1$  the system forms the Poggio - Miller - Chang - Harrington - Wu - Tsai formulation (PMCHWT) [178], and for  $\alpha_1 = \beta_1 = 1, \alpha_2 = -\frac{\epsilon_2}{\epsilon_1}, \beta_2 = -\frac{\mu_2}{\mu_1}$  the Müller formulation. According to [128], PMCHWT produces accurate results for high contrasts, whereas the Müller formulation is accurate for low contrasts.

### 3.1.3 Rao-Wilton-Glisson Basis Functions

The SIE mentioned above formulations are extensively used to solve the scattering problem of arbitrary surfaces. It is known that the most optimal discretization technique for such surfaces is the Delaunay triangulation - a Voronoi diagram based method. Furthermore, in order to obtain accurate results from the relevant numerical simulations, an appropriate choice of well-defined basis functions is of paramount importance. Such a set of functions are the well known Rao-Wilton-Glisson functions, introduced in the celebrated paper [180]. These basis functions are defined on pairs of adjacent triangular elements of the discretization and yield an accurate approximation of the equivalent surface electric current (free of line and point charges). RWG functions are the equivalent of the rooftop functions on rectangular patches [181].

An RWG function is associated with an interior edge of the patch model, as it is shown in 3.4, and it vanishes everywhere else, except in the two triangles that share this edge. Thus, it is defined as follows

$$\mathbf{f}_n(\mathbf{r}) = \begin{cases} \frac{l_n}{2a_n^+} \rho_n^+ & \mathbf{r} \in \mathcal{T}_n^+ \\ \frac{l_n}{2a_n^-} \rho_n^- & \mathbf{r} \in \mathcal{T}_n^- \\ 0, & \text{elsewhere} \end{cases}, \quad (3.22)$$

where  $l_n$  is the length of the shared edge,  $a_n^\pm$  is the area of the triangle  $\mathcal{T}_n^\pm$  and  $\rho_n^\pm$  is the vector that defines the position and the direction of the RWG inside the triangle.

The equivalent surface currents (both electric and magnetic) in the surface integral equation formulations have no component normal to the boundary of the triangles pair (excluding the

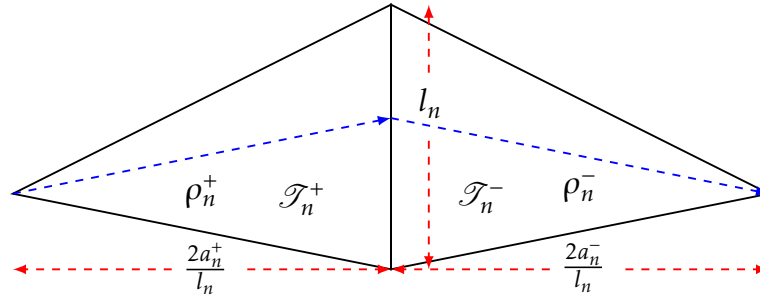


Figure 3.4: RWG functions defined on the common edge of two triangles.

joint edge), and hence no line charges exist along this boundary. Thus, the RWG functions are very well suited for the currents' approximation. Moreover, the normal, to the joint edge, component of the current is constant and continuous across the edge. We note that this is the reason for the multiplicative normalization factor  $\frac{l_n}{2a_n^\pm}$ . Finally, the divergence of RWG is

$$\nabla_s \mathbf{f}_n(\mathbf{r}) = \begin{cases} \frac{l_n}{a_n^+} & \mathbf{r} \in T_n^+ \\ -\frac{l_n}{a_n^-} & \mathbf{r} \in T_n^- \\ 0, & \text{elsewhere} \end{cases} . \quad (3.23)$$

From Maxwell's equations, we know that the divergence of the surface current is proportional to the surface charge density. Hence, according to 3.23, this density should be constant in each triangle and zero in every triangle pair with joint edges. Consequently, the surface currents can be written with the aid of RWG basis functions as

$$\mathbf{j}_{\text{eq}} = \sum_{n=1}^N \mathbf{j}_n \mathbf{f}_n(\mathbf{r}), \quad \mathbf{m}_{\text{eq}} = \sum_{n=1}^N \mathbf{m}_n \mathbf{g}_n(\mathbf{r}), \quad (3.24)$$

where  $N$  is the number of the non-boundary edges of the scatterer,  $\mathbf{f}_n(\mathbf{r})$  and  $\mathbf{g}_n(\mathbf{r})$  are the RWG basis functions on the edge  $n$  and  $\mathbf{j}, \mathbf{m}$  are the equivalent surface electric and magnetic current coefficients in the discretization elements, respectively. Each element  $\mathbf{j}_i, \mathbf{m}_i$  represents the normal component of electric and magnetic current density, respectively, flowing through the  $i^{\text{th}}$  edge. For open surfaces, on the boundary edges, the values of these components are zero, since we need to enforce the continuity of the normal current component.

The application of the MoM technique with RWG basis functions is quite simple. First of all, the testing functions are considered as RWG as well (Galerkin projection) and each element of the matrix is defined as follows

$$Z_{mn} = \sum_{p=1}^3 \sum_{q=1}^3 Q_{pq}^{mn}, \quad (3.25)$$

where  $Q^{mn}$  corresponds to the interactions between each edge  $p$  of the source triangle  $n$  with each edge  $q$  of the observation triangle  $m$ . A graphical representation is illustrated on 3.5 for two triangles  $\mathcal{T}_n$  and  $\mathcal{T}_m$ .

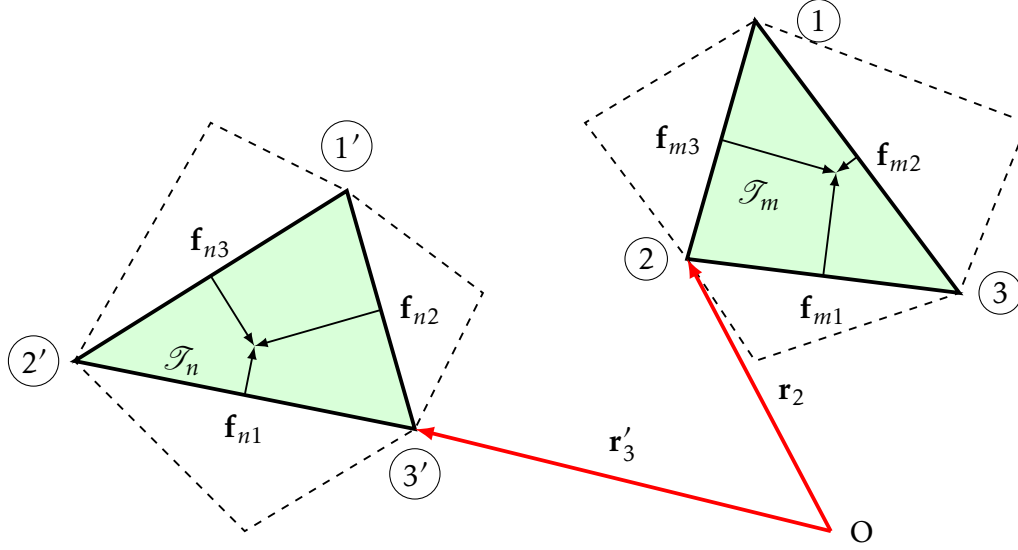


Figure 3.5: Interaction between two triangles  $\mathcal{T}_n$  and  $\mathcal{T}_m$ .

For a PEC surface, the electric field intensity on  $\mathbf{r}$  produced by the equivalent surface current  $\mathbf{j}_n(\mathbf{r}')$  on one element  $\mathcal{T}_n$ , is

$$\mathbf{e}(\mathbf{r}) = i\omega\mu \int_{\mathcal{T}_n} g(\mathbf{r}, \mathbf{r}') \mathbf{j}_n(\mathbf{r}') d\mathbf{r}' + \frac{1}{i\omega\epsilon} \nabla \int_{\mathcal{T}_n} g(\mathbf{r}, \mathbf{r}') \nabla' \cdot \mathbf{j}_n(\mathbf{r}') d\mathbf{r}'. \quad (3.26)$$

Thus, the elements of the MoM matrix (Galerkin projection with RWG) will have the following form

$$\begin{aligned} Z_{mn} &= - \int_{\mathcal{T}_m} \mathbf{j}_m(\mathbf{r}) \cdot \mathbf{e}[\mathbf{j}_n(\mathbf{r}')] d\mathbf{r} \\ Z_{mn} &= i\omega\mu \int_{\mathcal{T}_m} \mathbf{j}_m(\mathbf{r}) \int_{\mathcal{T}_n} g(\mathbf{r}, \mathbf{r}') \mathbf{j}_n(\mathbf{r}') d\mathbf{r}' d\mathbf{r} + \frac{1}{i\omega\epsilon} \int_{\mathcal{T}_m} \nabla \cdot \mathbf{j}_m(\mathbf{r}) \int_{\mathcal{T}_n} g(\mathbf{r}, \mathbf{r}') \nabla' \cdot \mathbf{j}_n(\mathbf{r}') d\mathbf{r}' d\mathbf{r} \\ Z_{mn} &= i\omega\mu \int_{\mathcal{T}_m} [\mathbf{f}_{m1}(\mathbf{r}), \mathbf{f}_{m2}(\mathbf{r}), \mathbf{f}_{m3}(\mathbf{r})]^T \int_{\mathcal{T}_n} g(\mathbf{r}, \mathbf{r}') [\mathbf{f}_{n1}(\mathbf{r}'), \mathbf{f}_{n2}(\mathbf{r}'), \mathbf{f}_{n3}(\mathbf{r}')] d\mathbf{r}' d\mathbf{r} \\ &\quad + \frac{1}{i\omega\epsilon} \int_{\mathcal{T}_m} [\nabla \cdot \mathbf{f}_{m1}(\mathbf{r}), \nabla \cdot \mathbf{f}_{m2}(\mathbf{r}), \nabla \cdot \mathbf{f}_{m3}(\mathbf{r})]^T \int_{\mathcal{T}_n} g(\mathbf{r}, \mathbf{r}') [\nabla' \cdot \mathbf{f}_{n1}(\mathbf{r}'), \nabla' \cdot \mathbf{f}_{n2}(\mathbf{r}'), \nabla' \cdot \mathbf{f}_{n3}(\mathbf{r}')] d\mathbf{r}' d\mathbf{r}. \end{aligned} \quad (3.27)$$

According to 3.25 and 3.27 the interactions between the edges  $p = n_1$  or  $n_2$  or  $n_3$  and  $q = m_1$  or  $m_2$  or  $m_3$  are

$$Q_{pq}^{mn} = i\omega\mu \int_{\mathcal{T}_m} \mathbf{f}_p(\mathbf{r}) \int_{\mathcal{T}_n} g(\mathbf{r}, \mathbf{r}') \mathbf{f}_q(\mathbf{r}') d\mathbf{r}' d\mathbf{r} + \frac{1}{i\omega\epsilon} \int_{\mathcal{T}_m} \nabla \cdot \mathbf{f}_p(\mathbf{r}) \int_{\mathcal{T}_n} g(\mathbf{r}, \mathbf{r}') \nabla' \cdot \mathbf{f}_q(\mathbf{r}') d\mathbf{r}' d\mathbf{r}. \quad (3.28)$$

### 3.1. Surface Integral Equations

---

The integrals can be calculated with a Gauss quadrature rule for triangles if we transform each triangular element to an orthogonal one by using its barycentric coordinates (more information regarding these methods in Appendix D).

For the discretization of the MFIE, a similar logic is followed and  $Q_{pq}^{mn}$  takes the following form

$$Q_{pq}^{mn} = \frac{1}{2} \int_{\mathcal{T}_m} \mathbf{f}_p(\mathbf{r}) \cdot \mathbf{f}_q(\mathbf{r}) d\mathbf{r} - \int_{\mathcal{T}_m} \hat{\mathbf{n}} \times \mathbf{f}_p(\mathbf{r}) \int_{\mathcal{T}_n} \nabla' g(\mathbf{r}, \mathbf{r}') \times \mathbf{f}_q(\mathbf{r}') d\mathbf{r}' d\mathbf{r}. \quad (3.29)$$

We note that the first term of the right-hand side is computed only when the two elements,  $\mathcal{T}_m$  and  $\mathcal{T}_n$  overlay ( $n = m$ ). In addition, in the literature, it is proven that MFIE discretized and tested with RWG functions is not as accurate as the EFIE. However, a variety of alternatives (here is a non-exhaustive list [182–188]) are used in order to make MFIE more accurate, e.g., testing with  $\hat{\mathbf{n}} \times \mathbf{f}_{\text{RWG}}$ .

For the PMCHWT formulation, the MoM matrix (by expanding both currents with RWG functions) is

$$Z = Z_{\text{in}} + Z_{\text{out}} = \begin{bmatrix} Z1_{\text{in}} + Z1_{\text{out}} & Z2_{\text{out}} + Z2_{\text{in}} \\ Z3_{\text{out}} + Z3_{\text{in}} & Z4_{\text{out}} + Z4_{\text{in}} \end{bmatrix} \quad (3.30)$$

The subscripts in and out denote the inside and outside of the scatterer, respectively. The elements  $Q_{pq}^{mn}$  are

$$\begin{aligned} Q1_{pq}^{mn} &= i\omega\mu \int_{\mathcal{T}_m} \mathbf{f}_p(\mathbf{r}) \int_{\mathcal{T}_n} g(\mathbf{r}, \mathbf{r}') \mathbf{f}_q(\mathbf{r}') d\mathbf{r}' d\mathbf{r} + \frac{1}{i\omega\epsilon} \int_{\mathcal{T}_m} \nabla \cdot \mathbf{f}_p(\mathbf{r}) \int_{\mathcal{T}_n} g(\mathbf{r}, \mathbf{r}') \nabla' \cdot \mathbf{f}_q(\mathbf{r}') d\mathbf{r}' d\mathbf{r} \\ Q2_{pq}^{mn} &= - \int_{\mathcal{T}_m} (\hat{\mathbf{n}}_m \times \mathbf{f}_p(\mathbf{r})) \cdot \mathbf{f}_q(\mathbf{r}) d\mathbf{r} - \int_{\mathcal{T}_m} \mathbf{f}_p(\mathbf{r}) \int_{\mathcal{T}_n} \nabla' g(\mathbf{r}, \mathbf{r}') \times \mathbf{f}_q(\mathbf{r}') d\mathbf{r}' d\mathbf{r} \\ Q3_{pq}^{mn} &= \eta \frac{\epsilon}{\mu} Q1_{pq}^{mn}, \quad Q4_{pq}^{mn} = \eta Q2_{pq}^{mn}. \end{aligned} \quad (3.31)$$

#### 3.1.3.1 Singular Integrals

The above 4D surface integrals contain the Green's function, which presents singularity when  $\mathbf{r}' = \mathbf{r}$ , or when the triangles overlay or share an edge or node. Such integrals are called singular (weakly for  $g(\mathbf{r}, \mathbf{r}')$  and strongly for  $\nabla g(\mathbf{r}, \mathbf{r}')$ ) and a variety of methods can be used to solve them, such as the semi-analytical calculations in [189–192]. The content of these articles is implemented as sophisticated software packages, dubbed DEMCEM [27], which we will use as a black-box in order to tackle the aforementioned integrals.

#### 3.1.4 Numerical Problems of EFIE

In this section, we will provide an insight into the most well-known problems of EFIE. Even though EFIE has been used extensively in the past in various applications, it is not free of problems. For example, either the applied discretization, the operating frequency, or the geometry of

the problem affect the condition number of the arising MoM matrix, thus making the convergence time of an iterative prohibitively slow.

#### 3.1.4.1 Combined Field Integral Equation

Let us consider that we are studying closed scatterers, e.g., a metallic sphere. Since the EFIE is imposed on the surface of the scatterer, it cannot distinguish the difference between a dense scatterer and a scatterer-shell, e.g., a dense metallic sphere is the same as a thin metallic spherical shell. Such a shell is a resonance cavity. Since the scatterer is approximated with triangular elements, electromagnetic energy can leak into the polygonic shell and, as a result, excite the internal resonance modes. These modes contribute to the equivalent surface currents and change their value from the expected solution in an EFIE solver. Besides, when the operating frequency and the resonance frequency are similar, the modes, as mentioned earlier, leak more energy to the exterior of the surface, thus, giving rise to erroneous scattered fields. When the operating frequency is close to the internal resonance frequency, the MoM matrix becomes ill-conditioned, and the EFIE has a null-space solution; thus, the surface current is nonunique [126,128,166,193].

An extended boundary condition has to be applied to enforce the interior field to be zero. The dual-surface electric and magnetic integral equations (DSEFIE, DSMFIE) [194] are two formulations that establish such boundary conditions. In both cases, an interior shell is placed just inside the first surface, and a combined integral equation arises, which satisfies the new boundary conditions and produces unique solutions at all frequencies. However, since this equation is solved for two times more unknowns, it is usually avoided. Alternatively, one can force the internal resonances of the shell to correspond to complex frequencies in order for the operating frequency to not coincide with them. To achieve this a linear combination of the EFIE and MFIE, referred to as the combined field integral equation is considered

$$Z^{\text{CFIE}} = \alpha Z^{\text{EFIE}} + (1 - \alpha) \frac{\eta}{k_0} Z^{\text{MFIE}}. \quad (3.32)$$

Since the null spaces of the EFIE and MFIE differ, the null-space of CFIE can only occur at complex resonance frequencies. Hence, the equation is free from the internal resonance problem, and the solution is unique. Moreover,  $\alpha$  is a free parameter, and it determines if CFIE will behave more as an EFIE or as an MFIE. The most common choices are  $\sim 0.2$  for MFIE,  $\sim 0.8$  for EFIE or  $\sim 0.5$  for similar behavior. The CFIE is an already established method and has been used extensively in the past for various applications [20, 151, 152, 195–199]. Finally, following a suchlike logic, one can define a CFIE for penetrable scatterers as in [200, 201].

#### 3.1.4.2 Low-Frequency Catastrophe of EFIE

EFIE appears to be problematic when the operation frequency is small [202], meaning that the maximum dimension of the scatterer is equal to only a few hundred wavelengths [203]. This phenomenon is called low-frequency breakdown (or catastrophe) of EFIE, and it happens because its first term is proportional to the angular momentum  $\omega$ , while the second term is in-

versely proportional to it [204]. The arising RWG-MoM matrix is ill-conditioned. Thus an iterative solver converges to the final solution extremely slow [205]. To tackle such a problem, we need to study the behavior of the electric current when  $\omega \rightarrow 0$ . According to Maxwell's equations, the electrostatic and the magnetostatic field decompose. A current irrotational component generates the electrostatic field and a solenoidal one, the magnetostatic. The use of RWG functions does not take into account such behavior for the equivalent surface electric current; thus, the breakdown appears. A new set of div-conforming basis functions can be used, such as the Loop-Star [206] or the Loop-Patch [207], to avoid the breakdown. More information can be found in [208], where the basis mentioned above are discussed.

#### 3.1.4.3 Calderón Preconditioner

In the previous subsection, we underlined that an EFIE solver based on RWG is no panacea. Not only the condition number grows as long as we increase the wavelength, but also when we h-refine the discretization. On the one hand, EFIE is extremely slow when it is applied to geometries with subwavelength features. On the other hand, MFIE does not suffer from such ill-conditioning problems: it is an integral equation of the second kind, and the identity operator of the first term on its right-hand side does not allow the eigenvalues of the MoM matrix to tend to zero. Moreover, the square of the EFIE operator is the MFIE operator, meaning that it has a self-regularizing property. Thus it can be physically preconditioned effectively. Such preconditioning techniques [209–212] tackle the ill-conditioning that comes from the discretization density. The most well-known is the Calderón multiplicative preconditioner [213], which can be easily applied over the RWG-based MoM matrix and it is based on div- and quasicurl-conforming basis functions [214] (Buffa-Christiansen, BC basis functions).

The PMCHWT formulation suffers from several drawbacks as well: the condition number grows arbitrarily large as long as we h-refine the geometry. Even though we could use the Müller integral equation, since it does not suffer from such breakdown, it is known that it is far less accurate in comparison with PMCHWT [215]. Thus, a Calderón multiplicative preconditioner [216] is used in such cases as well.

All the problems mentioned above are summarized in Figure 3.6. In both plots, the condition number of a SIE MoM matrix is portrayed, for various wavelengths. The first plot concerns a PEC sphere of unit radius, while the second plot studies a diamond sphere with  $\epsilon_r = 5.68 - i0.0023/(\epsilon_0\omega)$  and unit radius as well. For small wavelengths (high frequencies), a weird behavior is noted; this happens because the edge length of the triangles of the discretization is comparable with the wavelength. Thus an accurate approximation is impossible. For large wavelengths (low frequencies), we notice the catastrophe mentioned above for EFIE (and the dielectric formulations since they are related to EFIE). Besides, as long as we h-refine, the condition number of EFIE increases. Moreover, the low and steady condition number of MFIE for all frequencies indicate its well-posedness. Finally, in specific frequencies ( $\lambda \simeq 2.3$ ), the condition

number of EFIE presents sudden peaks, a phenomenon due to the similarity of the sphere's resonance frequency and the operating frequency. In such cases, CFIE presents a smaller condition number as expected.

### 3.1.5 Far Field Measurements

One of the most important measurements regarding antenna theory is the far-field, as it determines the antenna's radiation pattern. Moreover, antennas are frequently used for wireless communication for long distances. Thus, the far-zone region defines their field of operation. The electromagnetic field radiated by an antenna is a spherical wave, and it is proportional to  $1/r^n$ ,  $n = 1, 2, 3, \dots$ . Neglecting higher-order terms ( $n = 2, 3, \dots$ ) one can derive that the  $r$  component of each field goes to 0. Also, the electric and magnetic field components are orthogonal to each other at the far-zone, which is defined as the region where the radial distance is, at least, ten times larger than  $2d^2/\lambda$ .  $d$  is the maximum dimension of the scatterer. To find the far-field, we do not need to recalculate the integrals of SIE formulations since closed-form solutions exist in the relevant literature [25, 127]. In Figure 3.7 we illustrate the radiation pattern of a PEC sphere with unit radius for one azimuthal cut ( $\phi = 0$ ), irradiated by a linear polarized plane wave  $\mathbf{e}_{\text{inc}} = \hat{x}e^{-ik_0z}$  with operating wavelength 4 m. The far-field is obtained with Mie solution, the EFIE, the MFIE and the CFIE ( $\alpha = 0.5$ ) and for three discretizations with 230, 920 and 3280 triangular elements. In 3.8, 3.9, 3.10 the same radiation pattern is illustrated for a diamond ( $\epsilon_r = 5.68 - j0.0023/(\epsilon_0\omega)$ ), a concrete ( $\epsilon_r = 4.5$ ), and a titanium ( $\epsilon_r = 100$ ) sphere respectively with the Mie solution, the PMCHWT and the Müller formulations for the same discretizations as in the PEC case. For the PEC the diamond and the concrete spheres, the results are in great agreement with the Mie series, while for the titanium sphere (of high contrast with the surrounding vacuum), the results are relatively accurate for the finest discretization.

In Figure 3.11, the  $L_2$  relative error of the far-field, on the aforementioned azimuthal cut, is portrayed for the PEC and the diamond sphere, and 40 different wavelengths. As expected, the error decreases as long as we increase the operating frequency and refine the discretization. It is observed that EFIE is superior to MFIE and CFIE and that PMCHWT and Müller formulations have a similar relative error.

### 3.1.6 Computation of Power

For the computation of the absorbed or the scattered power in electromagnetics we can calculate the *Poynting vector* [217] as follows

$$\mathbf{s}_{\text{ext}} = \frac{1}{2} \mathcal{Re} \{ \mathbf{e}_{\text{inc}} \times \mathbf{h}_{\text{sca}}^* + \mathbf{e}_{\text{sca}} \times \mathbf{h}_{\text{inc}}^* \}. \quad (3.33)$$

However, this method requires the calculation of the scattered electromagnetic field, which requires post-processing of the solution of the respective linear system of the SIE. Thus, it would be beneficial if we could extract the power by using only the equivalent surface currents. Thankfully, in [218], the authors note that the power absorbed by a compact body can be computed

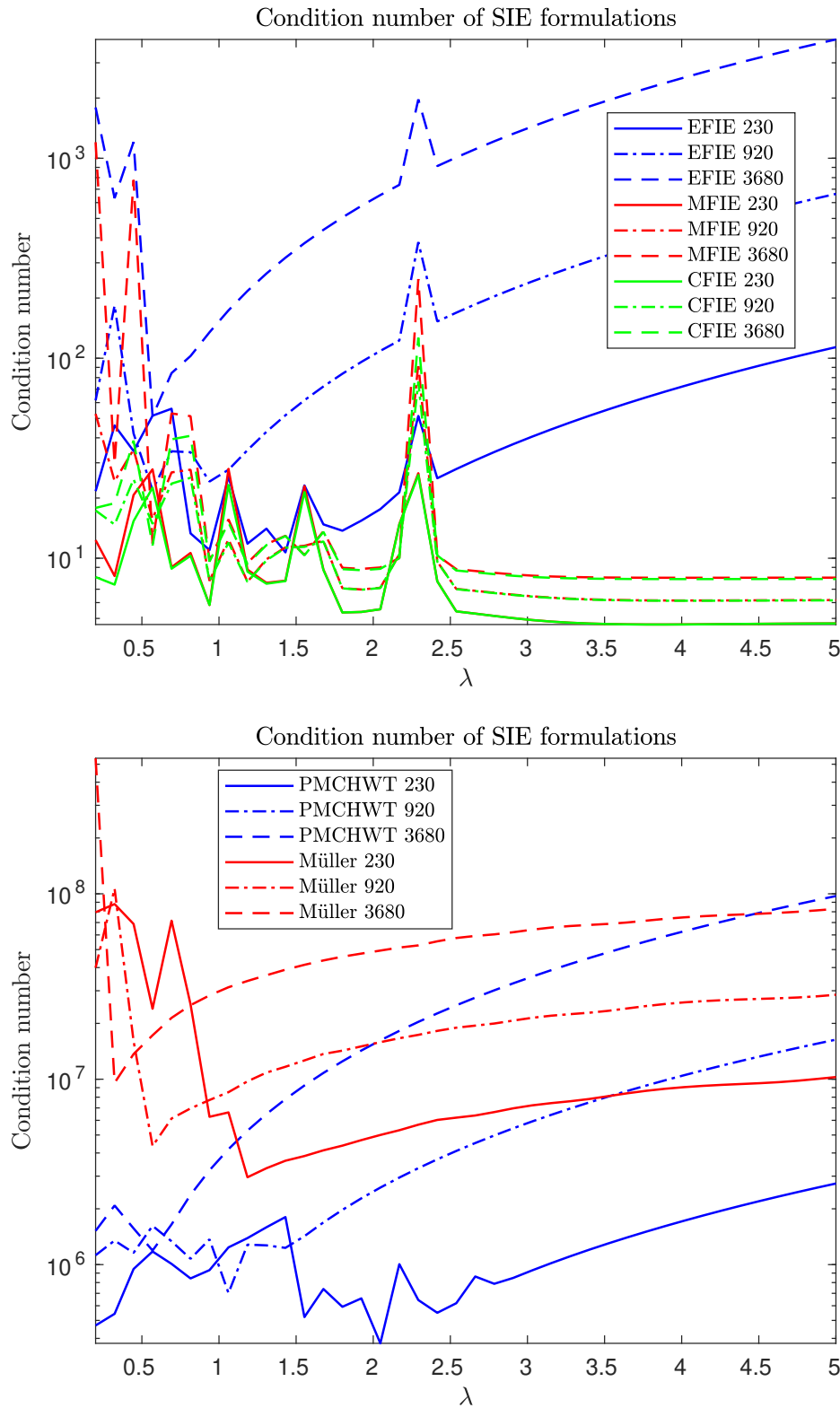


Figure 3.6: Condition number of the MoM matrix of the (top) EFIE, MFIE and CFIE formulations for a PEC sphere, and the (bottom) PMCHWT and Müller formulations for a diamond sphere with  $\epsilon_r = 5.68 - j0.0023/(\epsilon_0\omega)$ , of unit radii.

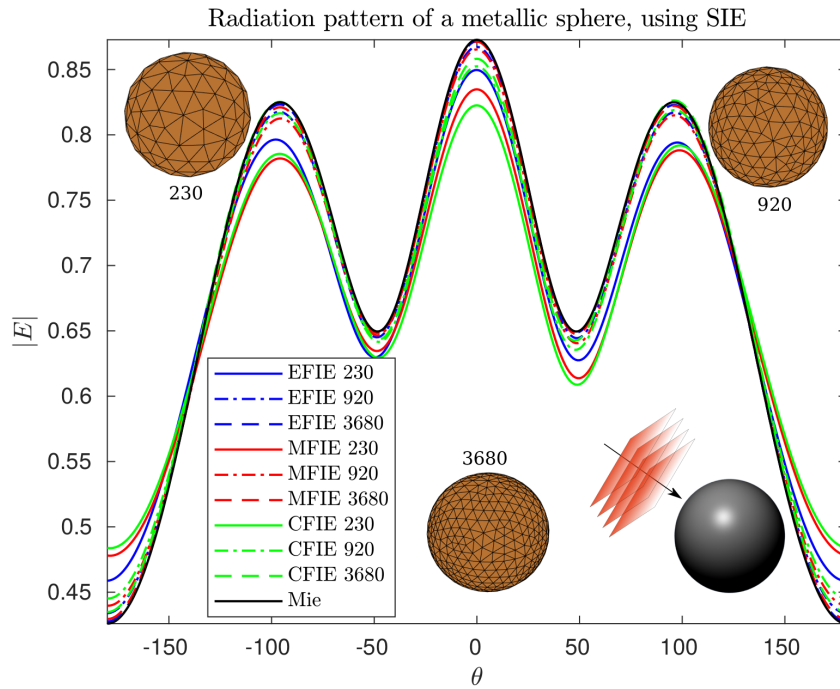


Figure 3.7: Radiation pattern of a PEC sphere with unit radius on the azimuthal cut  $\phi = 0$ . The incident field is a linear polarized plane wave. The far-field is obtained with the Mie solution and the EFIE, MFIE, CFIE, for three different discretizations.

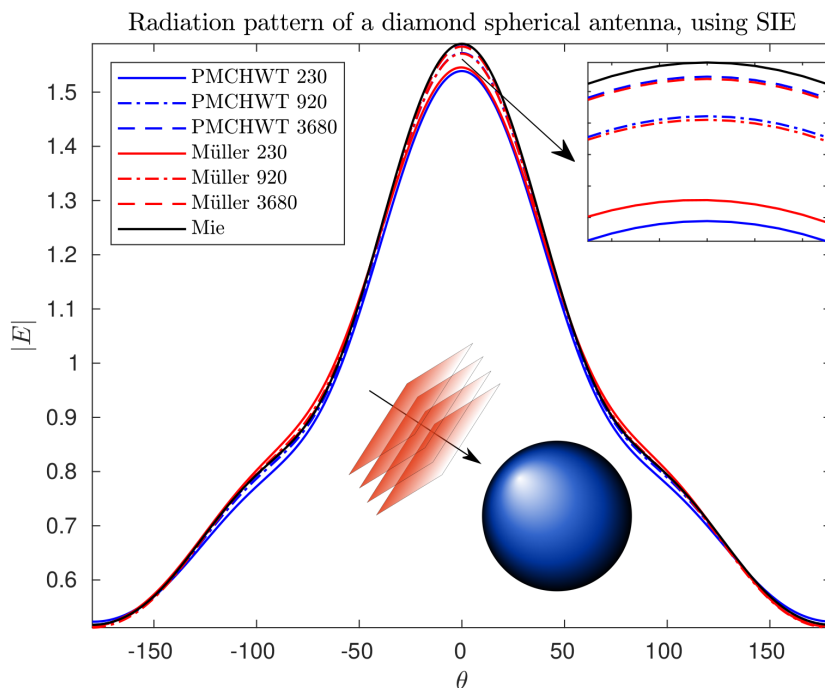


Figure 3.8: Radiation pattern of a diamond sphere with unit radius on the azimuthal cut  $\phi = 0$ . The incident field is a linear polarized plane wave. The far-field is obtained with the Mie solution and the PMCHWT, Müller, for three different discretizations.

### 3.1. Surface Integral Equations

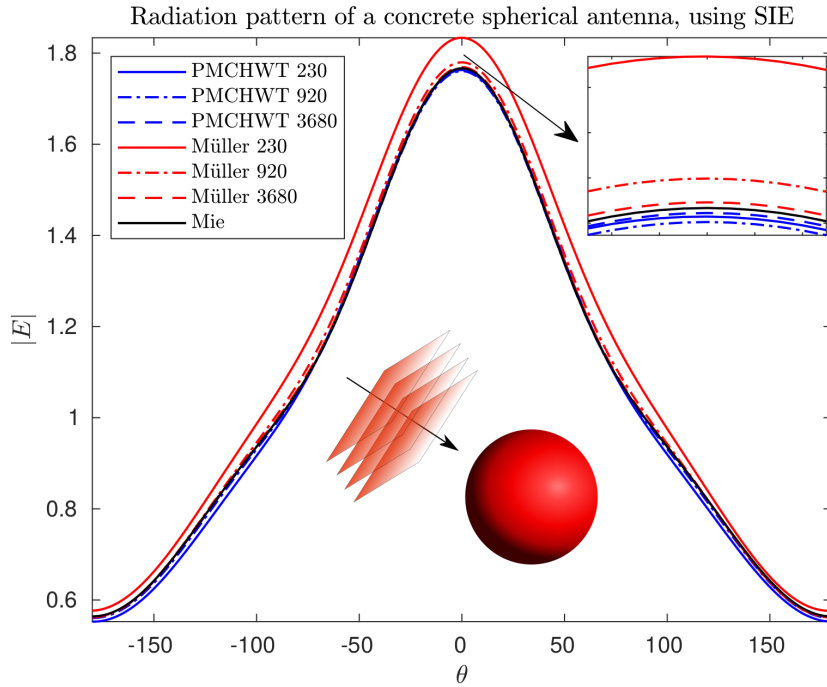


Figure 3.9: Radiation pattern of a concrete sphere with unit radius on the azimuthal cut  $\phi = 0$ . The incident field is a linear polarized plane wave. The far-field is obtained with the Mie solution and the PMCHWT, Müller, for three different discretizations.

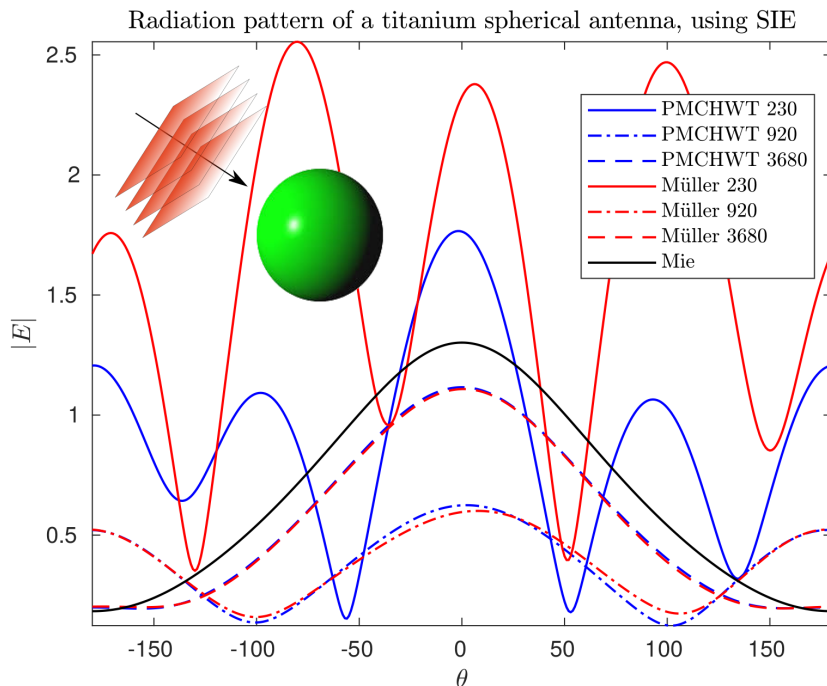


Figure 3.10: Radiation pattern of a titanium sphere with unit radius on the azimuthal cut  $\phi = 0$ . The incident field is a linear polarized plane wave. The far-field is obtained with Mie solution and the PMCHWT, Müller, for three different discretizations.

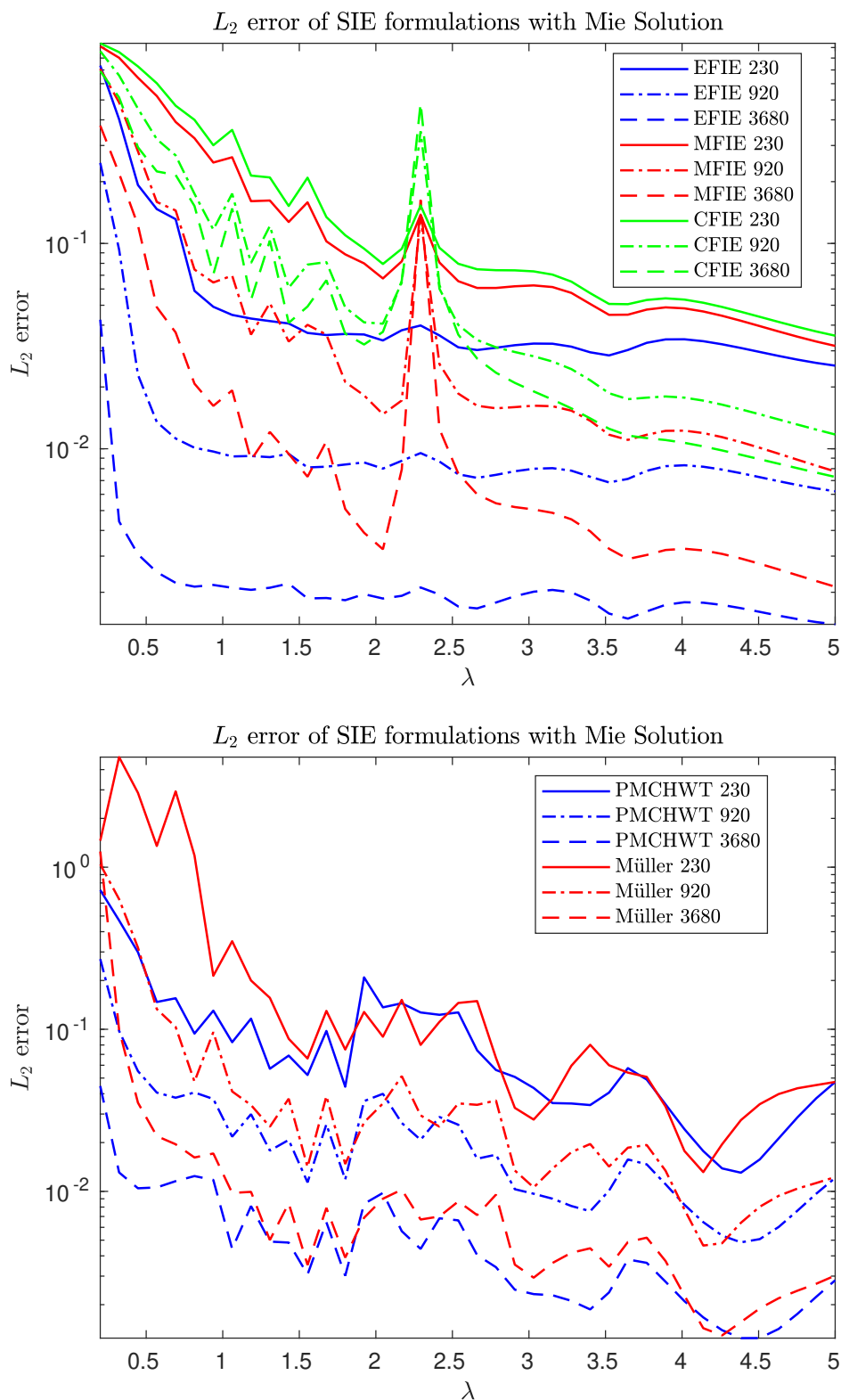


Figure 3.11:  $L_2$  relative error of the far-field of a (top) PEC and (bottom) a diamond sphere with unit radiuses on the azimuthal cut  $\phi = 0$ , in respect to the wavelength, using the (top) EFIE, MFIE, CFIE and (bottom) PMCHWT, Müller, for three different discretizations and comparing with the Mie solution.

### 3.1. Surface Integral Equations

---

directly from the surface currents without computing the scattered fields. Furthermore, in [219] clear and compact solutions are provided for the calculation of *Power*, *Force* and *Torque* (PFT) as a bilinear product<sup>1</sup> of the form

$$q = \mathbf{j}^* Q \mathbf{j}, \quad (3.34)$$

where  $q$  is the desired quantity,  $\mathbf{j}$  is the expansion coefficients vector of the equivalent surface current, and  $Q$  is a  $q$ -dependant matrix. Three different methods can be invoked based on classical electrodynamics such as the Poynting vector and the *first law of Joule* to express the matrix  $Q$ .

The first method is dubbed *Displaced Surface-Integral* (DSI), and it is based on the Poynting vector. The Poynting vector  $\mathbf{p}$  is integrated over a bounding surface  $\mathcal{S}_b$  surrounding the object  $\mathcal{S}$  of interest (but it is located away from it). The flux of energy is given from

$$\mathbf{p} \cdot \hat{\mathbf{n}} = (\mathbf{e}^* \times \mathbf{h}) \cdot \hat{\mathbf{n}}, \quad (3.35)$$

where  $\hat{\mathbf{n}}$  is the outward-pointing surface normal vector. The time-average absorbed power, of the enclosed object by  $\mathcal{S}_b$  is

$$p_{\text{abs}} = -\frac{1}{2} \text{Re} \left\{ \oint_{\mathcal{S}_b} (\mathbf{p}(\mathbf{r}) \cdot \hat{\mathbf{n}}) d\mathcal{S}_b \right\}. \quad (3.36)$$

Using the RWG equivalent surface current expansion 3.24 one can end up to the following equation for the absorbed power

$$p_{\text{abs}} = \sum_{i,j=1}^N [\mathbf{j}_i^* \mathbf{m}_i^*] \left\{ \sum_{m=1}^M -w_m [\mathcal{L}_2(\mathbf{r}_m) \cdot (\hat{\mathbf{n}} \times \mathcal{K}_2(\mathbf{r}_m)) + \mathcal{K}_2(\mathbf{r}_m) \cdot (\hat{\mathbf{n}} \times \mathcal{L}_2(\mathbf{r}_m))] \right\} \begin{bmatrix} \mathbf{j}_j \\ \mathbf{m}_j \end{bmatrix}, \quad (3.37)$$

where we considered that the points  $\mathbf{r}_m$  lie in a region with no sources, and the integration was performed using a Lebedev cubature rule with  $M$  weights  $w_m$  and points  $\mathbf{r}_m$  if we consider the bound surface as a sphere. The matrix  $Q$  is nothing else than the quantity inside the brackets of the equation 3.37, and the absorbed power can be expressed as a bilinear product of the form of 3.34. To significantly simplify this method, we consider  $\mathcal{S}_b$  to coincide with the surface of the object. The required electromagnetic fields exist only on the surface of the object, which means that we can directly use the surface equivalent currents instead of surface fields. This method is dubbed as *Overlap* method. After some operations, the absorbed power is

$$p_{\text{abs}} = \sum_{i=1}^N \sum_{j=1}^N [\mathbf{j}_i^* \mathbf{m}_i^*] \left\{ \frac{1}{4} \oint_{\mathcal{S}_b} [\mathbf{f}_i^* \cdot (\hat{\mathbf{n}} \times \mathbf{g}_j) - \mathbf{g}_i^* \cdot (\hat{\mathbf{n}} \times \mathbf{f}_j)] d\mathcal{S}_b \right\} \begin{bmatrix} \mathbf{j}_j \\ \mathbf{m}_j \end{bmatrix}, \quad (3.38)$$

---

<sup>1</sup>The PFT have a quadratic relation to the electromagnetic field intensities, thus to the equivalent surface currents as well

where the  $Q$  matrix is the quantity inside the brackets, and the integral can be evaluated with a Lebedev rule. The new  $Q$  matrix involves local overlaps between the basis functions, thus, in the case of RWG functions, the matrix is sparse (RWG has a support of two elements), and the computations can be significantly accelerated.

Instead of expressing the power as a quadratic form of the electromagnetic field intensities of the equivalent currents, we can express it as a product between fields and currents and derive the *Equivalence-Principle* formulation, which reminds us the Joule's first law of heating. By considering the equivalence principle and extinction theorem, we can replace the dielectric object  $\mathcal{S}$  with an empty volume  $\mathcal{V}$ , and equivalent electric and magnetic currents which flow on its bound. The absorbed power now is given from

$$p_{\text{abs}} = \frac{1}{2} \mathcal{Re} \left\{ \iiint_{\mathcal{V}} [\mathbf{j}^*(\mathbf{r}) \cdot \mathbf{e}(\mathbf{r}) + \mathbf{m}^*(\mathbf{r}) \cdot \mathbf{h}(\mathbf{r})] d\mathcal{V} \right\}. \quad (3.39)$$

Since the equation, 3.39, uses the electromagnetic field intensities on the surface of the object, and due to tangential continuity, we can either use the exterior or the interior ones. To avoid complicated operations we usually choose the domain where incident sources do not exist, i.e., for an exterior plane wave, the absorbed power is

$$p_{\text{abs}} = \frac{1}{2} \mathcal{Re} \left\{ [\mathbf{j}_i^* \ \mathbf{m}_i^*] Z_{\text{in}} \begin{bmatrix} \mathbf{j}_j \\ \mathbf{m}_j \end{bmatrix} \right\} = \frac{1}{2} [\mathbf{j}_i^* \ \mathbf{m}_i^*] \mathcal{Re} \{ Z_{\text{in}} \} \begin{bmatrix} \mathbf{j}_j \\ \mathbf{m}_j \end{bmatrix}. \quad (3.40)$$

Moreover, the extinction and scattered power can be easily calculated as follows

$$p_{\text{ext}} = \frac{1}{2} [\mathbf{j}_i^* \ \mathbf{m}_i^*] \mathcal{Re} \{ Z_{\text{in}} + Z_{\text{out}} \} \begin{bmatrix} \mathbf{j}_j \\ \mathbf{m}_j \end{bmatrix}, \quad p_{\text{scat}} = \frac{1}{2} [\mathbf{j}_i^* \ \mathbf{m}_i^*] \mathcal{Re} \{ Z_{\text{out}} \} \begin{bmatrix} \mathbf{j}_j \\ \mathbf{m}_j \end{bmatrix}. \quad (3.41)$$

To validate the robustness and accuracy of the Equivalence-Principle method, we will study a spherical scatterer for a wide range of frequencies, and we will compare the results with the Mie Solution (Appendix A). We consider a gold nanoparticle with radius  $r = 1 \mu\text{m}$  and complex permittivity

$$\epsilon_r = \epsilon_0 \left( 1 - \frac{\omega_p^2}{\omega(\omega - i\gamma)} \right), \quad (3.42)$$

where  $\omega_p = 1.37 \times 10^{16}$  and  $\gamma = 5.32 \times 10^{13}$ . Gold nanoparticles play a significant role in a variety of applications, such as electronics, photodynamic therapy, therapeutic agent delivery, sensors and diagnostics; thus, an accurate approximation of its power deposition is important. The nanoparticle is irradiated by a linear polarized plane wave  $\mathbf{e}_{\text{inc}}(\mathbf{r}) = \hat{x}e^{-ik_0z}$ . The PMCHWT formulation is used and the nanoparticle is discretized with 230,920 and 3280 triangular elements. For visualization purposes we will portray in 3.12 the absorption and the scattering power efficiencies  $\sigma/(\pi r^2)$ , where  $\sigma$  is the absorption ( $\sigma_{\text{abs}} = 2\eta p_{\text{abs}}$ ) or the scattering ( $\sigma_{\text{scat}} = 2\eta p_{\text{scat}}$ ) cross section. The results are extremely close to the analytical solution for the whole range of frequencies, even for small discretizations.

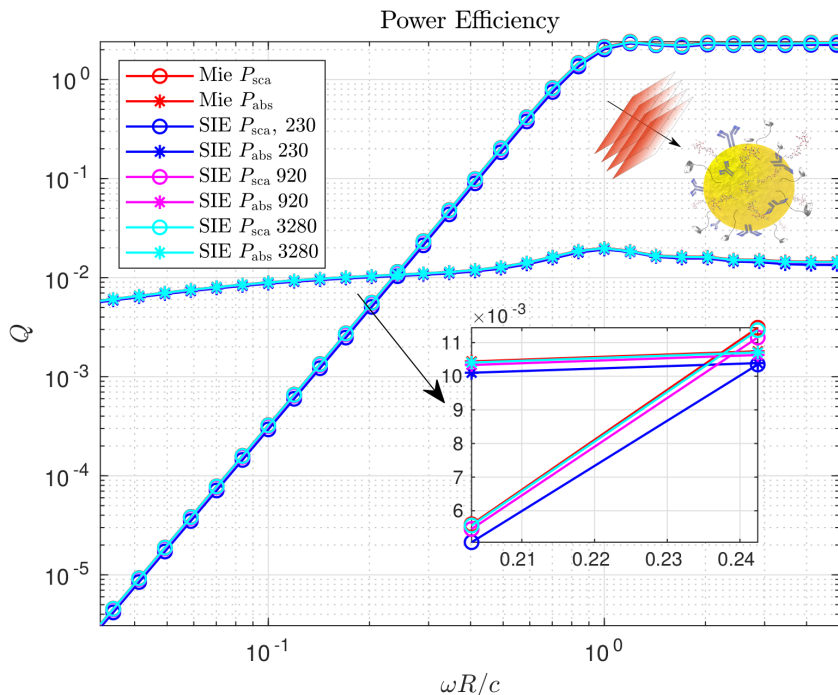


Figure 3.12: Absorbed and scattered power efficiencies for a gold nanoparticle, irradiated with a linearly polarized plane wave, for a wide range of frequencies. The image of the gold nanoparticle is obtained from the department of chemistry and molecular biology of the University of Gothenburg.

#### 3.1.7 Lumped Elements

In all MR-systems, one of the essential components is the radiofrequency coil that accompanies the scanner and generates the electromagnetic field required for the excitation of the hydrogen atoms inside the human body, in order to produce the desired MR image. Furthermore, the RF coils act as intermediary helpers for the interaction of electromagnetic fields of the scanner and biological tissue. Thus, each coil should be designed in a sophisticated manner for the application of choice, i.e., breast coils [220], head coils [221] and body coils [222]. Moreover, most MR coils operate as resonators since they are designed in a way to enforce a uniform  $|b_1^+|$  field inside the body. Therefore, good signal gains are generated, and as a result, the quality of the MR image is enhanced. In most cases, the coil is equipped with additional tuning capacitors in order to establish decoupling and resonance at the desired frequency.

Nowadays, the modeling of MRI RF coils can be easily implemented through a variety of computational electromagnetics-based techniques. For example, for low frequencies, the lumped-element circuit model has proven to be the method of choice [223–226] mostly because of its simplicity and speed. In this method, the conductive strips of the coil are modeled as inductances. Each strip couples with the other strips due to the mutual inductance appearing from their interaction. Additional capacitors and capacitive elements are modeled as lumped capaci-

tors. Therefore, the RF coil becomes an electric circuit and can be analyzed both analytically with Kirchhoff's laws, or with a sophisticated software package [227]. However, when the free-space wavelength decreases (increasing the magnetic resonance frequency), the method becomes inaccurate (especially for 7 Tesla MR scanners, which are the main interest of this thesis).

For higher frequencies and more accurate simulations, methods that are based on Maxwell's equations are needed. Methods such as the FD or the FEM, from the family of PDEs, can be used, but for reasons explained previously in this Chapter we choose to use the SIE which has been applied successfully for the simulation of unloaded [228–232] and loaded [23] MRI RF coils. For our applications of interest, the delta-gap method [230] is accurate enough. Notably, in the delta-gap method, each lumped element or feeding port of the coil is treated as sets of continuous and parallel edges of the triangular mesh, as in 3.13, where a capacitor is replaced with the red edge between two triangular elements of the discretization. The usage of triangular elements and RWG basis functions are crucial for this method's accuracy and feasibility, while the modeling of the geometry and the meshing process is straightforward and can be implemented easily with various packages [233, 234].

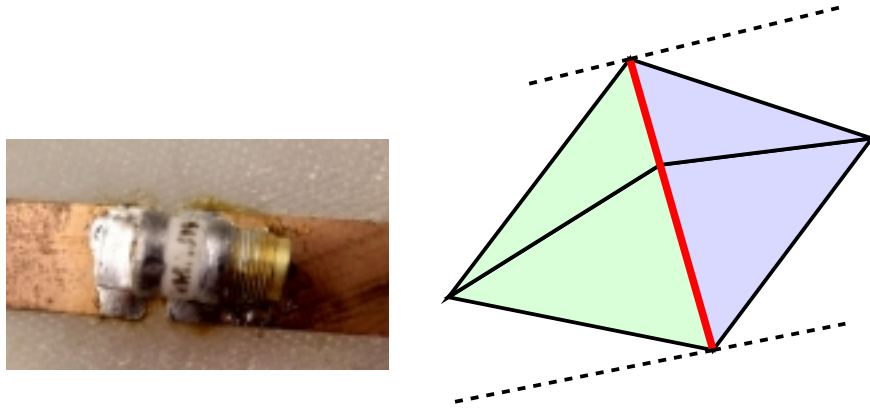


Figure 3.13: (left) Actual capacitive lumped element of an RF coil and (right) modelled element with the delta-gap method (red line).

Since most RF coils can be treated as open surfaces (infinitely small width) and they are created from copper (a highly conductive material), the EFIE for PEC objects can be used to model them. Each lumped element or feeding port introduces a voltage jump equal to  $v_\delta$ , therefore

$$\mathbf{e}_{\text{inc}}(\mathbf{r}) = v_\delta \delta(\mathbf{r} - \mathbf{r}') \hat{n}, \quad (3.43)$$

where  $\hat{n}$  is the normal to  $\mathbf{r}'$ , the location of the element, or the port. In the case of the feeding ports, after the Galerkin projection, the voltage across the edges that model the port becomes

$$v_{\text{port}} = - \sum_{i=1}^{\text{edges}} \iint_{\mathcal{T}_i} v_\delta \delta(\mathbf{r} - \mathbf{r}'_i) \hat{n}_i \cdot \mathbf{j}_i(\mathbf{r}) d\mathbf{r} = - \sum_{i=1}^{\text{edges}} l_i v_\delta, \quad (3.44)$$

### 3.1. Surface Integral Equations

where  $\mathcal{T}_i$  is the triangle that the edge  $i$  belongs to,  $l_i$  is the length of the edge and  $\mathbf{j}_i(\mathbf{r})$  is the current appearing on this edge. The same procedure is applied for multiport coils, and the right-hand-side of the MoM system becomes  $FV$ , i.e., for an  $n$  port network with  $m$  edges at each feeding port we have

$$F = \begin{bmatrix} F_1 & 0 & 0 & \cdots & 0 \\ 0 & F_2 & 0 & \cdots & 0 \\ \cdots & \cdots & \cdots & \cdots & \cdots \\ 0 & 0 & 0 & \cdots & F_n \\ 0 & 0 & 0 & \cdots & 0 \\ \cdots & \cdots & \cdots & \cdots & \cdots \\ 0 & 0 & 0 & \cdots & 0 \end{bmatrix}, \quad F_j = \begin{bmatrix} -l_{1j} \\ -l_{2j} \\ \cdots \\ -l_{mj} \end{bmatrix}, \quad (3.45)$$

where  $l_{ij}$  is the length of the  $i$ -th edge of port  $j$ .  $V$  is equal to  $\text{diag}(v_{\delta,i})$ ,  $i = 1, \dots, N$ .

In the case of lumped elements the equivalent electric field due to the voltage jump across the edges is

$$\mathbf{e}_{\text{inc}}(\mathbf{r}) = z_{\text{element}} \sum_{i=1}^{\text{edges}} \mathbf{j}_i l_i \delta(\mathbf{r}) \hat{\mathbf{n}}, \quad (3.46)$$

where  $z_{\text{element}}$  is the impedance of the lumped element. Thus, the voltage jump will be

$$v_{\text{port}} = -z_{\text{element}} l_{\text{port}} \left( \sum_{i=1}^{\text{edges}} \mathbf{b}_i l_i \right), \quad (3.47)$$

where  $\mathbf{b}$  is the vector with the RWG coefficients. Since the unknown surface equivalent current appears on the RHS of EFIE, we can move it to the LHS and update the appropriate elements of the MoM matrix  $Z$  as follows

$$Q_{pq}^{mn} = Q_{pq}^{mn} + z_{\text{element}} l_p l_q. \quad (3.48)$$

Here,  $m, n$  are the triangles that  $p, q$  edges belong to respectively.

#### 3.1.8 Network Parameters

The previously described RF coils consist of multiple excitation ports. Thus they can be modeled as black-box circuits with known network parameters [235]. Let us consider a coil, where each feeding port is expressed with just one edge of the discretization. The equivalent surface current can be written as

$$\mathbf{j}_{\text{eq}} = \sum_{n=1}^p \mathbf{j}_n \mathbf{f}_n(\mathbf{r}) + \sum_{n=p+1}^N \mathbf{j}_n \mathbf{f}_n(\mathbf{r}), \quad (3.49)$$

where  $t$  is the number of feeding ports on the coil,  $N$  is the total number of edges, and  $\mathbf{j}_n$  is the solution of the MoM system. The MoM system can be rewritten as

$$\begin{bmatrix} Z^{pp} & Z^{pe} \\ Z^{ep} & Z^{ee} \end{bmatrix} \begin{bmatrix} \mathbf{j}_{\text{eq}}^p \\ \mathbf{j}_{\text{eq}}^e \end{bmatrix} = \begin{bmatrix} \mathbf{v}^p \\ 0 \end{bmatrix}, \quad (3.50)$$

where  $Z^{pp}$  is the block matrix representing interactions between the edges that model the feeding ports, while  $Z^{ee}$  models the interactions between the rest of the edges of the mesh. The current of the feeding ports is  $\mathbf{j}_{\text{eq}}^p$  and of the rest of the edges  $\mathbf{j}_{\text{eq}}^e$ . Finally,  $\mathbf{v}^p$  is the vector of voltage excitations at the feeding ports. The impedance parameters of the circuit that models the coil can be found as the matrix  $Z^p$ , where

$$Z^p \mathbf{j}_{\text{eq}}^p = \mathbf{v}^p. \quad (3.51)$$

After a simple manipulation of 3.50 we derive the following equation for the impedance parameters of the coil

$$Z^p = Z^{pp} - Z^{pe} (Z^{ee})^{-1} Z^{ep}. \quad (3.52)$$

### 3.2 Volume Integral Equations

In this section, we will present the so-called FFT-based VIE methods. Specifically, on the contrary with SIEs, VIEs require an enormous amount of storage space for their MoM matrix, since the discretization concerns the whole domain (not only the 2D surrounding surface). In some cases (that will be studied later in this section), the matrix mentioned above would require around 200 PB, a prohibitive number for any computer's random-access memory (RAM). However, as mentioned before, a variety of techniques can be used for the extreme reduction of these unrealistic significant needs for storage, such as exploiting the translationally invariant property of the Green's function. If the discretization of the domain takes place over a uniform grid, the MoM matrix acquires a block-Toeplitz with Toeplitz-blocks (BTTB) form, and consequently, only its defining vector have to be stored for the implementation of the subsequent matrix-vector products. Relevant methods have been studied widely over the last three decades (here is a non-exhaustive list [52–55, 57, 236–246]) that exploit this property and solve for either the unknown electric field or electric flux density with div-conforming basis functions (rooftop).

However, the cases mentioned above are proved to be unstable [247, 248] for highly inhomogeneous scatterers, e.g., the human head. As a result, more competitive VIE methods arise [4, 24, 249] to tackle related biomedical applications and other challenging problems. These methods solve for the unknown polarization currents (both electric and magnetic) since the relevant integral equations are of the second kind; thus, well-posed for any scatterer. In the following, we will compare the current-based VIE (JMVIE) with the EVIE and DVIE and underline its superior convergence properties.

Moreover, we will briefly mention a discretization scheme for JMVIE with piecewise polynomial approximations as basis functions [4, 24] along with an electric flux-based formulation [53] that it is not entirely Galerkin-based. However, it is used in MR-community for the calculations of interactions between human tissue and electromagnetic waves. Finally, we will provide a plethora of results relevant to MRI applications.

### 3.2.1 Current-Based Volume Integral Equation

We consider the electromagnetic scattering by a penetrable object, in a closed domain  $\mathcal{V}$ , in the three-dimensional Euclidean space  $\mathbb{R}^3$  and we illustrate it in 3.14. The permittivity and permeability of the scatterer are functions of  $\mathbf{r}$ ,  $\epsilon = \epsilon_r(\mathbf{r})\epsilon_0$  and  $\mu = \mu_r(\mathbf{r})\mu_0$  respectively, where  $\epsilon_0$  and  $\mu_0$  are the free-space electromagnetic properties, and  $\epsilon_r(\mathbf{r})$ ,  $\mu_r(\mathbf{r})$  are the relative properties of the scatterer. The wavelength is  $\lambda$  and the wavenumber is  $k_0 = 2\pi/\lambda$ . The electric field, as a function of the equivalent electric and magnetic polarization currents ( $\mathbf{j}_p, \mathbf{m}_p$ ) is

$$\mathbf{e}(\mathbf{r}) = \mathbf{e}_{\text{inc}}(\mathbf{r}) + \frac{1}{c_e} (k_0^2 + \nabla \cdot \nabla) \iiint_{\mathcal{V}} g(\mathbf{r} - \mathbf{r}') \mathbf{j}_p(\mathbf{r}') d\mathbf{r}' - \nabla \times \iiint_{\mathcal{V}} g(\mathbf{r} - \mathbf{r}') \mathbf{m}_p(\mathbf{r}') d\mathbf{r}', \quad (3.53)$$

where

$$\begin{aligned} \mathbf{j}_p(\mathbf{r}) &\triangleq c_e \chi_e(\mathbf{r}) \mathbf{e}(\mathbf{r}), & \mathbf{m}_p(\mathbf{r}) &\triangleq c_m \chi_m(\mathbf{r}) \mathbf{h}(\mathbf{r}) \\ \chi_e(\mathbf{r}) &\triangleq \epsilon_r(\mathbf{r}) - 1, & \chi_m(\mathbf{r}) &\triangleq \mu_r(\mathbf{r}) - 1 \\ c_e &\triangleq i\omega\epsilon_0, & c_m &\triangleq i\omega\mu_0. \end{aligned} \quad (3.54)$$

According to the above, the current based VIE can be written with the following simple matrix form

$$\begin{bmatrix} \mathcal{M}_{\epsilon_r} - \mathcal{M}_{\chi_e} \mathcal{N} & c_e \mathcal{M}_{\chi_e} \mathcal{K} \\ -c_m \mathcal{M}_{\chi_m} \mathcal{K} & \mathcal{M}_{\mu_r} - \mathcal{M}_{\chi_m} \mathcal{N} \end{bmatrix} \begin{bmatrix} \mathbf{j}_p \\ \mathbf{m}_p \end{bmatrix} = \begin{bmatrix} c_e & 0 \\ 0 & c_m \end{bmatrix} \begin{bmatrix} \mathcal{M}_{\chi_e} & 0 \\ 0 & \mathcal{M}_{\chi_m} \end{bmatrix} \begin{bmatrix} \mathbf{e}_{\text{inc}} \\ \mathbf{h}_{\text{inc}} \end{bmatrix}. \quad (3.55)$$

The operator  $\mathcal{M}_\phi$  denotes a multiplication over the respective parameter  $\phi$ ,  $\mathcal{I}$  is the identity operator, and  $\mathcal{N}$  and  $\mathcal{K}$  are the integrodifferential Green's function operators, given from

$$\begin{aligned} \mathcal{N}(\mathbf{c}) &\triangleq \nabla \times \nabla \times \iiint_{\mathcal{V}} g(\mathbf{r} - \mathbf{r}') \mathbf{c}(\mathbf{r}') d\mathbf{r}' \\ \mathcal{K}(\mathbf{c}) &\triangleq \nabla \times \iiint_{\mathcal{V}} g(\mathbf{r} - \mathbf{r}') \mathbf{c}(\mathbf{r}') d\mathbf{r}'. \end{aligned} \quad (3.56)$$

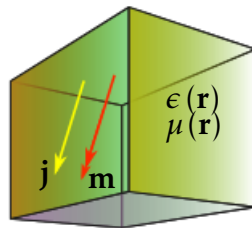


Figure 3.14: Scattering by a volume with permittivity  $\epsilon(\mathbf{r})$  and permeability  $\mu(\mathbf{r})$ .

Similar integral equations can be derived if we solve for the electric field or the electric-flux density instead of the equivalent polarization currents. In the present dissertation, we are focusing on problems of MRI, and specifically to the scattering of non-magnetic objects,  $\mu_r(\mathbf{r}) = 1$ ,

such as the biological tissue. Therefore, the VIE formulations can be simplified further as follows

$$\begin{aligned}
\text{EVIE: } & (\mathcal{M}_{\epsilon_r} - \mathcal{N}\mathcal{M}_{\chi_e}) \quad \mathbf{e} = \mathbf{e}_{\text{inc}} \\
\text{DVIE: } & (\mathcal{J} - \mathcal{L}\mathcal{M}_{\chi_e})\mathcal{M}_{1/\epsilon_r} \quad \mathbf{d} = \epsilon_0\mathbf{e}_{\text{inc}} \\
\text{JVIE: } & (\mathcal{M}_{\epsilon_r} - \mathcal{M}_{\chi_e}\mathcal{N}) \quad \mathbf{j} = c_e\mathcal{M}_{\chi_e}\mathbf{e}_{\text{inc}}.
\end{aligned} \tag{3.57}$$

The human body is a highly inhomogeneous scatterer, with high contrast. Hence, it is essential to study the behavior of the formulations mentioned above when  $\epsilon_r \rightarrow +\infty$ . In such limiting cases the VIE formulations become

$$\begin{aligned}
\lim_{\epsilon_r \rightarrow +\infty} \text{EVIE: } & (\mathcal{J} - \mathcal{N})\mathbf{e} = 0 \\
\lim_{\epsilon_r \rightarrow +\infty} \text{DVIE: } & -\mathcal{L}\mathbf{d} = \epsilon_0\mathbf{e}_{\text{inc}} \\
\lim_{\epsilon_r \rightarrow +\infty} \text{JVIE: } & (\mathcal{J} - \mathcal{N})\mathbf{j} = c_e\mathbf{e}_{\text{inc}}.
\end{aligned} \tag{3.58}$$

Only JVIE is an integral equation of the second kind, thus, well-conditioned. However, even though JVIE has a steady condition number, it requires many iterations for the convergence of the iterative solver [4] primarily when objects of high contrast are studied. Thus, a physically preconditioned version is preferred [24, 250] where, we need to divide JVIE with the electric permittivity, to ensure the existence of the identity operator on the first term on its left-hand side to prohibit the eigenvalues of the arising discretization matrix from tending to zero.

$$\text{JVIE-II: } (\mathcal{J} - \mathcal{M}_{\chi_e/\epsilon_r}\mathcal{N})\mathbf{j} = c_e\mathcal{M}_{\chi_e/\epsilon_r}\mathbf{e}_{\text{inc}}. \tag{3.59}$$

From now on, when we refer to JVIE, we will mean the preconditioned formulation JVIE-II.

### 3.2.1.1 Galerkin Linear System

Similar to the SIE case, we will employ the Galerkin projection method to create a linear system in order to solve for the unknown current components. According to [251, 252], the expansion functions should span the  $L^2$  dual of the range of the associated operator, and since there is no need for the satisfaction of a continuity condition (like in DVIE and EVIE), the functions can be polynomial. In [24], piecewise constant functions are used, which do not produce such accurate results for coarse and clinical resolutions. Hence we present a p-refinement with piecewise linear basis functions [4] that leads to superior numerical accuracy for coarse and clinical resolutions. Moreover, PWL basis functions are handy for the precise computation of the magnetic field, which by its nature is very smooth; thus, they are the method of choice for the inverse problem's performance, which is presented in Chapter 5. The functions are defined below

$$\mathbf{j}_q = \sum_{m=1}^{N_v} \sum_{l=1}^4 \mathbf{u}_m^{ql} \mathbf{c}_m^l(\mathbf{r}), \tag{3.60}$$

where  $N_v$  is the number of the voxels of the discretization,  $q \in \{x, y, z\}$  indicates the component of the current,  $m$  corresponds to a specific voxel with  $(x_m, y_m, z_m)$  being its center,  $\mathbf{u}_m^{ql}$  is the

### 3.2. Volume Integral Equations

unknown current coefficient at the  $m$ -th voxel and  $c_m^q$  are the scalar basis function per voxel, which are equal to

$$\begin{aligned}
 c_m^1(\mathbf{r}) &= p_m(\mathbf{r}) \\
 c_m^2(\mathbf{r}) &= \frac{x - x_m}{\Delta x} p_m(\mathbf{r}) \\
 c_m^3(\mathbf{r}) &= \frac{y - y_m}{\Delta y} p_m(\mathbf{r}) \\
 c_m^4(\mathbf{r}) &= \frac{z - z_m}{\Delta z} p_m(\mathbf{r}),
 \end{aligned} \tag{3.61}$$

where  $p_m$  is a volumetric pulse, equals to 1 inside the  $m$ -th voxel and 0 elsewhere ( $c_m^1(\mathbf{r})$  represents the PWC approximation), and  $\delta x, \delta y$  and  $\delta z$  are the dimensions of each voxel in the  $x, y$  and  $z$  directions respectively (resolution). Since we are dealing with 12 unknowns per voxel, the arising MoM matrices related to  $\mathcal{N}$  and  $\mathcal{K}$  operators will be of size  $12N_v \times 12N_v$ , each, or 144 smaller  $N_v \times N_v$  matrices. However, these matrices are BTTB, since the Green's function kernels are transnationally invariant over the uniform discretization grid. Thus, we only need to store the BTTB defining vectors of them in order to perform the matrix-vector products with the vector of the unknowns (a more detailed algorithm will be presented in the next section for the DVIE technique). Hence, the model reduces from 144 matrices to 144 vectors reshaped as tensors  $\mathcal{N}$  and  $\mathcal{K}$ . In addition, due to symmetries and zero entries, only 60 unique  $\mathcal{N}$  and 30 unique  $\mathcal{K}$  tensor components are stored in the memory. Finally, their elements are given via the standard  $L_2$  inner product (defined in Appendix D) as follows

$$\begin{aligned}
 \mathcal{N}_{ijk}^{q^l, q'^{l'}} &= \langle \mathbf{f}_{111}^{q^l}, \mathcal{N} \mathbf{f}_{ijk}^{q'^{l'}} \rangle \\
 \mathcal{K}_{ijk}^{q^l, q'^{l'}} &= \langle \mathbf{f}_{111}^{q^l}, \mathcal{K} \mathbf{f}_{ijk}^{q'^{l'}} \rangle,
 \end{aligned} \tag{3.62}$$

where  $\hat{q}, \hat{q}' \in \{\hat{x}, \hat{y}, \hat{z}\}$ , and

$$\begin{aligned}
 \mathbf{f}_{ijk}^{q'^{l'}} &= \mathbf{u}_{\{i,j,k\}}^{q'^{l'}} \mathbf{c}_{\{i,j,k\}}^{l'}(\mathbf{r}) \hat{q}' \\
 \mathbf{f}_{111}^{q^l} &= \mathbf{u}_{\{1,1,1\}}^{q^l} \mathbf{c}_{\{1,1,1\}}^l(\mathbf{r}) \hat{q}.
 \end{aligned} \tag{3.63}$$

For the calculation of the singular integral, in the  $\{1, 1, 1\}$  element of each tensor component, a sophisticated package is used [28]. The nature of these tensors will be studied in the next Chapter, where we will exploit their low-multilinear rank property.

#### 3.2.2 Flux-Based Volume Integral Equation

In the current subsection, we will analyze and solve the flux-based VIE formulation with the method introduced in 1992 by Peter Zwamborn [53, 253]. The particular method can solve challenging problems like the scattering from a highly inhomogeneous realistic human head, and it is used in the MR community up to this day [254]. However, a robust numerical study for this formulation does not exist. Therefore we will deepen in some specific assumptions of this model, and we will observe its convergence properties in comparison with the well-posed current-based

formulations. The integral equation to solve is the following

$$\mathbf{e}(\mathbf{r}) = \mathbf{e}_{\text{inc}}(\mathbf{r}) + \frac{k_0^2}{\epsilon_0} \iiint_{\mathcal{V}} \bar{\mathbf{G}}(\mathbf{r}, \mathbf{r}') \chi(\mathbf{r}') \mathbf{d}(\mathbf{r}') d\mathbf{r}', \quad (3.64)$$

where the incident electric field can be expressed through the following equation

$$\mathbf{e}_{\text{inc}}(\mathbf{r}) = \frac{\mathbf{d}(\mathbf{r})}{\epsilon(\mathbf{r})} - (k_0^2 + \nabla \cdot \nabla) \mathbf{a}(\mathbf{r}). \quad (3.65)$$

$\mathbf{a}$  is the magnetic vector potential, and it is given from

$$\mathbf{a}(\mathbf{r}) = \frac{1}{\epsilon_0} \iiint_{\mathcal{V}} g(\mathbf{r}, \mathbf{r}') \chi_e(\mathbf{r}') \mathbf{d}(\mathbf{r}') d\mathbf{r}'. \quad (3.66)$$

It is known that the normal component of  $\mathbf{d}(\mathbf{r})$  is continuous across the interface of surfaces (i.e., voxels). Thus, the equation can be employed to model highly inhomogeneous geometries (i.e., human head). Furthermore, it can tackle the scattering from anisotropic scatterers with some post-processing [255].

### 3.2.2.1 Galerkin Linear System

The domain of interest is a cuboid, and it is uniformly discretized with voxels. The expansion of the electric flux is done with rooftop basis functions [57, 256, 257], since they are divergence conforming, therefore, suitable to model the continuity of the electric flux along the voxels of the domain. Each voxel represents a different material (or tissue). The discretization can be formulated as

$$\mathbf{r}_{ijk} = \left\{ \left( n_1 - \frac{1}{2} \right) \delta x, \left( n_2 - \frac{1}{2} \right) \delta y, \left( n_3 - \frac{1}{2} \right) \delta z \right\}, \quad (3.67)$$

where  $n_1, n_2, n_3$  are the dimensions of the domain, and  $\delta x, \delta y, \delta z$  are the voxel's resolutions in each direction, which we choose to be the same  $\delta x = \delta y = \delta z = \delta$  for convenience. The rooftop basis function are given from the following equations

$$\begin{aligned} \psi_{ijk}^x(\mathbf{r}) &= \Lambda \left( x - x_{ijk} + \frac{1}{2} \delta; 2\delta \right) \Pi(y - y_{ijk}; \delta) \Pi(z - z_{ijk}; \delta) \\ \psi_{ijk}^y(\mathbf{r}) &= \Pi(x - x_{ijk}; \delta) \Lambda \left( y - y_{ijk} + \frac{1}{2} \delta; 2\delta \right) \Pi(z - z_{ijk}; \delta) \\ \psi_{ijk}^z(\mathbf{r}) &= \Pi(x - x_{ijk}; \delta) \Pi(y - y_{ijk}; \delta) \Lambda \left( z - z_{ijk} + \frac{1}{2} \delta; 2\delta \right), \end{aligned} \quad (3.68)$$

where  $\Lambda$  is the piecewise linear function with two voxels as a support, and  $\Pi$  is the piecewise constant function with support one voxel. In order to solve the equation 3.65, we will use a MoM technique. However, the authors of [53] use an irregular Galerkin projection implementation in which the testing procedure is applied (inner product with rooftop functions) first, and then each quantity (flux, potential, incident field) is expanded with the basis functions (rooftop), in contrast with the approach in [236]. We initiate the analysis with the testing procedure

$$\iiint_{\mathcal{V}} \psi_{ijk}^q(\mathbf{r}) \mathbf{e}_q^{\text{inc}}(\mathbf{r}) d\mathbf{r} = \iiint_{\mathcal{V}} \left( \psi_{ijk}^q(\mathbf{r}) \frac{\mathbf{d}_q(\mathbf{r})}{\epsilon(\mathbf{r})} d\mathbf{r} - k_0^2 \psi_{ijk}^q(\mathbf{r}) \mathbf{a}_q(\mathbf{r}) + \partial_q \psi_{ijk}^q(\mathbf{r}) \nabla \mathbf{a}_q(\mathbf{r}) \right) d\mathbf{r}, \quad (3.69)$$

### 3.2. Volume Integral Equations

where  $q = \{x, y, z\}$ . The Galerkin projection requires the expansion, of the electric flux, the magnetic vector potential, and the incident electric field in the same basis functions as follows

$$\mathbf{d}_q = \epsilon_0 \sum_{i,j,k=1}^{n_1, n_2, n_3} \mathbf{d}_{ijk}^q \psi_{ijk}^q \quad \mathbf{a}_q = \sum_{i,j,k=1}^{n_1, n_2, n_3} \mathbf{a}_{ijk}^q \psi_{ijk}^q, \quad \mathbf{e}_q^{\text{inc}} = \sum_{i,j,k=1}^{n_1, n_2, n_3} \mathbf{e}_{ijk}^{q, \text{inc}} \psi_{ijk}^q. \quad (3.70)$$

Since we are choosing rooftop functions as basis and testing functions, the equations 3.69 acquire the following form

$$\begin{aligned} \frac{\delta^3}{6} (\mathbf{e}_{i+1jk}^{x, \text{inc}} + 4\mathbf{e}_{ijk}^{x, \text{inc}} + \mathbf{e}_{i-1jk}^{x, \text{inc}}) &= \sum_{n=1}^3 \left[ b_n^{(x)} \mathbf{d}_{i+n-2jk}^x + c_n^{(x)} \mathbf{a}_{i+n-2jk}^x \right] + \\ &+ \sum_{n=1}^2 \sum_{m=1}^2 \left[ t_{nm}^{(z)} \mathbf{a}_{i+m-2j+n-1k}^y \right] + \sum_{n=1}^2 \sum_{l=1}^2 \left[ t_{nl}^{(y)} \mathbf{a}_{i+n-2jk+l-1}^z \right] \\ \frac{\delta^3}{6} (\mathbf{e}_{ij+1k}^{y, \text{inc}} + 4\mathbf{e}_{ijk}^{y, \text{inc}} + \mathbf{e}_{ij-1k}^{y, \text{inc}}) &= \sum_{m=1}^3 \left[ b_m^{(y)} \mathbf{d}_{ij+m-2k}^y + c_m^{(y)} \mathbf{a}_{ij+m-2l}^y \right] + \\ &+ \sum_{n=1}^2 \sum_{m=1}^2 \left[ t_{nm}^{(z)} \mathbf{a}_{i+m-1j+n-2k}^y \right] + \sum_{m=1}^2 \sum_{l=1}^2 \left[ t_{ml}^{(x)} \mathbf{a}_{ij+m-2k+l-1}^z \right] \\ \frac{\delta^3}{6} (\mathbf{e}_{ijk+1}^{z, \text{inc}} + 4\mathbf{e}_{ijk}^{z, \text{inc}} + \mathbf{e}_{ijk-1}^{z, \text{inc}}) &= \sum_{l=1}^3 \left[ b_l^{(z)} \mathbf{d}_{ijk+l-2}^z + c_l^{(z)} \mathbf{a}_{ijk+l-2}^z \right] + \\ &+ \sum_{n=1}^2 \sum_{l=1}^2 \left[ t_{ln}^{(y)} \mathbf{a}_{i+m-1jk+l-2}^y \right] + \sum_{m=1}^2 \sum_{l=1}^2 \left[ t_{lm}^{(x)} \mathbf{a}_{ij+m-1k+l-2}^z \right]. \end{aligned} \quad (3.71)$$

The coefficients,  $b$ ,  $c$ , and  $t$  are given from the following equations

$$b^{(x)} = \frac{\epsilon_0 \delta^3}{6} \begin{bmatrix} \frac{1}{\epsilon_{i-1jk}} \\ \frac{2}{\epsilon_{i-1jk}} + \frac{2}{\epsilon_{ijk}} \\ \frac{1}{\epsilon_{ijk}} \end{bmatrix}, \quad b^{(y)} = \frac{\epsilon_0 \delta^3}{6} \begin{bmatrix} \frac{1}{\epsilon_{ij-1k}} \\ \frac{2}{\epsilon_{ij-1k}} + \frac{2}{\epsilon_{ijk}} \\ \frac{1}{\epsilon_{ijk}} \end{bmatrix}, \quad b^{(z)} = \frac{\epsilon_0 \delta^3}{6} \begin{bmatrix} \frac{1}{\epsilon_{ijk-1}} \\ \frac{2}{\epsilon_{ijk-1}} + \frac{2}{\epsilon_{ijk}} \\ \frac{1}{\epsilon_{ijk}} \end{bmatrix}, \quad (3.72)$$

$$\begin{aligned} c^{(x)} = c^{(y)} = c^{(z)} &= -\frac{\delta^3 k_0^2}{6} \begin{bmatrix} 1 \\ 4 \\ 1 \end{bmatrix} + \delta \begin{bmatrix} -1 \\ 2 \\ -1 \end{bmatrix} \\ t^{(x)} = t^{(y)} = t^{(z)} &= \delta \begin{bmatrix} -1 & 1 \\ 1 & -1 \end{bmatrix}, \end{aligned} \quad (3.73)$$

the quantities  $\mathbf{d}$ ,  $\mathbf{a}$  and  $\mathbf{e}^{\text{inc}}$  are given from the following equations, due to the particular choice of rooftop functions as expansion functions

$$\mathbf{d}_{ijk}^q = \frac{\mathbf{d}_q(\mathbf{r}_{ijk} - \frac{1}{2}\delta\hat{q})}{\epsilon_0}, \quad \mathbf{a}_{ijk}^q = \mathbf{a}_q(\mathbf{r}_{ijk} - \frac{1}{2}\delta\hat{q}), \quad \mathbf{e}_{ijk}^{q, \text{inc}} = \mathbf{e}_q^{\text{inc}}(\mathbf{r}_{ijk} - \frac{1}{2}\delta\hat{q}). \quad (3.74)$$

To avoid the calculations of complex singular integrals, the *spherical mean*, (Appendix D.4) is used for the evaluation of the integrals of equations 3.74. The use of spherical mean is another

difference between the presented implementation and other standard implementations [236] that follow the appropriate Galerkin projection rules. The spherical mean of Green's function is

$$[G](\mathbf{r}) = \frac{\iiint_{|\rho|<\delta} g(\mathbf{r} + \rho) d\rho}{\iiint_{|\rho|<\delta} \rho d\rho}, \quad (3.75)$$

where  $\rho$  is the vector starting from the middle point of the voxel in-study and ends up on the surface of a sphere, with radius  $\delta$  and center the starting point of  $\rho$ . Therefore, one can come up with the following weak-form expression of the Green's function

$$[g](\mathbf{r}) = \begin{cases} \frac{\left(1 - \frac{1}{2}ik_0\delta\right)e^{\frac{1}{2}ik_0\delta} - 1}{\frac{1}{6}\pi k_0^2 \delta^3}, & \text{if } |\mathbf{r}| = 0, \\ \frac{\sinh(ik_0|\mathbf{r}|) \left[ \left(\frac{1}{2}ik_0\delta - 1\right)e^{\frac{1}{2}ik_0\delta} + ik_0|\mathbf{r}| \right]}{\frac{1}{6}i\pi (k_0\delta)^3 |\mathbf{r}|}, & \text{if } 0 < |\mathbf{r}| < \delta, \\ \frac{e^{ik_0|\mathbf{r}|} \left[ \frac{\sinh(\frac{1}{2}ik_0\delta)}{\frac{1}{2}ik_0\delta} - \cosh\left(\frac{1}{2}ik_0\delta\right) \right]}{\frac{1}{3}\pi (k_0\delta)^2 |\mathbf{r}|}, & \text{if } |\mathbf{r}| \geq \delta. \end{cases} \quad (3.76)$$

Thus, the spherical mean for the magnetic vector potential obtains the following form

$$[\mathbf{a}](\mathbf{r}) = \frac{1}{\epsilon_0} \iiint_V [g](\mathbf{r} - \mathbf{r}') \chi_e(\mathbf{r}') \mathbf{d}(\mathbf{r}') d\mathbf{r}', \quad (3.77)$$

by using a 3D trapezoidal rule, we have the following

$$[\mathbf{a}^q]_{ijk} = \delta^3 \sum_{i'=1}^{n_1} \sum_{j'=1}^{n_2} \sum_{k'=1}^{n_3} [g]((i-i')\delta, (j-j')\delta, (k-k')\delta) \chi_{e,i'j'k'}^{(q)} \mathbf{d}_{i'j'k'}^{(q)}, \quad (3.78)$$

where

$$\begin{aligned} \chi_{e,i'j'k'}^{(x)} &= \frac{\chi_e(\mathbf{r}_{i-1jk}) + \chi_e(\mathbf{r}_{ijk})}{2} \\ \chi_{e,i'j'k'}^{(y)} &= \frac{\chi_e(\mathbf{r}_{ij-1k}) + \chi_e(\mathbf{r}_{ijk})}{2} \\ \chi_{e,i'j'k'}^{(z)} &= \frac{\chi_e(\mathbf{r}_{ijk-1}) + \chi_e(\mathbf{r}_{ijk})}{2}. \end{aligned} \quad (3.79)$$

In the above analysis, an extra layer of voxels is required. Thus, vacuum is used as a boundary around the domain of interest and is discarded in the final results. With the usage of spherical mean, we avoid the analytic calculation of strongly singular integrals. Thus, the DVIE acquires a simple yet effective, weak formulation, and its integrals can be computed much faster. However, the averaging of contrast over neighboring voxels is arbitrary and can lead to numerical artifacts, especially if the contrast is high (the boundary between biological tissue and air, or different brain tissues).

The computation of the discrete convolution in 3.78 requires an immense amount of computational memory. However, the tensor  $[g]$  has a BTTB structure since the grid is uniform, and it depends only from the difference  $\mathbf{r} - \mathbf{r}'$  (transnationally invariance property), which allows us to accelerate the arising matrix-vector product with the help of the FFT. In the following subsection, we provide the implementation algorithm of such products, along with a brief background on the fundamental theory behind it. An extensive analysis of these particular matrix-vector products using tensor decomposition methods is done in Chapter 4.

#### 3.2.2.2 CG-FFT Matrix-Vector Products

We will focus on Toeplitz square matrices for simplicity. Let us consider a matrix  $A \in \mathbb{C}^{n \times n}$ , where  $A_{ij} = t_{i-j}$ . The matrix  $A$  (shown below) is called Toeplitz or diagonal-constant matrix named after Otto Toeplitz

$$A = \begin{bmatrix} t_0 & t_{-1} & t_{-2} & \cdots & t_{-n+1} \\ t_1 & t_0 & t_{-1} & \cdots & t_{-n+2} \\ t_2 & t_1 & \cdots & \cdots & \cdots \\ \cdots & \cdots & \cdots & \cdots & \cdots \\ t_{n-1} & \cdots & t_2 & t_1 & t_0 \end{bmatrix}. \quad (3.80)$$

In addition, let us define a matrix  $C \in \mathbb{C}^{n \times n}$  with elements given from

$$C = \begin{bmatrix} c_0 & c_{n-1} & c_{n-2} & \cdots & c_1 \\ c_1 & c_0 & c_{n-1} & \cdots & c_2 \\ c_2 & c_1 & \cdots & \cdots & \cdots \\ \cdots & \cdots & \cdots & \cdots & \cdots \\ c_{n-1} & c_{n-2} & c_{n-3} & \cdots & c_0 \end{bmatrix}. \quad (3.81)$$

This matrix is called circulant matrix and it is a special case of Toeplitz matrices. For all circulant matrices it is proven that  $C = 1/n \cdot F \text{diag}(F\mathbf{c})F$ , where  $F$  is the Fourier matrix  $\in \mathbb{C}^{n \times n}$ . We consider a function  $f(x) = c_0 + xc_1 + \cdots + x^{n-1}c_{n-1}$ , where  $x^n = 1$ . If we multiply  $f(x)$  with  $1, x, \dots, x^{n-1}$ ,  $n$  times we can easily derive the following equation

$$f(x) \begin{bmatrix} 1 & x & \dots & x^{n-1} \end{bmatrix} = \begin{bmatrix} 1 & x & \dots & x^{n-1} \end{bmatrix} C. \quad (3.82)$$

If  $x$  is chosen  $n$  times as an element of the Fourier matrix, then one can end up to  $\text{diag}(F\mathbf{c})F = FC$  or

$$C = \frac{1}{n} F^* \text{diag}(F\mathbf{c})F. \quad (3.83)$$

Thus, to perform the matrix-vector product between  $C$  and an arbitrary vector  $\mathbf{y}$  we only need the circulant defining vector  $\mathbf{c}$  and  $\mathcal{O}(n \log n)$  operations.

$$C\mathbf{y} = \text{ifft} \{ \text{fft} \{ \mathbf{c} \} \circ \text{fft} \{ \mathbf{y} \} \}. \quad (3.84)$$

Returning to integral equations, the matrix  $G$  (discretization of  $[g]$ ) is BTTB, and thus in order to be able to perform the matrix-vector product, we have to embed it in a block Circulant with Circulant blocks (BCCB) form. To do so, we can use the algorithm 1 below.

---

**Algorithm 1** FFT-Accelerated Matrix-Vector Product

---

- 1: Embed the BTTB defining vector, formulated as tensor  $\mathcal{G}$  in its BCCB defining tensor  $\mathcal{C}$  (following Matlab notation)

$$\mathcal{C}(1 : n_1, 1 : n_2, 1 : n_3) = \mathcal{G};$$

$$\mathcal{C}(n_1 + 1, :, :) = 0;$$

$$\mathcal{C}(:, n_2 + 1, :) = 0;$$

$$\mathcal{C}(:, :, n_3 + 1) = 0;$$

$$\mathcal{C}(n_1 + 2 : 2n_1, :, :) = \mathcal{G}(n_1 : -1 : 2, :, :);$$

$$\mathcal{C}(:, n_2 + 2 : 2n_2, :) = \mathcal{G}(:, n_2 : -1 : 2, :);$$

$$\mathcal{C}(:, :, n_3 + 2 : 2n_3) = \mathcal{G}(:, :, n_3 : -1 : 2);$$

$$\mathcal{C}(n_1 + 2 : 2n_1, n_2 + 2 : 2n_2, :) = \mathcal{G}(n_1 : -1 : 2, n_2 : -1 : 2, :);$$

$$\mathcal{C}(n_1 + 2 : 2n_1, :, n_3 + 2 : 2n_3) = \mathcal{G}(n_1 : -1 : 2, :, n_3 : -1 : 2);$$

$$\mathcal{C}(:, n_2 + 2 : 2n_2, n_3 + 2 : 2n_3) = \mathcal{G}(:, n_2 : -1 : 2, n_3 : -1 : 2);$$

$$\mathcal{C}(n_1 + 2 : 2n_1, n_2 + 2 : 2n_2, n_3 + 2 : 2n_3) = \mathcal{G}(n_1 : -1 : 2, n_2 : -1 : 2, n_3 : -1 : 2);$$

- 2: Calculate the elementwise products  $\chi_e^{(q)} \cdot \mathbf{d}^{(q)}$ ,  $q = \{x, y, z\}$  and store them to the tensors  $\Pi^q$ .
- 3: Pad the tensors  $\Pi^q$  with zeros, in order to match the dimensions of  $\mathcal{C}$ :

$$\Pi^q(n_1 + 1 : 2n_1, n_2 + 1 : 2n_2, n_3 + 1 : 2n_3) = 0.$$

- 4: Calculate the elementwise products between the DFT of  $\mathcal{C}$  and  $\Pi^q$ :

$$\mathcal{M}^q = \mathcal{F}\{\mathcal{C}\} \circ \mathcal{F}\{\Pi^q\}.$$

- 5: Calculate the IDFT of  $\mathcal{M}^q$  and discard the embedded elements and compute the magnetic vector potential tensor  $\mathcal{A}$ :

$$\mathcal{A}^q = \delta^3 \mathcal{F}^{-1}\{\mathcal{M}^q\}(1 : n_1, 1 : n_2, 1 : n_3).$$


---

In the above, the  $\mathbf{d}^q$  are the unknowns. Therefore, we can use an iterative solver and approximate them in each iteration by using the above algorithm; thus, the name of the method *conjugate-gradient-fast-Fourier-transform*. To complete the evaluation of the unknown, we will use the spherical mean on the incident field appearing on the right-hand side. For a plane wave, it is given from

$$[\mathbf{e}^{\text{inc}}](\mathbf{r}) = e_0 \hat{h} e^{ik_0(\hat{\theta}\mathbf{r})} \frac{12}{(k_0\delta)^2} \left[ \frac{\sinh\left(\frac{1}{2}ik_0\delta\right)}{\frac{1}{2}ik_0\delta} - \cosh\left(\frac{1}{2}ik_0\delta\right) \right] \quad (3.85)$$

$$\mathbf{e}_{ijk}^{q,\text{inc}} = [\mathbf{e}_q^{\text{inc}}](\mathbf{r}_{ijk} - \frac{1}{2}\delta\hat{q})$$

where  $e_0$  is the amplitude of the plane wave,  $\hat{h}$  the polarization, and  $\hat{\theta}$  the direction of the propagation.

#### 3.2.3 Scattering from Homogeneous Spheres

In this section, we will study the accuracy of the DVIE solver. To do so, we will calculate the scattered electric field from a dielectric sphere of radius  $r = 7.5$  cm, with its center in  $\{0, 0, 0\}$ , and we will compare the solution with the analytical one from the Mie scattering. Since we are highly interested in biomedical applications, we will consider homogeneous spheres whose material properties are the average of the gray and white matter [258], which exist in abundance in a human brain. The spheres are illuminated with the linear polarized plane wave  $\hat{x}e^{ik_0z}$ , for various frequencies that correspond to Larmor ones that appear in industrial and experimental MR scanners. We tabulate the aforementioned cases in 3.1.

Table 3.1: Simulation characteristics for various spheres

<i>Main MR field</i> (T)	<i>f</i> (MHz)	$\epsilon_r$	$\sigma_e$ (S/m)
0.5	21.29	227	0.25
1	42.58	184	0.3
1.5	63.87	141	0.35
3	127.74	68	0.5
7	298.06	64	0.51
14	596.12	56	0.62

We consider four different discretization schemes with voxel resolution  $dV = 7.5, 3.7, 1.9, 1.4$  mm<sup>3</sup> respectively. The generalized minimal residual method (GMRES) with 50 inner iterations, 200 outer iterations, and tolerance of  $10^{-5}$  was used for the solution of the system. The total electric field on the  $\hat{y}$  axis for the above cases is shown in 3.15 along with the relevant Mie series solution, in logarithmic scale. In 3.2 the number of iterations needed for the convergence of the solver, for each simulation, is depicted. As expected, the finer the discretization, the more accurate the approximation will be. However, even the finer discretization cannot accurately depict small details i.e., the side lobes of the radiation pattern, especially in low magnetic fields, a problem for which the staircase effect is responsible [259]. Besides, we notice the ill-conditioning of DVIE as long as we increase the operating frequency and the discretization. First, the DVIE is not truly an integral equation of the second kind and is unable to be transformed into one; thus,

it is an ill-posed formulation. Second, the high condition number in case of higher frequencies is a problem of IE in general [260]. The results above, even though accurate, are not enough in order to robustly abut to fruitful conclusions. Thus, we need to study the convergence properties and the accuracy of the method for inhomogeneous scatterers with high contrast, like a realistic human body model and compare the method with other VIE formulations to determine a panacea formulation for accurate simulations, in MR-based applications (especially in 7 Tesla).

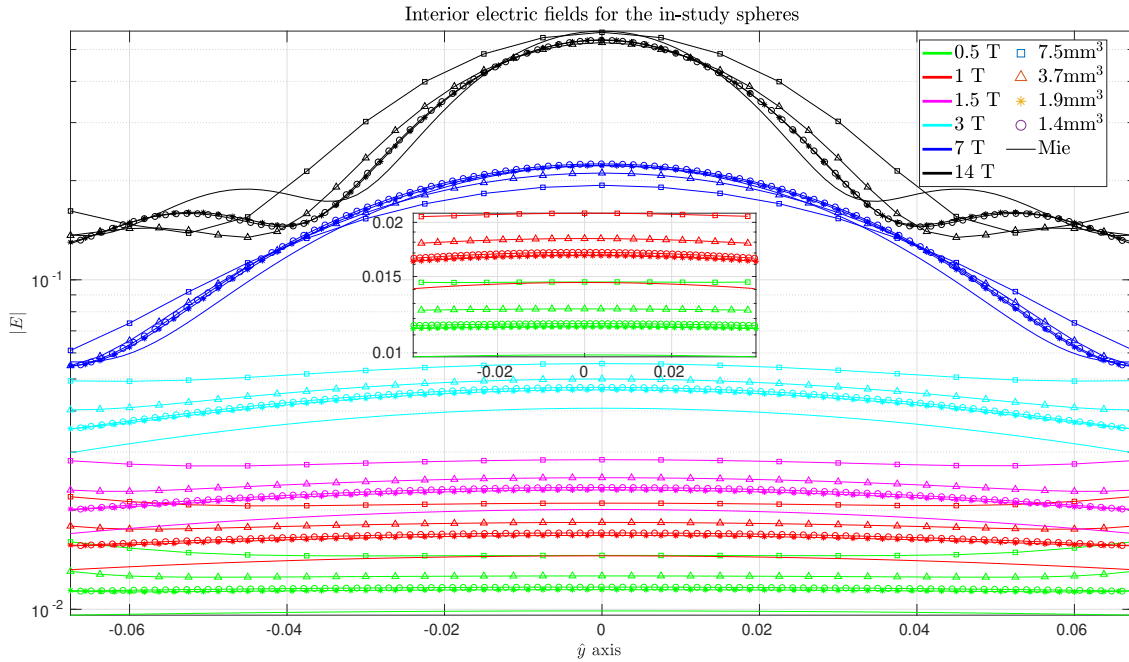


Figure 3.15: Total electric field on the  $\hat{y}$  axis of homogeneous spheres irradiated with a linear polarized plane wave, articulated from biological material properties, corresponding to 0.5 (green), 1 (red), 1.5 (magenta), 3 (cyan), 7 (blue), 14 (black) Tesla MRI. Each color represents a different sphere, and each marker a different resolution, according to the legend.

Table 3.2: Number of iterations of GMRES for tolerance  $10^{-5}$

$dV \setminus (\epsilon_r, \sigma_e)$	(227, 0.25)	(184, 0.3)	(141, 0.35)	(68, 0.5)	(64, 0.51)	(56, 0.62)
7.5 mm <sup>3</sup>	74	77	70	71	83	216
3.7 mm <sup>3</sup>	74	77	74	72	92	240
1.9 mm <sup>3</sup>	78	79	91	89	122	375
1.4 mm <sup>3</sup>	80	79	87	87	128	383

#### 3.2.4 Scattering from Realistic Human Body Models

In this subsection, we focus on the convergence properties and the interior electric field intensity measurements of a realistic human head model of a young girl dubbed “Billie”. The relative permittivity and the conductivity are provided through 7 Tesla, at  $f = 298$  MHz, MRI scans, and sophisticated geometrical reconstructions from [17] for three domain discretizations, namely with 5, 2 and 1 mm voxel isotropic resolutions. We will compare the performance of the JVIE (both for PWC and PWL) and DVIE to determine the most accurate approach. Firstly, we depict the relative residuals in 3.16 in order to study the numerical conditioning of the formulation. To be as accurate as possible, we used GMRES for all three cases, with the same settings as in the previous example. The superiority of JVIE-PWL is clear, since the required iterations remain almost the same for all discretizations, around 160, while the JVIE-PWC approaches this number as long as we h-refine the computational grid. The DVIE formulation has a higher condition number for such a highly inhomogeneous head case, and in contrast with the JVIE, the condition number significantly increases as we h-refine. These conclusions confirm the theoretical analysis done in [24, 260].

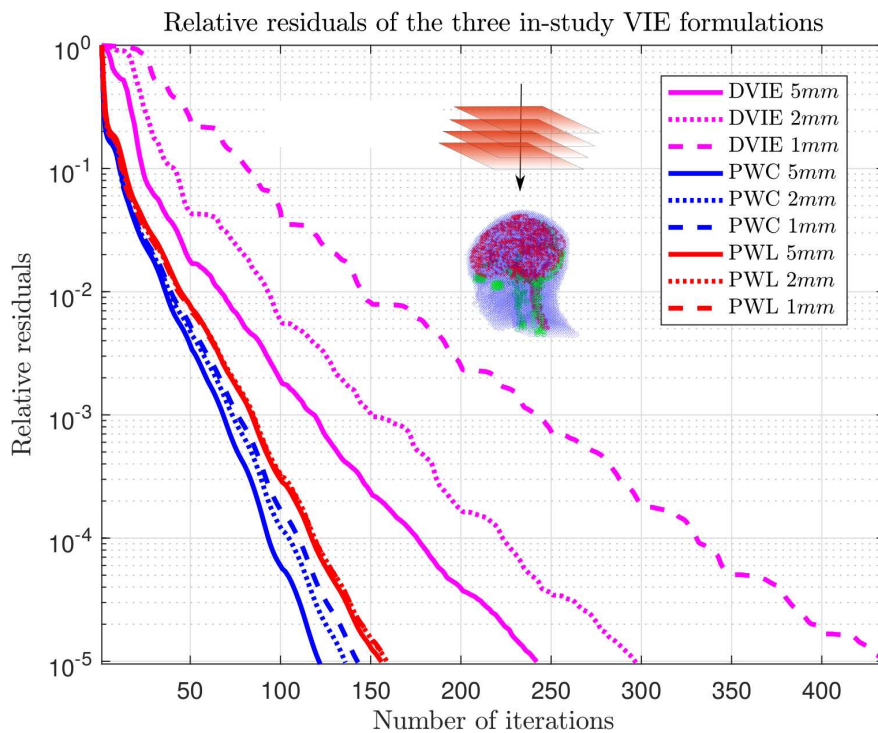


Figure 3.16: Convergence properties of JVIE (-PWC, -PWL) and DVIE formulations for the highly inhomogeneous realistic human body model “Billie”.

In the following we illustrate the total interior electric field in a sagittal, a coronal and an axial cut of the head model, calculated with the solvers mentioned above, when we illuminate the head model with a linearly polarized plane wave ( $\mathbf{e}^{\text{inc}} = \hat{x}e^{-ik_0z}$ ). The results are shown for all three discretizations in the figures 3.17 (sagittal), 3.18 (coronal), and 3.19 (axial), along with the EPs for the respective visualized slice. DVIE presents some extremely high-peaks on the boundary

of the head (skull), due to the averaging of the electrical properties between neighboring voxels (skull and vacuum), which are masked out (set to zero) for enhanced visualization. These catastrophic inaccuracies are mostly appearing on the boundary of the head (bottom bound of the axial cut, top and bottom bounds of the coronal cut, and top-left bound of the sagittal cut). The JVIE formulations are not affected by such a problem since the polynomial basis functions require only one voxel support, and there is no need for averaging the EPs of neighboring voxels. Although, the presence of the extreme inaccuracies on the boundaries, DVIE seem to produce similar results with JVIE-PWL on the rest of the head as long as we h-refine, albeit, JVIE-PWC converges to a different solution.

### 3.3 Volume-Surface Integral Equations

In the previous, we briefly studied the interactions of surface and volumetric geometries placed in free-space with electromagnetic waves and expressed them as integral equations. A challenging case that was not mentioned before is the interactions between conductive RF coils, human tissue, and electromagnetic waves, all in one integral equation. In this case, to compute the interior electromagnetic fields of the human tissue, neither a purely surface or a pure volume equation in the previous sense can be applied. SIEs are not enough to express the various EP in the human tissue, while VIE breakdown when the conductivity value increases significantly (in the case of PEC, it is equal to  $-i\infty$ ).

The simulation of such a phenomenon is crucial in MRI. Specifically, when a part of the RF coil is excited, surface equivalent currents are generated on the coil and scatter electromagnetic field. These fields illuminate the load of the coil (the human body); thus, an electric current distribution is generated on it. The body currents, in turn, scatter electromagnetic field to the outer space of the body, thus on the coil itself. As a result, the original surface currents of the coil are perturbed.

Thankfully, due to the nature of the integral equation solvers mentioned above, we can formulate a coupled solver, since both equations are solved through the Galerkin projection. Therefore, the discretized coupled system is

$$\begin{bmatrix} Z^{cc} & Z^{cb} \\ Z^{bc} & Z^{bb} \end{bmatrix} \begin{bmatrix} \mathbf{j}_c \\ \mathbf{j}_b \end{bmatrix} = \begin{bmatrix} \mathbf{v}_c \\ 0 \end{bmatrix} \quad (3.86)$$

where  $\mathbf{v}_c$  is the vector with the voltage excitations at the feeding ports,  $\mathbf{j}_c$  are the equivalent surface currents on the coil, and  $\mathbf{j}_b$  are the polarization currents on the body. The MoM block-matrix  $Z^{cc}$  models the interactions between the edges of the coil, while  $Z^{bb}$  is the block-MoM matrix that models interactions between the voxels of the computational grid.  $Z^{bc} = (Z^{cb})^T$  is the MoM block-matrix that models the interactions between edges of the coil (RWG functions) and voxels (PWC/PWL functions).

A straightforward construction of this system will require an immense amount of memory since the matrix  $Z^{bb}$  is very costly to be constructed. However, in [23], the authors exploited the

### 3.3. Volume-Surface Integral Equations

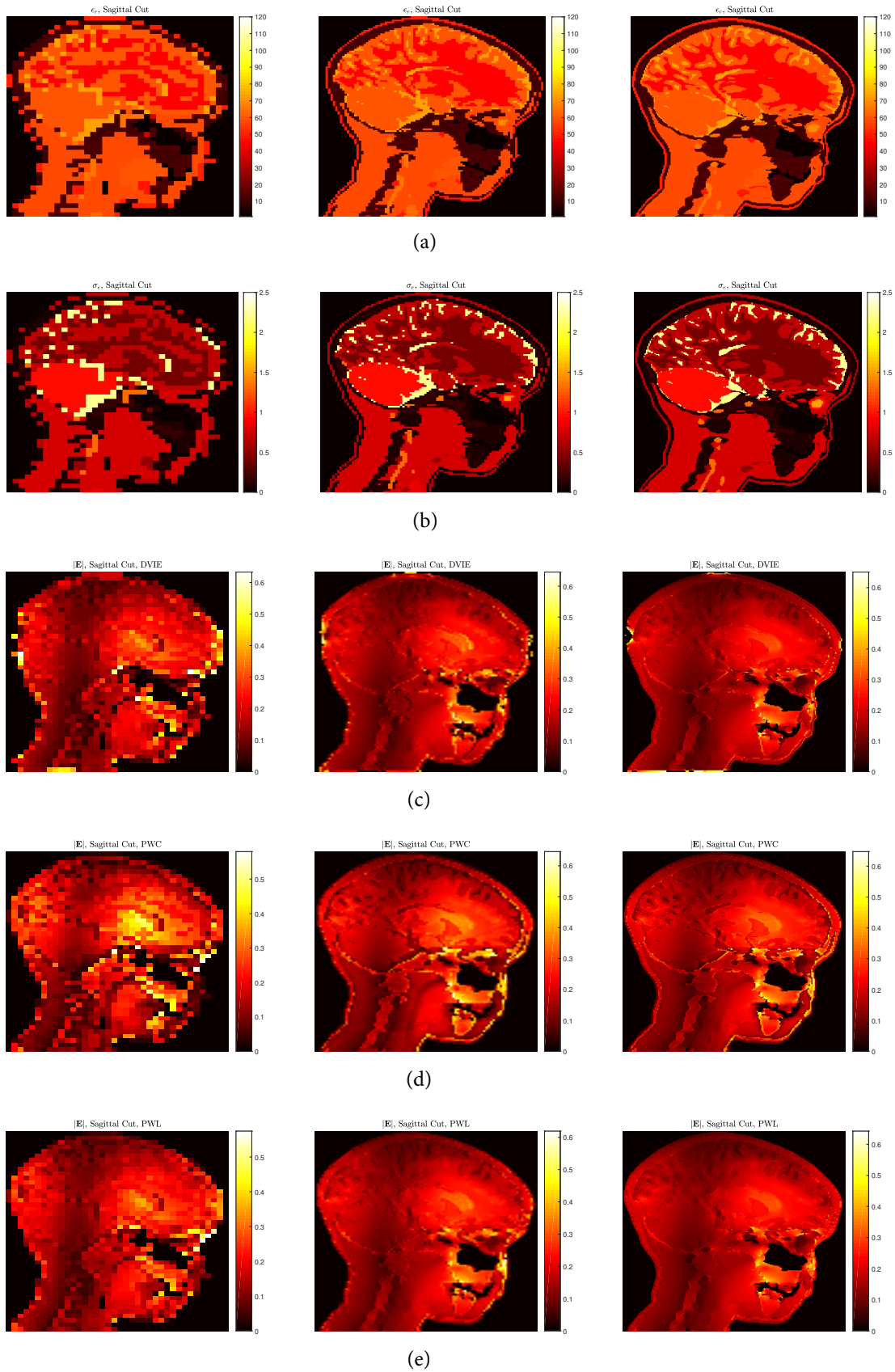


Figure 3.17: (a) Relative permittivity and (b) conductivity of a sagittal cut of “Billie” head, corresponding to 7T MR measurements. (c,d,e) Magnitude of the total electric field for the same sagittal cut calculated with DVIE, JVIE-PWC and JVIE-PWL respectively. (From left to right) 5, 2 and 1 mm<sup>3</sup> resolution.

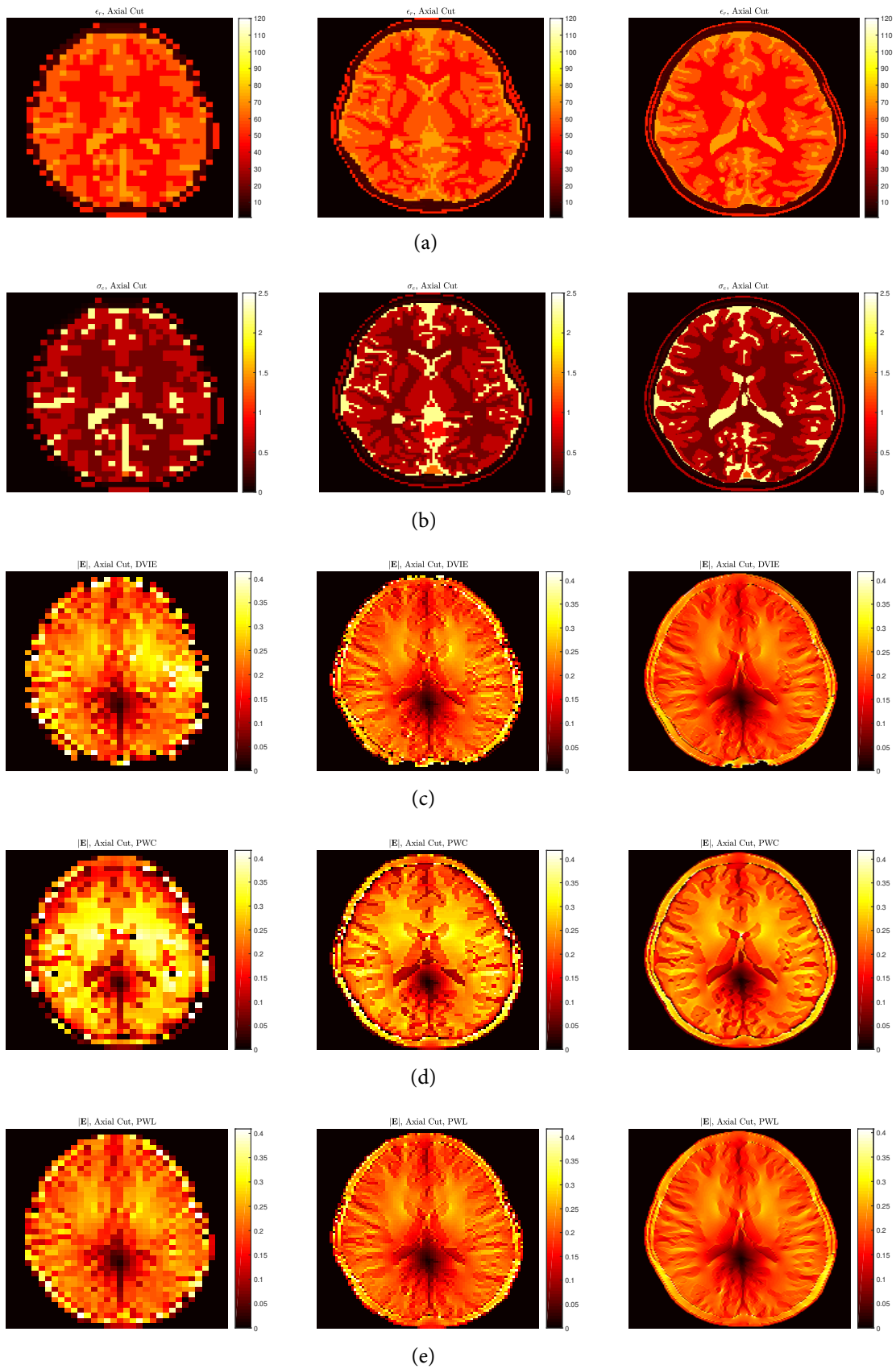


Figure 3.18: (a) Relative permittivity and (b) conductivity of an axial cut of ‘Billie’ head, corresponding to 7T MR measurements. (c,d,e) Magnitude of the total electric field for the same axial cut calculated with DVIE, JVIC-PWC and JVIC-PWL respectively. (From left to right) 5, 2 and 1 mm<sup>3</sup> resolution. (From left to right) 5, 2 and 1 mm<sup>3</sup> resolution.

### 3.3. Volume-Surface Integral Equations

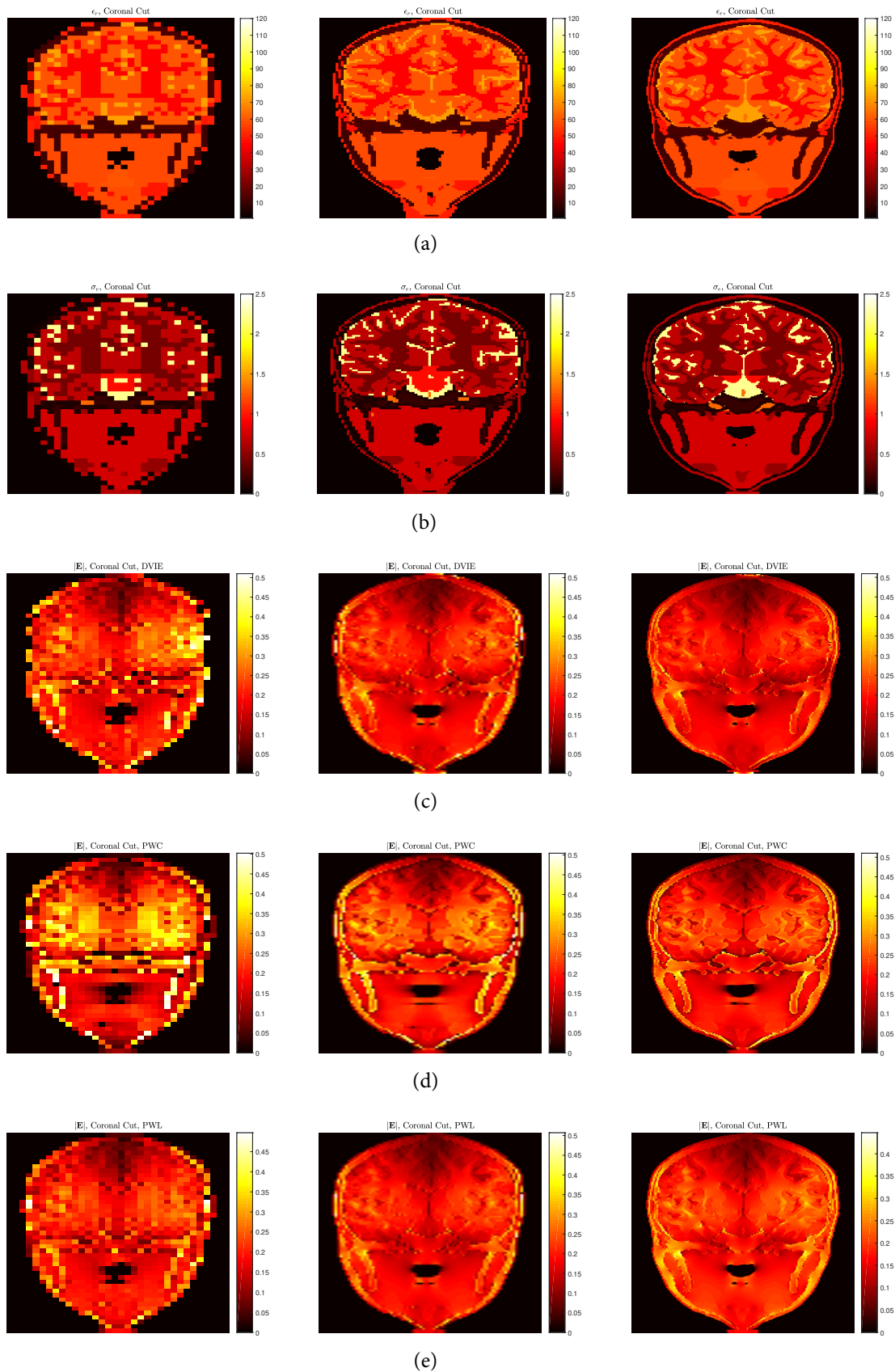


Figure 3.19: (a) Relative permittivity and (b) conductivity of a coronal cut of “Billie” head, corresponding to 7T MR measurements. (c,d,e) Magnitude of the total electric field for the same coronal cut calculated with DVIE, JVIC-PWC and JVIC-PWL respectively. (From left to right) 5, 2 and 1 mm<sup>3</sup> resolution. (From left to right) 5, 2 and 1 mm<sup>3</sup> resolution.

BTTB property of the matrix and solved the system without using an extensive amount of memory. This solver is implemented in the open-source software package MARIE [22]; therefore, we can adjust it to our needs and applications.

The usability of such solvers is a crucial component to the calculation of the network parameters of loaded RF coils in modern MRI applications. In particular, the existence of a human body inside the region of a coil tweaks its resonance frequency. Thus, additional tuning on its variable parameters, i.e., tuning capacitors, is needed. Moreover, the conductivity of a body allows decoupling between opposite neighbors, while it allows finding the best matching network in the feeding port of the coil (more on tuning, matching and decoupling on Chapter 5). The network parameters can be calculated by following the same approach as in the purely SIE case, although now the matrices appearing in the equations have to include the interaction with the voxels as well <sup>2</sup>.

---

<sup>2</sup>We refer the reader to [23] for additional information on VSIE solvers

This page is intentionally left blank.



# Chapter 4

## MEMORY FOOTPRINT REDUCTION FOR THE FFT-BASED VIE

---

**I**N the last decade, MRI modality has proven to be a powerful and essential tool for disease diagnosis, by providing extremely precise details of the anatomical structure of biological tissue. Indeed, with the usage of UHF MR scanners (which are clinically available [12]) the resonance frequency of the atomic nuclei of hydrogen ( $^1H$ ) inside the body increases and thus leads to shorter scanning times and improvements on both spatial and spectral resolutions, over conventional used systems [13]. In fact, in the last decade, a finger scan time was thirty minutes with a 1.5 Tesla scanner, while nowadays, a complete head scan requires just ten, using a 7 Tesla scanner. Faster acquisition times and higher quality images are strongly related to the SNR, which increases proportionally to the main magnetic field strength of the scanner. Regrettably, this results in higher operating RF of the coils in the scanner. Hence, the interactions between EM fields projected by the coils to tissue are dominant and not only can affect the quality of the images but also the safety of the patient. Therefore, accurate and robust simulations have to be employed for the modeling and design of the scanner and RF coils.

Such a simulation technique was presented in Chapter 3, where the fast and accurate FFT-based JVIE method was used for the efficient EM scattering calculations of complex, realistic anatomical models. We saw that, by expanding the unknowns of FFT-based VIE with higher-order polynomials [4], superior numerical accuracy is in place, contrary to standard low-order approximations, even for the challenging dielectric shimming technique [261–263]. However, the required memory footprint of the arising Green’s function tensors significantly increases, thus, forbidding the usage of heterogeneous computing techniques, and forcing the simulations to run for many hours or days, in CPU, until they converge. To scrutinize this impasse, we refer to [264], where it is proved that the Green’s function related integrodifferential operators, appearing in the integral equation approaches, that arise from two well-separated geometry blocks have low-rank properties. When we compute the MoM matrix, the off-diagonal blocks model such interactions; thus, are low-rank. The same property is extensively exploited in the celebrated

FMM [30]. In the case of uniform grids, where only the defining BTTB tensor is stored, the interactions between one voxel and all the others are modeled, meaning that we calculate interactions between distant voxels as well. Thus, a low multilinear rank approximation can be achieved in the tensor form of  $\mathcal{N}$  and  $\mathcal{K}$ . Moreover, according to [265], for 3D geometries, like the one's under study, the ranks are proportional to the operating frequency  $\mathcal{O}(k_0)$ . This low-rank property is proven to be useful for simulations in MHz (MRI problems) since the dimensions of the computational domain (human body) are comparable with the operating wavelength; thus, we expect a dramatic compression in the discretized operators.

For such purpose, one of the main scopes of this thesis revolves around methods of memory footprint reduction for FFT-based VIE formulations. Specifically, the celebrated Tucker decomposition [266] is employed to compress the Green's function tensors, thereby greatly reducing the required memory storage for numerical simulations. Consequently, the compressed components can fit inside a graphical processing unit on which highly parallelized computations can vastly accelerate the iterative solution of the arising linear system. Furthermore, the appearing element-wise products throughout the iterative solver's traditional approach require additional flops. Thus, we provide a variety of novel and efficient methods that maintain the linear complexity of the traditional element-wise product with an additional multiplicative small constant.

Moreover, as long as we h-refine the grid, the tensors of the unknowns (in their FFT form) are vast, thus cannot fit in GPU. For these extreme cases, we propose the usage of a sparse 3D FFT that is implemented partially in parallel with the element-wise products, which together with the Tucker compression can reduce the required memory even more. The utility of the new approaches is verified for the FFT-JVIE method expanded with PWL basis functions and for simulations for the MRI of a human head. For these simulations, we report an order of magnitude acceleration over standard techniques. We note that the methods presented herein are applicable for all FFT-based VIE formulations (like the DVIE, mentioned in Chapter 3, and EVIE). For the 2D equivalent FFT-VIE approach, matrix decomposition like singular value decomposition (SVD) or adaptive cross approximation (ACA) can be employed.

## 4.1 Tensor Decompositions

In the 3D problem of MRI and its respective electrodynamic counterpart, tensors are widely employed for efficient storage and computation. Indeed, tensors are an indispensable tool for multidimensional data analysis, in various scientific fields, and provide a natural representation of the quantities under study. Tensors can be defined simply as generalizations of matrices and vectors. Specifically, if  $n_1, n_2, \dots, n_m$  are positive integers, then  $\mathcal{A} \in \mathbb{C}^{n_1 \times n_2 \times \dots \times n_m}$  is a complex-valued tensor of order  $m$ . As in the case of matrix decompositions for efficient numerical algorithm implementations, a variety of tensor decompositions (or factorizations) can be employed for  $m$  dimensional problems.

Tensor decompositions originated with Frank Hitchcock in 1927 [267,268], followed by Ray-

mond Cattell in 1944 and 1952 [269,270] and Tucker in 1966 where he introduced the celebrated Tucker decomposition [266, 271, 272]. Later Richard Harshman and Douglas Carroll et al. introduced the *canonical polyadic decomposition* (CANDECOMP) and the *parallel factor analysis* (PARAFAC) respectively [273–275], which were equivalent and a generalization of the SVD concept in  $m$  dimensions.

It might seem unexpected, but most of the initial approaches on Tucker decomposition appeared in the field of psychometrics and not in mathematical literature [266,271,272]. It was only years later that Carl Appellof [276], and Rasmus Bro et al. introduced the Canonical polyadic decomposition in the field of chemometrics [277–280] where it was widely used [281–288]. Through the years, tensor decompositions found multiple applications: in signal processing [289–298], neuroscience [299, 300], neuroimaging [301, 302], bioinformatics [303], medicine and biology [304], data mining [305–309], graph theory [310–312], computer vision [313–320], computational statistics, [321, 322], numerical analysis [323–325]. Finally, the research in numerical linear algebra field is vast [326–341] and still ongoing. It was only a decade ago where Ivan Oseledets et al. introduced a new tensor decomposition, dubbed tensor train [74,342–344], that offers an alternative approach instead of Tucker and Canonical decompositions that works nicely for any number of dimensions and does not suffer from the *curse of dimensionality*. A method based on TT dubbed quantized TT was proposed later [345–347].

Tensor decompositions offer a natural approach that fits the real dimensions of the problem at hand, while matrix decompositions, such as the SVD, have only a two-mode representation. For example, one can consider the well-known *eigenfaces* [348] method, which is a low-dimensional representation of face images, with multiple applications in face recognition. The method works only if the input faces have the same conditions as the ones used to generate the eigenfaces. To tackle this impasse, Alex Vasilescu et al. [313], proposed the usage of a new multidimensional basis, called *tensorfaces*, where Tucker decomposition is employed for its generation. The new basis combines several modes, such as different geometries, expressions, poses, and illuminations of the faces. This example shows the superiority of tensor decompositions in higher-dimensional problems.

Finally, tensor decompositions found applications in integral equation problems for electromagnetics. The first approach was made in 2014, where Polimeridis et al. [68] used the Tucker decomposition to compress the individual tensor components of  $\mathcal{N}$  and  $\mathcal{K}$  in FFT-JVIE, using PWC basis functions. The observed compression was immense, thus, motivated by these results and attempting to tackle the high memory cost of FFT-JVIE with PWL basis functions, in this thesis, we employed multiple tensor decompositions to compress the  $\mathcal{N}$  and  $\mathcal{K}$  components, and propose novel matrix-vector products, efficient for GPU programming. Our work has been published in [1, 5]. In the last couple of years, scientists employed Tucker and TT decompositions for other integral equation methods [69, 70, 72].

### 4.1.1 Tucker Decomposition

Tucker decomposition is the mainly used decomposition scheme in this thesis. It is very stable since most of the algorithms implementing it are based on steady approaches. In addition, for 3D arrays, the achievable compression factor with Tucker decomposition algorithms is greater than the one obtained with other stable approaches. A three-dimensional array  $\mathcal{A} \in \mathbb{C}^{n_1 \times n_2 \times n_3}$  can be approximated with a prescribed accuracy  $\epsilon$  according to Tucker's model [266] as follows

$$\mathcal{A} \triangleq \tilde{\mathcal{A}} + \mathcal{E}, \quad \|\mathcal{E}\|_F = \epsilon. \quad (4.1)$$

Here  $\|\cdot\|_F$  is the *tensor Frobenius norm* (defined in Appendix D). Given three integers  $\{r_1, r_2, r_3\}$ , the approximation  $\tilde{\mathcal{A}}$  can be expressed as

$$\tilde{\mathcal{A}}_{ijk} = \sum_{\alpha=1}^{r_1} \sum_{\beta=1}^{r_2} \sum_{\gamma=1}^{r_3} \mathcal{G}_{\alpha\beta\gamma} U_{i\alpha}^1 U_{j\beta}^2 U_{k\gamma}^3. \quad (4.2)$$

The matrices  $U^q \in \mathbb{C}^{n_q \times r_q}$ ,  $q=1, 2, 3$  are orthogonal and they are called *Tucker factors*. The tensor  $\mathcal{G} \in \mathbb{C}^{r_1 \times r_2 \times r_3}$  is the *Tucker core* and has the property of all-orthogonality, meaning

$$\sum_{\alpha=1}^{r_1} \sum_{\beta=1}^{r_2} \mathcal{G}_{\alpha\beta\chi} \mathcal{G}_{\alpha\beta\psi} = \sum_{\alpha=1}^{r_1} \sum_{\gamma=1}^{r_3} \mathcal{G}_{\alpha\chi\gamma} \mathcal{G}_{\alpha\psi\gamma} = \sum_{\beta=1}^{r_2} \sum_{\gamma=1}^{r_3} \mathcal{G}_{\chi\beta\gamma} \mathcal{G}_{\psi\beta\gamma} = 0, \quad \chi \neq \psi. \quad (4.3)$$

The Tucker-core plays a similar role as the diagonal singular value matrix of the SVD; however, it does not have any diagonal structure. Tucker decomposition can be written in an elegant *Einstein summation convention* form using mode convolutions or *n-mode* products (also defined in Appendix D) as follows

$$\tilde{\mathcal{A}} = \mathcal{G} \times_1 U^1 \times_2 U^2 \times_3 U^3. \quad (4.4)$$

A graphical representation of the n-mode product form of Tucker decomposition of  $\mathcal{A}$  is visualized in 4.1.

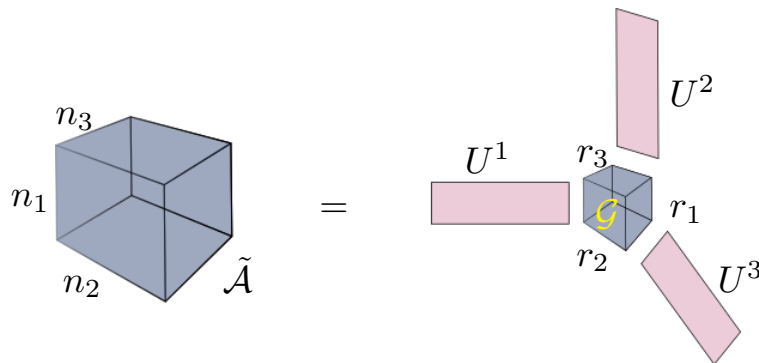


Figure 4.1: Tucker decomposition of a low multilinear rank tensor  $\mathcal{A}$ .

One can imagine that each Tucker factor multiplies from the left specifically oriented matrices of the Tucker core, i.e., Every column of  $\mathcal{G}$  is multiplied with  $U^1$ . The triplet  $\{r_1, r_2, r_3\}$  is called *Tucker rank* or *multilinear rank* of  $\mathcal{A}$  and depends from the algorithm of choice. We note that there are major differences between matrix and higher-order tensor ranks since there is not a stable equivalent generalization of singular value decomposition. Thus, tensor ranks cannot be defined uniquely (In the following, we will define the canonical rank and observe the major difference with the Tucker rank).

### 4.1.2 Canonical Polyadic Decomposition

Another important decomposition for  $n$ -dimensional arrays is the canonical polyadic model [267, 268]. Using the CP model, a 3D tensor  $\mathcal{A} \in \mathbb{C}^{n_1 \times n_2 \times n_3}$  can be decomposed, with a prescribed accuracy  $\epsilon$ , into the following sum

$$\mathcal{A} \approx \tilde{\mathcal{A}} = \sum_{l=1}^r \lambda_l V_l^1 \odot V_l^2 \odot V_l^3. \quad (4.5)$$

Here  $V^i \in \mathbb{C}^{n_i \times r}$ ,  $i = 1, 2, 3$  are the so-called *CP factors* of  $\mathcal{A}$  and  $r$  is the *canonical rank*, meaning the minimal number of terms for the decomposition to achieve the desired accuracy  $\epsilon$  (it is evident that the canonical rank is a single number, in contrast with the triplet Tucker rank). The scalar term  $\lambda_l$  is usually absorbed in the last CP factor for simplicity. The outer product  $\odot$  is defined in Appendix D, and the decomposition is visualized in 4.2.

CP decomposition is the equivalent of the SVD in two dimensions [273], since it approximates the original tensor with the sum of rank-one tensors. One can think CP as Tucker where, instead of a dense core  $\mathcal{G} \in \mathbb{C}^{r \times r \times r}$ , only the diagonal elements  $\mathcal{G}_{i,i,i} \neq 0$ ,  $i = 1, 2, \dots, r$ . Finally, CP is unique (under moderate conditions [290]), but in some cases the proposed algorithms are ill-posed, thus an optimal approximation might not exist at all for a specific number of terms [338].

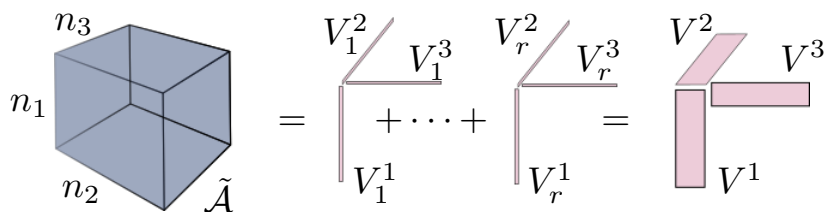


Figure 4.2: Canonical polyadic decomposition of a tensor  $\mathcal{A}$ .

### 4.1.3 Tensor Train Decomposition

In recent years a new tensor decomposition arose [343], dubbed Tensor Train decomposition, that can achieve excellent compression factors for higher dimensional tensors. Tucker

decomposition requires  $\mathcal{O}(dnr + r^d)$ , where  $n$  is tensor's linear size,  $r$  is one component of the Tucker rank, and  $d$  is the dimensionality of the tensor. It is obvious that for problems with  $d \gg 3$ , the Tucker core requires an exponentially increasing amount of storage memory, along with significantly more operations for its construction. To avoid this problem, we can always use the canonical decomposition, but the computation of the canonical rank is NP-hard [349], and the decomposition might be ill-posed. Thus, for such applications, TT has proven to be the method of choice. Consider a  $d$ -dimensional complex tensor  $\mathcal{A} \in \mathbb{C}^{n_1 \times \dots \times n_d}$ .  $\mathcal{A}$  can be approximated with  $\tilde{\mathcal{A}}$  as follows.

$$\tilde{\mathcal{A}}_{i_1, \dots, i_d} = \sum_{\alpha_1}^{r_1} \dots \sum_{\alpha_{d-1}}^{r_{d-1}} G_{i_1, \alpha_1}^{[1]} G_{\alpha_1, i_2, \alpha_2}^{[2]} \dots G_{\alpha_{d-1}, i_d}^{[d]}, \quad (4.6)$$

where

$$G^{[1]} \in \mathbb{C}^{n_1 \times r_1}, G^{[2]} \in \mathbb{C}^{r_1 \times n_2 \times r_2}, \dots, G^{[d]} \in \mathbb{C}^{r_{d-1} \times n_d}. \quad (4.7)$$

The decomposition can be represented elegantly by the following tensor-train network.

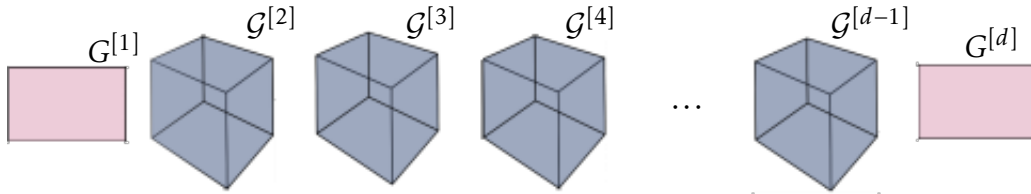


Figure 4.3: Tensor Train of  $\mathcal{A}$  in  $d$  dimensions.

The indexes  $r$  are the ranks of reshapes of  $\mathcal{A}$  to a matrix, as follows with Matlab notation

$$r_p = \text{rank}(A^{(k)}) = \text{rank} \left( \text{reshape} \left( \mathcal{A}, \prod_{i=1}^p n_i, \prod_{i=p+1}^d n_i \right) \right). \quad (4.8)$$

The memory complexity of TT is  $\mathcal{O}((d-2)nr^2 + 2rn)$  which is greater than the one of Tucker decomposition for  $d = 3$ , but much smaller for large  $d$ . Potentially, one can compress the TT scheme more ( $\mathcal{O}((dnr + (d-2)r^3)$ ) by using the Tucker decomposition on each tensor component of TT and reach the achieved Tucker compression for 3D cases. However, such an approach will require additional operations in the decompression of each tensor component, which is crucial in the time footprint of the novel matrix-vector product discussed in this Chapter. The most common algorithm to compute the tensor train is the TT-SVD [343]. In addition to TT, other decompositions are used for higher-order tensors, i.e., Quantized TT [340, 350] and hierarchical

Tucker decomposition [347].

## 4.2 Compression Algorithms

### 4.2.1 Higher-Order Singular Value Decomposition

The Tucker decomposition can be expressed as a convincing multilinear generalization of the SVD terminology or as a higher-order singular value decomposition. Specifically, the Tucker factors  $U^{1,2,3}$  and the Tucker core  $\mathcal{G}$  can be derived with a proven upper error bound on the approximation, based on the HOSVD algorithm, proposed in [328]. The algorithm is based entirely on the well-posed SVD; thus, it always exists, and it achieves an optimal fit to the initial array. The first step to approach the 3D problem with SVD is to introduce unfolding matrices of the tensor, shown in 4.4. By introducing the unfoldings, automatically we can use SVD for their compression, and obtain three ranks. Each of these ranks defines an element of the Tucker rank triplet.

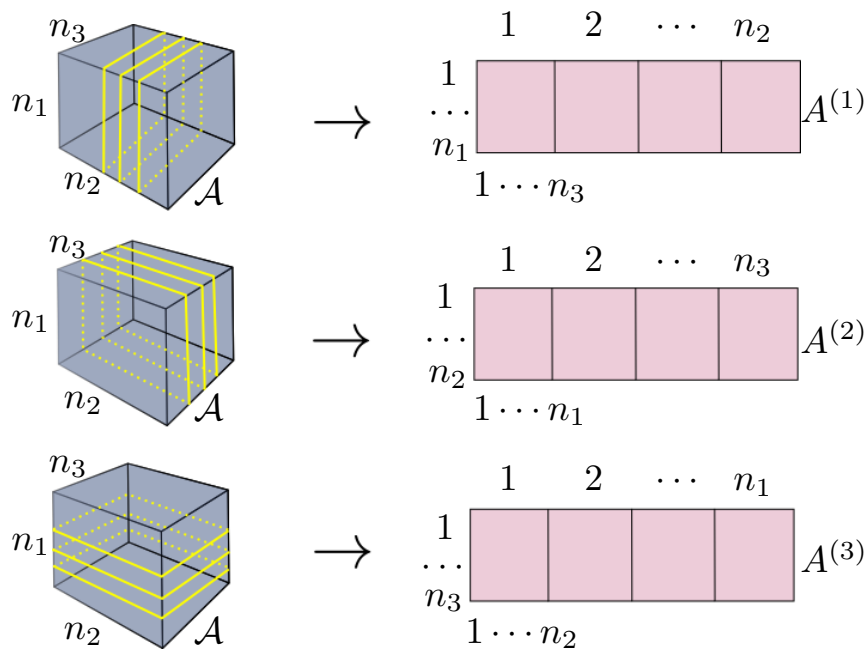


Figure 4.4: Unfoldings of  $\mathcal{A}$ .

According to the Tucker decomposition, every tensor  $\mathcal{A} \in \mathbb{C}^{n_1 \times n_2 \times n_3}$  can be written as

$$\mathcal{A} = \mathcal{G} \times_1 U^1 \times_2 U^2 \times_3 U^3. \quad (4.9)$$

where  $U^i \in \mathbb{C}^{n_i \times r_i}$ ,  $i = 1, 2, 3$  is unitary and  $\mathcal{G} \in \mathbb{C}^{n_1 \times n_2 \times n_3}$  with the all-orthogonality property and ordering. Thus, one can define the Frobenius norm of a slice matrix of  $\mathcal{G}$  as the  $n$ -mode

singular value of  $\mathcal{A}$ , and  $U^n$  as the  $n$ -mode singular matrix of  $\mathcal{A}$ . Concretely, one can use the following algorithm to perform the Tucker decomposition based on SVD.

---

**Algorithm 2** HOSVD
 

---

1: Assume  $\mathcal{A} \in \mathbb{C}^{n_1 \times n_2 \times n_3}$ .

2: Get the unfoldings of  $\mathcal{A}$

$$A^{(1)} \in \mathbb{C}^{n_1 \times (n_2 \cdot n_3)}$$

$$A^{(2)} \in \mathbb{C}^{n_2 \times (n_1 \cdot n_3)}$$

$$A^{(3)} \in \mathbb{C}^{n_3 \times (n_1 \cdot n_2)}.$$

In matlab notation:

$$A^{(1)} = \text{reshape}(\mathcal{A}, n_1, [])$$

$$A^{(2)} = \text{reshape}(\text{permute}(\mathcal{A}, [2, 1, 3]), n_2, [])$$

$$A^{(3)} = \text{reshape}(\text{permute}(\mathcal{A}, [3, 1, 2]), n_3, []).$$

3: Set the desired tolerance  $\epsilon$  for the SVD on the unfoldings

4: **for**  $i=1,2,3$  **do** truncated SVD on the unfoldings

$$A^{(i)} \approx U_{r_i}^i \Sigma_{r_i}^i (V_{r_i}^i)^*$$

$$r_i = \text{rank}(A^{(i)}).$$

5: Tucker Rank:  $\{r_1, r_2, r_3\}$ .

6: Tucker Factors:  $U^i = U_{r_i}^i$ .

7: Tucker Core:  $\mathcal{G} = \mathcal{A} \times_1 (U^1)^* \times_2 (U^2)^* \times_3 (U^3)^*$ .

---

The resulting tensor  $\tilde{\mathcal{A}}$  satisfies the quasi-optimality condition.

$$\|\mathcal{A} - \tilde{\mathcal{A}}\|_{\text{F}} \leq \sqrt{3} \|\mathcal{A} - \mathcal{A}_{\text{best}}\|_{\text{F}}, \quad (4.10)$$

where  $\mathcal{A}_{\text{best}}$  is the best Tucker approximation of  $\mathcal{A}$ .

#### 4.2.2 Tucker-Based Three-Dimensional Cross Approximation

Tucker decomposition can be constructed by using only some rows, columns, and fibers of  $\mathcal{A} \in \mathbb{C}^{n \times n \times n}$  with a cross-Tucker approximation algorithm. Various implementations exist in the literature [351, 352] and achieve the decomposition with linear complexity (best case:  $\mathcal{O}(nr^3)$ ) over the  $\mathcal{O}(n^3)$  complexity of HOSVD. Specifically, only  $r_1$  rows,  $r_2$  columns and  $r_3$  fibers are used of the initial BTTB defining tensor component. Specifically, in FFT-JVIE, each entry of these tensors requires the computation of a costly multidimensional integral; thus, cross approximation algorithms are ideal for fast approximations.

## 4.2. Compression Algorithms

---

The cross approximation (or skeleton decomposition algorithm) is a technique that approximates a low-rank matrix by using only a small set of rows and columns of it, thus skipping its complete construction. A variety of such algorithms exist in the literature like the *adaptive cross approximation* and the *maximum volume algorithm* (MaxVol), which are briefly explained in Appendix D. Such algorithms can be exploited efficiently in the case of Tucker decomposition, since we are dealing with the approximation of three low-rank matrices (unfoldings of  $\mathcal{A}$ ). For our applications, we choose an algorithm developed in [351] with linear complexity concerning tensor's linear size  $\mathcal{O}(nr^4)$ . The idea of the algorithm is to apply a cross approximation method and calculate only some columns ( $\mathcal{O}(n)$ ) and rows ( $\mathcal{O}(n^2)$ ) of each unfolded matrix. However, instead of calculating each long row (which requires  $n^2$  operations), the algorithm approximates it by reshaping it as a matrix ( $n \times n$ ) and applying a second inner cross approximation ( $\mathcal{O}(n)$ ). Below, we provide the algorithm for the unfolding  $A^{(3)}$ .

---

### Algorithm 3 Cross-Tucker

---

1: **Initialize:**

$\tilde{\mathcal{A}} = 0$ ,  $\mathcal{R} = 0$ ,  $p = 1$ , and a tolerance  $\epsilon$

Choose a random fiber  $\mathbf{k}_p$  of  $\mathcal{A}$  (for  $A^{(1)}$  a row, for  $A^{(2)}$  a column)

2: **loop**

3: ACA on  $\mathcal{R}_{::\mathbf{k}_p} = \mathcal{A}_{::\mathbf{k}_p} - \tilde{\mathcal{A}}_{::\mathbf{k}_p}$

$$\mathcal{R}_{::\mathbf{k}_p} = \sum_{q=1}^r B_{:q}^p (C_{:q}^p)^T$$

4: Find  $\max(\mathcal{R}_{::\mathbf{k}_p})$ , located at  $(\mathbf{i}_p, \mathbf{j}_p)$

5:  $\mathbf{w}^p = \mathcal{R}_{i_p j_p \mathbf{k}_p} / \max(\mathcal{R}_{::\mathbf{k}_p})$

6: Find  $\max(\mathbf{w}^p)$ , located at  $\mathbf{k}_{p+1} \neq \mathbf{k}_p$

7: Update the approximation  $\tilde{\mathcal{A}}$

$$\tilde{\mathcal{A}} = \tilde{\mathcal{A}} + \sum_{q=1}^r B_{:q}^p \odot C_{:q}^p \odot \mathbf{w}^p$$

8: **if**  $\omega \|\mathbf{w}^p\|_2 \|B^p\|_2 \|C^p\|_2 > \epsilon \|\tilde{\mathcal{A}}\|_F$  **then**  $p = p + 1$

9: **else Return**  $B, C, W$

---

In step (5), an approximant maximum element can be found with  $\mathcal{O}(r^2)$  operations via the MaxVol algorithm (Appendix D), in order to avoid the  $n^2$  searches in all the elements of the

matrix. After the termination of the algorithm, the approximation of  $\mathcal{A}$  admits the following form:

$$\tilde{\mathcal{A}}_{ijk} = \sum_{p=1}^r \left( \sum_{q=1}^r B_{iq}^p C_{jq}^p \right) \mathbf{w}_k^p = \sum_{t=1}^{r^2} B_{it} C_{jt} W_{kt}. \quad (4.11)$$

As a result, the Frobenius norm of  $\tilde{\mathcal{A}}$  can be calculated as follows:

$$\|\tilde{\mathcal{A}}\|_F^2 = \sum_{i=1}^{n_1} \sum_{j=1}^{n_2} \sum_{k=1}^{n_3} |\tilde{\mathcal{A}}_{ijk}|^2 = \sum_{\alpha=1}^{r^2} \sum_{\beta=1}^{r^2} \langle B_{:\alpha}, B_{:\beta} \rangle \langle C_{:\alpha}, C_{:\beta} \rangle \langle W_{:\alpha}, W_{:\beta} \rangle. \quad (4.12)$$

The stopping criterion in step (8) gives a good approximation of the error since we cannot calculate the exact Frobenius norm of the initial array<sup>1</sup>. The multiplicative scalar  $\omega$  is an arbitrary parameter, and, usually, it is equal to  $n - p$ .

After the repetition of the algorithm for all three unfoldings, we obtain the matrices  $W^1$ ,  $W^2$ ,  $W^3 \in \mathbb{C}^{n \times r^2}$ . To calculate the Tucker factors, we are using the QR decomposition on them, and retrieve three orthogonal matrices  $Q^1, Q^2, Q^3 \in \mathbb{C}^{n \times r}$ . Thus, the orthogonality property of Tucker factors is satisfied (since they correspond to singular vector matrices). The Tucker core is:

$$\mathcal{H}_{\alpha\beta\gamma} = \sum_{\delta=1}^{r^2} \langle W_{:\delta}^1, Q_{:\alpha}^1 \rangle \langle W_{:\delta}^2, Q_{:\beta}^2 \rangle \langle W_{:\delta}^3, Q_{:\gamma}^3 \rangle. \quad (4.13)$$

and the cross-Tucker decomposition of  $\mathcal{A}$  is written as

$$\mathcal{A} \approx \mathcal{H} \times_1 Q^1 \times_2 Q^2 \times_3 Q^3. \quad (4.14)$$

### 4.2.3 Tucker + Canonical Decomposition Method

Tucker decomposition methods achieve an excellent compression factor since they are based on already established numerical algorithms like SVD and ACA. On the contrary, the canonical decomposition is unstable when used on big tensors, since it is based on heuristic least square algorithms. However, it achieves the most compact representation of an array, since it only uses three factor-matrices, without any core-tensor. To exploit this compact form we can use the *Tucker+CP method* [278, 353], in which we apply Tucker decomposition on our array of interest, which is significantly faster and more stable than CP, and then we compress the Tucker core with CP, since it is small, as it is illustrated in 4.5. Therefore, the new tensor decomposition requires only three *Tucker+CP factors*. For the sake of completeness, we provide a short description of the algorithm below:

---

#### Algorithm 4 Tucker+CP

---

1: Assume  $\mathcal{A} \in \mathbb{C}^{n_1 \times n_2 \times n_3}$ .

---

<sup>1</sup>We can, but this requires the construction of the array.

### 4.3. Matrix-Vector Product Implementation

---

- 2: Tucker decomposition on  $\mathcal{A} \approx \mathcal{G} \times_1 U^1 \times_2 U^2 \times_3 U^3$ ,  $\mathcal{G} \in \mathbb{C}^{r_1 \times r_2 \times r_3}$ .
  - 3: Choose appropriate CP algorithm and canonical rank  $r$ .
  - 4: CP on  $\mathcal{G} \approx \sum_{l=1}^r V_l^1 \odot V_l^2 \odot V_l^3$ :  
 $V^i \in \mathbb{C}^{r_i \times r}$ ,  $i = 1, 2, 3$ .
  - 5: Create the Tucker+CP factors:  $W^i = U^i V^i$ .
- 

For our simulations, in step 3, the implementation of CP is done with the open-source Matlab software package *Tensorlab* [335] which approaches the problem with an alternating least squares (ALS) method. ALS minimizes 3 problems for each CP factor. For  $V^1$  we have

$$q(V^1) = \frac{1}{2} \left\| \mathcal{G}^{(1)} - V^1 (V^2 \otimes V^3)^T \right\|_F^2, \quad i = 1, 2, 3. \quad (4.15)$$

Here  $\otimes$  denotes the Khatri-Rao product (defined in Appendix D), and  $\mathcal{G}^{(1)}$  is the first unfolding of  $\mathcal{G}$  (see figure 4.4). The gradient of  $q$  gives the ALS update rule when it is equal to 0.

$$\begin{aligned} \frac{\partial J(V^1)}{\partial V^1} &= V^1 (V^2 \otimes V^3)^T (V^2 \otimes V^3) - \mathcal{G}^{(1)} (V^2 \otimes V^3), \\ V^1 &\leftarrow \mathcal{G}^{(1)} (V^2 \otimes V^3) \left( (V^2 \otimes V^3)^T (V^2 \otimes V^3) \right)^{-1}. \end{aligned} \quad (4.16)$$

Efficient computations of the gradient are crucial for the convergence speed of the CP, according to [298, 354]. Finally, the Tucker+CP approximation of  $\mathcal{A}$  is given from the following equation and is visualized in 4.5.

$$\tilde{\mathcal{A}} = \sum_{l=1}^r W_l^1 \odot W_l^2 \odot W_l^3. \quad (4.17)$$

### 4.3 Matrix-Vector Product Implementation

#### 4.3.1 Circulant Embedding and Fourier Transform

One of the tensor decompositions mentioned above can be employed for the compression of all the unique tensor components of  $\mathcal{N}$  and  $\mathcal{K}$ . The compression of the Green's function tensors can be performed either in their BTTB defining tensor form, their BCCB defining tensor form, or their BCCB defining tensor form after the application of the 3D FFT. In all these cases, the multilinear ranks will be the same, since the circulant embedding and the FFT are unitary transforms, and they do not affect the rank of the BTTB defining tensor (i.e., the Fourier matrix has a condition number of exactly 1). To avoid performing the SVD, required in the algorithms above, in large matrices, or performing the 3D FFT in large tensors (the circulant embedded ones) we will exploit the method in [352], where the authors propose to apply, univariate respective one-dimensional transforms along the columns of the Tucker or Tucker+CP factors. The Tucker core (if used) remains the same. Using this approach we are able to drastically reduce the operation and memory complexity to  $\mathcal{O}(r_i n_i \log n_i)$ , where  $n_i$ ,  $i \in \{1, 2, 3\}$  is the tensor's linear size.

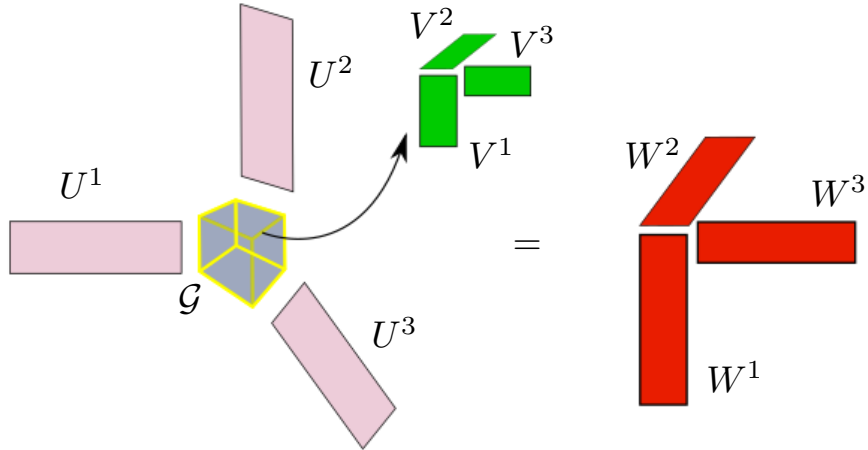


Figure 4.5: Visual representation of Tucker + CP method.

### 4.3.2 Matrix-Vector Product Cost

In this section, we will focus on an efficient implementation of the matrix-vector product arising in FFT-based VIE, where the Green's function tensors are compressed with the aforementioned Tucker-based decompositions. If the tensors of the unknowns (current, flux, field intensity) could be compressed with Tucker decomposition, one could use the methods in [355] and perform the element-wise products without the need for tensor decompositions. Regrettably, for an inhomogeneous head model, with an arbitrary excitation from an RF coil, the unknowns are by no means low-rank. Therefore, by default, the decomposition of the Green's function tensors cannot be avoided, and additional operations are required over the traditional approach. However, we do not have to decompress all tensors at once. Thus, the occupied memory remains much smaller than the traditional approach, and, as a result, we can fit the matrix-vector product in the limited memory of a GPU, and exploit its high parallel structure to accelerate it.

Without any decomposition, the matrix-vector product requires the implementation of element-wise products between the Green's function tensors and the tensors of the unknown currents, and multidimensional FFTs with  $\mathcal{O}(N_v)$  and  $\mathcal{O}(N_v \log N_v)$  complexity respectively. In this case, the required memory is significantly large, and, for our applications of interest, it overflows GPU's memory. By using a tensor compression algorithm, each Green's function tensor component is stored in a compressed form; thus, the implementation of the product requires an extra decomposition step, that can be implemented in two ways. First, we can decompress the appropriate component using the equations (4.4), (4.14), or (4.17) and then implement the element-wise product with the appropriate current component. Afterward, we repeat the same process for the rest of the components by using the same buffer in memory. Alternatively, we can avoid storing any Green's function tensor by doing the decompression and the element-wise product

### 4.3. Matrix-Vector Product Implementation

simultaneously via a 6D (Tucker) or a 4D (Tucker+CP) loop. In this case, we decompress only one element of the Green’s function tensor, then multiply it with the corresponding element of the appropriate current component, and repeat the same process for the rest of the elements, without occupying additional memory. Due to the presence of the Tucker core, this technique is inherently slow for Tucker decomposition, although it can be as fast as the previous approach if the Tucker+CP method is used. The FFTs are done as in the full-form case for the vector of the unknowns. These techniques summarize the novel matrix-vector products, which can overtake the previous memory overflow obstacle.

Regarding the methods mentioned earlier, for Tucker decomposition, the full tensor decomposition is much faster, but it requires the additional memory buffer, which for large problems, might lead to memory overflow in GPU (GPU memory is minimal, and our problems are large). Alternatively, we can use the element by element decomposition with Tucker+CP decomposition and avoid GPU’s memory overflow. Not only is the costly 6D loop of HOSVD reduced to a faster 4D loop (considering that the canonical rank is the minimum of Tucker ranks), but we also do not use any additional storage space. We summarize both the memory and the complexity of the operations of these matrix-vector product methods (the FFT cost is excluded since it is the same) in the table 4.1, for the multiplication of the 12 unknown current components with the relevant Green’s function tensors, in the case of FFT-JVIE. The Tucker and the canonical rank are  $\{r_1, r_2, r_3\}$  and  $r$  respectively and  $N_v$  is the number of voxels. Also, in 4.6, we show a graphical scheme of the tensor decomposition-based solvers. All 60 unique components of  $\mathcal{N}$  are compressed with HOSVD or cross-Tucker algorithm in CPU. Optionally, we can use the Tucker+CP decomposition for additional compression and the previously explained reasons. Then we pass the compressed tensors in GPU and implement one of the proposed matrix-vector product algorithms in each iteration of the iterative solver.

Table 4.1: Complexity of Novel Matrix-Vector Products

Decomposition	Method	Operations	Memory
-	Traditional implementation	$\mathcal{O}(N_v)$	$72N_v$
Tucker	Component decomposition	$\mathcal{O}(r_3N_v)$	$13N_v$
	Multidimensional loop	$\mathcal{O}(r_1r_2r_3N_v)$	$12N_v$
Tucker+CP	Component decomposition	$\mathcal{O}(rN_v)$	$13N_v$
	Multidimensional loop	$\mathcal{O}(rN_v)$	$12N_v$

#### 4.3.3 Time Footprint of the Matrix-Vector Product

In this subsection, we will shed some light on the time footprint of the proposed matrix-vector product implementations in the GPU and CPU. Since the operations in each iteration of the iterative solver and between different components are the same, we will focus only on one

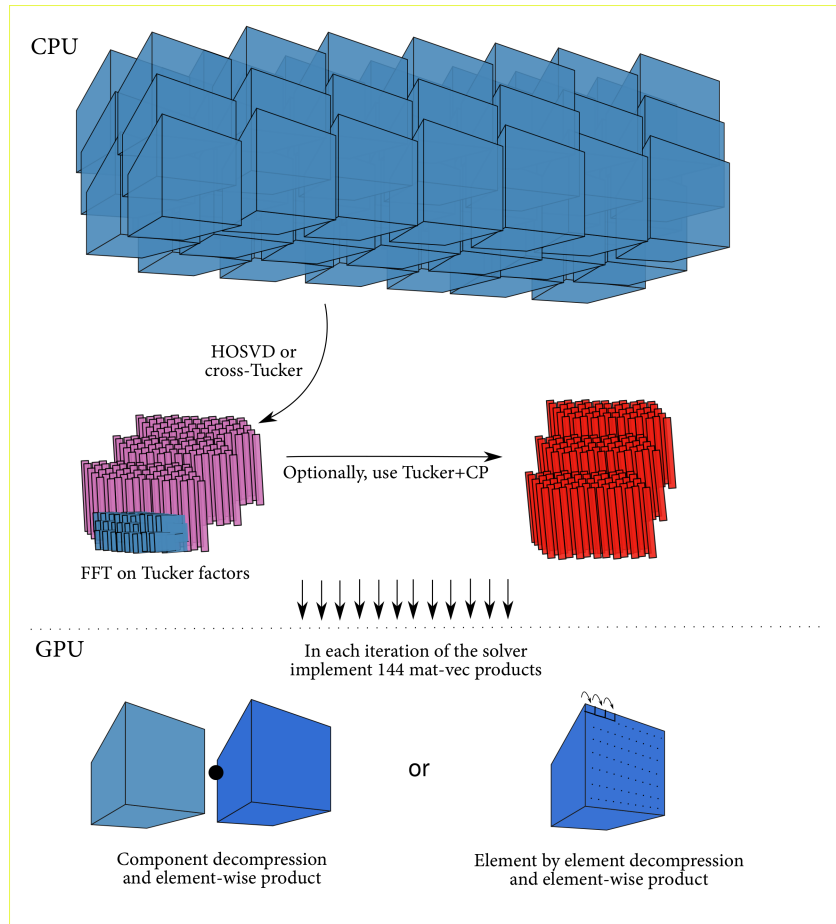


Figure 4.6: Visual representation of the tensor decomposition-based solvers.

product. We consider double precision complex random arrays: One tensor with dimensions  $n \times n \times n$  corresponding to the unknown current coefficients, one tensor with dimensions  $r \times r \times r$  corresponding to the Tucker core and three matrices with dimensions  $n \times r$  corresponding to the Tucker or Tucker+CP factors. In the previous Chapters, we showed that the realistic human head models require domains of size  $\sim 80 - 400$  (circulant defining tensor's linear size), thus for this experiment, we choose three sizes:  $n = 100, 200, \text{ and } 300$ . The Tucker and canonical ranks are set to 25 (this is a reasonable choice according to the results shown in the next section).

All the methods were implemented both in CPU and GPU. The measurements in CPU are needed since, for vast domains, even the vector of the unknowns is not able to fit in GPU, thus by employing the cross-Tucker method, we can perform simulations that required a tremendous amount of memory  $> 1$  TB. All the calculations were done in a CentOS 6.9 server equipped with the following:

- CPU: *Intel(R) Xeon(R) CPU E5-2699 v3 @ 2.30 GHz*, 36 cores, 2 threads per core, 378 GB memory
- GPU: *NVIDIA Tesla K40M*, 12 GB memory

For the CPU implementation, we used C++, compiled with *gcc 4.9.2* along with highly optimized Level 3 routines of BLAS and the FFTW [50]. The GPU coding was done in CUDA, compiled with *nvcc V8.0.61* along with the respective Level 3 routines of cuBLAS and the cuFFT. Moreover, the products were implemented in Matlab too, (version 9.2) both in CPU and GPU with a fully vectorized code, when it was possible. We note that the implementations can be further optimized with advanced programming techniques.

In table 4.2, we present the time footprint of the proposed methods. In the first two columns, we provide the time needed for the decompression methods, both with Tucker and Tucker+CP. In C++ and CUDA versions, both decompressions require similar times, however, in the Matlab implementation, since the Khatri-Rao product cannot be implemented with a fully vectorized code, the Tucker+CP decompression requires additional time. In the next two columns, the element-wise product through the multidimensional loop technique is presented. In this case, Matlab is significantly slower, since we are unable to construct a vectorized code. The lack of this vectorization leads the GPU implementation of it to an impasse; thus, it is not applicable. Besides, the loop implementation of Tucker+CP requires briefly more time, than the decompression cases, since it cannot be implemented optimally with BLAS and cuBLAS routines for the CPU and GPU respectively. However, it is hundreds of times faster than the HOSVD loops method as expected. Hence, it is an excellent choice for GPU programming, since it does not require the additional memory buffer that decompression approaches need. Finally, the last column provides the required time of the three-dimensional FFT. The use of cuFFT over FFTW is expected to significantly accelerate the convergence of the current-based VIE solver since it is used 13 times in every iteration of the solver of choice (12 FFTs on the unknown current components and 1 inverse FFT on the result of the element-wise product). What we are mostly interested in is the comparison between FFT in CPU and the novel matrix-vector products in GPU. Specifically, for  $n = 200$  we focus on the red colored entries in table 4.2 and we observe that the novel products of  $rn$  operations are  $\sim 3$  times faster than the FFT of  $n \log(n)$  operations. Therefore, a GPU implementation, of the tensor decomposition-based matrix-vector products, can offer a significant speed-up over the traditional CPU approach, considering that  $r = 25$  and  $\log(200) \approx 2.3$ .

## 4.4 Results

### 4.4.1 Multilinear Rank

In [264], it is proved that the Green's function related integrodifferential operators that arise from two well-separated geometry blocks have low-rank properties, with rank given as functions of the operating frequency. Therefore, the off-diagonal blocks of the Galerkin MoM matrix are low-rank since they represent such interactions. In the case of uniform grids, we do not exploit this property since only the defining BTTB tensor is stored. However, in this defining tensor, the interactions between one voxel and all the others are modeled (first column of the MoM ma-

Table 4.2: Time Footprint in ms of Matrix Vector Product

Dim	Case	HOSVD	HOSVD+CP	HOSVD	HOSVD+CP	FFT
		decomp.	decomp.	loops	loops	
100	C++	2.6	1.3	$2.4e+3$	3.3	1.2
	Matlab CPU	5.9	6.4	$2.5e+5$	522	2
	CUDA	0.96	0.79	855	1.28	0.58
	Matlab GPU	1.37	7.73	N.A.	N.A.	0.76
200	C++	25.2	22.9	$1.7e+4$	24.6	20.4
	Matlab CPU	47.3	56.4	$2e+6$	$3.2e+3$	24.6
	CUDA	6.03	5.79	$5.9e+3$	8.9	5.68
	Matlab GPU	7.09	13.58	N.A.	N.A.	7.14
300	C++	74.9	77.5	$5.8e+4$	81.6	55.5
	Matlab CPU	140	136.8	$1.5e+7$	$1e+4$	55.6
	CUDA	17.4	20.1	$1.9e+4$	29.4	26.9
	Matlab GPU	19.82	27.83	N.A.	N.A.	31.43

trix), meaning that distant interactions are still calculated. Therefore, it makes sense to wonder if there is a relation between the Tucker rank and the operating frequency. According to [265], for 3D geometries, the ranks of the discretized operators, corresponding to interactions between well-separated geometrical source and observation domains, are proportional to the operating frequency  $\mathcal{O}(k_0)$ , while for the 2D case the relation is  $\mathcal{O}(\sqrt{\log k_0})$ . The case presented herein is expected to share similarities in the dependence of the multilinear rank and frequency. However, since the voxel  $\{1, 1, 1\}$  is part of both domains, due to the form of the Green's function tensors (3.62), not an exact linear dependence is expected. To study this dependence, we construct the following simple Green's function operator for a cube with unit edge

$$\mathcal{G}(\mathbf{c}) = \iiint_{\mathcal{V}} g(\mathbf{r} - \mathbf{r}') \mathbf{c}(\mathbf{r}') d\mathbf{r}', \quad (4.18)$$

and discretize it using the Galerkin expansion and PWC basis functions. The matrix is BTTB, and Tucker decomposition can be applied to the defining tensor. Furthermore, we present the

#### 4.4. Results

maximum of all multilinear ranks of the unique  $\mathcal{N}$  and  $\mathcal{K}$  components expanded with PWL functions (the rank of the most memory consuming component). Since the Tucker rank is a triplet, we illustrate the largest of  $r_1$ ,  $r_2$ , and  $r_3$  for the above cases. The multilinear ranks are calculated with the HOSVD algorithm with SVD tolerance  $\epsilon = 10^{-8}$ . The frequency sweep analysis is implemented for the cases  $0.3i$  GHz,  $i = 1, \dots, 10$  and for three different discretizations with resolutions  $\lambda/10$ ,  $\lambda/20$  and  $\lambda/30$ . The results are summarized in 4.7, and as expected, the dependence between the ranks and the frequency is almost linear [265], and an excellent overall compression factor is established. For instance, the maximum rank of a  $300 \times 300 \times 300$  tensor is no greater than 32, which means that  $\mathcal{G}$  (and each component of  $\mathcal{N}$  and  $\mathcal{K}$ ) can be compressed at least  $\approx 440$  times.

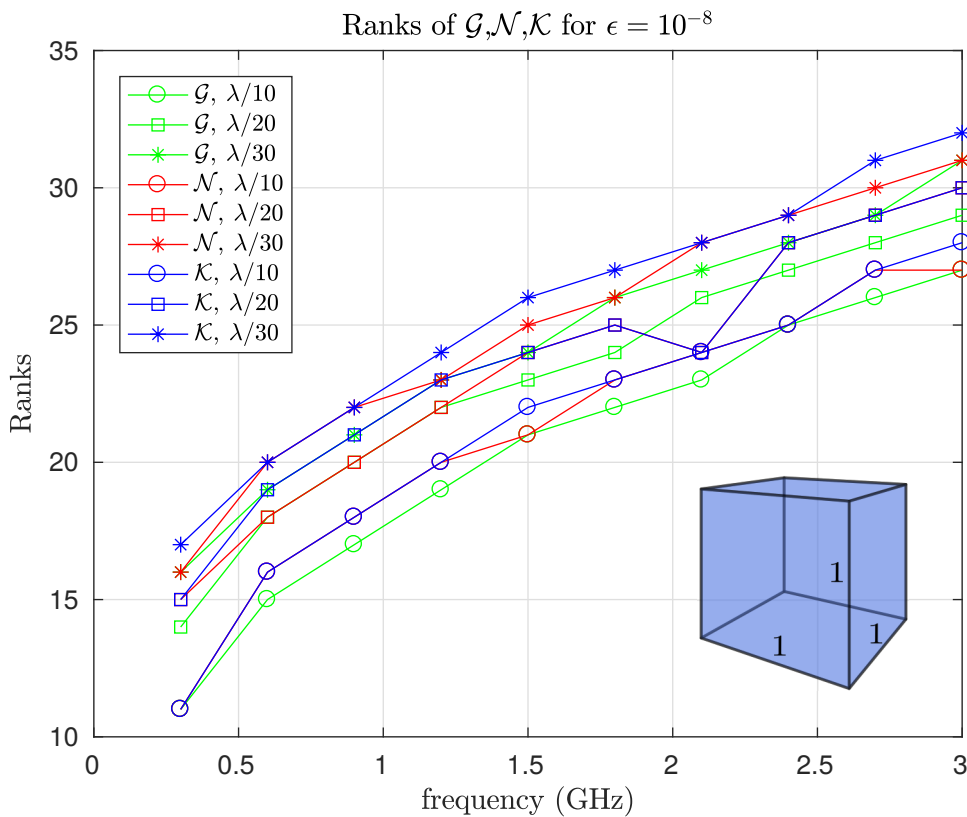


Figure 4.7: The maximum ranks of Green’s function tensors. They scale almost linearly with respect to frequency.

#### 4.4.2 Compression Factor

Focusing on MRI applications, we consider an example of a realistic human body model, relevant to 7 Tesla scanners, with operating frequency  $f = 297.2$  MHz. The domain is a cuboid with dimensions  $0.538 \times 0.28 \times 1.802$  m<sup>3</sup> with a voxel isotropic resolution equal to 2 mm. The discretized version of the domain requires  $270 \times 141 \times 902$  voxels. In table 4.3, we provide the memory footprint of the domain and the arising discretized  $\mathcal{N}$  operator, expanded with PWL

basis functions. The table presents the immense memory needed in the full Galerkin MoM matrix and the compressed one for the BTTB defining tensors.

Table 4.3: Memory Requirements of discretized  $\mathcal{N}$  with PWL functions

Array	Number of Elements	Storage Memory
Domain	$N_v$	256 MB
MoM matrix	$12N_v \times 12N_v$	2.35 EB
Symmetric MoM matrix	$(12N_v \times 12N_v)/2$	1.17 EB
BTTB defining tensors	$144N_v$	74 GB
Unique tensors	$60 \times N_v$	31 GB
Circulant embedding	$8 \times 60 \times N_v$	246 GB

According to 4.3 the overall memory for the unique circulant forms of  $\mathcal{N}$  is 245.6 GB (122.8 GB for  $\mathcal{K}$ ), a forbidden memory cost for any available GPU. It is evident that the uniform grid expansion and the translation-invariant property of Green's function offered a substantial compression of the initial MoM matrix, but not enough to implement the simulation in GPU. In table 4.4 we provide the memory of the decomposed,  $\mathcal{N}$  and  $\mathcal{K}$  unique tensor components, using the HOSVD [328], the cross-Tucker decomposition [351] and the TT-SVD algorithms<sup>2</sup>, in respect to the SVD and ACA tolerances.

Table 4.4: Memory (in MB) for the decomposed  $\mathcal{N}$  and  $\mathcal{K}$  tensors

Decomposition	$\epsilon$	$10^{-4}$	$10^{-5}$	$10^{-6}$	$10^{-7}$	$10^{-8}$	$10^{-9}$	$10^{-10}$
HOSVD	$\mathcal{N}$	18.04	24.16	32.10	40.94	50.82	60.90	71.71
	$\mathcal{K}$	12.06	16.26	21.24	26.15	31.03	35.69	40.96
Cross-Tucker	$\mathcal{N}$	19.77	27.73	37.20	47.15	57.37	68.53	79.74
	$\mathcal{K}$	14.59	19.52	24.70	29.51	35.58	41.47	47.00
TT-SVD	$\mathcal{N}$	23.79	37.90	59.56	86.45	118.68	154.92	192.78
	$\mathcal{K}$	19.19	30.55	45.68	62.28	79.40	96.85	115.97

The compression is tremendous. In 4.8 and 4.9, the dual-axis charts portray, on the red axis,

<sup>2</sup>For the TT-SVD we used the open-source TT-Toolbox [344] software package

the overall compression factor<sup>3</sup> of the tensor components, and on the blue axis, their maximum ranks with HOSVD, cross-Tucker decomposition, and TT-SVD, using the same SVD (or 2D cross) tolerances. On 4.8, the results are shown for the unique components of  $\mathcal{N}$  (60), and on 4.9 for the unique components of  $\mathcal{K}$  (30). The large compression factor (between 1000 and 11000 for all the cases) allows us to easily fit the decomposed  $\mathcal{N}$  and  $\mathcal{K}$  components in a single GPU or personal laptop's CPU, instead of using servers equipped with significantly large RAM. Moreover, as expected, Tucker-based algorithms can achieve a significantly better compression than TT-SVD ( $\sim 2.5$  times less memory for a tolerance of  $10^{-10}$ ). Even if a TT-based compression of 1000 is still remarkable, Tucker decomposition is preferred.

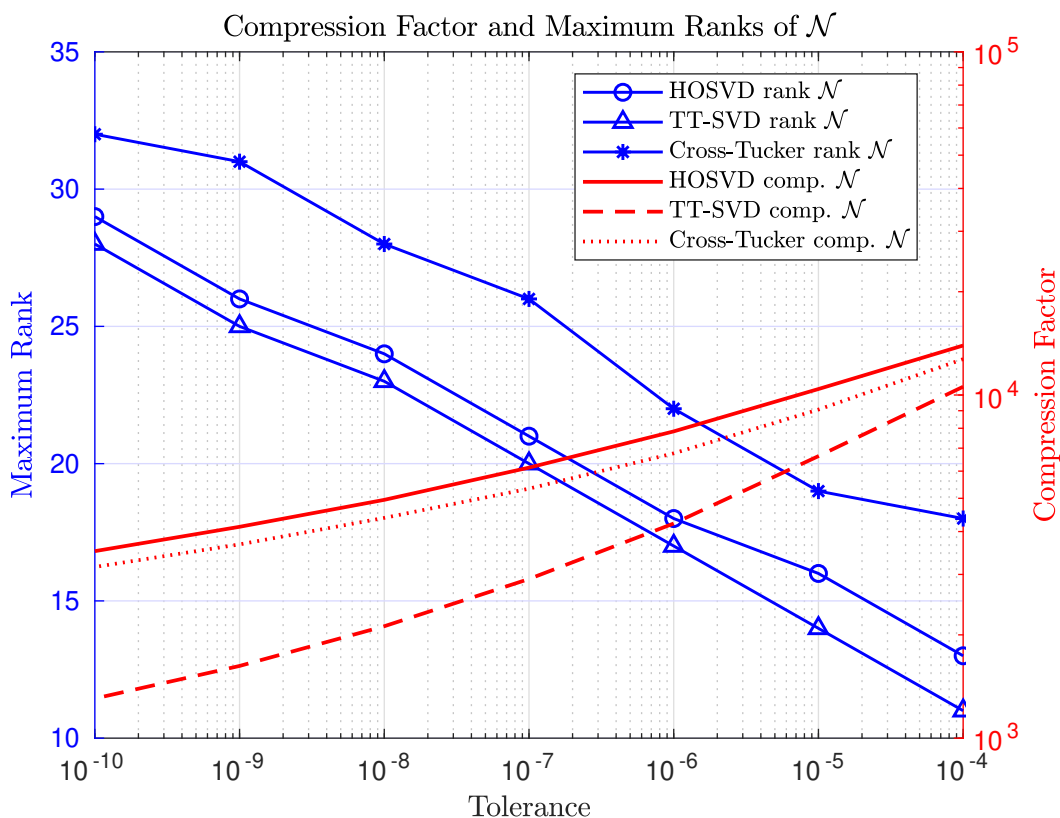


Figure 4.8: (Left axis) Maximum rank of the triplet  $\{r_1, r_2, r_3\}$  for the worst case scenario and (right axis) overall compression factor for all the unique components of  $\mathcal{N}$ . Results are shown for various tolerances.

#### 4.4.3 EM Simulations for Realistic Human Body Models

In this section, we implement an EM simulation for a realistic human head in order to observe the accuracy of the solver, in case tensor decompositions, are used. We excite the “Duke” highly inhomogeneous realistic human head model [17], with a linear polarized plane wave  $\mathbf{e}_{\text{inc}} = \hat{x}e^{-ik_0z}$ . The model has corresponding relative dielectric permittivity and conductivity

<sup>3</sup>Number of elements of the full forms divided with the number of elements of the decomposed forms

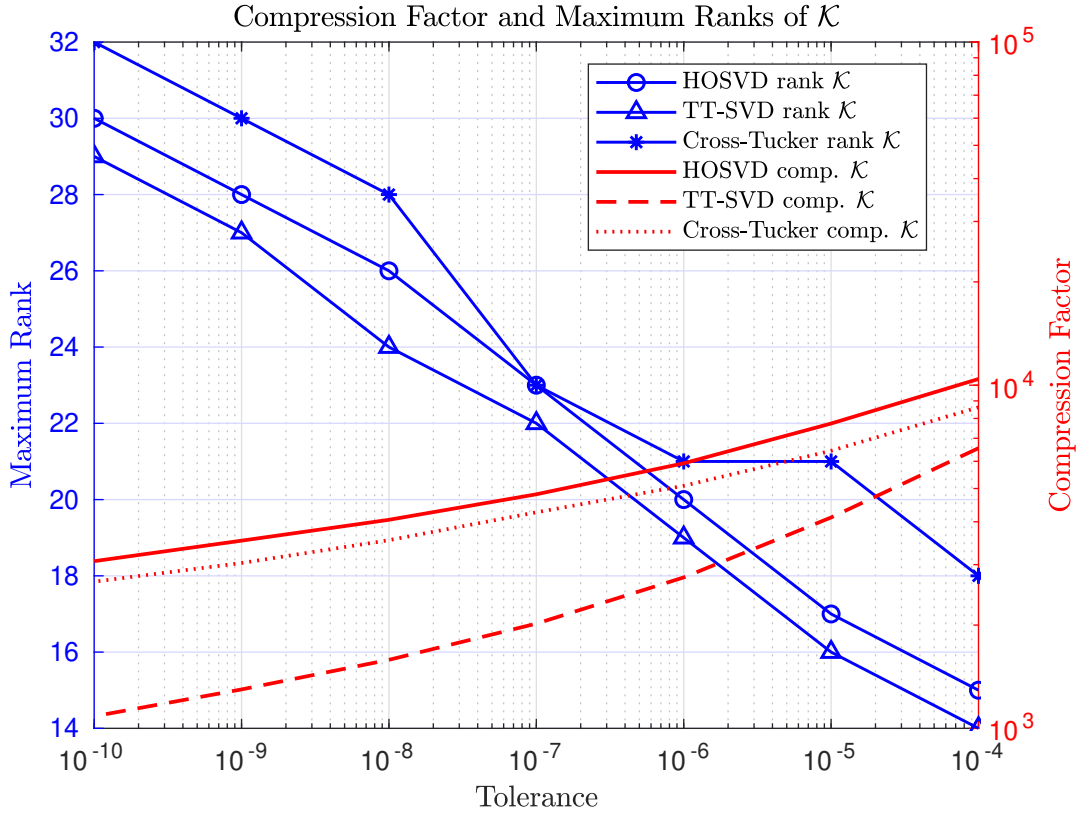


Figure 4.9: (Left axis) Maximum rank of the triplet  $\{r_1, r_2, r_3\}$  for the worst case scenario and (right axis) overall compression factor for all the unique components of  $\mathcal{K}$ . Results are shown for various tolerances.

relevant to 7 Tesla MR measurements, which are shown in 4.11 (left) on a sagittal (a) a coronal (b) and an axial (c) cut of the head. Finally, the domain is a cuboid, discretized with  $93 \times 119 \times 125$  voxels with  $2 \text{ mm}^3$  resolution, and the currents are expanded with PWL functions.

The matrix-vector product calculations were performed with Matlab (version 9.2) with our in-house suite MARIE [22], by embedding the decompositions mentioned above and PWL implementation in it. The iterative solver of choice is the GMRES with tolerance  $10^{-5}$  and inner and outer iterations 50 and 200, respectively. The traditional FFT-JVIE implementation leads to a memory overflow in GPU since it requires a vast amount of computational memory; thus, it is executed in CPU. On the contrary, tensor decomposition methods (namely HOSVD and HOSVD+CP) tackle this problem and can fit the simulation in GPU and drastically reduces the convergence time of the solver. The time footprint for the three solves is tabulated in 4.5. It is observed that an order of magnitude acceleration has been achieved, even though more flops are required for the matrix-vector product when tensor decompositions are used ( $\mathcal{O}(rN_v)$  over  $\mathcal{O}(N_v)$ ). Undoubtedly, tensor decomposition methods are veritable workhorses for exploiting the GPU architecture, in FFT-based VIE simulations.

In 4.10, the  $L_2$  relative error of the absorbed power  $p_{\text{abs}}$  and the absolute value of the trans-

Table 4.5: Convergence time of GMRES

Method	PU	Time footprint
Traditional implementation	CPU	2h 39' 58"
HOSVD decompression	GPU	14' 11"
HOSVD+CP decompression	GPU	16' 01"

verse magnetic flux density  $|b_1^+|$  between the Tucker decomposition-based implementations and the traditional FFT-JVIE are presented. The aforementioned EM quantities are

$$p_{\text{abs}} = \frac{1}{2}\sigma_e|\mathbf{e}|^2, \quad |b_1^+| = |\mathbf{h}_x + i\mathbf{h}_y|. \quad (4.19)$$

We have chosen to portray the absorbed power [356] since it is a realistic magnitude that provides the power deposition of the human body, and the  $|b_1^+|$  which expresses the transmitted RF field in MR scanners. Both magnitudes are fundamental for the MRI community [13]. We perform the numerical simulation for 9 different SVD tolerances ( $10^{-4}, 10^{-5}, \dots, 10^{-12}$ ) and for a 1000 iterations for the CP decomposition. It is observed that the error of HOSVD reduces linearly with respect to the given tolerance. On the contrary, Tucker+CP does not have a linear dependence with the SVD tolerance, since the CP decomposition does not achieve an optimal fit of the Tucker cores.

In 4.11, we illustrate (for SVD tolerance:  $10^{-10}$ ) the aforementioned absorbed power and the  $|b_1^+|$  on a sagittal, a coronal, and an axial slice of the head model. The mentioned scalar magnitudes are masked outside the head for enhanced visualization. The results seem to be in striking visual resemblance.

Given that FFT-based VIE is already faster than differential methods, which require dozens of hours for realistic head model simulations, a speed-up from  $\approx 3$  hours to  $\approx 15$  minutes, might not seem so significant. However, the time comparison is relative to the problem, and a simulation requiring a day to converge can be completed within 2 hours when the novel matrix-vector products are used in tandem with GPU programming. Such inherently slower problems appear when high contrast objects are part of the scatterer, i.e., an implant modeled as a dielectric material with high conductivity. In those cases, regrettably, the VIE formulations are significantly ill-posed. Therefore, the required number of iterations vastly increases, even if a second-kind integral formulation is used.

Such challenging problem are the EM simulations for the *dielectric shimming* technique [261–263]. Specifically, dielectric shimming is a recently proposed method, where high permittivity dielectric pads, i.e., barium pads with  $\epsilon_r = 300$  and  $\sigma_e = 0.25$  S/m, are placed between the RF coils of the MR scanner and the human body to effectively address the RF transmit field inhom-

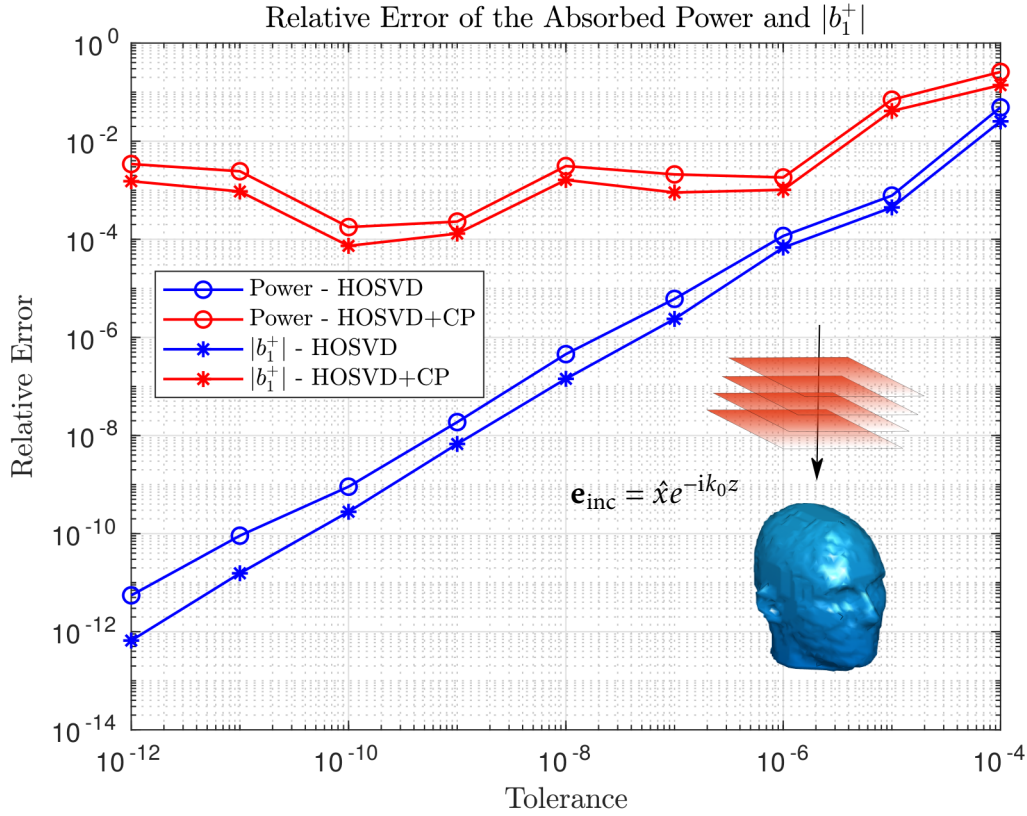


Figure 4.10: Relative error of the absorbed power and  $|b_1^+|$ , between the Tucker decomposition-based approaches and the traditional one.

generity, reduce the specific absorption rate and increase the signal to noise ratio, in UHF MRI. The effect of placing the pad close to the head introduces a strong asymmetry in the  $|b_1^+|$  maps, which enables the illumination of darker areas, where nulls occur without the pad. Potentially shading artifacts can be removed from the final MR image. However, for the patient's safety, accurate simulations have to be employed for designing and positioning the dielectric pad. Due to the extremely high contrast and inhomogeneity of the scatterer, only higher-order basis functions can establish the superior numerical accuracy for the EM field estimations [4]. However, due to the high contrast, even the robust FFT-JVIE (JVIE-II) expanded with PWL basis functions require hundreds of iterations for small iterative solver's tolerance, and it converges in more than 9 hours in CPU (for a voxel isotropic resolution of 2 mm), for the example shown in [4]. In this case, the usage of HOSVD is indispensable and reduces the convergence time, with the aid of GPU, to less than an hour for an SVD tolerance  $\epsilon = 10^{-8}$  (same system and GMRES settings with the previous example).

Finally, the importance of p-refinement (PWL basis functions) is highlighted when coarse resolutions are studied (namely  $5 \text{ mm}^3$ ), since the traditional approach can fit in GPU, and the results are accurate enough. However, when we model the scattering from large domains, such

#### 4.4. Results

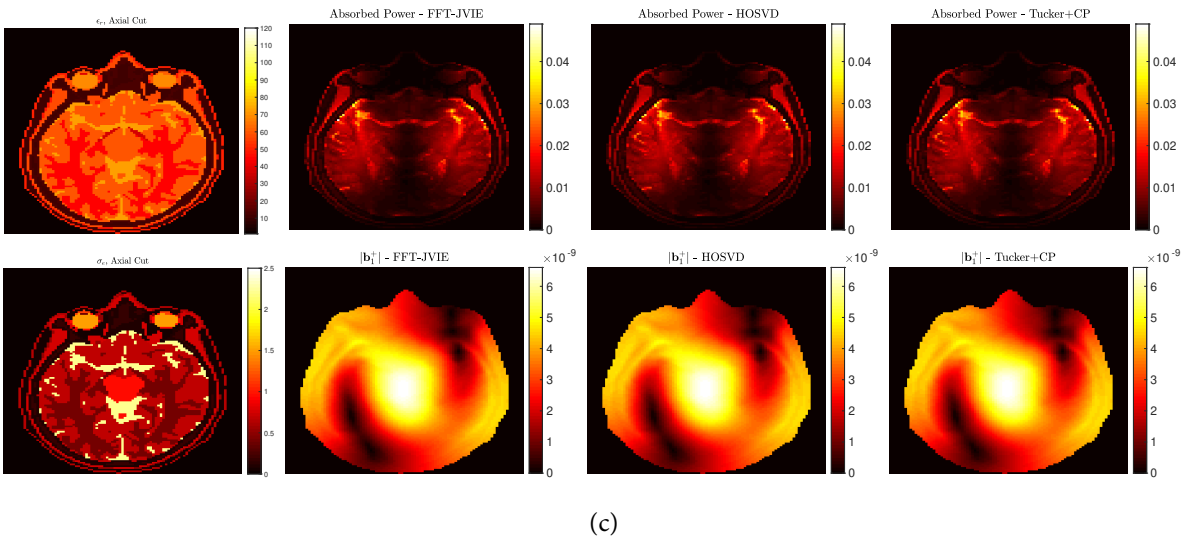
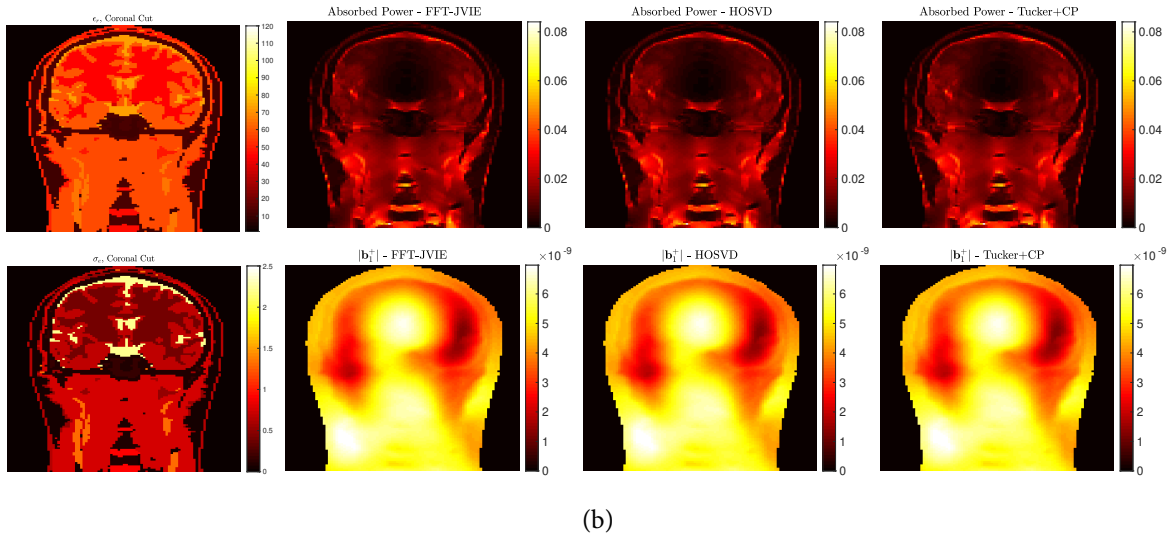
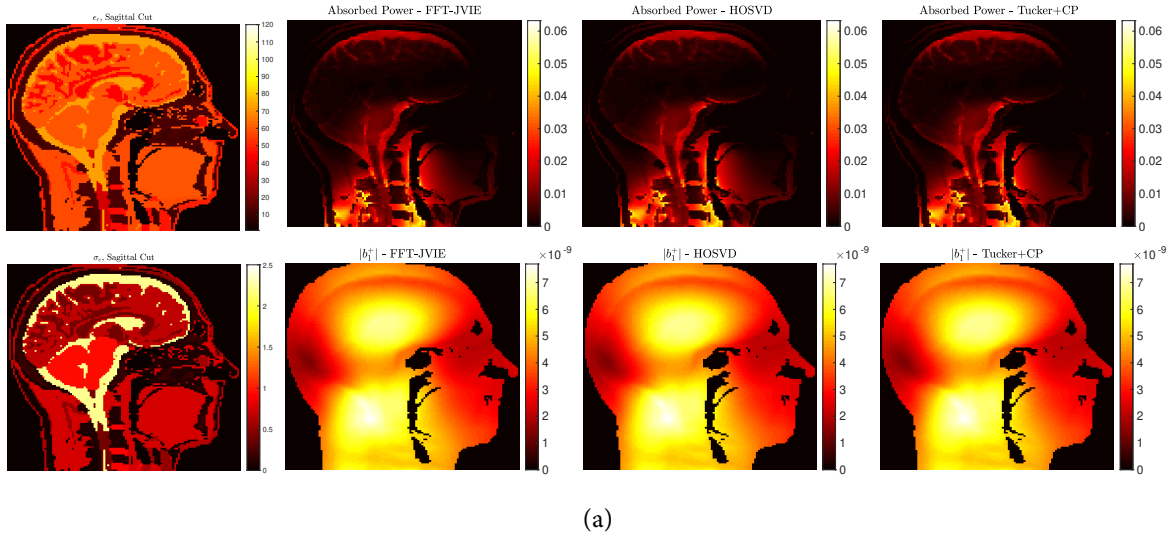


Figure 4.11: (from left to right and top to bottom) Relative permittivity, absorbed power calculated with the FFT-JVIE traditional solver, the HOSVD-based solver, and the Tucker+CP solver, conductivity and  $|b_1^+|$  calculated with the same solvers respectively for a (a) sagittal, coronal (b) and an axial (c) cut of “Duke” realistic human head model, corresponding to 7 Tesla MRI applications.

as the whole body, even for these coarse resolutions, the problem is large enough, and the simulations cannot be executed in GPU with the traditional FFT-JVIE approach. In the same logic as in the previous examples, tensor decomposition-based methods, compress the simulation to fit in GPU easily and, thus, requiring only  $\approx 15$  minutes to converge, in the same system as before and the same parameters for the iterative solver, (SVD tolerance was  $10^{-7}$ ). In figure 4.12, we present the electrical properties, the electric field, the magnetic field, the polarisation current, the absorbed power, the  $|b_1^+|$  and the  $|b_1^-|$ , for a coronal cut of “Billie” realistic human body model, using the HOSVD-based method. All the values are masked outside the body for enhanced visualization.

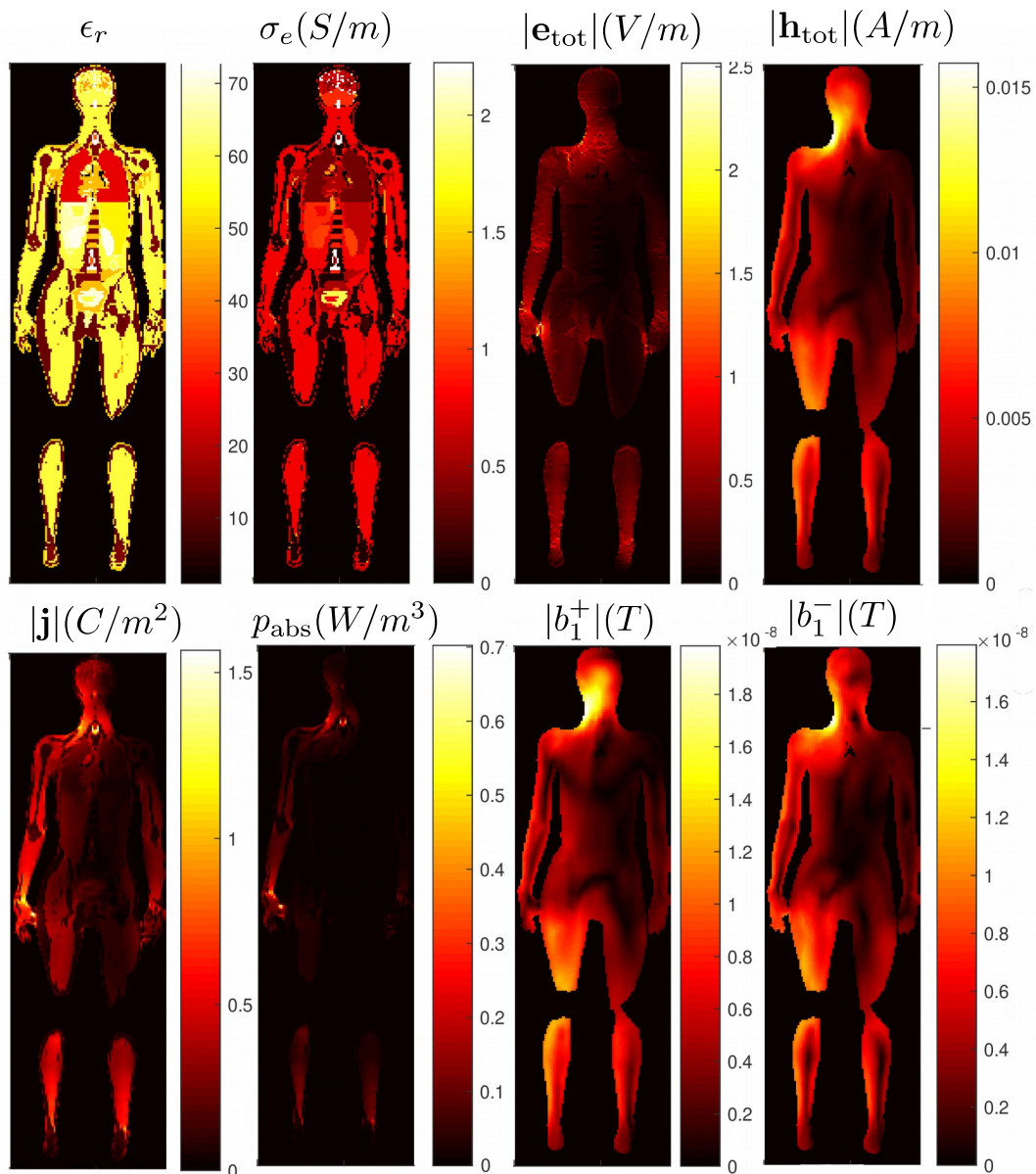


Figure 4.12: (from left to right and top to bottom) Relative permittivity and conductivity on a coronal cut of “Billie” body model, corresponding to 7 Tesla MR-measurements. Total electric field, total magnetic field, polarisation current, absorbed power,  $|b_1^+|$  and  $|b_1^-|$ .

### 4.4.4 Scaling Properties of Memory Compressed Approaches

Here we study the scaling properties of the Tucker decomposition-based approaches in comparison with the traditional method, namely time convergence and memory footprint, as we refine the grid, thus, increasing the number of the unknowns. Concretely, we choose a homogeneous sphere of radius 0.15 m and electric properties  $\epsilon_r = 65$ ,  $\sigma_e = 0.6$ . The EP and the dimensions were picked in order to create a tissue-mimicking scatterer, which is illuminated by a linear polarized plane wave  $\mathbf{e}_{\text{inc}} = \hat{x}e^{-ik_0z}$  at 298 MHz (7 Telsa MRI). The domain is a cuboid of length 0.3m, and the voxel's isotropic resolution is 10, 5, 3.3, 2.5, 2 mm for each h-refinement of the computational grid. Such resolutions result to  $\sim 0.3, 2.6, 8.7, 20.7, 40.5$  million unknowns respectively, for PWL basis functions. The GMRES tolerance is set to  $10^{-5}$  and the SVD tolerance to  $10^{-8}$ . The CP model is allowed to run for 1000 iterations with machine precision tolerance. We perform the simulation with the traditional FFT-JVIE, the HOSVD, and the Tucker+CP approaches. In 4.13, on the left axis, the time convergence of GMRES is shown, which runs for  $\sim 250$  iterations for all the refinements and solvers, while on the right axis the memory requirements of the unique  $\mathcal{N}$  components are portrayed. We can conclude that for coarse resolutions (up to  $3.3 \text{ mm}^3$ ), the traditional FFT-JVIE approach can fit in the limited memory of GPU and, as expected, is the fastest solver. For finer resolutions, the memory requirements of the unique  $\mathcal{N}$  components are high. Thus, the simulation is forced to run in CPU, and the time footprint explodes from  $\sim 11$  to  $\sim 486$  minutes for a  $3.3$  to  $2 \text{ mm}^3$  refinement. For these resolutions, the use of compression algorithms, like HOSVD or Tucker+CP, is crucial if we want to accelerate the solution with GPU programming. Their time footprint, e.g., for HOSVD, starts from  $\sim 13$  and grows to  $\sim 45$  minutes as we refine the grid (zoomed part of 4.13), guaranteeing an order of magnitude of acceleration. For finer resolutions, the memory of the unknown currents in their zero-padded + FFT form is larger than the memory of modern GPU cards; thus, such problems require additional compression techniques that will be discussed in the next section.

Finally, in 4.14, the relative error between the scalar absorbed power of the CEM simulations, and the analytic solution of the Mie series is shown. The error between the traditional FFT-JVIE and the HOSVD approach is identical as expected since only the SVD is used for compression, while the absorbed power calculated with the Tucker+CP approach does not necessarily lead to more accurate results as we refine the computational grid. The relative error might seem high even for fine discretizations, given that we are using PWL basis functions for our simulations, although this is not surprising at all since the voxelized grid creates a staircase approximation of the sphere [259].

## 4.5 Current Compression on the FFT-based VIE

In the previous sections we proved that the memory of the Green's function tensors appearing in FFT-based VIE could be vastly compressed through the Tucker decomposition, thus, allowing the implementation of the matrix-vector product in GPU [1], even for large domains,

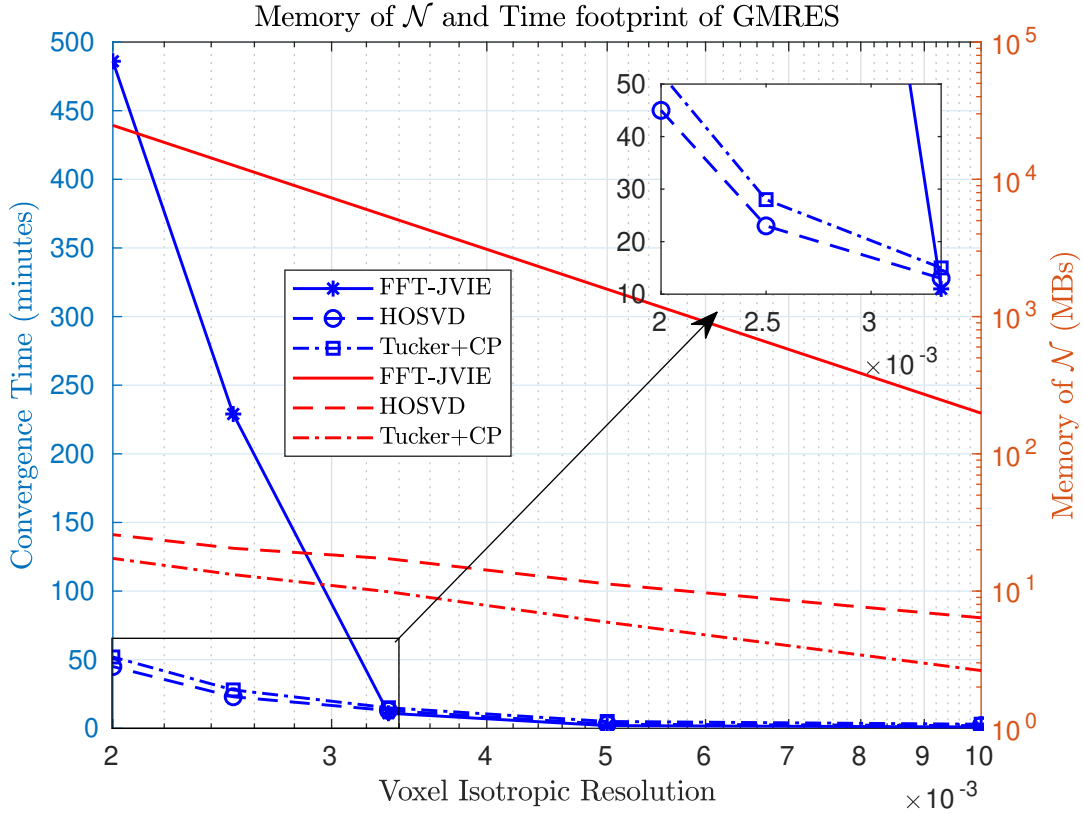


Figure 4.13: (Left axis) Convergence time of GMRES and (right axis) memory footprint for all the unique components of  $\mathcal{N}$ . On the top right corner we zoom on the convergence time of finer resolutions for enhanced visualization.

leading to an order of magnitude of acceleration over the traditional method. Nevertheless, in case of very fine resolutions of realistic human body models for MRI applications, e.g., 1 mm voxel isotropic resolution of a head model, even the memory requirements of the FFT tensor of the unknowns, appearing in the matrix-vector product, is larger than the memory limit of modern GPUs thus, forcing the problem to be executed in CPU for many hours. In this section, we present a memory-efficient implementation of the 3D FFT applied to the vector of the unknowns. Correctly, we implement 1D FFTs in two dimensions, while we hold the last 1D FFT to be executed in parallel with the element-wise multiplication, with a purpose to reduce the memory storage 8/5 times. The new approach leads to additional operations but allows higher memory compressions when it is combined with the Tucker decomposition-based matrix-vector product of the Green's function tensors, thus, making the usage of a GPU feasible.

The traditional implementation of the matrix-vector product requires the zero-padding, followed by a 3D FFT, of the tensors of the unknown currents, in order to match the dimensions of the circulant embedding of the Green's function tensor. In each iteration of the iterative solver, eight times more elements are needed for the unknowns. Alternatively, one can follow the novel, memory-efficient strategy: First, we zero-pad the tensor of the unknowns over one dimension,

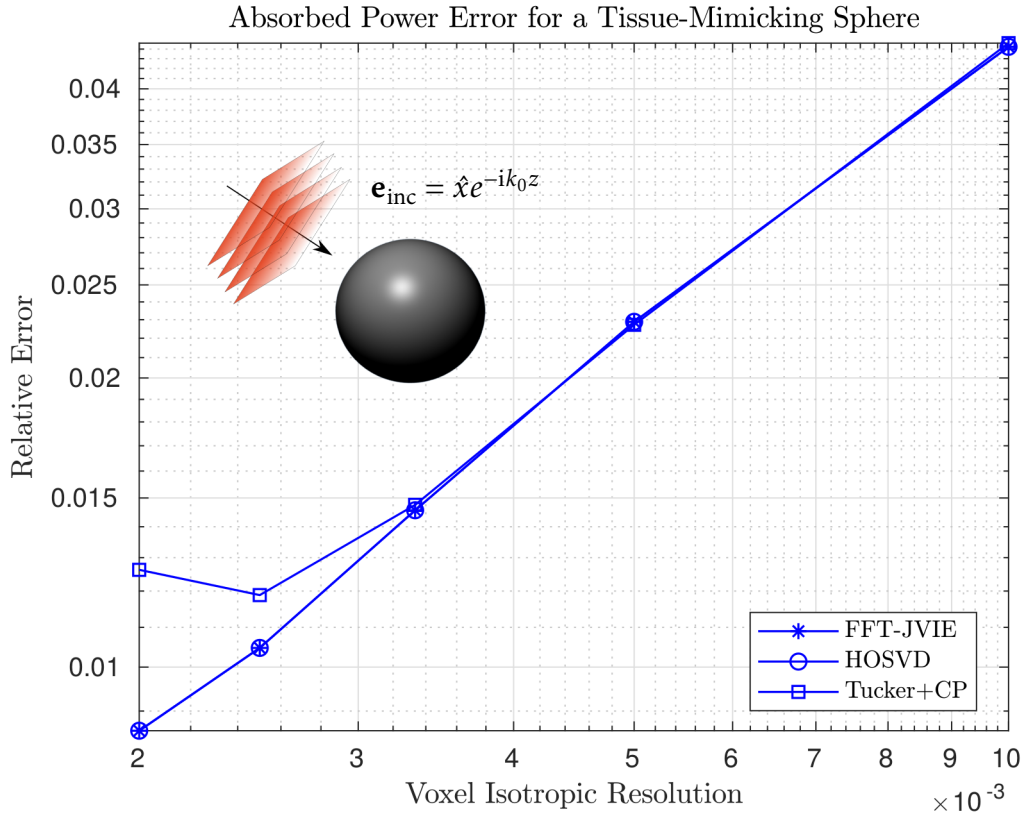


Figure 4.14: The relative error of the scalar absorbed power between the traditional FFT-JVIE, HOSVD, Tucker+CP methods, and the Mie series.

e.g.,  $x$  followed by multiple 1D FFTs, and we repeat the process for the second dimension, e.g.,  $y$ . Now, the required memory of the unknowns is four times their initial size. This is illustrated in the left of figure 4.15. For the implementation of the element-wise product, we use the following algorithm in each iteration.  $n$  is the number of Green's function tensors  $\mathcal{G}$ , appearing in the VIE formulation.

---

**Algorithm 5** Memory-Efficient Matrix-Vector Product

---

- 1: **for**  $i=1:n$  **do**
  - 2:     Decompress  $\mathcal{G}_i$ .
  - 3:     **for**  $j=1:4$  **do**
  - 4:         Zero pad  $j$ -th cubic set of unknowns over the last dimension, e.g.,  $z$ .
  - 5:         Apply 1D FFTs on  $j$ -th cubic set (Figure: 4.15 right).
  - 6:         Element-wise multiplication between the  $j$ -th sets of the unknown's elements and the respective set of  $\mathcal{G}_i$ 's elements.
  - 7:         Clear the buffer of memory for the  $j$ -th cubic set of unknowns.
-

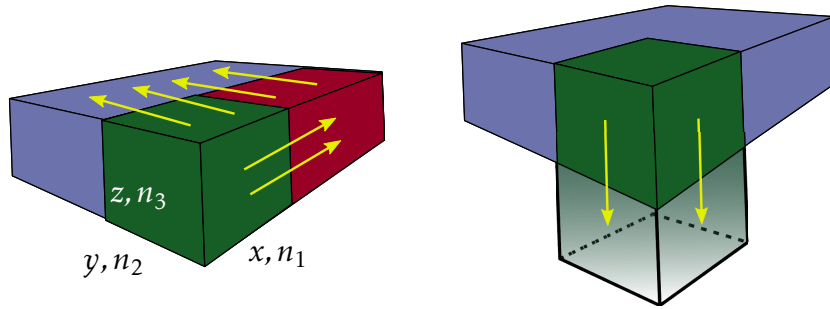


Figure 4.15: Sparse FFTs on the tensor of the unknown currents (green array). The yellow arrows define the direction of the zero-padding and the 1D FFTs. (left) Implementation of 1D FFTs over  $x$  and  $y$  dimensions and (right) 1D FFTs on the  $z$  direction for one cubic set of unknowns.

With this approach, the overall memory of the unknowns is  $8/5$  times less than the traditional one. The trade-off is the additional operations in step 2 and 3. However, the additional operations come from the FFT, which is a favorable operation for GPU, through the highly optimized library cuFFT, according to the results shown in 4.2.

To test the efficiency of the novel matrix-vector product, we perform an EM simulation for a realistic human head model, since UHF MR scanners motivate the method. Concretely, we choose the highly inhomogeneous realistic human head model of “Billie”, and we illuminate it with a linear polarized plane wave  $\mathbf{e}_{\text{inc}} = \hat{x}e^{-ik_0z}$ . The working frequency is 298 MHz and corresponds to a 7 Telsa MR scanner. The voxel’s isotropic resolution of the grid is 1 mm and the overall size of the domain is  $16.8 \times 18.8 \times 22.2 \text{ cm}^3$  or  $168 \times 188 \times 222$  voxels. We use the FFT-JVIE [4] formulation and expand the unknown currents with piecewise linear basis functions, resulting in a vast number of 84 million unknowns for the entire domain. The Green’s function tensors are compressed with HOSVD, and SVD tolerance  $10^{-8}$ . The iterative solver of choice is GMRES with a tolerance of  $10^{-5}$ . The operating system is the same as in the previous examples. For this problem, the memory requirements of the unknown currents (in their zero-padded + FFT form) are too big for the limited memory of GPU; thus, the methods presented in [1] and the previous sections, are not suitable. The time footprint of the iterative solver for the traditional and the novel approaches are summarized in the following table.

Table 4.6: Convergence time of GMRES

Method	PU	Time
Traditional FFT-JVIE	CPU	11h 35’ 47”
Memory-efficient matrix-vector product	GPU	1h 44’ 47”

The relative error between the scalar absorbed power of both methods, calculated with the

formulas presented in [356], is  $1.9 \cdot 10^{-7}$ . Finally, for a qualitative validation, in 4.16, we present the voxel-wise absorbed power, for both methods, at a sagittal and an axial cut of the head model. Both cases lead to identical results.

### Absorbed Power - Billie

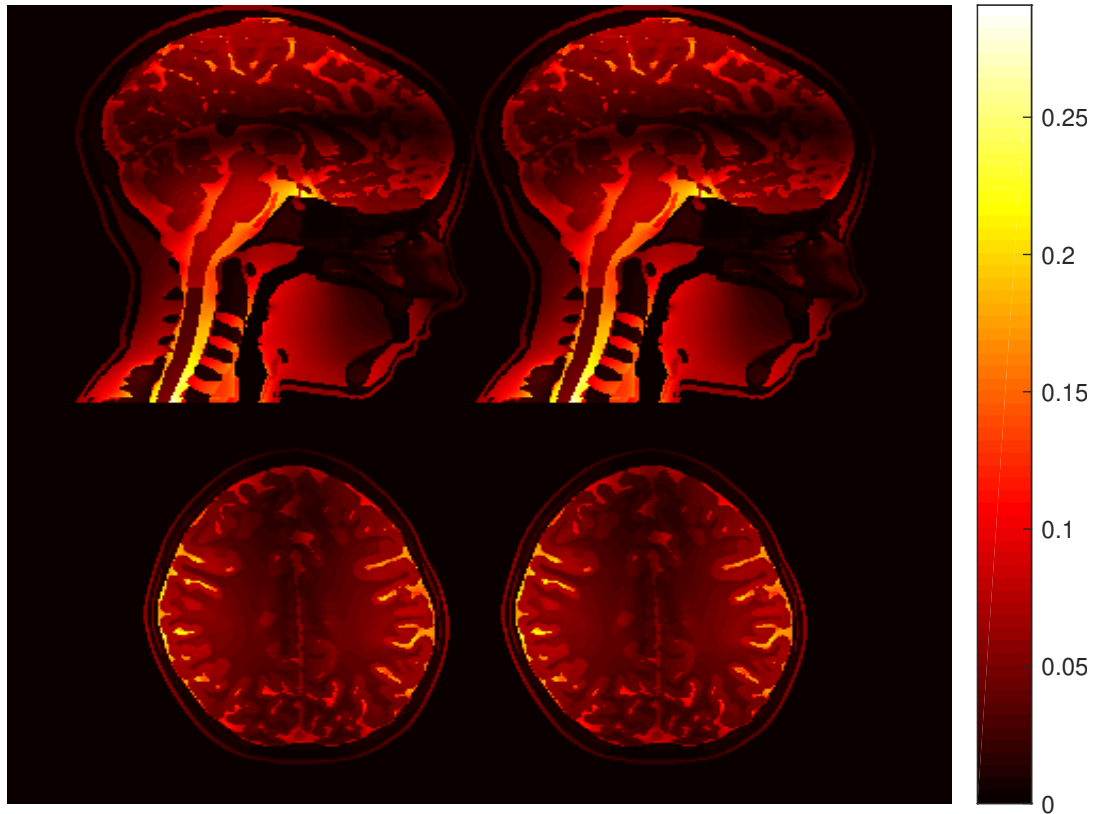


Figure 4.16: Local absorbed power on (top) a sagittal and (bottom) an axial cut of “Billie”. (left) Traditional FFT-JVIE and (right) memory-efficient MatVec approach. The field is masked outside the head for enhanced visualization.

## 4.6 Summary

In this chapter, we presented a method for significant memory reduction of Green’s function tensors arising in current-based VIE, via Tucker-based decompositions. This immense compression allows us to efficiently handle higher-order polynomial basis functions and use the highly parallel performance of GPU programming to significantly accelerate the numerical evaluation of relevant EM simulations. Similar compression is expected for other FFT-based VIE formulations (flux and field-based) since they consist of similar Green’s function-based kernels. Finally, the presented work can be used to speed-up the time-consuming inverse EM scattering problems, e.g., GMT, where the forward problem needs to be solved hundreds of times to retrieve an accurate dielectric property mapping of biological tissue.



# Chapter 5

## RF COIL DESIGN FOR GLOBAL MAXWELL TOMOGRAPHY

---

**E**ACH individual material in the nature can be characterized electrodynamically, with a set of electrical properties, namely electric permittivity and conductivity (Maxwell's equations), in the same manner as in the spin-dynamics with the relaxation times and the proton density (Bloch's equations). The EPs are a mean for the interaction between EM fields and materials and are of paramount importance for human tissue characterization [357, 358]. Specifically, an EP tomography of brain tissue could be used for the significant improvement of therapeutic modalities, such as magnetic resonance imaging. Moreover, medical and biomedical applications could be further improved with an EP map. For example, electrochemotherapy and hyperthermia [359, 360], could use these maps as additional biomarkers for tumor characterization. Finally, (RF) ablation [361, 362] and transcranial magnetic stimulation [363, 364] can also be improved.

Regrettably, the EPT is by no means a trivial task, since, an imaging technique as in MRI, using specific EM field encodings, does not exist. Therefore, the problem requires the inverse solution of Maxwell's equations. Thus, the EPT is an extremely ill-posed problem, since antennas can only be placed in the exterior of the head and can only measure the scattered field at their location, thus neglecting the interior field intensities in the brain. Thankfully, MRI can assist the EPT tremendously, since it provides magnetic field measurements from the interior structure of the brain, that encode and reflect the EP structure and values. A significant amount of research has been done over the so-called MR-EPT in simulation, and the proposed methods are divided into the PDE, and IE approaches.

MR-EPT is an inverse scattering problem. Mark Haacke et al. proposed the first approach in 1991 [108], where he attempted to solve the inverse differential form of Maxwell equations directly. Specifically, he estimated the conductivity of a 1D problem, using the complex-valued transmit magnetic field ( $b_1^+$ ). The inverse problem was iterative, and in every iteration, a better guess of the electrical conductivity was calculated. The first 3D MR-EPT was proposed more

than fifteen years later from Ulrich Katscher et al. [110, 365]. However, the MR-EPT method required assumptions that restrict its application in a realistic environment. First, the receive and transmit phases of the magnetic field were considered to be equal <sup>1</sup>. Second, the magnetic field intensity at the  $\hat{z}$  direction was zero. Third, the proposed method neglects the EP gradients, which leads to erroneous assumptions between boundaries of different tissues [110, 366] (in the case of a highly inhomogeneous head, many artifacts appear with the method). Unfortunately, these assumptions are only valid in the central region of the head, and only if it excited with a traditional birdcage coil, at 1.5 Tesla (or lower) MR scanners.

In the last decade, MR and EM scientists attempted to tackle these assumptions and propose additional novel techniques. Firstly, MR-EPT was extended for transmit and receive coils with multiple channels [367, 368], while more robust PDE methods were used to address the ill-conditioning of the problem [369]. Moreover, the usage of the  $b_1^+$  phase was proposed as a quicker electrical conductivity mapping technique [370], which is free of the transceive phase assumption and the EP gradients' neglect at the boundaries between different tissues [115]. Moreover, other simplifications were proposed that assumed constant EP over a specified axis [371], which is not always the case. In 2012 Daniel Sodickson et al. proposed a PDE method [372], dubbed Local Maxwell Tomography that is free of assumptions. The method leads to good results in simulation, but the required number of fields (both from transmit and receive channels of the RF coils) was too large. Furthermore, MR-EPT was combined with another method dubbed electrical impedance tomography for higher accuracy, which, however, is invasive to the human body [373–376]. To overpass the impasses of noise, other approaches used only the robust to noise, receive magnetic field sensitivities  $b_1^-$ . Also, the authors in [377] attempted to remove the noise from the  $b_1^+$  before MR-EPT. Others proposed the usage of classic image denoising regularizers in their iterative reconstruction [116], which smooth the EP maps and, as a result, information on the boundaries between different tissues is lost.

On the one hand, all methods arising from PDE are by default limited, since the numerical approximations of the derivatives significantly amplify the noise. On the other hand, one can use integral kernels, that are more robust to noise, since the gradients can be easily expressed with respective Hermitian-adjoint operators. As in the PDE case, many techniques were proposed mainly in the last five years. However, most of them require assumptions, such as the transceive phase assumption [118, 378], the zeroing of the  $\mathbf{b}_z$  [379] and the knowledge of the complex-valued  $b_1^+$  [380]. Finally, an assumption-free MR-EPT method, dubbed Global Maxwell Tomography (counterpart of LMT with IE formulations), was proposed by Jose Serrallés et al. recently [160]. GMT attempts to reconstruct cross-sectional mappings of the electrical properties distributions of human tissue, using MR measurements obtained from 7 Tesla MR scanners. The reason behind the employment of UHF MR scanners [12] is that the  $b_1^+$  becomes inhomogeneous as we increase the operating frequency; thus, it encodes additional information for the

---

<sup>1</sup>This is known as “transceive phase assumption”

## 5.1. Theoretical background on Global Maxwell Tomography

---

anatomical EP structure of the head under-study.

GMT is a fully 3D global inverse scattering algorithm that uses higher-order FFT-based VIEs and employs them through a non-linear least squares optimization routine to estimate the  $b_1^+$  by updating the unknown electrical properties in every iteration until specific criteria are met. GMT differs from alternative EP reconstruction methods because it does not require any simplifying assumptions considering that it uses only the measurable absolute value and the relative phase of the  $b_1^+$  [112]. In addition, it does not suffer from boundary artifacts or noise amplification.

In previous works on GMT [160,381,382] the scatterer of interest was excited using a numerical ultimate EM basis to investigate the technique independently from coil design. The scope of this approach was to generate a set of orthonormal (unitary) incident fields for scatterer illumination. Prior results have shown that the numerical conditioning of GMT strongly depends on the number and spatial distribution of the measured  $b_1^+$ . The numerical EM basis offered inhomogeneous fields, thus favorable for GMT, and was preferred over a standard transmit RF coil since the coil might not be able to generate the quality of excitations needed. Regrettably, to perform in-vivo experiments, the EM basis is not easily applicable, because the arising surface currents are difficult to generate in precisely the same way using a realistic transmit RF coil. Thus, GMT has its limitations as well.

The scope of this Chapter is dedicated to the investigation of GMT's performance with realistic RF coils, in simulation, for the EP reconstruction of tissue-mimicking phantoms and more complex structures such as highly inhomogeneous human head models. Since GMT operates in 7 Tesla MRI, there is not a standard problem-dedicated coil design to be used for an EP reconstruction application, and most coils in this frequency are only experimentally available. Therefore, we propose a novel problem-dedicated 8-channel head coil design for 7 Tesla and investigate its performance with GMT for different voltage calibration patterns and loads (head models). Our focus resolves around coils that can produce distinguishable (orthogonal)  $b_1^+$  maps from each channel since they favor GMT's cost function. A working coil design for GMT will enable its application in realistic environments and potentially provide the first accurate EP maps of human heads.

### 5.1 Theoretical background on Global Maxwell Tomography

GMT is an inverse problem with scope to recover the unknown electrical properties of human tissue in the presence of noise. The measurable EM field quantities from a modern MR scanner is the absolute value of  $b_1^+$  from each channel of the transmit coil and their relative phase. Therefore, we can write a cost function that exploits all the aforementioned quantities and estimates the degree of difference between them and predicted ones from a highly accurate numerical simulation, to predict underlying EP maps of the unknown tissue. The cost function,  $f(\epsilon_r, \sigma_e)$ , includes a hand-crafted regularizer,  $f_r(\alpha, \beta, \gamma, \epsilon_r, \sigma_e)$ , where the three parameters  $\alpha, \beta, \gamma$  can be changed depending the problem and the level of noise. GMT is an optimization problem without

bounds, or more properly with box constraints that do not allow unrealistic EP measurements, namely  $\epsilon_r \geq 1$  and  $\sigma_e \geq 0$ . The optimization problem is expressed below

$$\begin{aligned} \underset{\epsilon_r, \sigma_e \in \mathbb{C}^{N_s}}{\text{arg min}} \quad & f(\epsilon_r, \sigma_e) + f_r(\alpha, \beta, \gamma, \epsilon_r, \sigma_e) \\ \text{s.t.} \quad & \text{Re}\{\epsilon\} \geq 1 \\ & -\text{Im}\{\epsilon\} \geq 0. \end{aligned} \quad (5.1)$$

Note that the unknowns are the  $\epsilon_r$  and  $\sigma$ , however, for consistency in their magnitudes, we choose to optimize over the complex-valued  $\epsilon$ . The cost function  $f$  is real, with complex arguments. Therefore its derivative can be computed using the  $\mathbb{C}\mathbb{R}$ -Calculus (Appendix B) by exploiting the solution of VIE using Hermitian adjoint operators. To avoid the costly computation of the Hessian, the L-BFGS-B algorithm [383], is used, which estimates the Hessian with rank one updates of the gradient. Finally, The cost function is given from

$$f(\epsilon_r, \sigma_e) = \frac{\sqrt{\sum_{i=1}^8 \sum_{j=1}^8 \left\| w_i \circ w_j \circ (\hat{b}_{1,i}^+ \circ (\hat{b}_{1,j}^+)^* - b_{1,i}^+ \circ (b_{1,j}^+)^*) \right\|_2^2}}{\sqrt{\sum_{i=1}^8 \sum_{j=1}^8 \left\| w_i \circ w_j \circ (\hat{b}_{1,i}^+ \circ (\hat{b}_{1,j}^+)^*) \right\|_2^2}} + f_r(\alpha, \beta, \gamma, \epsilon_r, \sigma_e), \quad (5.2)$$

where

$$b_{1,i}^+ \circ (b_{1,j}^+)^* \equiv |b_{1,i}^+| \circ |(b_{1,j}^+)^*| \circ e^{i(\phi_i^+ - \phi_j^+)}. \quad (5.3)$$

The two summations over  $i$  and  $j$  iterate over all unique field maps of a multiple-channel (usually 8 channel, for 7 Tesla MRI) transmit array. The  $b_{1,i}^+$  and  $\hat{b}_{1,i}^+$  refer to the estimated and measured  $b_1^+$  maps, that correspond to the  $i^{\text{th}}$  channel, respectively. The relative phase between the maps  $i$  and  $j$  is given from  $(\phi_i^+ - \phi_j^+)$ . We choose to express the cost function in this form, because the predicted complex  $b_1^+$  is computable from the simulation, while the experimental one is given from the scanner without knowing the absolute phase information. The absolute phase of the transmit fields cannot be measured with standard MRI experiments [372]. The weights  $w_i$  are chosen in such a way to prioritize regions with higher SNR when estimating EP.

To calculate the  $b_1^+$ , we are solving the FFT-based JVIE using piecewise linear basis functions for supreme numerical accuracy. The polarisation currents can be seamlessly mapped to the  $b_1^+$  through the  $\mathcal{K}$  operator as:

$$\mathbf{b}_1^+ = \mu_0 \mathbf{h}_{\text{tot}} = \mu_0 \left[ \mathbf{h}_x^{\text{inc}} + K \mathbf{j}_x + i \left( \mathbf{h}_y^{\text{inc}} + K \mathbf{j}_y \right) \right]. \quad (5.4)$$

The subscripts  $x$  and  $y$  denote the appropriate cartesian component of the particular EM measurements. The matrix  $K$  is the discretization of the  $\mathcal{K}$  operator that maps electric polarisation currents to magnetic fields.

GMT is mainly a reconstruction problem, but in the presence of noise, it should behave as a denoising one as well. Therefore a regularization term is essential to cancel the noise from multiple sources, appearing in an MR scan [384]. The authors in [3] proposed the so-called match

regularizer that operates on the finite-difference approximation of the EPs along each direction  $|\Delta_q \epsilon|$ , where  $q \in \{x, y, z\}$ , and for every voxel. The regularizer is given from the following complicated formula:

$$f_r(\alpha, \beta, \gamma, \epsilon_r, \sigma_e) = \alpha \frac{1}{3N_v^{\frac{2}{3}}} \sum_{n \in N_v} \sum_{q \in \{x, y, z\}} \left( 1 - e^{-\frac{\gamma^2}{|\beta|^2 \sqrt{\gamma^2 + |\beta|^2}} (\gamma - \sqrt{\gamma^2 + |\Delta_q \epsilon_n|^2})} \right), \quad (5.5)$$

where  $N_v$  is the number of voxels of the scatterer and  $\Delta_q \epsilon_n$  is the difference of voxel's  $n$  EP with neighboring ones over  $q$  direction. The regularizer behaves like a classic total variation  $L_2$  when the difference in the neighboring EPs is small, and as they increase, it becomes an  $L_1$  or an  $L_0$  regularizer. The scope of this approach is to model small jumps between the EPs as noise, while higher ones as different tissues, through the optimization procedure. Those above are related to a triplet of parameters  $\{\alpha, \beta, \gamma\}$  that can be set for each problem independently and highly determine the performance of the regularizer. The match regularizer has shown excellent performance for boundaries with high contrast since it behaves as an  $L_0$  regularizer; however, for low contrast, it behaves like a total variation which, results in blurring. Since GMT is a costly problem, it is next to impossible to test various triplets and measure their performance in order to pick the best. A possible solution to this problem is to train a neural network to optimize these parameters. This thinking is motivated by the recently developed variational networks [385], where the network is built as an outer iteration loop around the optimizer and trains the parameters of the so-called fields of experts regularizer [386]. For additional information on the regularizer, we refer to [3].

## 5.2 RF Coil Design for Global Maxwell Tomography

The area of EP reconstruction is not mature enough for clinical applications. Therefore specific RF coils do not exist for such a purpose, and the traditional ones, employed for MR imaging, are used. Besides, 7 Tesla scanners became clinically available only recently [12]; thus, the number of available RF coils is limited in this frequency. For this purpose, using the theory introduced in Chapter 3, we will model and simulate problem-dedicated RF coils for the non-invasive cross-sectional mapping of the electrical property distributions of human tissue.

Thus far, GMT has been demonstrated in simulation employing eight orthogonal incident fields, constructed using a numerical EM basis, as the transmit fields of a hypothetical coil array [381]. Using the EM basis, it was shown that GMT could accurately estimate the relative permittivity and electric conductivity for simulations. However, these basis incident fields are difficult to generate with actual coils and, therefore, GMT performance could become worse in practice. To shed some light on this issue, we investigate the performance of GMT in simulation, using incident EM fields generated by realistic 8-element transmit arrays illustrated in 5.1. Specifically, we design a cylindrical 8-channel transmit-receive triangular loop array, based on a previously proposed coil [119, 120] for tissue-mimicking phantom simulations [6, 7] and a similar design for heads on a stadium substrate. The main reason behind such coil design is

because they can be highly decoupled and produce strongly diverse  $b_1^+$ , favorable for GMT's cost function.

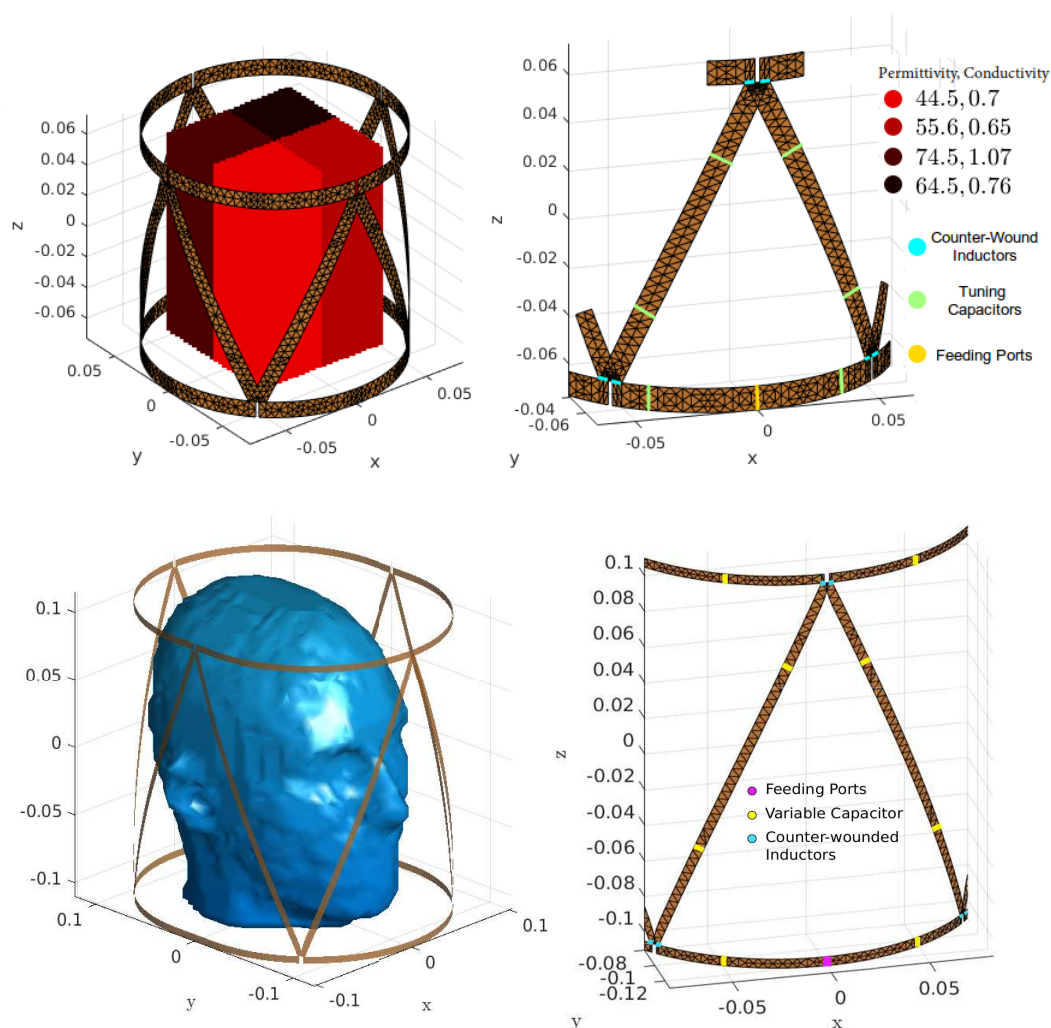


Figure 5.1: (top) Cylindrical coil and (bottom) Stadium coil. (left) The 8-channel triangular loop array loaded with the 4-compartment tissue-mimicking phantom (the relative permittivity and conductivity of each compartment are indicated in the legend) and the head model. (right) The locations of the lumped elements are shown for a representative array element.

In this section, we focus on the design of the coil, the tuning procedure, and the calculation of the scattered fields to the interior free-space (or the incident fields for the loading scatterer), in a 7 Tesla MRI-realistic environment. The simulations are performed using the EFIE for the PEC surface of the coil along with the delta-gap method for lumped elements modeling. Both coil designs have similar properties: The nearest neighbors can be decoupled through a set of tuning capacitors, while the next-nearest neighbors with a pair of counter-wound inductors. Each feeding port is matched to  $50\Omega$  by a series and a parallel capacitor placed across the port. The positions of the lumped elements are shown in 5.1 (right) for one representative loop. The cylindrical coil is loaded with a tissue-mimicking four-compartment phantom, with

## 5.2. RF Coil Design for Global Maxwell Tomography

relative permittivity {44.5, 55.6, 74.5, 64.5} and electric conductivity {0.7, 0.65, 1.07, 0.76} for each compartment also shown in 5.1 (left, top), while the stadium coil is loaded with the head model “Duke” from the Virtual Family population [17] (left, bottom). In tables 5.1 and 5.2 we present some information for the proposed RF coils.

Table 5.1: Information on the cylindrical 8-channel RF coil

Diameter	15.2 cm
Height	14.6 cm
Width of the conductor	1 cm
32 tuning capacitors	1 – 19 pF
8 matching parallel capacitors	5.6, 4.7 pF (top and bottom ports respectively)
8 pairs of counter wounded inductors	22 nH each, $-0.9$ mutual inductance coefficient
Cable trap at each port	Excitation only at 297.2 MHz
Discretization	728 Triangles

Table 5.2: Information on the stadium 8-channel RF coil

Radius of semicircles	10.2 cm
Length of the edge of the rectangle	3.8 cm
Height	22 cm
Width of the conductor	1 cm
32 tuning capacitors	1 – 5 pF
8 variable matching in series capacitors	1-50 pF
8 variable matching parallel capacitors	1-2 pF
8 pairs of counter wounded inductors	22 nH each, $-0.9$ mutual inductance coefficient
Cable trap at each port	Excitation only at 297.2 MHz
Discretization	1852 Triangles

In the lumped element analysis shown in Chapter 3, the delta-gap method updates the elements of the MoM matrix only when a lumped element exists across the respective edges of the triangular mesh. Therefore we need to generalize the theory in order to include the mutual inductance phenomenon as well. Explicitly, we model each inductor as a voltage jump across its edge, due to its impedance, and as a voltage jump across the edge of the mutually coupled inductor, due to their shared mutual inductance impedance. From classic electric circuit theory [387]

we know the following

$$\begin{bmatrix} v_1 \\ v_2 \end{bmatrix} = \begin{bmatrix} i\omega L_1 & ki\omega\sqrt{L_1L_2} \\ ki\omega\sqrt{L_1L_2} & i\omega L_2 \end{bmatrix} \begin{bmatrix} i_1 \\ i_2 \end{bmatrix}, \quad (5.6)$$

where  $v_n, i_n, L_n$ ,  $n = 1, 2$  are the voltage, current and inductance of the  $n$ -th inductor, and  $k$  is the mutual inductance coefficient. If we consider that  $L_1$  exists on a set of edges  $i = 1, \dots, n$  and  $L_2$  on  $j = 1, \dots, m$ , then the aforementioned equations can be translated easily to the delta-gap method as follows

$$\begin{aligned} Q_{i,i'} &= Q_{i,i'} + i\omega L_1 l_i l_{i'} \\ Q_{j,j'} &= Q_{j,j'} + i\omega L_2 l_j l_{j'} \\ Q_{i,j'} &= Q_{i,j'} + ki\omega\sqrt{L_1L_2} l_i l_{j'} \\ Q_{j,i'} &= Q_{j,i'} + ki\omega\sqrt{L_1L_2} l_j l_{i'}, \end{aligned} \quad (5.7)$$

where  $i', j'$  are edges of the set of  $i$  and  $j$  respectively.

### 5.2.1 Tuning, Matching and Decoupling Optimization

In order to make sure that the coil resonates at the frequency of choice (297.2 MHz), we need to make adjustments to the values of the tuning capacitors, thus perform the so-called *tuning*. Furthermore, in order to make sure that the power does not reflect on the feeding port, we need to adjust the values of the matching capacitors appropriately or perform the so-called *matching*. Finally, to ensure that the power is transferred from the coil's feeding ports to the load and not to the other feeding ports, we need to perform the so-called *decoupling*.

Decoupling is by no means a trivial choice, especially in multiport network-coils, since shifting the value of one capacitor might decrease the coupling between two ports, but increase the coupling between two other ports. Thus, specific adjustments to the lumped elements are required in an optimization sense. Instead, other approaches are used in the literature like geometrical decoupling techniques [388], which are useful for first-order neighbor decoupling, or the usage of external circuitry [389], which is validated for up to four coil channels, and might require complicated matching circuitry for excellent performance in eight channels. In the coils presented herein, a set of tuning capacitors distributed in the legs of each loop is used to decouple first order neighbors, while a set of counter wounded inductors is used to decouple second-order neighbors. For third and fourth (opposite) neighbors, the decoupling is performed through the conductivity of the load.

From those mentioned above, the shrewd reader would have noticed that for the presented coil designs, only adjustments to the lumped elements are required in order to perform all three, tuning, matching and decoupling, procedures for the 7 Tesla scanner's frequency. In terms of the impedance ( $Z$ ) parameter matrix, tuning minimizes the imaginary part of all elements (resonance), matching sets the real part of the diagonal elements to be equal to the impedance of the feeding cable in each port (usually  $z_0 = 50\Omega$ ), and decoupling minimizes the real part of the off-diagonal elements. All the above lead to a scattering ( $S$ ) parameter matrix with minimum

absolute values. In real experiments, the capacitors are adjusted using a screwdriver until the maximum possible power is transferred to the body inside the scanner. In the case of simulations, these adjustments can be expressed as an optimization procedure, i.e., a simple approach is to minimize over the Frobenius norm of the  $S$  parameter matrix, for the values of the tunable lumped elements  $\mathbf{c}$ .

$$\arg \min_{\mathbf{c}} \frac{1}{2} \|\mathbf{S}(\mathbf{c})\|_{\text{fro}}^2. \quad (5.8)$$

Let us consider the cylindrical RF coil loaded with the aforementioned four-compartment phantom. A straightforward minimization of the  $S$  parameters will require updates in the MoM matrix of SIE, thus, thousands of solutions of the EFIE and, as a result, the coupling solver between the body and the coil [23]. To avoid this costly computation we can consider all the tuning elements of the RF coil as feeding ports and then solve the EFIE 40 (8 original ports and 32 tuning capacitors) times by applying 1 Voltage excitation at 297.2 MHz at one port, while the rest are short-circuited. This method leads to a  $40 \times 40$   $S$  parameter matrix, which can be reduced to an  $8 \times 8$  matrix by attaching lumped elements to the appropriate ports since the coupling between them and the body is insignificant. This reduction can be made very fast inside an optimization procedure multiple times until the resulting  $S$  parameter matrix has small enough values. Afterward, the lumped elements, with their resulting values from the optimization routine, can be reattached to the coil. To find the surface equivalent currents on the coil, we need to solve the coupled solver 8 times, where we excite one feeding port with 1 Voltage, while the rest are closed with their matching circuitry (in this case just one capacitor or two capacitors) in parallel to the resistance of the feeding cable, which is usually  $50\Omega$ . Finally, the scattered electric and magnetic field from the coil to the interior free-space can be computed by projecting the currents with the volume integrodifferential operators  $\mathcal{N}$  (electric current to the electric field) and  $\mathcal{K}$  (electric current to the magnetic field), as

$$\mathbf{e}_{\text{inc},i} = \mathcal{N}(\mathbf{j}_{\text{eq},i}), \quad \mathbf{h}_{\text{inc},i} = \mathcal{K}(\mathbf{j}_{\text{eq},i}), \quad (5.9)$$

where  $i = 1, \dots, 8$  is the excited port and  $\mathbf{j}_{\text{eq},i}$  is the surface equivalent current generated by the excited port  $i$ .

We perform the optimization for the tissue-mimicking four-compartment phantom in order to decouple the nearest and next-nearest neighbors. In the optimization algorithm, first, we reattach the tuning capacitors in the admittance ( $Y$ ) parameter matrix. The multiport network  $Y_n$  is reduced to  $Y_m$  by combining the following equations.

$$\begin{bmatrix} Y_n^{pp} & Y_n^{pl} \\ Y_n^{lp} & Y_n^{ll} \end{bmatrix} \begin{bmatrix} I^p \\ I^l \end{bmatrix} = \begin{bmatrix} V^p \\ V^l \end{bmatrix} \quad (5.10)$$

$$Y_L I^l = -V^l.$$

Here,  $Y_n^{pp}$  is the block of  $Y_n$  corresponding to the actual feeding ports of the coil, and  $Y_n^{ll}$  is the block corresponding to the ports where the tuning capacitors will be reattached. Withal,  $Y_L$  is

a diagonal matrix with the admittance values of the tuning capacitors that are reattached to the ports  $l$ . By solving the system of equations, we end up to the following

$$\left( Y_n^{pp} - Y_n^{pl} (Y_n^{ll} + Y_L)^{-1} Y_n^{lp} \right) I^p = V^p. \quad (5.11)$$

The reduced  $Y_m$  parameter matrix is equal to  $Y_n^{pp} - Y_n^{pl} (Y_n^{ll} + Y_L)^{-1} Y_n^{lp}$ . To attach the parallel matching capacitors to  $Y_m$ , we have to add a diagonal matrix with their admittances. In case we want to include series elements between the feeding port and the feeding cable, we have to invert the new  $Y_m$  matrix and add a diagonal matrix with the impedances of these elements (for the stadium RF coil case). At this point, the resulting  $Y_m$  matrix can be transformed to an  $S_m$  matrix. The cost function of the optimization problem is nothing else than the Frobenius norm of the Hadamard product between a matrix of weights,  $W$ , and the  $S_m$  matrix.

$$f(c) = \|W \odot S_m(c)\|_{\text{fro}}. \quad (5.12)$$

We choose to include this weight matrix in case we want to prioritize the reduction of the values of specific elements, i.e., tuning and matching focus on the diagonal while decoupling focuses on specific off-diagonal elements. For faster and more reliable computations in the optimization process, we include the gradient of the cost function in our optimization routine (the calculations of the derivatives are shown in Appendix E). The above procedure can be followed for an RF coil that requires tuning, matching, and decoupling with any lumped elements even with complex impedances. In this case, the cost function is real-valued with complex arguments; thus, its gradient can be computed with the  $\mathbb{C}\mathbb{R}$ -Calculus (Appendix B).

In 5.2, the  $S$  parameters are shown after the optimization process for the cylindrical coil loaded with the 4-compartment phantom. The indexing follows a right-hand orientation with indices 1, 3, 5, 7 for the top ports and 2, 4, 6, 8 for the bottom ports (1, 2 are first-order neighbors, 1, 3 next nearest, and 1, 5 across ones). From the matrix, we can conclude that no power returns to the feeding ports, while the first and second-order neighbors are almost perfectly decoupled (values less than  $-15$  dB). Ports across of each other have stronger coupling since there is nothing but free-space between them (the length of the phantom is smaller than the length of the coil). In 5.3 we show the  $S$  parameters for the stadium coil while loaded with the head model ‘‘Duke’’. The optimization leads to even better results in this case since the selected geometry of the coil likens the structure of the head; thus, it does not allow much free-space in the interior region, which could result in a stronger coupling between the channels and lower SNR in MRI experiments.

## 5.2.2 Numerical Results

### 5.2.2.1 Projected Electromagnetic Fields

The VIE-based version of GMT requires as an input the  $b_1^+$  measurements and a set of incident fields that generate these  $b_1^+$  maps, for the EP distribution of the scatterer in the study. In the case of the four-compartment phantom and the cylindrical coil, the set of these incident fields are

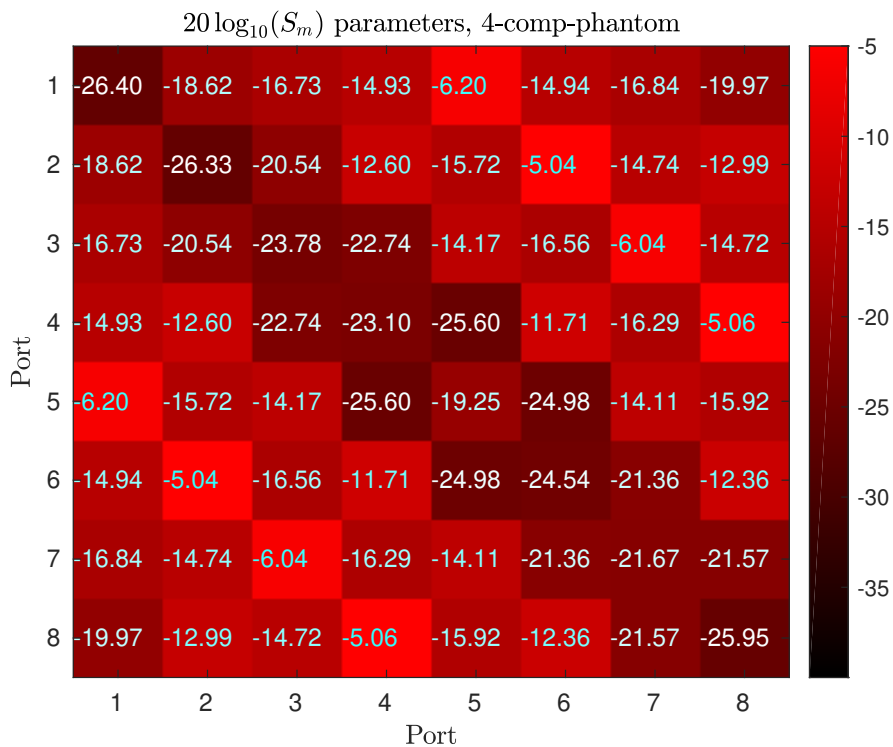


Figure 5.2: The  $S$  parameters of the cylindrical coil, while loaded with the 4-compartment phantom, after optimizing for the values of the variable capacitors.

shown in 5.4. The fields are used as one input in GMT. Intuitively we expect that orthogonal MR measurements are in favor of GMT's cost function since it operates on all eight measurements (7 Tesla MR scanners can support up to eight channels). As a result, since the coil is decoupled, the incident fields look different from each other. Thus, a well-conditioned set of  $|b_1^+|$  is expected to be generated with these incident fields.

Using the current-based VIE formulation expanded with PWL basis functions, we generate the eight  $b_1^+$  maps on the region of the phantom. The maps are not orthogonal but do form a well-conditioned set (with condition number  $\sim 7.7$ ). Additionally, we corrupted the maps with a Gaussian noise appearing in MR-systems (peak SNR = 100, corresponding to mean SNR from 23 to 28 for all 8 maps) and then used as synthetic MR measurements in the GMT algorithm. In 5.5 we portray the absolute value of the eight synthetic MR measurements for the central axial section of the tissue-mimicking phantom.

Using the same logic as for the four-compartment phantom, we generate a set of incident fields for the head model and the stadium coil and portray them for an axial cut in 5.6. The resulting  $b_1^+$  maps in the interior of the head form a well-conditioned matrix ( $\sim 4.75$ ). We corrupt again the maps with Gaussian noise of peak SNR = 200, corresponding to mean SNR from 82 to 88 for all 8 maps. The absolute values of the  $b_1^+$  are shown in 5.7. To be precise, in an MRI environment, it is the measured signal that is corrupted with Gaussian noise, which propagates to the  $b_1^+$ , which is obtained later through a technique based on MRI fingerprinting [390]. The

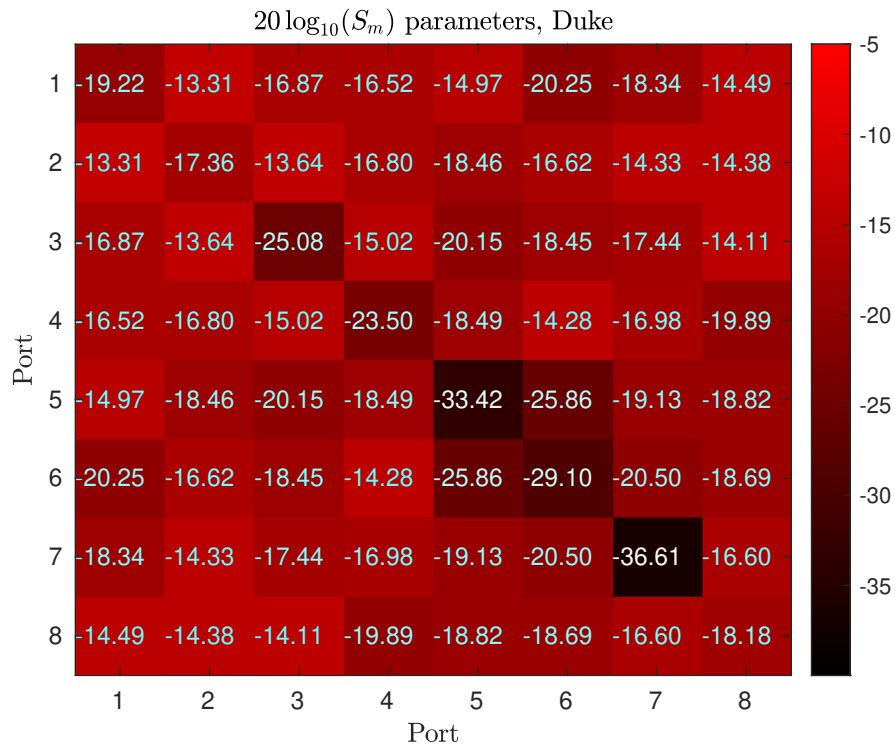


Figure 5.3: The  $S$  parameters of the stadium coil, while loaded with the “Duke” head model, after optimizing for the values of the variable capacitors.

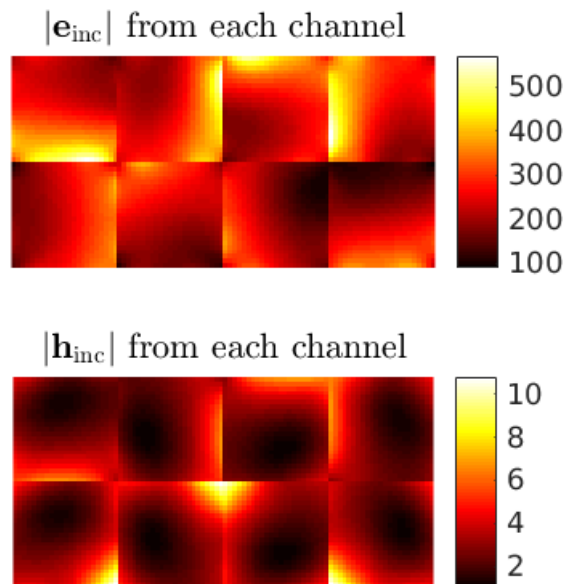


Figure 5.4: (from left to right and top to bottom) The scattered electric and magnetic fields from each channel of the cylindrical coil, used as incident fields for GMT.

noise propagation comes across as a little backward in the noise modeling and requires additional investigation in future work.

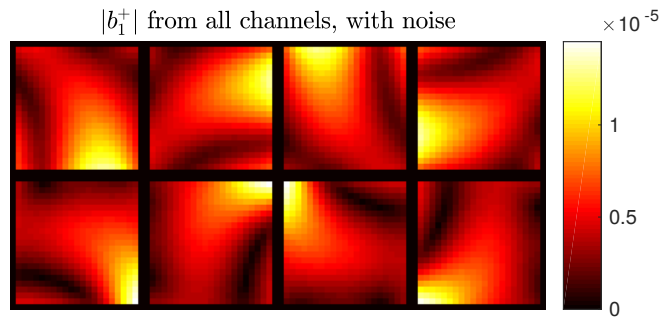


Figure 5.5: (from left to right and top to bottom) Synthetic noisy MR measurements ( $|b_1^+|$ ) for each of the eight transmit coils, inside the central axial section of the tissue mimicking phantom. Peak SNR was set to 100.

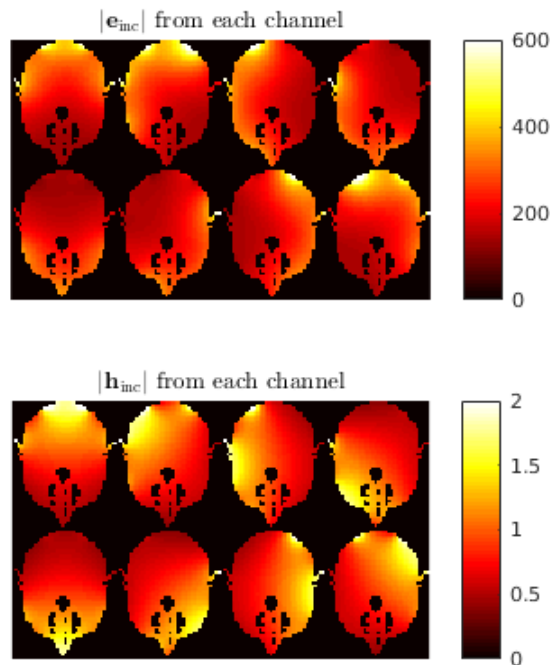


Figure 5.6: (from left to right and top to bottom) The scattered electric and magnetic fields from each channel of the stadium coil, used as incident fields for GMT.

### 5.2.2.2 Voltage Calibration Patterns

The incident electric and magnetic field intensities in the space occupied by the phantom can be calculated by projecting the surface currents through the  $\mathcal{N}$  and  $\mathcal{H}$  operators as in 5.9. From the incident fields, we can compute the total magnetic field intensity distribution for each coil channel (eight separate VIE simulations) inside the head model and generate the corresponding synthetic  $b_1^+$  maps that can be used directly in GMT. We dub this approach as “one port at a time” calibration.

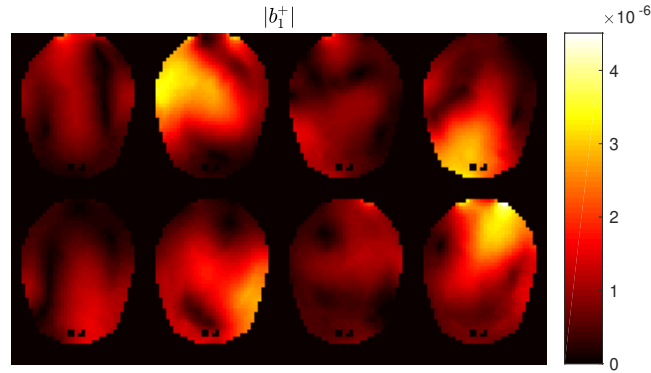


Figure 5.7: (from left to right and top to bottom) Synthetic noisy MR measurements ( $|b_1^+|$ ) for each of the eight transmit coils, inside an axial section of the head model. Peak SNR was set to 200. The field is masked outside the head for enhanced visualization.

In [3], it was shown that GMT results depend strongly on the orthogonality of the  $b_1^+$  maps, and optimal reconstruction was achieved using an ultimate EM basis for excitation. Therefore, we tried to investigate on the problem's conditioning by performing different excitation (or more correctly voltage calibration) patterns. First, an ‘‘SVD shimming’’ was performed to calibrate the driving voltages (both absolute value and phase) at each coil to construct orthonormal  $b_1^+$  maps. The SVD was applied on the reshaped matrix of the  $b_1^+$  maps  $B^{N_v \times 8} = USV^*$ , where  $N_v$  is the number of voxels. The resulting left singular vectors  $U$  were used as an orthonormalized set of  $b_{1\text{svd}}^+$  maps. The voltage calibration for this approach lies in a matrix of weights  $Q$ , which can be easily obtained as  $Q = VS^{-1}$ . Since the condition number for this approach will always be 1, the GMT reconstruction is expected to improve from the ‘‘one port at a time’’ case and result in similar reconstruction as in the ultimate basis approach. However, in actual experiments, where the impasse to replicate the coil in simulation and reality in an exact manner appears, this approach could lead to unwanted biases between the experimental  $b_1^+$  maps and those synthetically generated by solving the forward problem, which would negatively affect GMT. If  $B$  is not well-conditioned, to begin with (e.g., poorly tuned, matched, and decoupled), the entries of  $Q$  matrix could significantly differ from each other, which might result into additional problems. Moreover, the SVD is applied to the complex  $b_1^+$  maps, which are not fully available in reality. Finally, to experimentally obtain the  $b_{1\text{svd}}^+$  maps, one has to perform two MRI scans on the same patient (first to find the  $b_1^+$ , and compute  $Q$ , and the second to obtain the  $b_{1\text{svd}}^+$ ), which should be avoided, given that the patient has to remain still inside the scanner for the whole procedure.

Finally, in LMT [372], the authors attempted to minimize the nulls in  $b_1^+$  maps. This approach dubbed ‘‘all but one’’ will lead to strong  $b_1^+$  in all regions of the scatter, but since it is generated by constructively adding all the  $b_1^+$  in the middle voxel in an attempt to cancel out the phase differences there, it might not be optimal for GMT. In 5.8, we show the relative phases for the ‘‘one port at a time’’ case between the first channel and the rest seven, and we can easily observe

the differences between each measurement, which will be lost with the new approach.

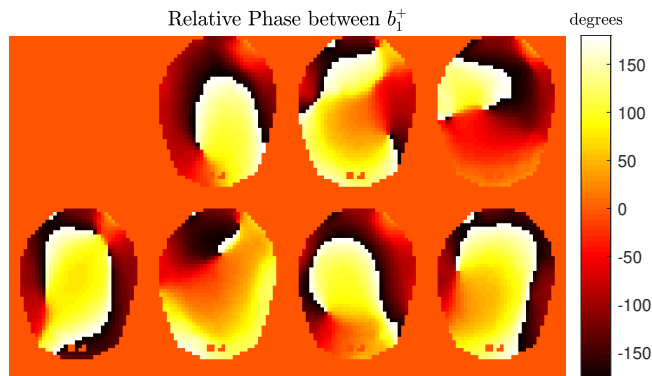


Figure 5.8: Relative phase between the  $b_1^+$  produced from the first channel and the rest in the interior structure of the head model with the stadium coil (port 1 to 8, from left to right and top to bottom).

The eight new  $b_1^+$  maps are created by subtracting, one at a time, the individual coils'  $b_1^+$  from the combined map. We then used the combined map and the first seven “all but one” maps as the eight  $b_1^+$  maps for the simulated GMT experiment. In an actual GMT experiment, this RF shimming approach could be achieved by calculating the RF shims to constructively combine all  $b_1^+$  at the center and turning off (i.e., zero voltage) one channel at a time to create the distinct excitations.

### 5.2.2.3 Tuning-Matching-Decoupling Sensitivity

The GMT results presented in this dissertation are purely in simulation, however in future work, if one wants to perform an in-vivo experiment, one of the impasses that will appear is the sensitivity of the coil in respect to its tuning, matching, and decoupling. In figure 5.9 we show that the optimization lead to pretty small values for the  $S_m$  matrix for capacitor values between 1 and 5 pF (a typical range for 7T coils). Specifically, the small entries in the diagonal elements ( $-36.61$  to  $-17.36$  dB), indicate good tuning and matching at 297.2 MHz, whereas the small off-diagonal elements ( $-25.86$  to  $-13.31$  dB) confirm that the channels were well-decoupled. Regrettably, since the broadband geometric decoupling [388] is not able to give good EP reconstructions (see next section), it was not used, and the sensitivity of the  $S_m$  parameters has to be assessed concerning the load. To perform this, we calculated a new  $S_m$  matrix after loading the stadium coil with the “Ella” head model, from the Virtual family population [17]), which had a different shape and interior structure than “Duke” which was used to tune, match and decouple the coil initially. In particular, “Ella” consists of 20 different tissues, and it is in a domain of dimensions equal to  $17.5 \times 21 \times 24$  cm<sup>3</sup>, whereas “Duke” has 21 tissues with unique EP and it is larger (enclosed in a domain of  $19 \times 23.5 \times 23$  cm<sup>3</sup>). The new setup and the corresponding  $S_m$  are shown in 5.9. The results are auspicious since the tuning and matching remain stable. Practically,

this translates to the following: the surface coil currents alternation due to the presence of the head is similar no matter the different head model that loads the coil. The off-diagonal element entries ( $S_{12}$ ,  $S_{18}$  and  $S_{23}$ ) are slightly higher and approximately equal to  $-10$  dB. These higher values are a normal phenomenon, since first-order neighbor decoupling is done through tuning capacitors and, therefore, is heavily affected by the loading condition.

#### 5.2.2.4 Electrical Properties Reconstruction

In the case of the cylindrical, triangular coil, and the four-compartment phantom, starting from a homogeneous guess (mean of the phantom's EPs), GMT optimization procedure iteratively simulated  $b_1^+$  maps. The incident fields generated from each coil channel ("one port at a time approach") were used to generate these maps. Finally, GMT updated the guess of the EP until the difference between the simulated  $b_1^+$  maps and the synthetic MR measurements reached a minimum. To measure the error between the ground truth and the reconstructed EP, we used the peak normalized absolute mean error (PNAME). The PNAME, between a ground truth  $X$  and a reconstruction  $\hat{X}$  for  $n$  samples, is given from the following equation

$$\frac{\frac{1}{n} \sum_{i=1}^n |X_i - \hat{X}_i|}{\max\{X\}}. \quad (5.13)$$

The PNAME over the entire volume of the phantom (14112 voxels at 4 mm voxel isotropic resolution) was  $\sim 0.45\%$  and  $\sim 0.6\%$  for the reconstructed relative permittivity and the reconstructed conductivity, respectively. We note that the mean error we found is similar to that previously reported for the same numerical phantom, using a peak SNR of 50 and the ultimate EM basis elements as incident fields [3]. In 5.10 we show the reconstructed EP for the central axial plane of the scatterer.

The reconstruction of the head model is a much more challenging problem, due to its complicated structure and to the finer details of the brain tissue. Starting from the mean value of the EP of all head voxels, we performed three GMT reconstructions for 500 iterations each, with all three proposed voltage calibration patterns. In figure 5.11 the ground truth and the three reconstructions are shown for an axial, a sagittal, and a coronal cut of the head model. For all cases, we notice that the interior structure of the head is preserved. However, some expected blurring occurs between specific regions of similar EP, e.g., at grey and white matter boundaries. The blurring is an effect of the TV regularization component of the match regularizer used in the cost function of GMT [3]. Regrettably, these settings are not optimal for the head reconstruction, and a perfect calibration of the regularization parameters is by far a non-trivial task. Each inverse problem requires many hours (or days) to converge, and as a result, a cross-validation technique is quite costly for all three parameters, while machine-learning approaches such as the recently proposed variational networks [385] need months of training. Moreover, in the "all but one" approach, zeroings appear in the middle head region, an expected outcome due to the lack of relative phase differences there. The condition number for this case was  $\sim 40$ , which explains

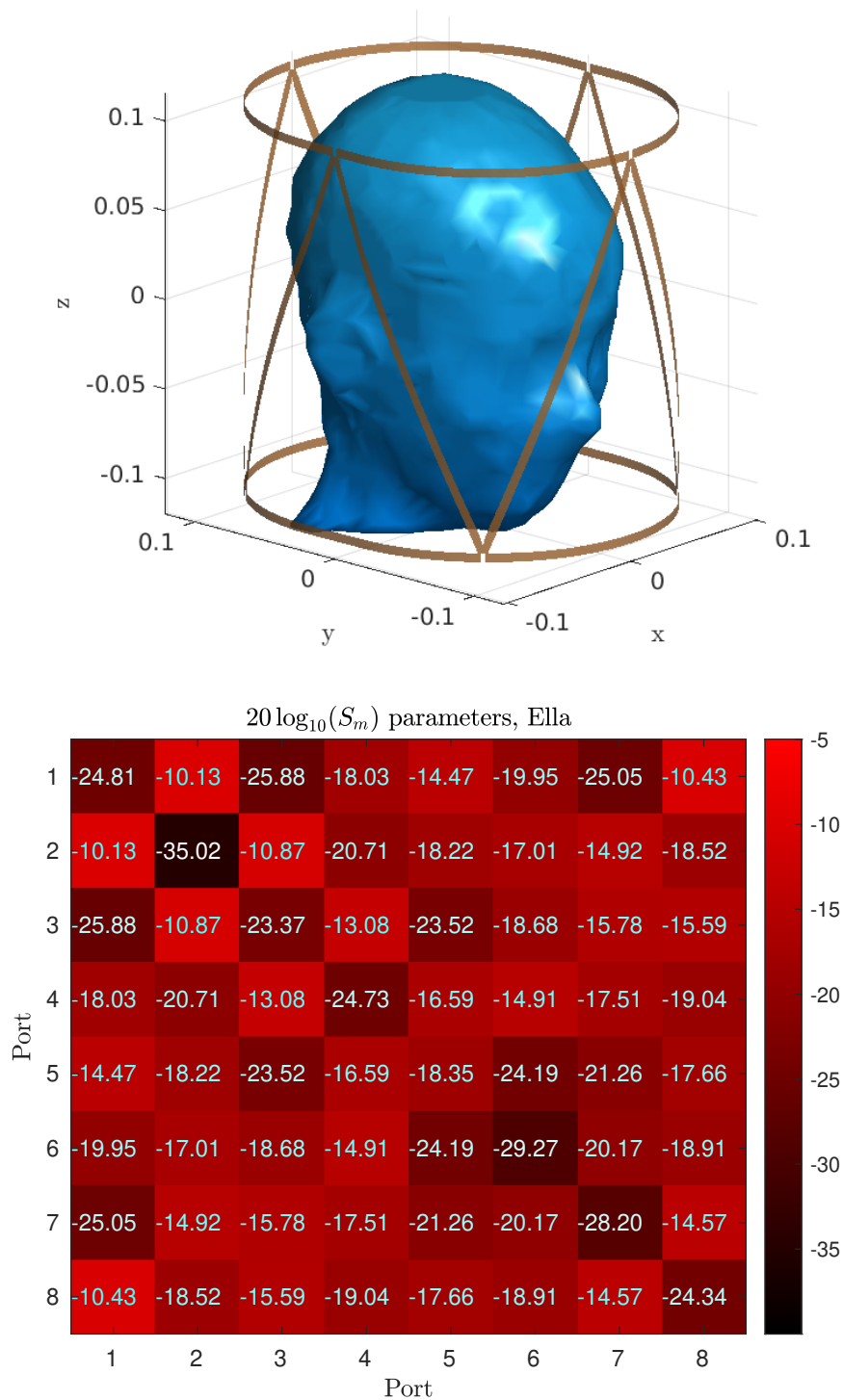


Figure 5.9: (top) The stadium triangular coil loaded with the realistic human head model “Ella”. (bottom) The new  $S_m$  parameters of the RF coil while loaded with “Ella” head model. The coil was tuned, matched and decoupled with “Duke” head model as a load.

the higher PNAME. All PNAME for the head voxels, both for the relative permittivity and the conductivity, are summarized in 5.3.

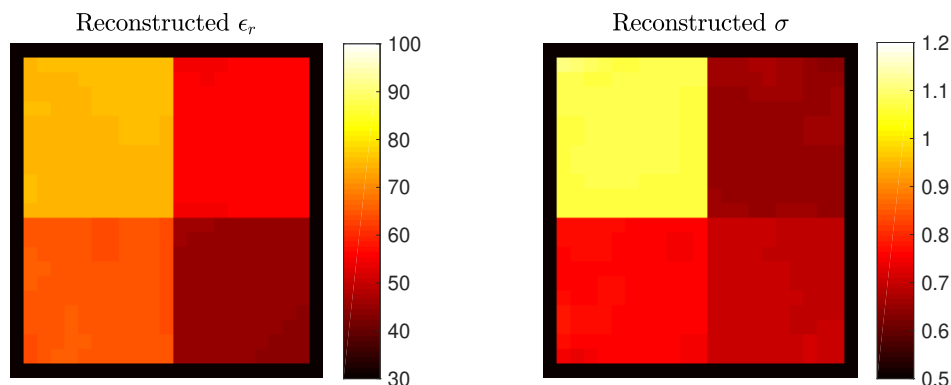


Figure 5.10: Reconstructed EP using GMT with a homogeneous initial guess for the middle axial section of the phantom. Both EP were estimated with negligible error.

Table 5.3: PNAME for the EP reconstructions

Excitation Pattern	EP	“Duke”	“Ella”	Four-Comp. Ph.	“Billie” (overlap coil)
SVD calibration	$\epsilon_r$	5.7%	NA	NA	NA
	$\sigma_e$	3.6%	NA	NA	NA
One port at a time	$\epsilon_r$	7.5%	9.5%	0.45%	15.2%
	$\sigma_e$	4.8%	7.2%	0.6%	11.3%
All but one	$\epsilon_r$	11.4%	NA	NA	NA
	$\sigma_e$	7.0%	NA	NA	NA

To test the sensitivity of GMT in respect to the  $S_m$  parameters, we perform the reconstruction for “Ella” with the “one port at a time” approach, without retuning the coil. The reconstruction is shown in 5.12 and the PNAME is tabulated in 5.3. As expected, the error is higher, and the reconstruction is not qualitatively as good as it was for the “Duke” head model.

To show the superior performance of the stadium design coil, we excited a cropped head model of “Billie” using the “one port at a time” approach with an overlapping coil design. The coil is shown in 5.13. It consists of eight individual coils with four next-nearest neighbors existing on a cylinder of radius 10.8 cm while the rest four are in a cylinder of radius 11 cm. The overlapping distance was found to give the best possible decoupling for all first-order neighbors at 2 cm ( $\sim -10$  dBs). Finally, the length of the coil was 13 cm, and the capacitor values<sup>2</sup> were optimized, with lower and upper bounds 1 and 19 pF respectively, using the aforementioned tuning-matching-decoupling optimizer. The reconstruction with this approach is shown in 5.14, and it is clear that the performance is sub-optimal. Finally, the PNAME is much higher than all the cases with the stadium coil, and it is included in table 5.3. Nevertheless, additional

<sup>2</sup>6 spread symmetrically across each loop, one parallel and one in series in each feeding port, which is located at the middle of the bottom side of each loop

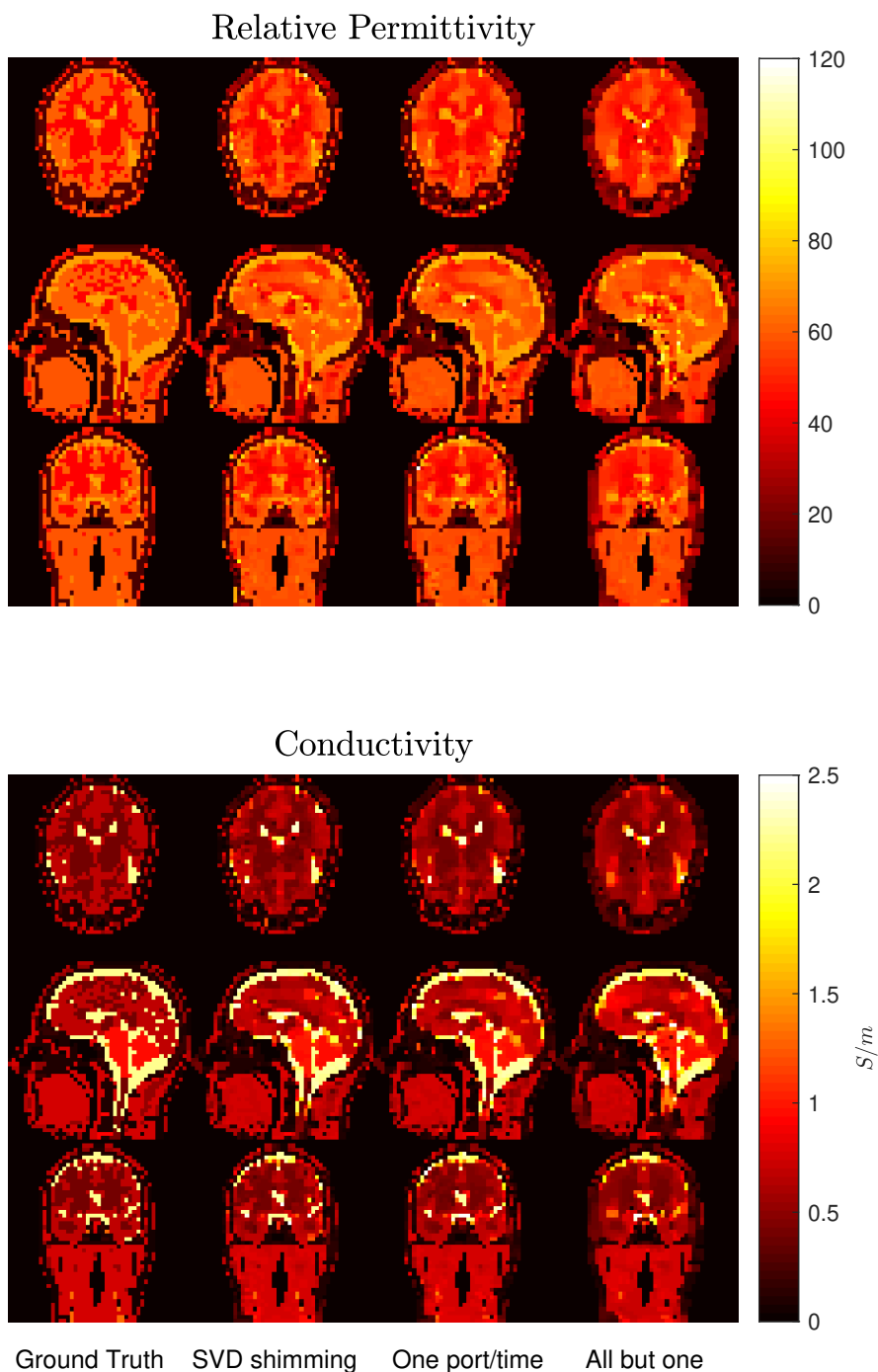


Figure 5.11: Reconstructed relative permittivity (top) and conductivity (bottom) for an axial, a sagittal and a coronal slice of “Duke” head model, using three different excitation patterns. From left to right, ground truth EP are compared with results for “SVD shimming”, “one port at a time”, and “all but one” voltage calibration patterns.

investigation is required for a robust conclusion on geometrically decoupled coils.

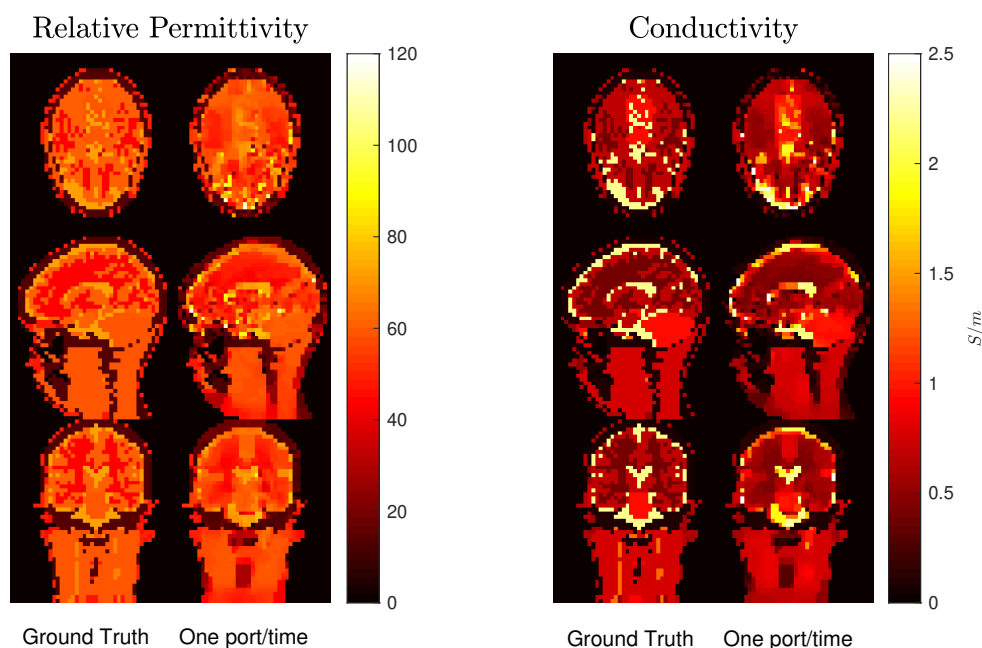


Figure 5.12: Reconstructed relative permittivity (left sub-figure) and conductivity (right sub-figure) are compared with ground truth EP, for an axial, a sagittal and a coronal plane of “Ella”, using the “one port at a time” excitation pattern.

To show a quantitative voxel by voxel comparison, we choose the peak normalized absolute error (PNAE) defined as

$$\frac{X_i - \hat{X}_i}{\max\{X\}} \quad (5.14)$$

The PNAE is preferred over other metrics (such as the relative error) because small differences between low valued EPs will result in high errors, and the histograms will be biased. The PNAE histograms are shown in 5.15 only for the “Duke” head model case and all three excitation patterns since the other cases do not require additional results for further conclusions.

### 5.2.2.5 Estimated Electromagnetic Field Distribution

One strong motivation behind the EPs reconstruction problem is their usage for patient-specific simulations: test various coils and the respective power deposition measurements, to ensure optimal imaging and the safety of the patients. In this subsection, we will use the reconstructed EP with the “one port at a time” approach to calculate EM field related measurements generated with an excitation that is similar to the one used in traditional MRI scans (circularly polarized mode of birdcage coils [391], first incident field of the “all but one approach”). The resulting EM field measurements are compared to the ones obtained with the ground truth EP.

Since the power deposition<sup>3</sup> is one of the most interesting measurements in radiology, we

<sup>3</sup>And the specific absorption rate, which includes the proton density, as in 1.1

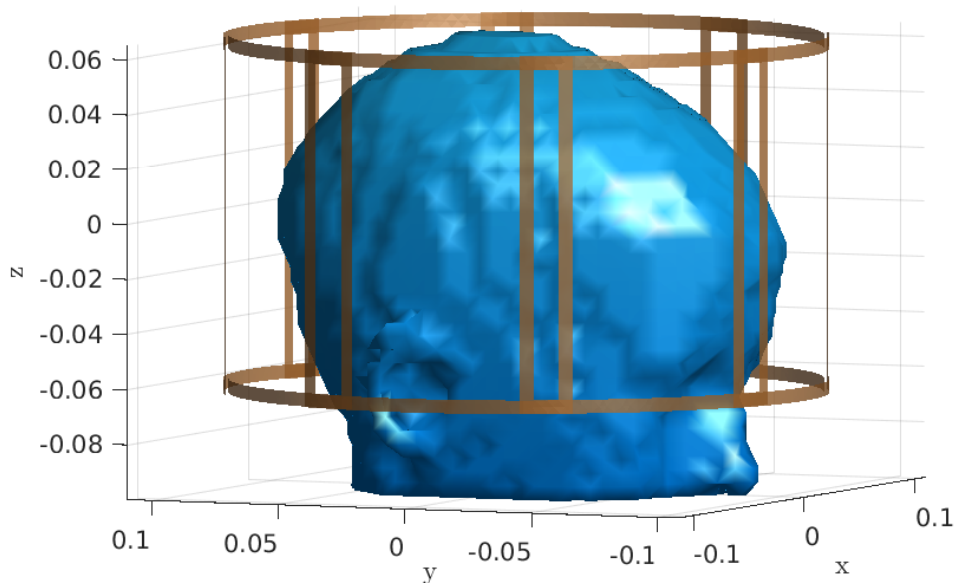


Figure 5.13: The overlapping coil loaded with a cropped realistic human head model “Billie”. The coil was tuned, matched and decoupled with the same cropped head model as a load.

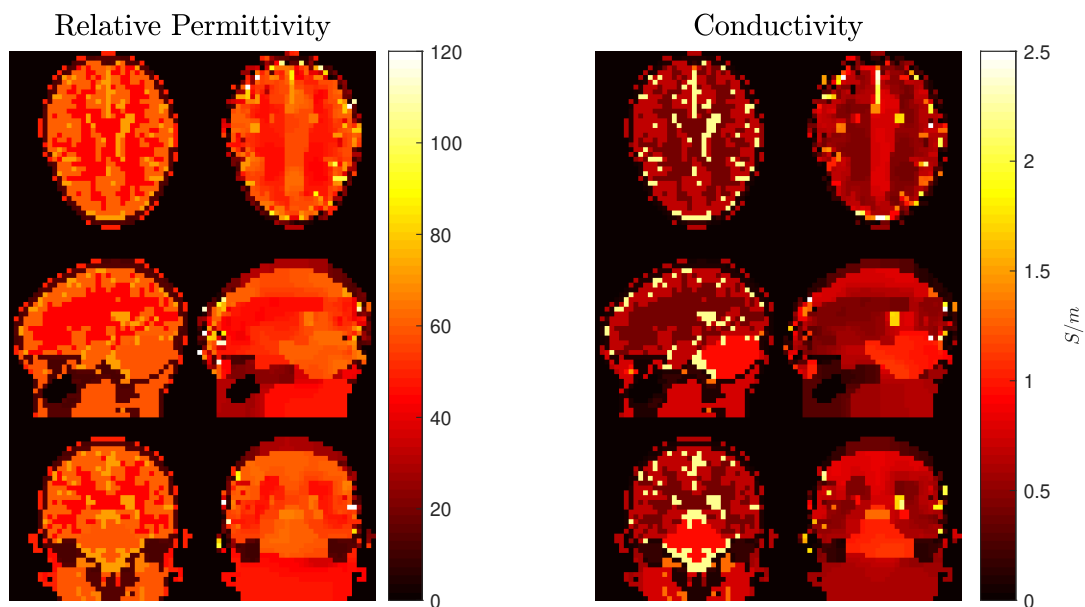


Figure 5.14: Reconstructed relative permittivity (left sub-figure) and conductivity (right sub-figure) are compared with ground truth EP, for an axial, a sagittal and a coronal plane of “Billie”, using the “one port at a time” excitation pattern and an overlapping RF coil desing.

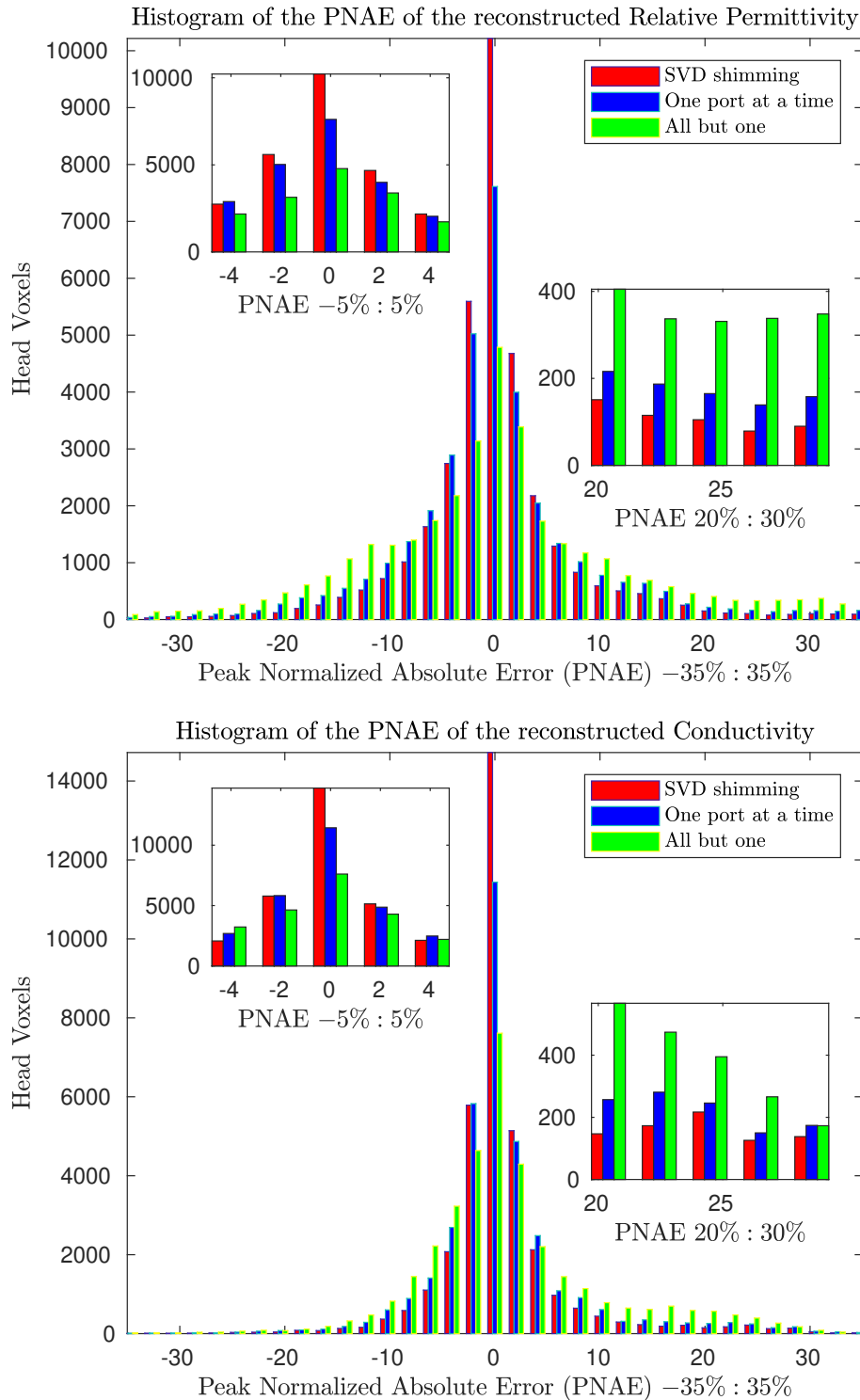


Figure 5.15: Histograms of the PNAE for all voxels in the “Duke” head model. The error distribution is shown for (top) relative permittivity and (bottom) conductivity. Zoomed view of two regions of the histograms are also shown to highlight differences among the three excitation patterns.

computed the local absorbed power at each voxel as  $p_{\text{abs}} = 1/2\sigma_e|\mathbf{e}|^2$ , along with the  $b_1^+$  distribution (which is inferred from the MR signal). The results are summarized in 5.16.

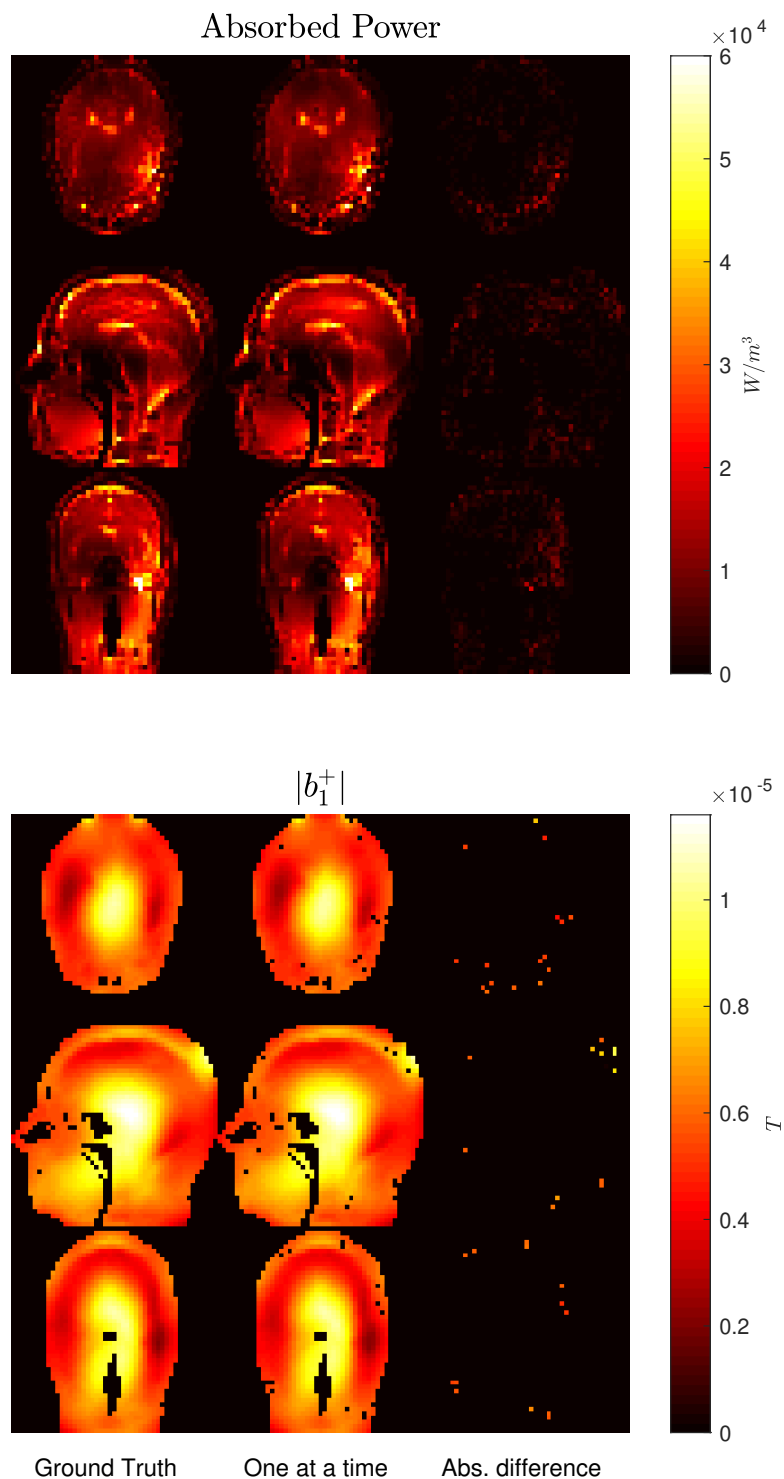


Figure 5.16: (top) Absorbed power and (bottom)  $|b_1^+|$  for an axial, a sagittal and a coronal planes of the “Duke” head model. Maps were calculated for a circularly polarized mode excitation using the ground truth EP (left) and the EP reconstructed with the “one port at a time” excitation pattern (middle). A map of the absolute difference is shown for each estimated measurement (right).

Even though the PNAME of the EP was 7.5% and 4.8% for the relative permittivity and the conductivity respectively, the PNAE histograms in 5.17 shows that the error for the absorbed power was mostly within  $-5\%$  and  $5\%$ , whereas for the  $|b_1^+|$  the error was strictly between  $-1\%$  and  $1\%$ . In 5.4, additional comparisons are shown, including one for the scalar absorbed power and one for the scalar scattered power, calculated with the formulas in [356], along with the PNAME for the absorbed power and the  $|b_1^+|$ . The table includes the number of iterations that GMRES requires to converge to  $10^{-5}$  tolerance. Since the reconstructed properties have artifacts, the contrast increases significantly, making the problem more ill-posed, thus the number of iterations increases.

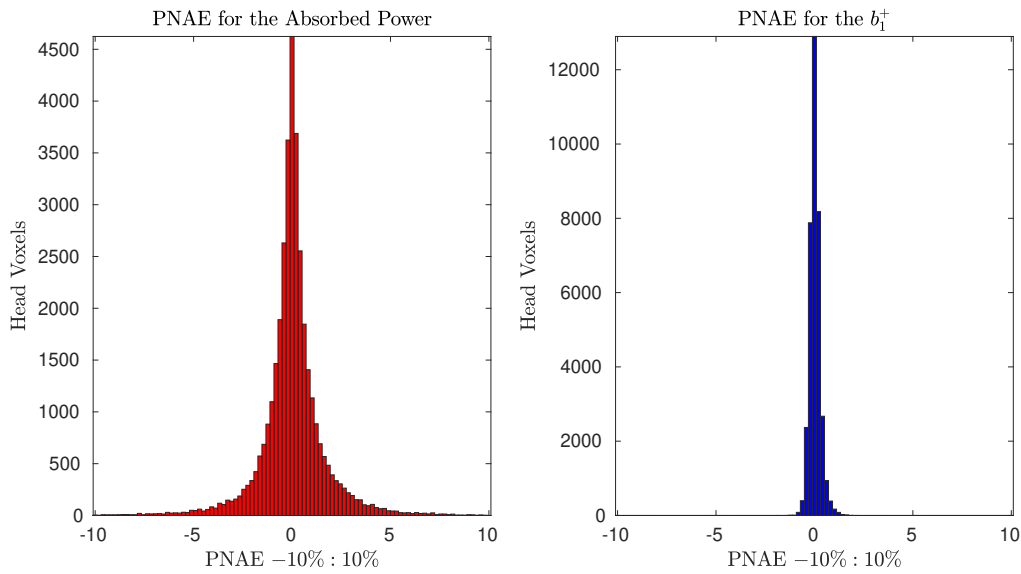


Figure 5.17: Histogram of the peak normalized absolute error for the (left) absorbed power and the (right)  $|b_1^+|$  calculated using the EP reconstructed with the “one port at a time” approach for the “Duke” head model and the stadium triangular coil.

Table 5.4: Comparison of estimated EM field quantities

Measurement	Ground Truth EP	Reconstructed EP
PNAME $p_{\text{abs}}$	NA	0.46%
PNAME $ b_1^+ $	NA	0.38%
Absorbed Power (Watt)	52.81	52.54
Scattered Power (Watt)	6.56	6.48
Iteration Count	183	266

### 5.2.2.6 Brain Tumor Detection

A wide variety of research in the past decades showed that the conductivity of tissue is sensitive to the presence of cancer. Specifically, the conductivity of cancerous tissue differs from the

ones of neighboring healthy tissues [78, 79] and can be three times higher compared to white matter in the case of brain tumors [392]. Due to this fact, we aim to use GMT as a diagnostic tool for brain tumor detection. To evaluate its diagnostic performance, in a clinical scenario, we inserted a numerical tumor into the “Duke” head model. Based on [393], we used relative permittivity and conductivity of 68 and 1.1, respectively. Of course, these values are not entirely realistic but pose an excellent initial approach towards a more robust diagnostic GMT-based tool. To achieve the most accurate reconstruction possible, we retuned the coil and performed the GMT reconstruction for 500 iterations, using Gaussian noise in the  $b_1^+$  of peak SNR of 200 as in the previous cases, in tandem with the “SVD shimming” voltage calibration pattern. The initial guess was the ground truth EPs (without the tumor) of the head model to resemble the detection of an abnormality (the tumor) in a healthy brain. The reconstructed EPs are compared with the actual EPs distributions in 5.18, showing that the tumor was correctly detected.

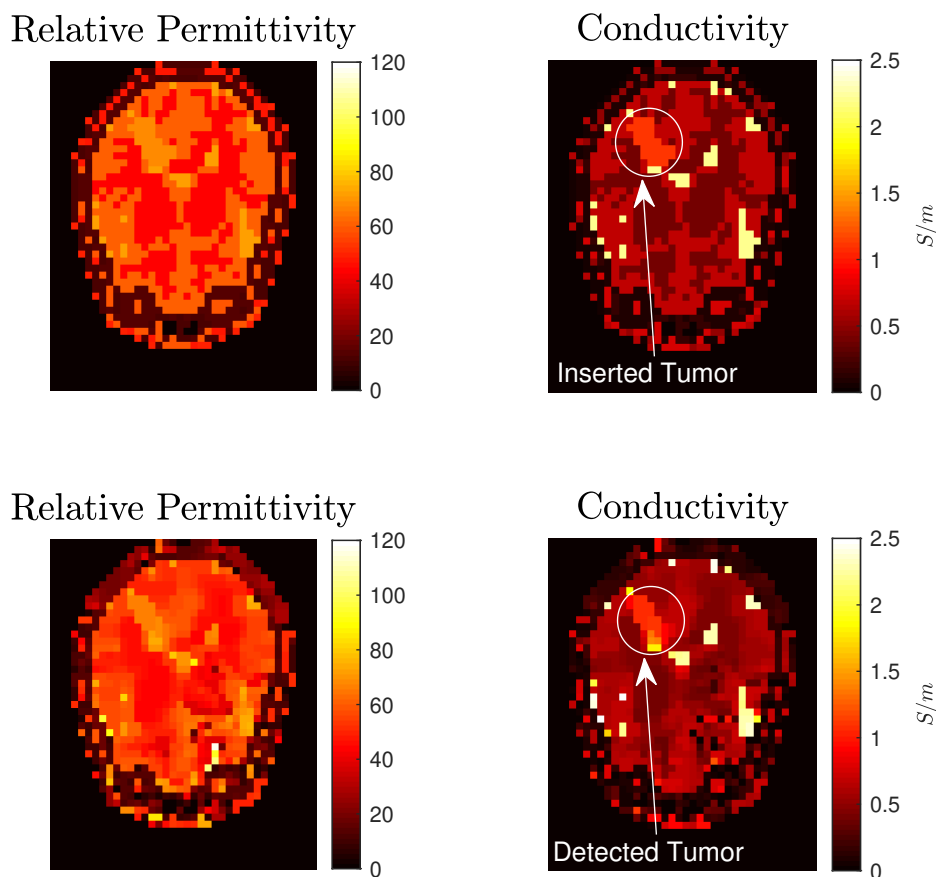


Figure 5.18: Relative permittivity (left) and conductivity (right) maps of “Duke” head model with a numerically inserted tumor. Ground Truth EP (top) and GMT reconstructions (bottom) are compared for the central axial plane of the tumor.

The presence of noise results in blurring between the tumor and its neighboring brain tissue,

therefore it is essential to depict the position of the reconstructed tumor and compare it to the real one. In 5.19 (top), we show a segmentation of the reconstructed and real tumors in their respective 3D position inside the head periphery (we classified values between 0.8 and 1.2 for the conductivity as tumor voxels, for the reconstructed EP). Since the number of voxels is small, we show the values of the reconstructed conductivity of the segmented tumor voxels, instead of an error metric, in the histogram of figure 5.19. The tumor was accurately detected, although outliers in the histogram suggest that its boundaries were blurred by the GMT reconstruction, due to sub-optimal noise regularization. Precisely, we inserted the tumor in the place of a cerebral spinal fluid, which has high conductivity, thus the high values  $\sim 1.4$  appearing in the reconstruction. The smaller values appear in the boundary of the tumor with the white and grey matters of the brain, where GMT mixed the respective EP values and resulted in a mean one between the two. The results will improve with better regularization or additional iterations.

### 5.3 Electrical Properties Reconstruction Using Deep Convolutional Neural Networks

In those mentioned above, it was shown that GMT is a powerful tool for the non-invasive cross-sectional mapping of the electrical property distributions of biological tissue. Its high accuracy, the lack of assumptions, and the novel problem-dedicated coil designs can be used in tandem with experimental measurements to perform in-vivo experiments soon. However, the time footprint of the method is quite large, and the reconstruction of a 5 mm voxel isotropic resolution head model needs days to converge. For finer resolution (clinical resolution: up to 2 mm), the Tucker decomposition can be employed (Chapter 4) in order to exploit the high parallel architecture of modern GPUs, but still, the problem will be slow. A significant speed-up can be achieved if optimal regularization parameters are used, which is still an open problem for GMT and requires additional research. Alternatively, since GMT uses a quasi-Newton method for the Hessian estimation, a better initial guess will be able to reduce the iteration cost for GMT highly.

One can infer a  $T_2$  weighted image from the MR scan and project it to an EP map using the Virtual Family population measurements [17]. One advantage of this approach is the sensitivity to tumors [394], similarly to the electric conductivity. However, there is not a robust one-to-one relationship between the relaxation time parameters and the EP of biological tissue; thus, an initial guess obtained in such a way will lead to inaccuracies that GMT will have to handle in the reconstruction process. In [3], it was shown that the reconstruction of a four-compartment phantom is faster if the initial guess is vacuum instead of the traditionally used mean value, therefore the strategy mentioned above is not the best option. Besides, we proved that the traditional circular polarized mode used to retrieve the MR images is not the best option for the EP reconstruction problem; thus, multiple scans will be required to perform a good  $T_2$  extraction. Alternatively, deep learning [121, 395] approaches have shown extremely great promise in various scientific fields, and one could exploit them in the EP reconstruction as well and train

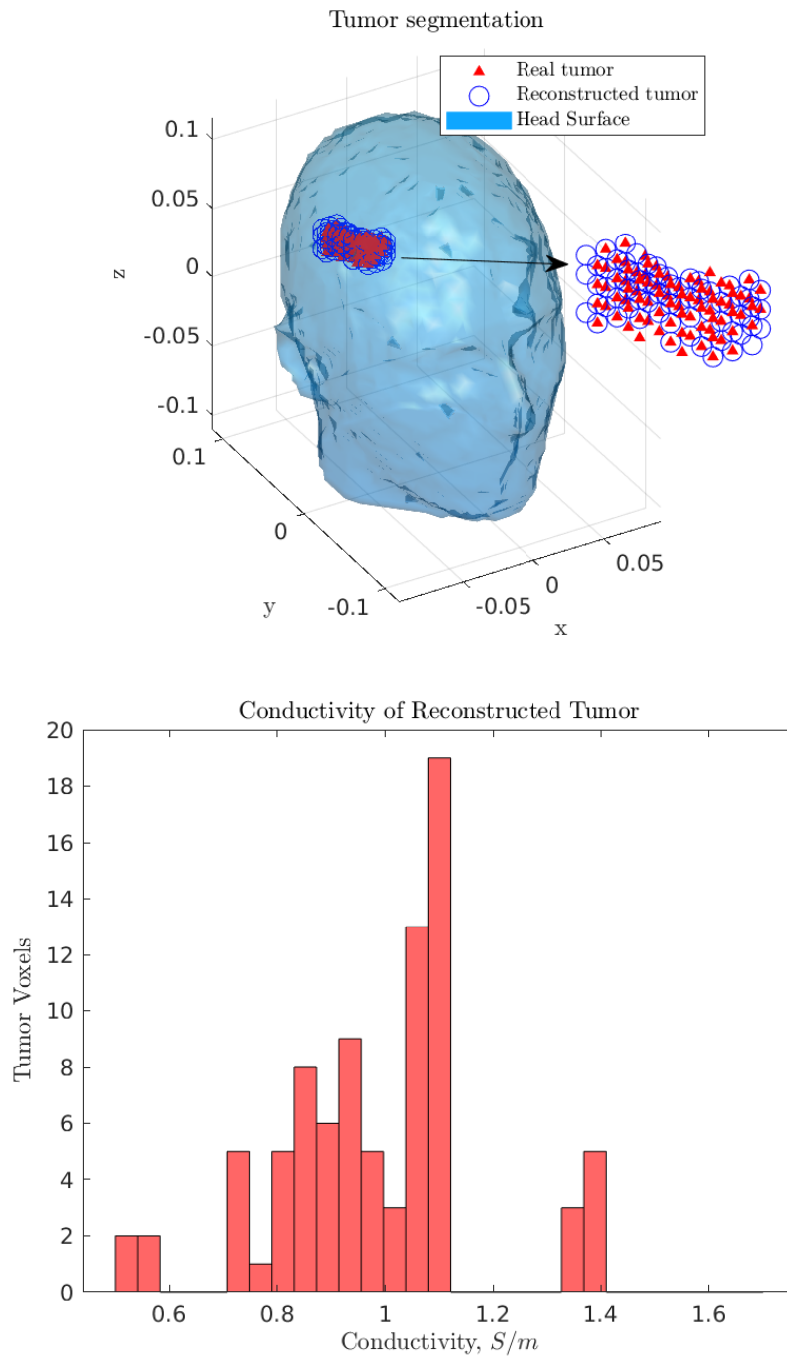


Figure 5.19: The numerically inserted tumor is compared with the tumor segmented from the reconstructed conductivity map (top). The histogram of the reconstructed conductivity for the tumor voxels (bottom), showing that values were clustered around the actual value of 1.1 S/m.

a tensor-to-tensor translation network between measurable MR measurements and EPs. If the network is robust and manages to learn the inverse form of Maxwell's equations for a specific coil excitation, it could be used in tandem with GMT (or replace it) as a generator of an EP map and significantly accelerate the inverse problem.

Deep learning's performance has already been investigated for the EP reconstruction [77].

The authors in [77] trained an image-to-image translation network between one slice of the absolute value of the  $b_1^+$  and the same slice of one electrical property (training of two networks, one for the relative permittivity and one for electric conductivity). This approach seems the right choice as a first attempt, but unfortunately, the 3D nature of Maxwell's equations is lost

Another limitation in the EP reconstruction is the lack of rich datasets. Data for the EP of brain tissue does not exist in abundance in the literature, and it seems that the only realistic source is the Virtual Family population [17]. Of course, a variety of transformations can be applied to the existing head models, but in any case, it is hard to create a suitable dataset that can be used for the excellent training of the network. This impasse highlights the importance of the traditional optimization approaches such as GMT and their need for excellent accuracy. Thus, to surpass it, the right way is to perform multiple in-vivo experiments and use them as training examples in the network.

In this section of the thesis, we aimed to understand if a neural network could be used to learn the inverse form of Maxwell's equations in simple scatterers and investigate some parameter values of the network. The proposed network is feasible because of the highly fast and accurate simulations of higher-order VIE. Specifically, the FFT-JVIE can be exploited as a high-speed data generator using the incident fields produced by one of the coil designs mentioned above. PWL basis functions are used to ensure high accuracy in the resulting  $b_1^+$  measurements for each data-point.

### 5.3.1 Data Generation

The most crucial point in machine learning methods is the acquisition of so-called “good” data. To investigate if a tensor-to-tensor translation network is feasible for our problem, we will use the cylindrical, triangular coil as an excitation model and generate 10900  $b_1^+$  for tissue-mimicking phantoms. All scatterers were enclosed in a cuboid domain (see 5.20 of dimensions  $8.8 \times 8.8 \times 12.8 \text{ cm}^3$  with voxel isotropic resolution of 4 mm. The frequency corresponds to 7 Tesla MR scans, for reasons explained in the previous sections.

The shape and structure of each individual tissue-mimicking phantom varied randomly between a cylinder, a cuboid, or an ellipsoid with random dimensions and different homogeneous tissue-mimicking properties. Inside each scatterer, we inserted randomly 3 to 12 spherical features with arbitrary radiuses and random tissue-mimicking properties (for each feature) to introduce inhomogeneity. Four characteristic data points are shown in 5.21.

For the data generation, we tuned, matched, and decoupled the coil with the optimization procedure described in Chapter 5, while it was loaded with a homogeneous cylinder. Afterward, the incident field patterns were generated only once and used as a right-hand side in the FFT-JVIE solver (we neglected the surface equivalent coil current alternations due to different loads for faster data generation). The scatterer was excited with the “one port at a time” approach, to introduce highly inhomogenous  $b_1^+$  maps. The FFT-JVIE simulation for each data-point, re-

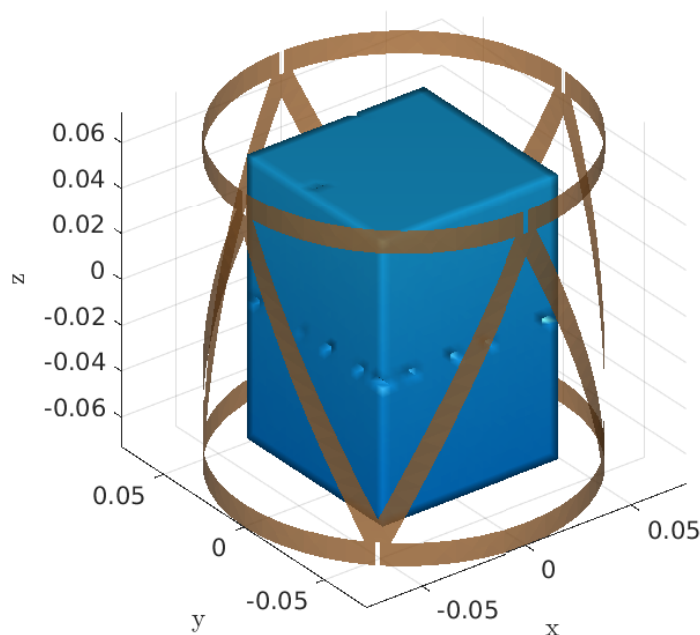


Figure 5.20: Domain of interest that encloses all possible scatterers of choice (homogeneous cylinders, ellipsoids, and cuboids with random dimensions, where 3 to 12 spherical features with different EP were placed in their interior). The scatterers load the 8 channel radiofrequency cylindrical, triangular coil. The working frequency was 297.2 MHz, corresponding to 7 Tesla MRI.

quired at most 30 seconds, for GMRES tolerance of  $10^{-4}$ , to converge. For the previously shown data-points, we illustrate the measurable MR quantities, along with their EP, in figure 5.22. On top, we portray the absolute value of the  $b_1^+$  from each channel of the cylindrical coil. In the middle, we show the relative phase of the  $b_1^+$  between the first channel and the rest seven, while in the bottom of the four subfigures, we portray the EP distributions. All values are masked outside the scatterer for enhanced visualization. All results are shown for a representative axial cut.

### 5.3.2 Convolutional Neural Network

The choice of an optimal neural network is by no means trivial for the EP reconstruction problem. On the one hand, one can train a fully connected network (FCN) [396] to make sure that the global nature of the problem is preserved. On the other hand, convolutional neural networks (CNN) [397, 398], with a specific chosen kernel size, could lead to high accuracy without the need of large datasets required for a FCN's training. However, by looking at 5.22, we cannot observe a one-to-one interaction between the EP and the magnetic field measurements, and the individual features cannot be inferred from the magnetic field, as in an image-to-image translation problem [399]. Thus, the usage of convolution kernels might not work for this problem.

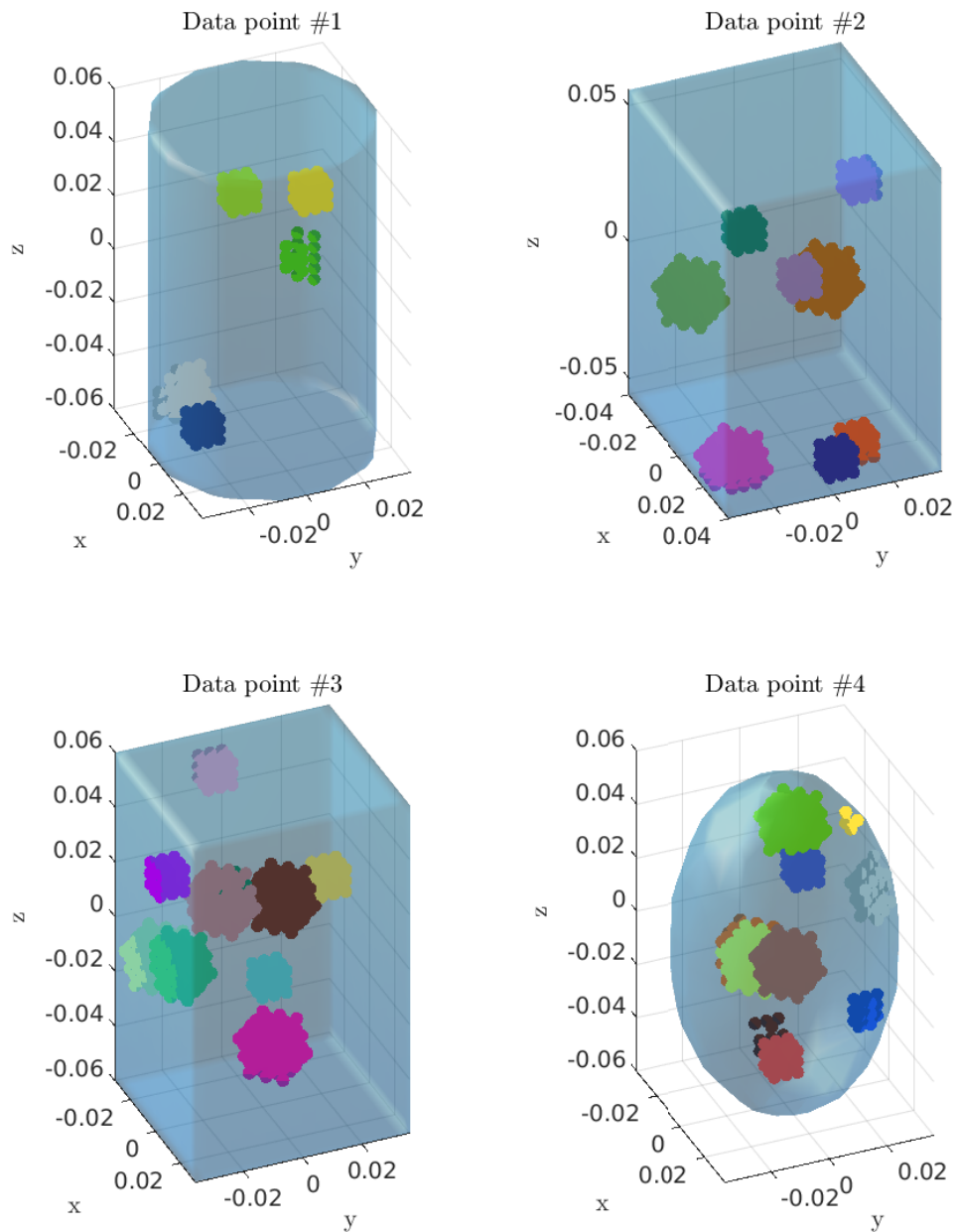


Figure 5.21: Four randomly generated data-point geometries from a 10900 long dataset. Different colors indicate different spherical features. Each individual feature has different tissue-mimicking EPs.

Finally, to determine an exact convolutional kernel size, we have to compute the effect of local  $b_1^+$  perturbations to the EP. However, a closed-form solution does not exist, and only inverse scattering approaches such as GMT can be exploited to provide EP estimations, but the accuracy of these methods is not enough to estimate small local perturbations of the EP (that can be used to calculate the gradient of the EP in respect to  $b_1^+$ ).

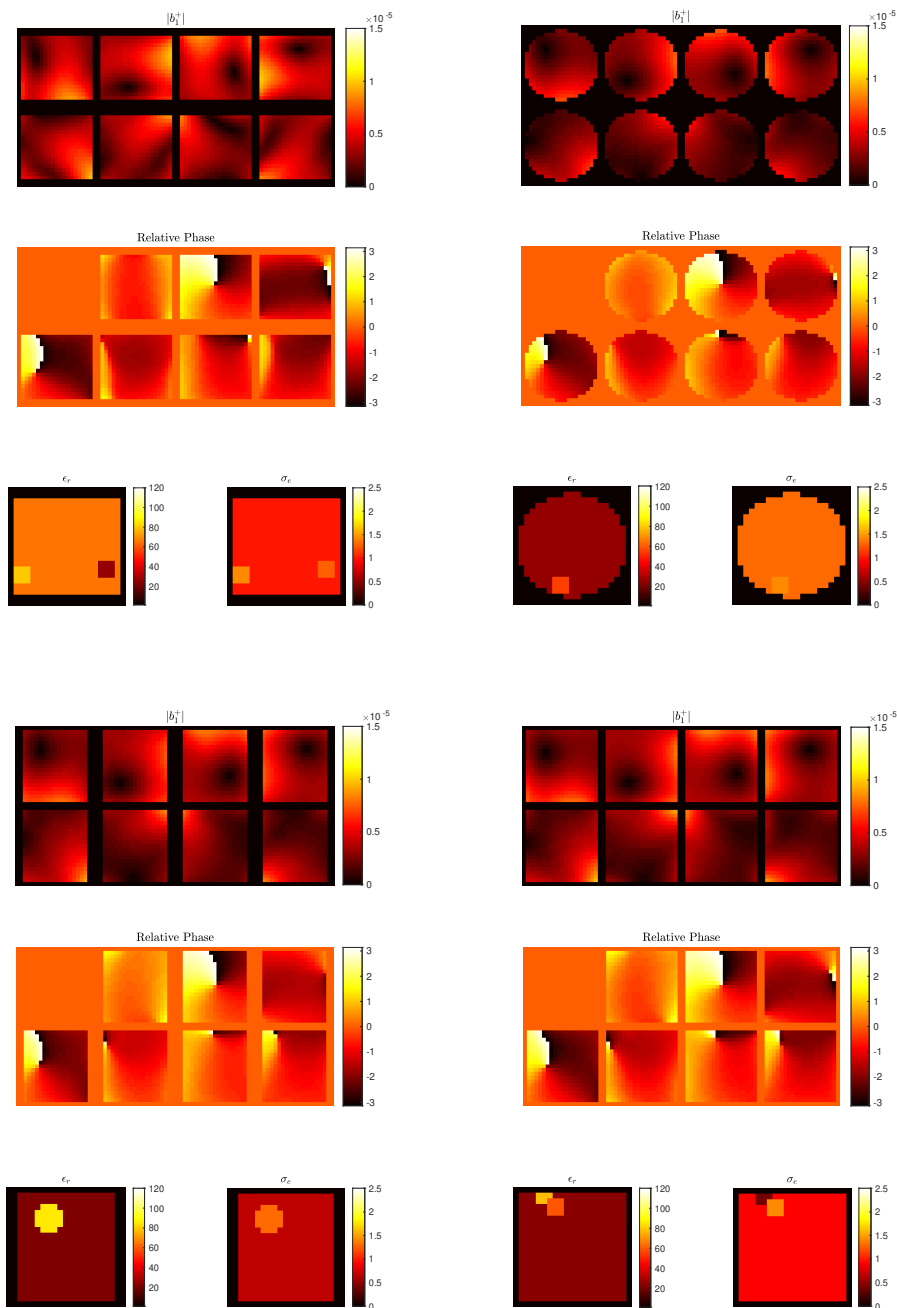


Figure 5.22: Measurable MR quantities and EPs of four characteristic tissue-mimicking phantoms. (top)  $|b_1^+|$  and (middle) relative phase between the first and the remaining seven channels (the orientation of the channels is left to right and top to bottom). (bottom, left) Relative permittivity and (bottom, right) electric conductivity.

#### 5.3.2.1 UNET Architecture

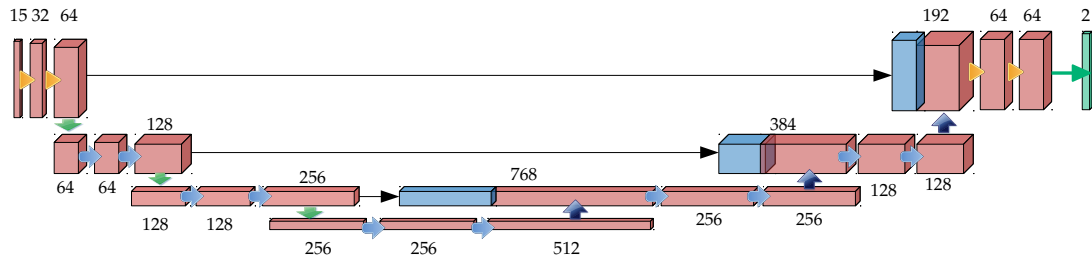
The deep learning field is mature enough, and many architectures have been proposed over the past decade, that can tackle very challenging problems. For example, the UNET was proposed

initially for biomedical imaging segmentation [76] but had thousand other applications in the last five years, especially because it needs a small number of data concerning the number of its training parameters. UNET is not a typical CNN for classification, instead it aims to translate an input of specific dimensions  $x \times x \times \dots$  to an output of dimensions  $y \times y \times \dots$ . The main idea is to follow the input layer of the network with convolutional and max-pooling layers, while at some point shift the max-pooling layers to transpose convolutions (or up-convolutions, or upsampling operators in the literature) to increase the resolution of the output. This architecture is the so-called autoencoder [75]. The UNET differs from autoencoders by concatenating the output of the max-pooling layers to the inputs of the transpose convolution layers. The layers' concatenation enables the network to learn more precise details.

For our problem at hand, we aim to compress the input tensor up to a small dimensional tensor through the max-pooling layers so the network will be able to learn as much as possible information for the relationship between the MR measurements and the EP. The inputs of the network are 3D tensors with 15 channels, where the first 8 are the absolute values of the  $b_1^+$ , and the rest 7 are the relative phases. The output is 2 channel 3D tensor containing the relative permittivity and the electric conductivity. The fact that our problem is 3D, instead of a classic 2D one, does not create any problem since the UNET is easily generalizable to 3D cases [400]. The network is detailed in 5.23, where the size of each layer's channel is shown above the schematics. The choice of a  $3 \times 3 \times 3$  convolutional kernel size is used to account for the strong local interactions between the  $b_1^+$  and the EP. A hidden layer with the same kernel was inserted after the first layer to enlarge this region to  $6 \times 6 \times 6$  voxels. The network consists of an analysis and a synthesis step. In the analysis, after down-sampling with max-pooling, we double the size of the channels, while in the synthesis, we halve them after each transpose convolution.

The network was build in PyTorch [401]. All convolutions had paddings of 1 to be consistent with the dimensionality of the problem, except the last one who had zero paddings. The padding mode was a reflection and was preferred over the zero one. The max-pooling operators had a kernel size of  $2 \times 2 \times 2$  and a stride of 2 to reduce the dimensionality. The transpose convolution had a kernel size of  $2 \times 2 \times 2$  and stride of 2 exactly as the max pooling operations. A dilation of  $2 \times 2 \times 1$ ,  $1 \times 1 \times 1$  and  $2 \times 2 \times 1$  was need for consistency in the dimensions, for the fourth, third and second level of synthesis respectively. The rectified linear unit (ReLU) functions on the analysis were leaky with a slope of 0.2 while in the synthesis were not leaky. Batch normalization (BN) followed the convolution operations in all layers, except the output layer. We cross-validated on various regularization cases, and we observed that dropout with a rate of 0.1, 0.25 and 0.5 applied to the second, third and final level of both analysis and synthesis steps is the most optimal choice to account for overfitting and fast training. For the training process, we used the mean squared error (MSE) between reconstructed and true EP as the cost-function and applied the Adam solver with learning rate 0.0002 and momentum parameters 0.5 and 0.999. The values for most of the parameters above were picked from [399], where a UNET is used as a generator in

### 5.3. Electrical Properties Reconstruction Using Deep Convolutional Neural Networks



Operation	Symbol
Concatenation	→
Max Pooling	↓
Conv. + BN + ReLu	▶
Conv. + BN + Dropout + ReLu	➡
Conv.	➡
Transp. Conv.	⬆

Figure 5.23: 3D UNET. (top) The chosen architecture of the network. The number of channels is shown above each layer. Each operation is followed by appropriate padding and dilation sizes to keep the dimensions consistent. (bottom) The table denotes the operations through the hidden layers of the network.

a conditional generative adversarial network (cGAN) [402] and performs excellently in multiple image-to-image translation problems.

### 5.3.3 Training and Testing

We trained the network on 10000 noise-free data, with a batch size of 4, and tested on the remaining 900. The training loss (defined as the sum of the MSE of all training examples) is shown in 5.24 (left) for 400 epochs. We terminated the training early to avoid overfitting issues. In 5.24 (right), we show the histogram of the MSE for all testing examples and all voxels of the domain. The error is between 0% and 10% for most cases, and in general, it is quite small for the whole testing dataset (there are no arbitrarily large errors).

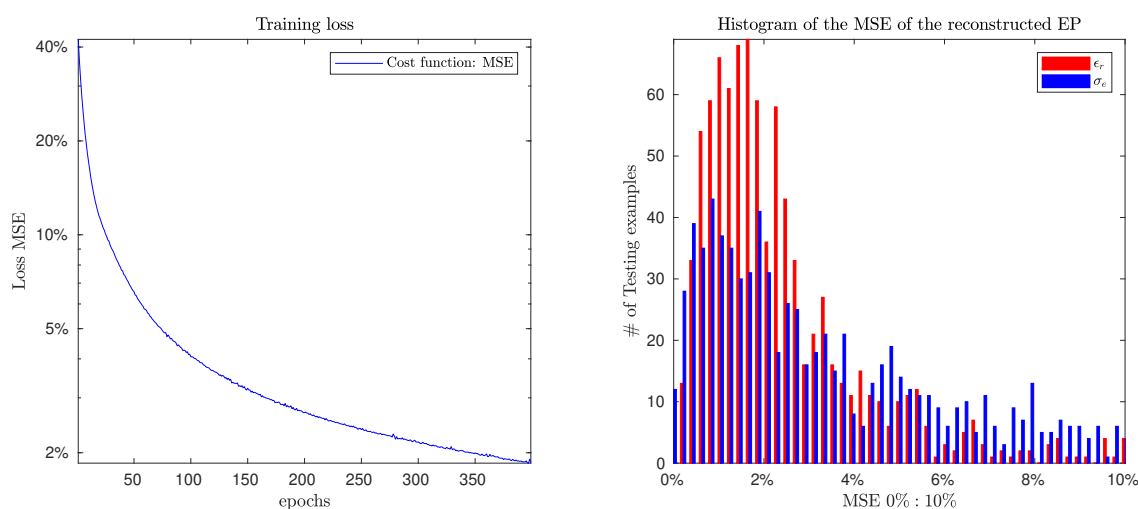


Figure 5.24: (left) Sum of mean squared errors for all training examples. An error close to 2% indicates good training, without overfitting. (right) Histogram of the MSE for both the relative permittivity and the conductivity for all individual 900 testing examples. The error remains small between 0% and 10%.

In 5.25 (top, left), we show the reconstructed EP, for the middle sagittal slice, for two representative, noise-free, testing examples, that did not exist on the training set. The network performs well both for the features position and the EP values. In 5.25 (top, right), we show the performance of the network, after corrupting the  $b_1^+$  of a testing example with Gaussian noise of peak SNR of 200, 150 and 100 respectively. Accurately, the network performs well for high SNR, but for peak values around 100, it treats the noise as different MR measurements, thus attempts to reconstruct a different scatterer than the expected one. We note that the network was developed as an initial reconstruction attempt, and we did not investigate deeply on denoising regularizers. A possible solution to this problem is to train the network both for denoising and reconstruction as in [403]. In 5.25 (bottom), we compare the three steps dropout regularizer with a combination of an  $L_2$  regularizer of weight 0.0001 added on the cost-function and a dropout of rate 0.5 applied only on the fourth step of the network. The effect of the  $L_2$  regularizer smooths the reconstruction as expected, and as a result, some spherical features are not detected. This conclusion is similar for a higher number of training epochs.

## 5.4. Summary

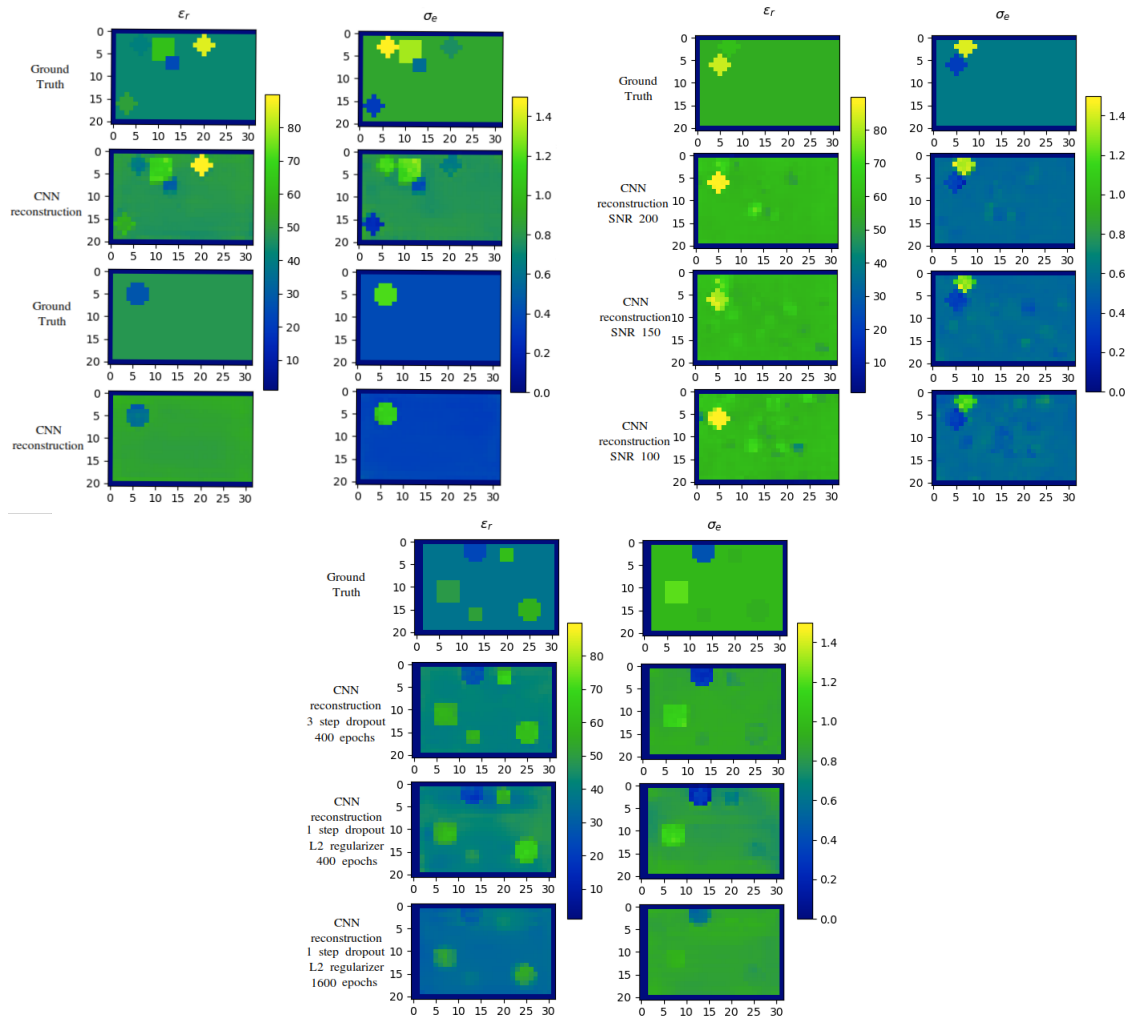


Figure 5.25: EP reconstruction using the proposed convolutional 3D UNET. (top, left) Reconstruction on two testing examples. (top, right) Reconstruction in the presence of additive Gaussian noise to the  $b_1^+$  with peak SNR (second line) 200, (third) 150, and (fourth) 100. (bottom) Reconstruction using different regularizers: (first line) Ground Truth, (second) CNN trained for 400 epochs, using dropout on the second third and fourth step of analysis and synthesis with rate 0.1, 0.25 and 0.5 respectively, (third and fourth) CNN Trained for 400 and 1600 epochs using dropout on the fourth step with rate 0.5 and  $L_2$  regularizer with weight 0.0001.

## 5.4 Summary

In conclusion, we showed that GMT can accurately estimate EP of tissue-mimicking phantom and realistic human head models at 7 Tesla and detect a simulated brain tumor using problem-dedicated 8-channel transmit arrays, that yield inhomogeneous and distinct  $b_1^+$  distributions. The proposed triangular arrays could be used for GMT directly, without RF shimming, by exciting one port at a time with 1 Volt. RF power deposition and transmit field distribution in tissues could be accurately predicted despite estimation errors in EP. Future work will focus on building the designed array, matching its S parameter matrix with the simulation, and, finally,

performing GMT experiments on human subjects.

Furthermore, the proposed UNET can model the relation between the EP and measurable MR measurements for simple tissue-mimicking phantoms and a specific excitation. As a result, this CNN could be used on its own or in tandem with GMT as a fast generator of a reasonable initial guess to reduce the required number of iterations of the optimizer considerably. Finally, one can train a similar network for the forward problem using the EP as the input and an electromagnetic field-related measurement as the output.

This page is intentionally left blank.



# Chapter 6

## CONCLUSION

---

### 6.1 Conclusions and Contributions

THE present work, discusses the EM scattering problems from biological tissue, in a simulated MRI environment. The analysis was based on IE methods, both for the conductive RF coils (SIE) and the inhomogeneous human tissue (VIE). Specifically, the current-based VIE was used for the precise modeling of the interactions between EM waves and tissue, using higher-order polynomial basis functions and the Galerkin projection technique. IE was immediately preferred to other families of methods of computational electromagnetism (FDTD, FEM) since it allows tailoring of fast algorithms for the single-frequency problem of MRI. The application of such an algorithm is one of the main contributions of this thesis.

The necessary background for this effort was provided by the in-depth investigation of the VIE method in the frequency domain, where the basic problems were identified and understood. Specifically, we found that the DVIE is ill-posed for highly inhomogeneous scatterers, while the JVIE, is more robust, but, is not as accurate for clinical MRI resolutions ( $2 \text{ mm}^3$ ) if expanded with PWC basis functions in a Galerkin manner. Nevertheless, JVIE expanded with PWL basis functions is the appropriate choice leading to superior numerical accuracy and stability over other VIE methods and, consequently, to algebraic systems with better numerical behavior. The increase in memory footprint due to the usage of PWL basis functions leads to slower simulations, which, regardless, can be heavily accelerated with GPU programming. Toward this direction, Tucker decomposition methods were employed to dramatically reduce the memory footprint of the discretized Green's function operators (namely  $\mathcal{N}$  and  $\mathcal{K}$ ) from hundreds of GB to dozens of MB. The resulting compressed operators can fit in GPU, and the simulation is an order of magnitude faster in contrast to the one using the traditional method, which is compelled to run in CPU. This acceleration is achievable through the proposed novel matrix-vector product techniques, depending on the tensor decomposition and compression algorithm used, between the tensor of the unknowns and the compressed Green's function tensors. Concretely, if HOSVD or cross-Tucker approximation are employed for a sufficient compression of the Green's function

tensors, the matrix-vector product can be operated fast with an additional small multiplicative constant over the element-wise product complexity, and an additional buffer of memory. This buffer can be discarded if the Tucker+CP decomposition is used, with a small trade-off in the resulting accuracy of the problem. Nevertheless, the utilization of GPU is bounded from the memory of the FFT form of the unknowns' tensors. To tackle this impasse, the FFT can be applied sparsely, thus allowing additional memory compression, if used in tandem with tensor decompositions, which is crucial for clinical resolution simulations, i.e.,  $1 \text{ mm}^3$ . The increase in the operations' complexity is insignificant over the secured speed-up provided by the highly parallelizable structure of GPU. The EM scattering simulation for a realistic human head model, with voxel isotropic resolution of 2 mm, required  $\sim 15'$  with the novel methods in GPU, while the traditional approach was limited to run in CPU for  $\sim 2\text{h } 40'$ . For 1 mm resolutions, the sparse FFT in tandem with HOSVD allows the convergence of the simulation in less than 2 hours, over the  $\sim 12$  hours of the traditional method.

The presented methods of memory footprint reduction can be applied to other FFT-based VIE formulations (electric flux and electric field-based), yielding similar compression factors for the arising Green's function tensors. Finally, the new, accurate and fast simulations can be used to significantly speed-up the inverse EM scattering problem, since they are called thousands of times, in order to retrieve an accurate EP cross-sectional mapping of biological tissue. Until now, costly inverse problems are solved for coarse resolutions, but it is desirable to be able to use clinical resolutions for in-vivo experiments, which requires additional h-refinements of the computational grid. As a result, the proposed methods are veritable workhorses for this application.

The second contribution of the thesis was the design of tailored RF coils for GMT. GMT was introduced recently as an assumption-free EP quantitative reconstruction for brain tissue using measurable MR quantities. First, it was shown that GMT could accurately estimate the EP of a tissue-mimicking four-compartment phantom on a simulated experiment using a realistic RF coil model, in the presence of Gaussian noise of peak SNR of 100, a reasonable assumption at 7 Tesla MRI. The work presented herein showed that for an RF coil array to work well with GMT, it needs to generate distinct  $b_1^+$  maps, which reflect the inhomogeneity of the underlying EP distribution while providing acceptable SNR throughout the volume of the object of interest. Note that this requirement pulls in the opposite direction of traditional coil design, which aims at maximizing  $b_1^+$  homogeneity. If the eight channels of the coil are driven independently and produce eight different excitation patterns, the desired inhomogeneity is achieved. The distinctness of the  $b_1^+$  maps is preserved if the coil is adequately matched, tuned, and decoupled, for which we proposed an optimization algorithm to adjusting the variable capacitors spread across it. This optimization ensures different fields in the interior of the scatterer of interest. The routine employs SIE for the modeling of the RF coil, while the variable lumped elements are treated as short-circuits. The resulting network parameters are optimized using circuit theory by adjust-

ing the variable lumped elements on the scattering parameter matrix until its Frobenius norm reaches a minimum.

For brain EP reconstruction, to fulfill the above requirements, we introduced a new coil design by arranging eight triangularly shaped coils symmetrically around a quasi-elliptical cylindrical (stadium) surface and employing the same tuning-matching-decoupling optimization algorithm. The inhomogeneity of the resulting fields can be quickly evaluated by looking at the condition number of the eight-column matrix containing the fields at every voxel. From the simulations performed, we showed that a condition number around 4 is achievable; thus, almost ideal orthogonality can be ensured. As a result, the mean PNAE over a realistic head model was 7.5% and 4.8% after 500 GMT iterations exciting with one coil element at a time, for the relative permittivity and conductivity, respectively. The error is quite small, given that the  $b_1^+$  maps were corrupted with Gaussian noise of peak SNR equal to 200, and the inverse problem is ill-posed.

A properly tuned, matched, and well-decoupled coil allows logical voltage calibration patterns that can result in even lower condition numbers. Specifically, an SVD-based shimming could bring the condition number to 1, although the effect on the accuracy of GMT was shown to be small, suggesting the near optimality performance of the designed coil. Furthermore, we must note that it could be challenging to apply the “SVD shimming” in actual experiments, since it would require a lengthy pre-scan to obtain the  $b_1^+$  of each coil, while the SVD could result in a wide range of values for the amplitude and phase RF shims at each port, which may be challenging to achieve in practice. Finally, the condition number metric is large if a traditional RF shimming technique is used that leads to homogeneous  $b_1^+$  maps. In this case, the EP reconstruction is less accurate.

Historically, the EP reconstruction is proposed mainly for two reasons: Patient-specific EM field estimations in an UHF MRI environment and brain tumor detection. The reconstruction shown in this thesis, with proper coil optimization, presents a slight degree of blurring in regions with small differences in EP. However, this is not crucial, since the RF field interactions with tissues are profoundly affected by small voxel-by-voxel changes in the EP. Our results show that despite an error  $\leq 7.5\%$  in the EP estimation, the associated  $|b_1^+|$  and absorbed power distributions can be calculated with average errors smaller than 0.5%, for a traditional MRI excitation. The occurred blurring has a more substantial effect on the diagnosis of focal lesions. However, since the EP properties of tumors have shown to be significantly different from the surrounding tissue, GMT could still detect it accurately. Specifically, an arbitrarily shaped brain tumor inserted on a healthy brain model was correctly detected despite sub-optimal regularization. Specifically, for most voxels within the cancer region, the estimated conductivity was sufficiently close to the actual value to discriminate against the lesion from the surrounding tissue correctly. The most significant estimation errors were found at the edges of the tumor, but we expect this would improve by optimizing the regularizer. Such improvement would be even more critical for the goal of characterizing heterogeneous tumor lesions, rather than merely detecting them.

GMT is an optimization problem, and it is costly for an arbitrary initial guess. However, since the optimizer is quasi-Newton, the reconstruction can be massively accelerated by optimizing the choice of the initial guess. For in-vivo applications, one approach could be to segment the principal tissues on a suitable MRI acquisition and pre-assign EP values based on literature. An alternative approach could be based on machine learning. Specifically, the final contribution of this thesis is the investigation of the performance of CNN to infer the EP from measurable MR quantities. The proposed UNET can model the relation between the EP and the  $b_1^+$  for simple tissue-mimicking phantoms and a specific excitation using one of the proposed coil designs. The suggested UNET could be used in tandem with GMT as a fast generator of a reasonable initial guess to reduce the required number of iterations of the optimizer considerably.

## 6.2 Future Research

One of the interests of the presented thesis was focused on the acceleration of the FFT-based VIE simulations using tensor decompositions. Further acceleration can be attained with heavily optimized CUDA code or using single precision, since most GPUs are optimized for it, instead of double. An alternative approach for additional speed-up is the usage of NNs as a tensor-to-tensor translation. The network can be trained in pairs of head model EPs and excitations as inputs and electrical polarisation currents as outputs. The resulting currents will be used as an initial guess for the iterative solver employed in the FFT-based VIE simulations. With this method, a significant number of iterations will be discarded, without yielding any accuracy reduction in the result, since the EM simulator will always be used for (at least) the final iteration.

Particular future research interests are presented for the MR-based EP reconstruction problem. First of all, GMT is mature enough to be used for in-vivo experiments, with the need for modifications in the code. In this work, we used the real EP of the head models to calibrate the current distribution on the coil conductors, which is used to compute the incident fields. This step consists of a VSIE coupling, which was performed before the GMT optimization. This calibration cannot be applied to in-vivo experiments since the EP distribution of the object is unknown. Alternatively, an initial calibration could be performed with a phantom of known EP and used for in-vivo GMT experiments. However, since our proposed coil is close fitting to the head, such an approach could lead to erroneous results, because the current distribution would be sensitive to the different head sizes and EP distributions of the subjects. The most accurate approach would be to update not only the guess of EP (polarisation currents) but also the currents on the coil conductors at every iteration of GMT. That would require performing a VSIE coupling calculation for each GMT iteration, which with the existing EM solver, would be computationally expensive since the coupling matrix between the coil and the body requires a large amount of memory. A novel approach that could avoid this costly step is to project the triangular mesh of the coil onto voxels with the pFFT method, in order to employ the FFT and the proposed tensor decomposition-based techniques to accelerate the matrix-vector products.

This method would remove the computational burden of performing the VSIE coupling step, as shown in [404].

We can further enhance the performance of GMT by reducing the condition number of the  $b_1^+$  maps matrix if the decoupling between coil array elements is improved. Additional decoupling can be achieved by including the inductor pairs and the mutual inductance coefficient in the tuning-matching-decoupling optimization, or by using a more complex circuit at each port. However, both solutions could make the matching between simulated and experimental incident fields, which is critical for GMT accuracy, more challenging. Besides, it is not clear by how much the EP estimation would improve, since the errors we observed in this work could be due to nonoptimal settings of the regularizer, rather than imperfect excitations. As for all inverse problems affected by noise, the performance of the regularizer is important for GMT. Match regularization performs intrinsically well at boundaries with high contrast where it behaves as an  $L_0$  regularizer, but in regions of low contrast, where it behaves as total variation, it can result in blurring. The regularizer's performance could be improved by manually tweaking the three parameters upon which it depends, but the computational cost of running GMT multiple times for different settings have prevented such optimization. A possible alternative that could be explored in future work would involve training a neural network to optimize the regularization term, as was proposed for a different MR-related inverse problem in [385]. Finally, another approach to make the inverse problem more well-posed will be to modify the cost function to include the receive sensitivity information as well as the transmitted fields. It is shown in [372], that the combination of transmitting and receive field information is sufficient to resolve fundamental indeterminacies related to the absolute field phase. Though GMT uses a specific coil model to circumvent the problem of unknown coil phases, the incorporation of additional receive-related information present in MR signals would likely improve the performance of GMT as well. However, the computation time would considerably increase.

In this dissertation, only a minor deep learning application was attempted for the EP reconstruction problem. Therefore, there is still a wide variety of techniques and methods to investigate on. First of all, the robustness of the network needs to be studied, and if proven untrustworthy, other networks should be studied, like a cGAN. Specifically, since IE software, like MARIE, can be extremely fast for EM simulations in the MRI environment, one could use them instead of one of the networks in a cGAN. MARIE could act like the discriminator (or the generator) of a cGAN, while the generator (or the discriminator) will be the trainable network. In such a way, MARIE would force additional constraints in the network, driving it for the learning of the inverse form of Maxwell's equations instead of image similarities. Furthermore, in future work, the performance of the network in the presence of noise should be thoroughly studied. In the last years, machine learning has shown exceptional performance for denoising; thus, it will be useful to combine this capability with a reconstruction architecture. Moreover, machine learning is only as good as its training dataset. Therefore, the data generation for heterogeneous

head models is one of the main concerns in future research. Specifically, only a small number of realistic data is available; as a result, either GMT has to be employed accurately for in-vivo experiments, or a generalization technique of the existing dataset should be found, i.e., creating a basis. Finally, in [405] NNs are employed for topology optimization. Specifically, the input of the network is the guess of the optimizer after a small number of iterations along with the value of the gradient of the cost-function at this iteration, and the output is the ground truth solution. This idea seems promising for application in inverse problems, such as the EP reconstruction. The network aims to learn the behavior of the optimizer itself and not the highly non-linear inverse form of Maxwell's equations.

From the results presented in this thesis, it is evident that the superior performance of GMT in the EP reconstruction of an object is achieved when the RF coil is tuned, matched, and decoupled when loaded with the same object. Regrettably, the traditional RF coil tuning is implemented once, for an arbitrary phantom, and it is not changed again in ensuing scans. For future clinical applications of GMT, it would be ideal to perform patient-specific tuning; thus achieving optimal EP reconstructions. It makes sense to investigate automated tuning-matching-decoupling processes, while the coil is loaded with the patient, i.e., [406]. An automatic tuning-matching-decoupling is indeed a very challenging problem since traditionally, the adjustment of variable capacitor values is made with a screwdriver by an RF coil scientist, which is a generally slow method. In future research, it might be worthwhile to investigate an automatic control system, placed inside the scanner, that can adjust the capacitor values of the coil to reduce the scattering parameter values of the coil-network as much as possible. A bolder proposal is to discard the lumped elements and the conductors completely and instead build the next-generation MRI coils with a different material, and the capability of motion, for each channel on a substrate, to ensure optimal performance.

This page is intentionally left blank.



# References

---

- [1] **Giannakopoulos, Ilias I**, M. S. Litsarev, and A. G. Polimeridis, “Memory footprint reduction for the FFT-based volume integral equation method via tensor decompositions,” *IEEE Transactions on Antennas and Propagation*, vol. 67, no. 12, pp. 7476–7486, 2019.
- [2] **Giannakopoulos, Ilias**, J. E. Serrallés, L. Daniel *et al.*, “Magnetic-resonance-based electrical property mapping using global maxwell tomography with an 8-channel head coil at 7 tesla: a simulation study,” *IEEE Transactions on Biomedical Engineering*, 2020.
- [3] J. E. Serralles, **Giannakopoulos, Ilias**, B. Zhang *et al.*, “Noninvasive estimation of electrical properties from magnetic resonance measurements via Global Maxwell Tomography and match regularization,” *IEEE Transactions on Biomedical Engineering*, vol. 67, no. 1, pp. 3–15, 2019.
- [4] I. P. Georgakis, **Giannakopoulos, Ilias I**, M. S. Litsarev, and A. G. Polimeridis, “A fast volume integral equation solver with linear basis functions for the accurate computation of electromagnetic fields in MRI,” *arXiv preprint arXiv:1902.02196*, under review in *IEEE Transactions on Antennas and Propagation*, 2019.
- [5] **Giannakopoulos, Ilias I**, M. S. Litsarev, and A. G. Polimeridis, “3D cross-Tucker approximation in FFT-based volume integral equation methods,” in *2018 IEEE International Symposium on Antennas and Propagation & USNC/URSI National Radio Science Meeting*. IEEE, 2018, pp. 2507–2508.
- [6] **Giannakopoulos, Ilias I**, J. E. Serralles, B. Zhange *et al.*, “Electrical properties mapping in a tissue-mimicking phantom using Global Maxwell Tomography with a realistic coil model at 7 Tesla,” in *2nd International Workshop on MR-based Electrical Properties Tomography*. IMEP, 2019, pp. 82–83.
- [7] **Giannakopoulos, Ilias I**, J. E. Serrallés, B. Zhang *et al.*, “Global Maxwell Tomography using an 8-channel radiofrequency coil: simulation results for a tissue-mimicking phantom at 7T,” in *2019 IEEE International Symposium on Antennas and Propagation and USNC-URSI Radio Science Meeting*. IEEE, 2019, pp. 823–824.

- [8] Giannakopoulos, Ilias I, J. E. Serrallés, G. Guryev *et al.*, “On the usage of deep neural networks as a tensor-to-tensor translation between MR measurements and electrical properties,” in *Proc. ISMRM*, 2020, p. 3193.
- [9] P. C. Lauterbur, “Image formation by induced local interactions: examples employing nuclear magnetic resonance,” *Nature*, 1973.
- [10] F. Bloch, “Nuclear induction,” *Physical review*, vol. 70, no. 7-8, p. 460, 1946.
- [11] E. M. Purcell, H. C. Torrey, and R. V. Pound, “Resonance absorption by nuclear magnetic moments in a solid,” *Physical review*, vol. 69, no. 1-2, p. 37, 1946.
- [12] SIEMENS Healthineers, (2017, August 22), [Press release], “With 7 Tesla scanner Magnetom Terra, Siemens Healthineers introduces new clinical field strength in MR imaging.”
- [13] R. Lattanzi, D. K. Sodickson, A. K. Grant, and Y. Zhu, “Electrodynamic constraints on homogeneity and radiofrequency power deposition in multiple coil excitations,” *Magnetic resonance in medicine*, vol. 61, no. 2, pp. 315–334, 2009.
- [14] J. Jin and J. Chen, “On the SAR and field inhomogeneity of birdcage coils loaded with the human head,” *Magnetic resonance in medicine*, vol. 38, no. 6, pp. 953–963, 1997.
- [15] X. Zhang, J. Liu, S. Schmitter, P.-F. Van de Moortele, and B. He, “Predicting temperature increase through local SAR estimation by B1 mapping: A phantom validation at 7T,” in *Engineering in Medicine and Biology Society (EMBC), 2014 36th Annual International Conference of the IEEE*. IEEE, 2014, pp. 1107–1110.
- [16] M. Cosottini, D. Frosini, L. Biagi *et al.*, “Short-term side-effects of brain MR examination at 7 T: a single-centre experience,” *European radiology*, vol. 24, no. 8, pp. 1923–1928, 2014.
- [17] A. Christ, W. Kainz, E. G. Hahn *et al.*, “The Virtual Family—development of surface-based anatomical models of two adults and two children for dosimetric simulations,” *Physics in Medicine & Biology*, vol. 55, no. 2, p. N23, 2009.
- [18] L. Alon, C. M. Deniz, G. Carluccio *et al.*, “Effects of anatomical differences on electromagnetic fields, SAR, and temperature change,” *Concepts in Magnetic Resonance Part B: Magnetic Resonance Engineering*, vol. 46, no. 1, pp. 8–18, 2016.
- [19] J. C. Maxwell, “VIII. A dynamical theory of the electromagnetic field,” *Philosophical transactions of the Royal Society of London*, no. 155, pp. 459–512, 1865.
- [20] W. C. Chew, E. Michielssen, J. Song, and J.-M. Jin, *Fast and efficient algorithms in computational electromagnetics*. Artech House, Inc., 2001.

- [21] T. Rylander, P. Ingelström, and A. Bondeson, *Computational electromagnetics*. Springer Science & Business Media, 2012.
- [22] J. S. A. G. Polimeridis, J. F. Villena, “Marie - magnetic resonance integral equation suite, available online,” URL <https://github.com/thanospol/MARIE> Available online, 2015.
- [23] J. F. Villena, A. G. Polimeridis, Y. Eryaman *et al.*, “Fast electromagnetic analysis of MRI transmit RF coils based on accelerated integral equation methods,” *IEEE Transactions on Biomedical Engineering*, vol. 63, no. 11, pp. 2250–2261, 2016.
- [24] A. G. Polimeridis, J. F. Villena, L. Daniel, and J. K. White, “Stable FFT-JVIE solvers for fast analysis of highly inhomogeneous dielectric objects,” *Journal of Computational Physics*, vol. 269, pp. 280–296, 2014.
- [25] A. Orlandi, “Advanced engineering electromagnetics (balanis, ca; 2012)[book review],” *IEEE Electromagnetic Compatibility Magazine*, vol. 4, no. 4, pp. 47–47, 2012.
- [26] R. F. Harrington, “Field computation by method of moments,” *NY Mc Millan*, 1968.
- [27] A. G. Polimeridis, “DEMCEM: a Matlab/C++ package for the computation of singular integrals arising in Galerkin EM SIE formulations,” [pdf] Available at: [http://web.mit.edu/thanos\\_p/www/ReadMe\\_DEMCEM.pdf](http://web.mit.edu/thanos_p/www/ReadMe_DEMCEM.pdf), 2016.
- [28] A. G. Polimeridis, F. Vipiana, J. R. Mosig, and D. R. Wilton, “DIRECTFN: Fully numerical algorithms for high precision computation of singular integrals in galerkin SIE methods,” *IEEE Transactions on Antennas and Propagation*, vol. 61, no. 6, pp. 3112–3122, 2013.
- [29] L. Greengard and V. Rokhlin, “On the efficient implementation of the fast multipole method,” Technical Report YALEU/DCS/RR-602, Dept. of Computer Science, Yale Univ., New Haven, CT, Tech. Rep., 1988.
- [30] V. Rokhlin, “Rapid solution of integral equations of scattering theory in two dimensions,” *Journal of Computational Physics*, vol. 86, no. 2, pp. 414–439, 1990.
- [31] C.-C. Lu and W. C. Chew, “A multilevel algorithm for solving a boundary integral equation of wave scattering,” *Microwave and Optical Technology Letters*, vol. 7, no. 10, pp. 466–470, 1994.
- [32] J. Song, C.-C. Lu, and W. C. Chew, “Multilevel fast multipole algorithm for electromagnetic scattering by large complex objects,” *IEEE Transactions on Antennas and Propagation*, vol. 45, no. 10, pp. 1488–1493, 1997.
- [33] B. Dembart and E. Yip, “A 3D fast multipole method for electromagnetics with multiple levels,” in *11th Annual Review of Progress in Applied Computational Electromagnetics*, vol. 1, 1995, pp. 621–628.

- [34] J. Song and W. C. Chew, "Large scale computations using FISC," in *IEEE Antennas and Propagation Society International Symposium. Transmitting Waves of Progress to the Next Millennium. 2000 Digest. Held in conjunction with: USNC/URSI National Radio Science Meeting (C)*, vol. 4. IEEE, 2000, pp. 1856–1859.
- [35] A. A. Ergin, B. Shanker, and E. Michielssen, "The plane-wave time-domain algorithm for the fast analysis of transient wave phenomena," *IEEE Antennas and Propagation Magazine*, vol. 41, no. 4, pp. 39–52, 1999.
- [36] C. Brennan and P. J. Cullen, "Tabulated interaction method for UHF terrain propagation problems," *IEEE Transactions on Antennas and Propagation*, vol. 46, no. 5, pp. 738–739, 1998.
- [37] C. Brennan and P. J. Cullen, "Application of the fast far-field approximation to the computation of UHF pathloss over irregular terrain," *IEEE Transactions on Antennas and Propagation*, vol. 46, no. 6, pp. 881–890, 1998.
- [38] F. X. Canning, "Transformations that produce a sparse moment method matrix," *Journal of Electromagnetic Waves and Applications*, vol. 4, no. 9, pp. 893–913, 1990.
- [39] E. Michielssen and A. Boag, "Multilevel evaluation of electromagnetic fields for the rapid solution of scattering problems," *Microwave and Optical Technology Letters*, vol. 7, no. 17, pp. 790–795, 1994.
- [40] S. Jaffard, "Wavelet methods for fast resolution of elliptic problems," *SIAM Journal on Numerical Analysis*, vol. 29, no. 4, pp. 965–986, 1992.
- [41] B. Alpert, G. Beylkin, R. Coifman, and V. Rokhlin, "Wavelet-like bases for the fast solution of second-kind integral equations," *SIAM Journal on Scientific Computing*, vol. 14, no. 1, pp. 159–184, 1993.
- [42] H. Kim and H. Ling, "On the application of fast wavelet transform to the integral-equation solution of electromagnetic scattering problems," *Microwave and Optical Technology Letters*, vol. 6, no. 3, pp. 168–173, 1993.
- [43] B. Z. Steinberg and Y. Leviatan, "On the use of wavelet expansions in the method of moments (em scattering)," *IEEE Transactions on Antennas and Propagation*, vol. 41, no. 5, pp. 610–619, 1993.
- [44] R. L. Wagner, G. P. Otto, and W. C. Chew, "Fast waveguide mode computation using wavelet-like basis functions," *IEEE microwave and guided wave letters*, vol. 3, no. 7, pp. 208–210, 1993.

- [45] K. Sabetfakhri and L. P. Katehi, "Analysis of integrated millimeter-wave and submillimeter-wave waveguides using orthonormal wavelet expansions," *IEEE transactions on microwave theory and techniques*, vol. 42, no. 12, pp. 2412–2422, 1994.
- [46] G. Wang, G. Pan, and B. Gilbert, "A hybrid wavelet expansion and boundary element analysis for multiconductor transmission lines in multilayered dielectric media," *IEEE transactions on microwave theory and techniques*, vol. 43, no. 3, pp. 664–675, 1995.
- [47] R. L. Wagner and W. C. Chew, "A study of wavelets for the solution of electromagnetic integral equations," *IEEE Transactions on Antennas and Propagation*, vol. 43, no. 8, pp. 802–810, 1995.
- [48] W. L. Golik, "Sparsity and conditioning of impedance matrices obtained with semi-orthogonal and bi-orthogonal wavelet bases," *IEEE Transactions on Antennas and Propagation*, vol. 48, no. 4, pp. 473–481, 2000.
- [49] H. Deng and H. Ling, "On a class of predefined wavelet packet bases for efficient representation of electromagnetic integral equations," *IEEE Transactions on Antennas and Propagation*, vol. 47, no. 12, pp. 1772–1779, 1999.
- [50] M. Frigo and S. G. Johnson, "The design and implementation of FFTW3," *Proceedings of the IEEE*, vol. 93, no. 2, pp. 216–231, 2005.
- [51] J. R. Phillips and J. K. White, "A precorrected-FFT method for electrostatic analysis of complicated 3-D structures," *IEEE Transactions on Computer-Aided Design of Integrated Circuits and Systems*, vol. 16, no. 10, pp. 1059–1072, 1997.
- [52] D. Borup and O. Gandhi, "Fast-Fourier-transform method for calculation of SAR distributions in finely discretized inhomogeneous models of biological bodies," *IEEE transactions on microwave theory and techniques*, vol. 32, no. 4, pp. 355–360, 1984.
- [53] P. Zwamborn and P. M. Van Den Berg, "The three dimensional weak form of the conjugate gradient FFT method for solving scattering problems," *IEEE Transactions on Microwave Theory and Techniques*, vol. 40, no. 9, pp. 1757–1766, 1992.
- [54] M. F. Catedra, E. Gago, and L. Nuno, "A numerical scheme to obtain the RCS of three-dimensional bodies of resonant size using the conjugate gradient method and the fast Fourier transform," *IEEE transactions on antennas and propagation*, vol. 37, no. 5, pp. 528–537, 1989.
- [55] C. Y. Shen, K. J. Glover, M. I. Sancer, and A. D. Varvatsis, "The discrete Fourier transform method of solving differential-integral equations in scattering theory," *IEEE Transactions On Antennas and Propagation*, vol. 37, no. 8, pp. 1032–1041, 1989.

- [56] E. Bleszynski, M. Bleszynski, and T. Jaroszewicz, "AIM: Adaptive integral method for solving large-scale electromagnetic scattering and radiation problems," *Radio Science*, vol. 31, no. 5, pp. 1225–1251, 1996.
- [57] H. Gan and W. C. Chew, "A discrete BCG-FFT algorithm for solving 3D inhomogeneous scatterer problems," *Journal of Electromagnetic Waves and Applications*, vol. 9, no. 10, pp. 1339–1357, 1995.
- [58] K. Lumme and J. Rahola, "Light scattering by porous dust particles in the discrete-dipole approximation," *The Astrophysical Journal*, vol. 425, pp. 653–667, 1994.
- [59] C. H. Chan, C. M. Lin, L. Tsang, and Y. F. Leung, "A sparse-matrix/canonical grid method for analyzing microstrip structures," *IEICE transactions on electronics*, vol. 80, no. 11, pp. 1354–1359, 1997.
- [60] W. C. Chew, J. Lin, and X. Yang, "An FFT T-matrix method for 3D microwave scattering solutions from random discrete scatterers," *Microwave and Optical Technology Letters*, vol. 9, no. 4, pp. 194–196, 1995.
- [61] J. Lin and W. C. Chew, "BiCG-FFT T-matrix method for solving for the scattering solution from inhomogeneous bodies," *IEEE transactions on microwave theory and techniques*, vol. 44, no. 7, pp. 1150–1155, 1996.
- [62] J. Mallorqui and M. Rodriguez, "GRATMA method for biomedical applications: Comparison with the CGM-FFT," in *IEEE Antennas and Propagation Society International Symposium. 1995 Digest*, vol. 3. IEEE, 1995, pp. 1581–1584.
- [63] C. Wang and J. Jin, "Simple and efficient computation of electromagnetic fields in arbitrarily shaped inhomogeneous dielectric bodies using transpose-free QMR and FFT," *IEEE transactions on microwave theory and techniques*, vol. 46, no. 5, pp. 553–558, 1998.
- [64] F. Ling, D. Jiao, and J.-M. Jin, "Efficient electromagnetic modeling of microstrip structures in multilayer media," *IEEE Transactions on Microwave Theory and Techniques*, vol. 47, no. 9, pp. 1810–1818, 1999.
- [65] S. S. Bindiganavale, J. L. Volakis, and H. Anastassiou, "Scattering from planar structures containing small features using the adaptive integral method (AIM)," *IEEE Transactions on Antennas and Propagation*, vol. 46, no. 12, pp. 1867–1878, 1998.
- [66] T. F. Chan and J. A. Olkin, "Circulant preconditioners for Toeplitz-block matrices," *Numerical Algorithms*, vol. 6, no. 1, pp. 89–101, 1994.
- [67] S. P. Groth, A. G. Polimeridis, and J. K. White, "Accelerating the discrete dipole approximation via circulant preconditioning," *Journal of Quantitative Spectroscopy and Radiative Transfer*, vol. 240, p. 106689, 2020.

- [68] A. G. Polimeridis and J. K. White, “On the compression of system tensors arising in FFT-VIE solvers,” in *Antennas and Propagation Society International Symposium (APSURSI), 2014 IEEE*. IEEE, 2014, pp. 2144–2145.
- [69] A. C. Yücel, L. J. Gomez, and E. Michielssen, “Compression of translation operator tensors in FMM-FFT-accelerated SIE solvers via Tucker decomposition,” *IEEE Antennas and Wireless Propagation Letters*, vol. 16, pp. 2667–2670, 2017.
- [70] C. Qian, Z. Chen, and A. C. Yucel, “Tensor decompositions for reducing the memory requirement of translation operator tensors in fmm-fft accelerated ie solvers,” in *2019 International Applied Computational Electromagnetics Society Symposium (ACES)*. IEEE, 2019, pp. 1–2.
- [71] J. M. Taboada, M. G. Araujo, J. M. Bertolo *et al.*, “MLFMA-FFT parallel algorithm for the solution of large-scale problems in electromagnetics,” *Progress In Electromagnetics Research*, vol. 105, pp. 15–30, 2010.
- [72] Z. Chen, S. Zheng, and V. Okhmatovski, “Tensor train acceleration of method of moments solution of volume integral equation on structured and unstructured meshes,” in *2019 International Conference on Electromagnetics in Advanced Applications (ICEAA)*. IEEE, 2019, pp. 1321–1321.
- [73] Z. Chen, S. Zheng, and V. I. Okhmatovski, “Tensor train accelerated solution of volume integral equation for 2-D scattering problems and magneto-quasi-static characterization of multiconductor transmission lines,” *IEEE Transactions on Microwave Theory and Techniques*, vol. 67, no. 6, pp. 2181–2196, 2019.
- [74] I. Oseledets and E. Tyrtyshnikov, “TT-cross approximation for multidimensional arrays,” *Linear Algebra and its Applications*, vol. 432, no. 1, pp. 70–88, 2010.
- [75] P. Vincent, H. Larochelle, Y. Bengio, and P.-A. Manzagol, “Extracting and composing robust features with denoising autoencoders,” in *Proceedings of the 25th international conference on Machine learning*. ACM, 2008, pp. 1096–1103.
- [76] O. Ronneberger, P. Fischer, and T. Brox, “U-net: Convolutional networks for biomedical image segmentation,” in *International Conference on Medical image computing and computer-assisted intervention*. Springer, 2015, pp. 234–241.
- [77] S. Mandija, E. F. Meliadó, N. R. Huttinga, P. R. Luijten, and C. A. van den Berg, “Opening a new window on MR-based Electrical Properties Tomography with deep learning,” *Scientific Reports*, vol. 9, no. 1, p. 8895, 2019.
- [78] A. P. O’Rourke, M. Lazebnik, J. M. Bertram *et al.*, “Dielectric properties of human normal, malignant and cirrhotic liver tissue: in vivo and ex vivo measurements from 0.5 to 20 GHz

- using a precision open-ended coaxial probe,” *Physics in Medicine & Biology*, vol. 52, no. 15, p. 4707, 2007.
- [79] A. J. Surowiec, S. S. Stuchly, J. R. Barr, and A. Swarup, “Dielectric properties of breast carcinoma and the surrounding tissues,” *IEEE Transactions on Biomedical Engineering*, vol. 35, no. 4, pp. 257–263, 1988.
- [80] Y. Lu, B. Li, J. Xu, and J. Yu, “Dielectric properties of human glioma and surrounding tissue,” *International journal of hyperthermia*, vol. 8, no. 6, pp. 755–760, 1992.
- [81] B. Kos, A. Zupanic, T. Kotnik *et al.*, “Robustness of treatment planning for electrochemotherapy of deep-seated tumors,” *The Journal of membrane biology*, vol. 236, no. 1, pp. 147–153, 2010.
- [82] M. Cemazar, Y. Tamzali, G. Sersa *et al.*, “Electrochemotherapy in veterinary oncology,” *Journal of veterinary internal medicine*, vol. 22, no. 4, pp. 826–831, 2008.
- [83] F. K. Storm, D. L. Morton, L. R. Kaiser *et al.*, “Clinical radiofrequency hyperthermia: a review,” *National Cancer Institute monograph*, vol. 61, pp. 343–350, 1982.
- [84] M. De Greef, H. Kok, D. Correia *et al.*, “Uncertainty in hyperthermia treatment planning: the need for robust system design,” *Physics in Medicine & Biology*, vol. 56, no. 11, p. 3233, 2011.
- [85] P. Metherall, D. Barber, R. Smallwood, and B. Brown, “Three-dimensional electrical impedance tomography,” *Nature*, vol. 380, no. 6574, p. 509, 1996.
- [86] J. L. Mueller, D. Isaacson, and J. C. Newell, “A reconstruction algorithm for electrical impedance tomography data collected on rectangular electrode arrays,” *IEEE Transactions on Biomedical Engineering*, vol. 46, no. 11, pp. 1379–1386, 1999.
- [87] B. Harrach and M. N. Minh, “Enhancing residual-based techniques with shape reconstruction features in electrical impedance tomography,” *Inverse Problems*, vol. 32, no. 12, p. 125002, 2016.
- [88] A. Hauptmann, M. Santacesaria, and S. Siltanen, “Direct inversion from partial-boundary data in electrical impedance tomography,” *Inverse Problems*, vol. 33, no. 2, p. 025009, 2017.
- [89] H. Garde and K. Knudsen, “Distinguishability revisited: depth dependent bounds on reconstruction quality in electrical impedance tomography,” *SIAM Journal on Applied Mathematics*, vol. 77, no. 2, pp. 697–720, 2017.
- [90] Y. Zou and Z. Guo, “A review of electrical impedance techniques for breast cancer detection,” *Medical engineering & physics*, vol. 25, no. 2, pp. 79–90, 2003.

- [91] H.-Y. Wei and M. Soleimani, “Electromagnetic tomography for medical and industrial applications: Challenges and opportunities [point of view],” *Proceedings of the IEEE*, vol. 101, no. 3, pp. 559–565, 2013.
- [92] H.-Y. Wei and M. Soleimani, “Hardware and software design for a National Instrument-based magnetic induction tomography system for prospective biomedical applications,” *Physiological Measurement*, vol. 33, no. 5, p. 863, 2012.
- [93] S. H. Oh, B. I. Lee, E. J. Woo *et al.*, “Electrical conductivity images of biological tissue phantoms in MREIT,” *Physiological Measurement*, vol. 26, no. 2, p. S279, 2005.
- [94] J. K. Seo and E. J. Woo, “Magnetic resonance electrical impedance tomography (MREIT),” *SIAM review*, vol. 53, no. 1, pp. 40–68, 2011.
- [95] E. J. Woo and J. K. Seo, “Magnetic resonance electrical impedance tomography (MREIT) for high-resolution conductivity imaging,” *Physiological measurement*, vol. 29, no. 10, p. R1, 2008.
- [96] H. J. Kim, Y. T. Kim, A. S. Minhas *et al.*, “In vivo high-resolution conductivity imaging of the human leg using MREIT: the first human experiment,” *IEEE transactions on medical imaging*, vol. 28, no. 11, pp. 1681–1687, 2009.
- [97] Y. Xu and B. He, “Magnetoacoustic tomography with magnetic induction (MAT-MI),” *Physics in Medicine & Biology*, vol. 50, no. 21, p. 5175, 2005.
- [98] X. Li, K. Yu, and B. He, “Magnetoacoustic tomography with magnetic induction (MAT-MI) for imaging electrical conductivity of biological tissue: a tutorial review,” *Physics in Medicine & Biology*, vol. 61, no. 18, p. R249, 2016.
- [99] H. Wen, J. Shah, and R. S. Balaban, “Hall effect imaging,” *IEEE transactions on biomedical engineering*, vol. 45, no. 1, pp. 119–124, 1998.
- [100] E. H. Hall, “On a new action of the magnet on electric currents,” *American Journal of Mathematics*, vol. 2, no. 3, pp. 287–292, 1879.
- [101] H. Wen and E. Bennett, “The feasibility of Hall effect imaging in humans,” in *2000 IEEE Ultrasonics Symposium. Proceedings. An International Symposium (Cat. No. 00CH37121)*, vol. 2. IEEE, 2000, pp. 1619–1622.
- [102] E. J. Bond, X. Li, S. C. Hagness, and B. D. Van Veen, “Microwave imaging via space-time beamforming for early detection of breast cancer,” *IEEE Transactions on Antennas and Propagation*, vol. 51, no. 8, pp. 1690–1705, 2003.

- [103] E. C. Fear, X. Li, S. C. Hagness, and M. A. Stuchly, "Confocal microwave imaging for breast cancer detection: Localization of tumors in three dimensions," *IEEE Transactions on biomedical engineering*, vol. 49, no. 8, pp. 812–822, 2002.
- [104] R. O. Mays, N. Behdad, and S. C. Hagness, "Array sensitivity for model-based microwave breast imaging," *IEEE Transactions on Antennas and Propagation*, vol. 65, no. 6, pp. 2958–2965, 2017.
- [105] B. J. Mohammed, A. M. Abbosh, S. Mustafa, and D. Ireland, "Microwave system for head imaging," *IEEE Transactions on Instrumentation and Measurement*, vol. 63, no. 1, pp. 117–123, 2013.
- [106] S. Mustafa, B. Mohammed, and A. Abbosh, "Novel preprocessing techniques for accurate microwave imaging of human brain," *IEEE Antennas and Wireless Propagation Letters*, vol. 12, pp. 460–463, 2013.
- [107] L. Farina, R. Scapatucci, J. T. Vasquez *et al.*, "Microwave imaging technology for in-line food contamination monitoring," in *2019 IEEE International Symposium on Antennas and Propagation and USNC-URSI Radio Science Meeting*. IEEE, 2019, pp. 817–818.
- [108] E. Haacke, L. Petropoulos, E. Nilges, and D. Wu, "Extraction of conductivity and permittivity using magnetic resonance imaging," *Physics in medicine and biology*, vol. 36, no. 6, p. 723, 1991.
- [109] H. Wen, "Noninvasive quantitative mapping of conductivity and dielectric distributions using RF wave propagation effects in high-field MRI," in *Medical Imaging 2003: Physics of Medical Imaging*, vol. 5030. International Society for Optics and Photonics, 2003, pp. 471–477.
- [110] U. Katscher, T. Voigt, C. Findekklee *et al.*, "Determination of electric conductivity and local SAR via B1 mapping," *IEEE transactions on medical imaging*, vol. 28, no. 9, pp. 1365–1374, 2009.
- [111] A. L. Lier, A. Raaijmakers, T. Voigt *et al.*, "Electrical properties tomography in the human brain at 1.5, 3, and 7T: a comparison study," *Magnetic resonance in medicine*, vol. 71, no. 1, pp. 354–363, 2014.
- [112] F. Wiesinger, F. Seifert, H. Koenig, and K. P. Pruessmann, "Prospects of absolute B1 calibration," *Unsolved Problems and Unmet Needs in Magnetic Resonance, ISMRM*, vol. 14, 2006.
- [113] X. Zhang, J. Liu, and B. He, "Magnetic-resonance-based electrical properties tomography: a review," *IEEE reviews in biomedical engineering*, vol. 7, pp. 87–96, 2014.

- [114] J. Liu, X. Zhang, S. Schmitter, P.-F. Van de Moortele, and B. He, “Gradient-based magnetic resonance electrical properties imaging of brain tissues,” in *Engineering in Medicine and Biology Society (EMBC), 36th Annual International Conference of the IEEE*. IEEE, 2014, pp. 6056–6059.
- [115] N. Gurler and Y. Z. Ider, “Gradient-based electrical conductivity imaging using MR phase,” *Magnetic resonance in medicine*, vol. 77, no. 1, pp. 137–150, 2017.
- [116] A. Borsic, I. Perreard, A. Mahara, and R. J. Halter, “An inverse problems approach to MR-EPT image reconstruction,” *IEEE transactions on medical imaging*, vol. 35, no. 1, pp. 244–256, 2016.
- [117] K. M. Ropella and D. C. Noll, “A regularized, model-based approach to phase-based conductivity mapping using MRI,” *Magnetic resonance in medicine*, vol. 78, no. 5, pp. 2011–2021, 2017.
- [118] E. Balidemaj, C. A. van den Berg, J. Trinks *et al.*, “CSI-EPT: a contrast source inversion approach for improved MRI-based electric properties tomography,” *IEEE transactions on medical imaging*, vol. 34, no. 9, pp. 1788–1796, 2015.
- [119] G. Chen, B. Zhang, M. A. Cloos, D. K. Sodickson, and G. C. Wiggins, “A highly decoupled transmit–receive array design with triangular elements at 7 T,” *Magnetic resonance in medicine*, 2018.
- [120] G. C. Wiggins, B. Zhang, G. Chen, and D. Sodickson, “A highly decoupled 8 channel transmit-receive loop array for 7T with diverse B1 profiles,” in *Proc. ISMRM*, 2012, p. 309.
- [121] Y. LeCun, Y. Bengio, and G. Hinton, “Deep learning,” *Nature*, vol. 521, no. 7553, pp. 436–444, 2015.
- [122] A. Glisson, “Advanced engineering electromagnetics, by Constantine A. Balanis [book review],” *IEEE Antennas and Propagation Society Newsletter*, vol. 31, no. 6, pp. 24–26, 1989.
- [123] J. D. Jackson, “Classical electrodynamics,” 1999.
- [124] R. Mittra, *Computer Techniques for Electromagnetics: International Series of Monographs in Electrical Engineering*. Elsevier, 2013, vol. 7.
- [125] D. H. Staelin, *Electromagnetics and applications*. Massachusetts Institute of Technology, 2011.
- [126] W. C. Gibson, *The method of moments in electromagnetics*. Chapman and Hall/CRC, 2014.

- [127] J. Volakis, *Integral equation methods for electromagnetics*. The Institution of Engineering and Technology, 2012.
- [128] W. C. Chew, M. S. Tong, and B. Hu, “Integral equation methods for electromagnetic and elastic waves,” *Synthesis Lectures on Computational Electromagnetics*, vol. 3, no. 1, pp. 1–241, 2008.
- [129] G. Green, *An essay on the application of mathematical analysis to the theories of electricity and magnetism*. Wezäta-Melins Aktiebolag, 1828.
- [130] P. M. Morse and H. Feshbach, “Methods of theoretical physics,” *American Journal of Physics*, vol. 22, no. 6, pp. 410–413, 1954.
- [131] C.-T. Tai, *Dyadic Green functions in electromagnetic theory*. Institute of Electrical & Electronics Engineers (IEEE), 1994.
- [132] J. A. Kong, “Theory of electromagnetic waves,” *New York, Wiley-Interscience, 1975. 348 p.*, 1975.
- [133] A. D. Yaghjian, “Electric dyadic Green’s functions in the source region,” *Proceedings of the IEEE*, vol. 68, no. 2, pp. 248–263, 1980.
- [134] J. A. Stratton and L. Chu, “Diffraction theory of electromagnetic waves,” *Physical Review*, vol. 56, no. 1, p. 99, 1939.
- [135] W. Franz, “Zur formulierung des huygensschen prinzipts,” *Zeitschrift für Naturforschung A*, vol. 3, no. 8-11, pp. 500–506, 1948.
- [136] R. Fitzpatrick, “Electromagnetism and Optics: An introductory course,” July 2007.
- [137] R. F. Harrington, *Time-harmonic electromagnetic fields*. McGraw-Hill, 1961.
- [138] G. Mie, “Beiträge zur Optik trüber Medien, speziell kolloidaler Metallösungen,” *Annalen der Physik (in german)*, vol. 330, no. 3, pp. 377–445, 1908.
- [139] C. M. Studio, “CST Studio Suite 2011,” *Computer Simulation Technology AG*, 2013.
- [140] H. Ansys, “High frequency electromagnetic field simulation,” *High Frequency Structure Solver*, 2013.
- [141] R. W. Pryor, *Multiphysics modeling using COMSOL®: a first principles approach*. Jones & Bartlett Publishers, 2009.
- [142] K. Yee, “Numerical solution of initial boundary value problems involving Maxwell’s equations in isotropic media,” *IEEE Transactions on antennas and propagation*, vol. 14, no. 3, pp. 302–307, 1966.

- [143] A. Taflove and S. C. Hagness, *Computational electrodynamics: the finite-difference time-domain method*. Artech house, 2005.
- [144] S. D. Gedney, “Introduction to the finite-difference time-domain (FDTD) method for electromagnetics,” *Synthesis Lectures on Computational Electromagnetics*, vol. 6, no. 1, pp. 1–250, 2011.
- [145] O. C. Zienkiewicz, R. L. Taylor, P. Nithiarasu, and J. Zhu, *The finite element method*. McGraw-hill London, 1977, vol. 3.
- [146] J. L. Volakis, A. Chatterjee, and L. C. Kempel, *Finite element method electromagnetics: antennas, microwave circuits, and scattering applications*. John Wiley & Sons, 1998, vol. 6.
- [147] J.-M. Jin, *The finite element method in electromagnetics*. John Wiley & Sons, 2015.
- [148] Y. Zhu and A. C. Cangellaris, *Multigrid finite element methods for electromagnetic field modeling*. John Wiley & Sons, 2006, vol. 28.
- [149] T. J. Peters and J. L. Volakis, “Application of a conjugate gradient FFT method to scattering from thin planar material plates,” *IEEE transactions on antennas and propagation*, vol. 36, no. 4, pp. 518–526, 1988.
- [150] T. Sarkar, E. Arvas, and S. Rao, “Application of FFT and the conjugate gradient method for the solution of electromagnetic radiation from electrically large and small conducting bodies,” *IEEE Transactions on Antennas and Propagation*, vol. 34, no. 5, pp. 635–640, 1986.
- [151] J. Song and W. C. Chew, “Multilevel fast-multipole algorithm for solving combined field integral equations of electromagnetic scattering,” *Microwave and Optical Technology Letters*, vol. 10, no. 1, pp. 14–19, 1995.
- [152] X. Q. Sheng, J.-M. Jin, J. Song, W. C. Chew, and C.-C. Lu, “Solution of combined-field integral equation using multilevel fast multipole algorithm for scattering by homogeneous bodies,” *IEEE Transactions on Antennas and Propagation*, vol. 46, no. 11, pp. 1718–1726, 1998.
- [153] X.-M. Pan and X.-Q. Sh, “A sophisticated parallel MLFMA for scattering by extremely large targets [EM Programmer’s Notebook],” *IEEE Antennas and Propagation Magazine*, vol. 50, no. 3, pp. 129–138, 2008.
- [154] Ö. Ergül and L. Gürel, “Rigorous solutions of electromagnetic problems involving hundreds of millions of unknowns,” *IEEE Antennas and Propagation Magazine*, vol. 53, no. 1, pp. 18–27, 2011.
- [155] R. F. Harrington, *Field computation by moment methods*. Wiley-IEEE Press, 1993.

- [156] P. Dimbylow, “FDTD calculations of the whole-body averaged SAR in an anatomically realistic voxel model of the human body from 1 MHz to 1 GHz,” *Physics in Medicine & Biology*, vol. 42, no. 3, p. 479, 1997.
- [157] C. M. Collins and M. B. Smith, “Calculations of B1 distribution, SNR, and SAR for a surface coil adjacent to an anatomically-accurate human body model,” *Magnetic Resonance in Medicine: An Official Journal of the International Society for Magnetic Resonance in Medicine*, vol. 45, no. 4, pp. 692–699, 2001.
- [158] S. Kühn, W. Jennings, A. Christ, and N. Kuster, “Assessment of induced radio-frequency electromagnetic fields in various anatomical human body models,” *Physics in Medicine & Biology*, vol. 54, no. 4, p. 875, 2009.
- [159] R. Lee and A. C. Cangellaris, “A study of discretization error in the finite element approximation of wave solutions,” *IEEE Transactions on Antennas and Propagation*, vol. 40, no. 5, pp. 542–549, 1992.
- [160] J. E. Serrallés, L. Daniel, J. K. White *et al.*, “Global Maxwell tomography: a novel technique for electrical properties mapping based on MR measurements and volume integral equation formulations,” in *2016 IEEE International Symposium on Antennas and Propagation (APSURSI)*. IEEE, 2016, pp. 1395–1396.
- [161] J. Song, C. Lu, W. Chew, and S. Lee, “Fast illinois solver code (FISC),” *IEEE Antennas and Propagation Magazine*, vol. 40, no. 3, pp. 27–34, 1998.
- [162] B. Dembart and E. Yip, “A 3D fast multipole method for electromagnetics with multiple levels,” in *11th Annual Review of Progress in Applied Computational Electromagnetics*, vol. 1, 1995, pp. 621–628.
- [163] S. Velamparambil, W. C. Chew, and J. Song, “10 million unknowns: is it that big?[computational electromagnetics],” *IEEE Antennas and Propagation Magazine*, vol. 45, no. 2, pp. 43–58, 2003.
- [164] M. L. Hastriter, “A study of MLFMA for large-scale scattering problems,” ILLINOIS UNIV CHAMPAIGN, Tech. Rep., 2003.
- [165] R. Coifman, V. Rokhlin, and S. Wandzura, “The fast multipole method for the wave equation: A pedestrian prescription,” *IEEE Antennas and Propagation Magazine*, vol. 35, no. 3, pp. 7–12, 1993.
- [166] N. Morita, J. R. Mautz, and N. Kumagai, *Integral equation methods for electromagnetics*. Artech house, 1990.

- [167] J. M. Rius, E. Ubeda, and J. Parrón, “On the testing of the magnetic field integral equation with RWG basis functions in method of moments,” *IEEE Transactions on Antennas and Propagation*, vol. 49, no. 11, pp. 1550–1553, 2001.
- [168] R. C. Hansen, “Geometric theory of diffraction.” *Geometric theory of diffraction.*, by Hansen, RC. *IEEE Press Selected Reprint Series. New York, NY (USA): John Wiley & Sons, 7+ 406 p.*, 1981.
- [169] P. Waterman, “Scattering by dielectric obstacles(integral equation method for electromagnetic scattering by perfectly conducting obstacles modified for volume scattering regions involving disparities in dielectric constant, permeability or conductivity),” *Alta Frequenza*, vol. 38, pp. 348–352, 1968.
- [170] A. Ludwig, “The generalized multipole technique,” *Computer Physics Communications*, vol. 68, no. 1-3, pp. 306–314, 1991.
- [171] M. A. Morgan, *Finite element and finite difference methods in electromagnetic scattering*. Elsevier, 2013.
- [172] A. Taflove and K. R. Umashankar, “Review of FD-TD numerical modeling of electromagnetic wave scattering and radar cross section,” *Proceedings of the IEEE*, vol. 77, no. 5, pp. 682–699, 1989.
- [173] P. P. Silvester and R. L. Ferrari, *Finite elements for electrical engineers*. Cambridge university press, 1996.
- [174] J. Richmond, “Scattering by a dielectric cylinder of arbitrary cross section shape,” *IEEE Transactions on Antennas and Propagation*, vol. 13, no. 3, pp. 334–341, 1965.
- [175] J. Richmond, “Te-wave scattering by a dielectric cylinder of arbitrary cross-section shape,” *IEEE Transactions on Antennas and Propagation*, vol. 14, no. 4, pp. 460–464, 1966.
- [176] A. J. Poggio and E. K. Miller, *Integral equation solutions of three-dimensional scattering problems*. MB Assoc., 1970.
- [177] E. K. Miller, L. Medgyesi-Mitschang, and E. H. Newman, *Computational electromagnetics: frequency-domain method of moments*. IEEE Press, 1992.
- [178] L. Medgyesi-Mitschang, J. Putnam, and M. Gedera, “Generalized method of moments for three-dimensional penetrable scatterers,” *JOSA A*, vol. 11, no. 4, pp. 1383–1398, 1994.
- [179] J. R. Mautz and R. F. Harrington, “Electromagnetic scattering from a homogeneous body of revolution,” SYRACUSE UNIV NY DEPT OF ELECTRICAL AND COMPUTER ENGINEERING, Tech. Rep., 1977.

- [180] S. Rao, D. Wilton, and A. Glisson, "Electromagnetic scattering by surfaces of arbitrary shape," *IEEE Transactions on antennas and propagation*, vol. 30, no. 3, pp. 409–418, 1982.
- [181] A. Glisson and D. Wilton, "Simple and efficient numerical methods for problems of electromagnetic radiation and scattering from surfaces," *IEEE Transactions on Antennas and Propagation*, vol. 28, no. 5, pp. 593–603, 1980.
- [182] E. Ubeda and J. M. Rius, "Monopolar RWG MoM-MFIE formulation outperforming the conventional dipolar RWG MoM-MFIE in the electromagnetic scattering analysis," in *Antennas and Propagation Society International Symposium, 2005 IEEE*, vol. 4. IEEE, 2005, pp. 276–279.
- [183] E. Ubeda and J. M. Rius, "MFIE MoM-formulation with curl-conforming basis functions and accurate kernel integration in the analysis of perfectly conducting sharp-edged objects," *Microwave and Optical Technology Letters*, vol. 44, no. 4, pp. 354–358, 2005.
- [184] E. Ubeda and J. M. Rius, "Novel monopolar MFIE MoM-discretization for the scattering analysis of small objects," *IEEE Transactions on Antennas and Propagation*, vol. 54, no. 1, pp. 50–57, 2006.
- [185] L. Zhang, A. Deng, and M. Wang, "Application of a novel formulation to the MFIE using RWG basis functions in method of moments," *Engineering analysis with boundary elements*, vol. 33, no. 6, pp. 880–884, 2009.
- [186] L. Zhang, A. Deng, M. Wang, and S. Yang, "Numerical study of a novel MFIE formulation using monopolar RWG basis functions," *Computer Physics Communications*, vol. 181, no. 1, pp. 52–60, 2010.
- [187] O. Ergul and L. Gurel, "Improved testing of the magnetic-field integral equation," *IEEE microwave and wireless components letters*, vol. 15, no. 10, pp. 615–617, 2005.
- [188] O. Ergul and L. Gurel, "The use of curl-conforming basis functions for the magnetic-field integral equation," *IEEE Transactions on Antennas and Propagation*, vol. 54, no. 7, pp. 1917–1926, 2006.
- [189] A. G. Polimeridis and T. V. Yioultis, "On the direct evaluation of weakly singular integrals in Galerkin mixed potential integral equation formulations," *IEEE Transactions on Antennas and Propagation*, vol. 56, no. 9, pp. 3011–3019, 2008.
- [190] A. G. Polimeridis and J. R. Mosig, "Complete semi-analytical treatment of weakly singular integrals on planar triangles via the direct evaluation method," *International journal for numerical methods in engineering*, vol. 83, no. 12, pp. 1625–1650, 2010.

- [191] A. G. Polimeridis and J. R. Mosig, "On the direct evaluation of surface integral equation impedance matrix elements involving point singularities," *IEEE Antennas and Wireless Propagation Letters*, vol. 10, pp. 599–602, 2011.
- [192] A. G. Polimeridis, J. M. Tamayo, J. M. Rius, and J. R. Mosig, "Fast and accurate computation of hypersingular integrals in Galerkin surface integral equation formulations via the direct evaluation method," *IEEE transactions on antennas and propagation*, vol. 59, no. 6, pp. 2329–2340, 2011.
- [193] A. F. Peterson, S. L. Ray, R. Mittra, I. of Electrical, and E. Engineers, *Computational methods for electromagnetics*. IEEE press New York, 1998, vol. 2.
- [194] R. A. Shore and A. D. Yaghjian, "Dual-surface integral equations in electromagnetic scattering," *IEEE Transactions on Antennas and Propagation*, vol. 53, no. 5, pp. 1706–1709, 2005.
- [195] J. Guan, S. Yan, and J.-M. Jin, "A multi-solver scheme based on combined field integral equations for electromagnetic modeling of highly complex objects," *IEEE Transactions on Antennas and Propagation*, vol. 65, no. 3, pp. 1236–1247, 2017.
- [196] B. H. Jung, T. Sarkar, and Y.-S. Chung, "A survey of various frequency domain integral equations for the analysis of scattering from three-dimensional dielectric objects," *Electrical Engineering and Computer Science*, vol. 65, 2002.
- [197] P. Yla-Oijala and M. Taskinen, "Calculation of cfi impedance matrix elements with rwg and n/spl times/rwg functions," *IEEE Transactions on Antennas and Propagation*, vol. 51, no. 8, pp. 1837–1846, 2003.
- [198] Y. Chen and C.-F. Wang, "Characteristic mode analysis of PEC bodies using combined field integral equation," in *Antennas and Propagation & USNC/URSI National Radio Science Meeting, 2015 IEEE International Symposium on*. IEEE, 2015, pp. 1474–1475.
- [199] D. R. Wilton, "Review of current status and trends in the use of integral equations in computational electromagnetics," *Electromagnetics*, vol. 12, no. 3-4, pp. 287–341, 1992.
- [200] S. M. Rao and D. R. Wilton, "E-field, H-field, and combined field solution for arbitrarily shaped three-dimensional dielectric bodies," *Electromagnetics*, vol. 10, no. 4, pp. 407–421, 1990.
- [201] P. Yla-Oijala and M. Taskinen, "Application of combined field integral equation for electromagnetic scattering by dielectric and composite objects," *IEEE Transactions on Antennas and Propagation*, vol. 53, no. 3, pp. 1168–1173, 2005.

- [202] D. Wilton and A. Glisson, "On improving the electric field integral equation at low frequencies," *Proc. URSI Radio Sci. Meet. Dig.*, vol. 24, 1981.
- [203] J. Mautz and R. Harrington, "An E-field solution for a conducting surface small or comparable to the wavelength," *IEEE Transactions on Antennas and Propagation*, vol. 32, no. 4, pp. 330–339, 1984.
- [204] M. Burton and S. Kashyap, "A study of a recent, moment-method algorithm that is accurate to very low frequencies," *Applied Computational Electromagnetics Society Journal*, vol. 10, pp. 58–68, 1995.
- [205] D. Wilton, J. Lim, and S. Rao, "A novel technique to calculate the electromagnetic scattering by surfaces of arbitrary shape," in *URSI Radio Science Meeting*, 1993, p. 322.
- [206] J.-F. Lee, R. Lee, and R. J. Burkholder, "Loop star basis functions and a robust preconditioner for Efe scattering problems," *IEEE Transactions on Antennas and Propagation*, vol. 51, no. 8, pp. 1855–1863, 2003.
- [207] S. Uckun, T. K. Sarkar, S. M. Rao, and M. Salazar-Palma, "A novel technique for analysis of electromagnetic scattering from microstrip antennas of arbitrary shape," *IEEE Transactions on microwave theory and techniques*, vol. 45, no. 4, pp. 485–491, 1997.
- [208] G. Vecchi, "Loop-star decomposition of basis functions in the discretization of the Efe," *IEEE Transactions on Antennas and Propagation*, vol. 47, no. 2, pp. 339–346, 1999.
- [209] R. J. Adams, "Physical and analytical properties of a stabilized electric field integral equation," *IEEE Transactions on Antennas and Propagation*, vol. 52, no. 2, pp. 362–372, 2004.
- [210] H. Contopanagos, B. Dembart, M. Epton *et al.*, "Well-conditioned boundary integral equations for three-dimensional electromagnetic scattering," *IEEE Transactions on Antennas and Propagation*, vol. 50, no. 12, pp. 1824–1830, 2002.
- [211] S. H. Christiansen and J.-C. Nédélec, "A preconditioner for the electric field integral equation based on Calderon formulas," *SIAM Journal on Numerical Analysis*, vol. 40, no. 3, pp. 1100–1135, 2002.
- [212] S. Borel, D. P. Levadoux, and F. Alouges, "A new well-conditioned integral formulation for Maxwell equations in three dimensions," *IEEE transactions on antennas and propagation*, vol. 53, no. 9, pp. 2995–3004, 2005.
- [213] F. P. Andriulli, K. Cools, H. Bagci *et al.*, "A multiplicative calderon preconditioner for the electric field integral equation," *IEEE Transactions on Antennas and Propagation*, vol. 56, no. 8, pp. 2398–2412, 2008.

- [214] A. Buffa and S. Christiansen, “A dual finite element complex on the barycentric refinement,” *Mathematics of Computation*, vol. 76, no. 260, pp. 1743–1769, 2007.
- [215] P. Ylä-Oijala, M. Taskinen, and S. Järvenpää, “Analysis of surface integral equations in electromagnetic scattering and radiation problems,” *Engineering Analysis with Boundary Elements*, vol. 32, no. 3, pp. 196–209, 2008.
- [216] K. Cools, F. P. Andriulli, and E. Michielssen, “A calderón multiplicative preconditioner for the PMCHWT integral equation,” *IEEE transactions on Antennas and Propagation*, vol. 59, no. 12, pp. 4579–4587, 2011.
- [217] A. M. Kern and O. J. Martin, “Surface integral formulation for 3D simulations of plasmonic and high permittivity nanostructures,” *JOSA A*, vol. 26, no. 4, pp. 732–740, 2009.
- [218] A. M. Kern and O. J. Martin, “Pitfalls in the determination of optical cross sections from surface integral equation simulations,” *IEEE Transactions on Antennas and Propagation*, vol. 58, no. 6, pp. 2158–2161, 2010.
- [219] M. H. Reid and S. G. Johnson, “Efficient computation of power, force, and torque in BEM scattering calculations,” *IEEE Transactions on Antennas and Propagation*, vol. 63, no. 8, pp. 3588–3598, 2015.
- [220] S. Heywang-Köbrunner, P. Viehweg, A. Heinig, and C. Küchler, “Contrast-enhanced MRI of the breast: accuracy, value, controversies, solutions,” *European journal of radiology*, vol. 24, no. 2, pp. 94–108, 1997.
- [221] B. Biswal, F. Zerrin Yetkin, V. M. Haughton, and J. S. Hyde, “Functional connectivity in the motor cortex of resting human brain using echo-planar MRI,” *Magnetic resonance in medicine*, vol. 34, no. 4, pp. 537–541, 1995.
- [222] J. Vaughan, G. Adriany, C. Snyder *et al.*, “Efficient high-frequency body coil for high-field MRI,” *Magnetic Resonance in Medicine: An Official Journal of the International Society for Magnetic Resonance in Medicine*, vol. 52, no. 4, pp. 851–859, 2004.
- [223] R. Pascone, T. Vullo, J. Farrelly, and P. T. Cahill, “Explicit treatment of mutual inductance in eight-column birdcage resonators,” *Magnetic resonance imaging*, vol. 10, no. 3, pp. 401–410, 1992.
- [224] M. D. Harpen, “Equivalent circuit for birdcage resonators,” *Magnetic resonance in medicine*, vol. 29, no. 2, pp. 263–268, 1993.
- [225] M. C. Leifer, “Resonant modes of the birdcage coil,” *Journal of Magnetic Resonance*, vol. 124, no. 1, pp. 51–60, 1997.

- [226] J. Tropp, "Mutual inductance in the bird-cage resonator," *Journal of Magnetic Resonance*, vol. 126, no. 1, pp. 9–17, 1997.
- [227] P. W. Tuinenga, *SPICE: a guide to circuit simulation and analysis using PSpice*. Prentice Hall Englewood Cliffs, 1995, vol. 1.
- [228] S. Wang and J. H. Duyn, "Analysing radio-frequency coil arrays in high-field magnetic resonance imaging by the combined field integral equation method," *Physics in Medicine & Biology*, vol. 51, no. 12, p. 3211, 2006.
- [229] J.-H. Chen, S.-K. Jeng, F.-H. Lin, and W.-P. Kuan, "Quantitative analysis of magnetic resonance radio-frequency coils based on method of moments," *IEEE transactions on magnetics*, vol. 35, no. 4, pp. 2118–2127, 1999.
- [230] D. Jiao and J.-M. Jin, "Fast frequency-sweep analysis of RF coils for MRI," *IEEE transactions on biomedical engineering*, vol. 46, no. 11, pp. 1387–1390, 1999.
- [231] Y. H. Lo, S. He, L. Jiang, and W. C. Chew, "Finite-width gap excitation and impedance models," in *2011 IEEE International Symposium on Antennas and Propagation (APSURSI)*. IEEE, 2011, pp. 1297–1300.
- [232] Y. H. Lo, L. J. Jiang, and W. C. Chew, "Finite-width feed and load models," *IEEE Transactions on Antennas and Propagation*, vol. 61, no. 1, pp. 281–289, 2013.
- [233] C. Geuzaine and J.-F. Remacle, "Gmsh: A 3-D finite element mesh generator with built-in pre-and post-processing facilities," *International journal for numerical methods in engineering*, vol. 79, no. 11, pp. 1309–1331, 2009.
- [234] P. Cignoni, M. Callieri, M. Corsini *et al.*, "Meshlab: an open-source mesh processing tool." in *Eurographics Italian chapter conference*, vol. 2008, 2008, pp. 129–136.
- [235] G. V. Eleftheriades and J. R. Mosig, "On the network characterization of planar passive circuits using the method of moments," *IEEE Transactions on Microwave Theory and Techniques*, vol. 44, no. 3, pp. 438–445, 1996.
- [236] J. Jin, J. Chen, W. Chew *et al.*, "Computation of electromagnetic fields for high-frequency magnetic resonance imaging applications," *Physics in Medicine & Biology*, vol. 41, no. 12, p. 2719, 1996.
- [237] D. Schaubert, D. Wilton, and A. Glisson, "A tetrahedral modeling method for electromagnetic scattering by arbitrarily shaped inhomogeneous dielectric bodies," *IEEE Transactions on Antennas and Propagation*, vol. 32, no. 1, pp. 77–85, 1984.

- [238] S. Antenor de Carvalho and L. de Souza Mendes, "Scattering of EM waves by inhomogeneous dielectrics with the use of the method of moments and 3-D solenoidal basis functions," *Microwave and Optical Technology Letters*, vol. 23, no. 1, pp. 42–46, 1999.
- [239] C.-C. Lu, "A fast algorithm based on volume integral equation for analysis of arbitrarily shaped dielectric radomes," *IEEE transactions on antennas and propagation*, vol. 51, no. 3, pp. 606–612, 2003.
- [240] M. Li and W. C. Chew, "Applying divergence-free condition in solving the volume integral equation," *Progress In Electromagnetics Research*, vol. 57, pp. 311–333, 2006.
- [241] G. Rubinacci and A. Tamburrino, "A broadband volume integral formulation based on edge-elements for full-wave analysis of lossy interconnects," *IEEE transactions on antennas and propagation*, vol. 54, no. 10, pp. 2977–2989, 2006.
- [242] M. I. Sancer, K. Sertel, J. L. Volakis, and P. Van Alstine, "On volume integral equations," *IEEE transactions on antennas and propagation*, vol. 54, no. 5, pp. 1488–1495, 2006.
- [243] N. A. Ozdemir and J.-F. Lee, "A nonconformal volume integral equation for electromagnetic scattering from anisotropic materials," in *Antennas and Propagation Society International Symposium 2006, IEEE*. IEEE, 2006, pp. 2889–2892.
- [244] N. A. Ozdemir and J.-F. Lee, "A nonconformal volume integral equation for electromagnetic scattering from penetrable objects," *IEEE Transactions on Magnetics*, vol. 43, no. 4, pp. 1369–1372, 2007.
- [245] L. Sun and W. Chew, "A novel formulation of the volume integral equation for electromagnetic scattering," *Waves in Random and Complex Media*, vol. 19, no. 1, pp. 162–180, 2009.
- [246] J. Markkanen, C.-C. Lu, X. Cao, and P. Yla-Oijala, "Analysis of volume integral equation formulations for scattering by high-contrast penetrable objects," *IEEE Transactions on Antennas and Propagation*, vol. 60, no. 5, pp. 2367–2374, 2012.
- [247] M. Van Beurden and S. Van Eijndhoven, "Gaps in present discretization schemes for domain integral equations," in *Electromagnetics in Advanced Applications, 2007. ICEAA 2007. International Conference on*. IEEE, 2007, pp. 673–675.
- [248] M. Van Beurden and S. Van Eijndhoven, "Well-posedness of domain integral equations for a dielectric object in homogeneous background," *Journal of Engineering Mathematics*, vol. 62, no. 3, pp. 289–302, 2008.
- [249] J. Markkanen, P. Yla-Oijala, and A. Sihvola, "Discretization of volume integral equation formulations for extremely anisotropic materials," *IEEE Transactions on Antennas and Propagation*, vol. 60, no. 11, pp. 5195–5202, 2012.

- [250] N. V. Budko and A. B. Samokhin, “Spectrum of the volume integral operator of electromagnetic scattering,” *SIAM Journal on Scientific Computing*, vol. 28, no. 2, pp. 682–700, 2006.
- [251] J. Markkanen and P. Ylä-Oijala, “Numerical comparison of spectral properties of volume-integral-equation formulations,” *Journal of Quantitative Spectroscopy and Radiative Transfer*, vol. 178, pp. 269–275, 2016.
- [252] G. C. Hsiao and R. E. Kleinman, “Mathematical foundations for error estimation in numerical solutions of integral equations in electromagnetics,” *IEEE transactions on Antennas and Propagation*, vol. 45, no. 3, pp. 316–328, 1997.
- [253] P. Zwamborn, *Scattering by objects with electric contrast*. Delft, 1991.
- [254] S. Y. Huang, Z.-H. Ma, L. Wan, W. Yu, and J. T. Vaughan, “Fast full-wave calculation of electromagnetic fields based on weak-form volume integral equation for MRI applications,” *The Journal of Engineering*, vol. 2018, no. 9, pp. 762–767, 2018.
- [255] P. Zwamborn and P. M. van den Berg, “Computation of electromagnetic fields inside strongly inhomogeneous objects by the weak-conjugate-gradient fast-Fourier-transform method,” *JOSA A*, vol. 11, no. 4, pp. 1414–1421, 1994.
- [256] L. Gürel, I. Sendur, and K. Sertel, “Quantitative comparison of rooftop and RWG basis functions,” in *Antennas and Propagation Society International Symposium, 1997. IEEE., 1997 Digest*, vol. 2. IEEE, 1997, pp. 796–799.
- [257] L. Gürel, K. Sertel, and I. K. Şendur, “On the choice of basis functions to model surface electric current densities in computational electromagnetics,” *Radio science*, vol. 34, no. 6, pp. 1373–1387, 1999.
- [258] C. Gabriel, “Compilation of the dielectric properties of body tissues at rf and microwave frequencies.” KING’S COLL LONDON (UNITED KINGDOM) DEPT OF PHYSICS, Tech. Rep., 1996.
- [259] E. Popov, M. Nevière, B. Gralak, and G. Tayeb, “Staircase approximation validity for arbitrary-shaped gratings,” *JOSA A*, vol. 19, no. 1, pp. 33–42, 2002.
- [260] P. Ylä-Oijala, J. Markkanen, S. Jarvenpää, and S. P. Kiminki, “Surface and volume integral equation methods for time-harmonic solutions of Maxwell’s equations,” *Progress In Electromagnetics Research*, vol. 149, pp. 15–44, 2014.
- [261] W. M. Brink and A. G. Webb, “High permittivity pads reduce specific absorption rate, improve B1 homogeneity, and increase contrast-to-noise ratio for functional cardiac MRI at 3 T,” *Magnetic resonance in medicine*, vol. 71, no. 4, pp. 1632–1640, 2014.

- [262] W. M. Brink, R. F. Remis, and A. G. Webb, “A theoretical approach based on electromagnetic scattering for analysing dielectric shimming in high-field MRI,” *Magnetic resonance in medicine*, vol. 75, no. 5, pp. 2185–2194, 2016.
- [263] K. Koolstra, P. Börnert, W. Brink, and A. Webb, “Improved image quality and reduced power deposition in the spine at 3 T using extremely high permittivity materials,” *Magnetic resonance in medicine*, vol. 79, no. 2, pp. 1192–1199, 2018.
- [264] W. Chai and D. Jiao, “Theoretical study on the rank of integral operators for broadband electromagnetic modeling from static to electrodynamic frequencies,” *IEEE Transactions on Components, Packaging and Manufacturing Technology*, vol. 3, no. 12, pp. 2113–2126, 2013.
- [265] H. Liu and D. Jiao, “A theoretical study on the rank’s dependence with electric size of the inverse finite element matrix for large-scale electrodynamic analysis,” in *Antennas and Propagation Society International Symposium (APSURSI), 2012 IEEE*. IEEE, 2012, pp. 1–2.
- [266] L. R. Tucker, “Some mathematical notes on three-mode factor analysis,” *Psychometrika*, vol. 31, no. 3, pp. 279–311, 1966.
- [267] F. L. Hitchcock, “The expression of a tensor or a polyadic as a sum of products,” *Studies in Applied Mathematics*, vol. 6, no. 1-4, pp. 164–189, 1927.
- [268] F. L. Hitchcock, “Multiple invariants and generalized rank of a P-way matrix or tensor,” *Studies in Applied Mathematics*, vol. 7, no. 1-4, pp. 39–79, 1928.
- [269] R. B. Cattell, ““parallel proportional profiles” and other principles for determining the choice of factors by rotation,” *Psychometrika*, vol. 9, no. 4, pp. 267–283, 1944.
- [270] R. B. Cattell, “The three basic factor-analytic research designs—their interrelations and derivatives,” *Psychological bulletin*, vol. 49, no. 5, p. 499, 1952.
- [271] L. R. Tucker, “Implications of factor analysis of three-way matrices for measurement of change,” *Problems in measuring change*, vol. 15, pp. 122–137, 1963.
- [272] L. R. Tucker, “The extension of factor analysis to three-dimensional matrices,” *Contributions to mathematical psychology*, vol. 110119, 1964.
- [273] R. A. Harshman, “Foundations of the PARAFAC procedure: Models and conditions for an “explanatory” multimodal factor analysis,” *UCLA Working Papers in Phonetics*, vol. 16, pp. 1–84, 1970.

- [274] J. D. Carroll, S. Pruzansky, and J. B. Kruskal, "CANDELINC: A general approach to multidimensional analysis of many-way arrays with linear constraints on parameters," *Psychometrika*, vol. 45, no. 1, pp. 3–24, 1980.
- [275] J. D. Carroll and J.-J. Chang, "Analysis of individual differences in multidimensional scaling via an N-way generalization of "Eckart-Young" decomposition," *Psychometrika*, vol. 35, no. 3, pp. 283–319, 1970.
- [276] C. J. Appellof and E. R. Davidson, "Strategies for analyzing data from video fluorometric monitoring of liquid chromatographic effluents," *Analytical Chemistry*, vol. 53, no. 13, pp. 2053–2056, 1981.
- [277] R. Bro, "PARAFAC. tutorial and applications," *Chemometrics and intelligent laboratory systems*, vol. 38, no. 2, pp. 149–171, 1997.
- [278] R. Bro and C. A. Andersson, "Improving the speed of multiway algorithms: Part II: Compression," *Chemometrics and intelligent laboratory systems*, vol. 42, no. 1-2, pp. 105–113, 1998.
- [279] R. Bro, "Multi-way analysis in the food industry," *Models, Algorithms, and Applications. Academish proefschrift. Dinamarca*, 1998.
- [280] R. Bro, "Review on multiway analysis in chemistry—2000–2005," *Critical reviews in analytical chemistry*, vol. 36, no. 3-4, pp. 279–293, 2006.
- [281] C. M. Andersen and R. Bro, "Practical aspects of PARAFAC modeling of fluorescence excitation-emission data," *Journal of Chemometrics*, vol. 17, no. 4, pp. 200–215, 2003.
- [282] N. D. Sidiropoulos and R. Bro, "On the uniqueness of multilinear decomposition of N-way arrays," *Journal of chemometrics*, vol. 14, no. 3, pp. 229–239, 2000.
- [283] C. A. Andersson and R. Bro, "The N-way toolbox for MATLAB," *Chemometrics and intelligent laboratory systems*, vol. 52, no. 1, pp. 1–4, 2000.
- [284] S. Gourvénec, G. Tomasi, C. Durville *et al.*, "Cubatch, a MATLAB® interface for n-mode data analysis," *Chemometrics and Intelligent Laboratory Systems*, vol. 77, no. 1-2, pp. 122–130, 2005.
- [285] R. Henrion, "Body diagonalization of core matrices in three-way principal components analysis: Theoretical bounds and simulation," *Journal of chemometrics*, vol. 7, no. 6, pp. 477–494, 1993.
- [286] A. K. Smilde, Y. Wang, and B. R. Kowalski, "Theory of medium-rank second-order calibration with restricted-Tucker models," *Journal of Chemometrics*, vol. 8, no. 1, pp. 21–36, 1994.

- [287] H.-L. Wu, M. Shibukawa, and K. Oguma, “An alternating trilinear decomposition algorithm with application to calibration of HPLC–DAD for simultaneous determination of overlapped chlorinated aromatic hydrocarbons,” *Journal of Chemometrics: A Journal of the Chemometrics Society*, vol. 12, no. 1, pp. 1–26, 1998.
- [288] H. A. Kiers, “A three-step algorithm for CANDECOMP/PARAFAC analysis of large data sets with multicollinearity,” *Journal of Chemometrics*, vol. 12, no. 3, pp. 155–171, 1998.
- [289] L. De Lathauwer and B. De Moor, “From matrix to tensor: Multilinear algebra and signal processing,” in *Institute of Mathematics and Its Applications Conference Series*, vol. 67. Citeseer, 1998, pp. 1–16.
- [290] N. D. Sidiropoulos, R. Bro, and G. B. Giannakis, “Parallel factor analysis in sensor array processing,” *IEEE transactions on Signal Processing*, vol. 48, no. 8, pp. 2377–2388, 2000.
- [291] P. Comon, “Tensor decompositions—State of the art and applications, keynote address in IMA Conf,” *Mathematics in Signal Processing, Warwick, UK*, 2000.
- [292] D. FitzGerald, M. Cranitch, and E. Coyle, “Non-negative tensor factorisation for sound source separation,” *Irish Signals and Systems Conference*, 2005.
- [293] D. Muti and S. Bourennane, “Multidimensional filtering based on a tensor approach,” *Signal Processing*, vol. 85, no. 12, pp. 2338–2353, 2005.
- [294] L. De Lathauwer, J. Castaing, and J.-F. Cardoso, “Fourth-order cumulant-based blind identification of underdetermined mixtures,” *IEEE Transactions on Signal Processing*, vol. 55, no. 6, pp. 2965–2973, 2007.
- [295] L. De Lathauwer and A. de Baynast, “Blind deconvolution of DS-CDMA signals by means of decomposition in rank- $(1, l, l)$  terms,” *IEEE Transactions on Signal Processing*, vol. 56, no. 4, pp. 1562–1571, 2008.
- [296] A. Cichocki, R. Zdunek, A. H. Phan, and S.-i. Amari, *Nonnegative matrix and tensor factorizations: applications to exploratory multi-way data analysis and blind source separation*. John Wiley & Sons, 2009.
- [297] P. Comon, “Tensors: a brief introduction,” *IEEE Signal Processing Magazine*, vol. 31, no. 3, pp. 44–53, 2014.
- [298] G. Zhou, A. Cichocki, Q. Zhao, and S. Xie, “Nonnegative matrix and tensor factorizations: An algorithmic perspective,” *IEEE Signal Processing Magazine*, vol. 31, no. 3, pp. 54–65, 2014.

- [299] M. De Vos, L. De Lathauwer, B. Vanrumste, S. Van Huffel, and W. Van Paesschen, “Canonical decomposition of ictal scalp EEG and accurate source localisation: Principles and simulation study,” *Computational intelligence and neuroscience*, vol. 2007, 2007.
- [300] M. Mørup, L. K. Hansen, and S. M. Arnfred, “ERPWAVELAB: A toolbox for multi-channel analysis of time–frequency transformed event related potentials,” *Journal of neuroscience methods*, vol. 161, no. 2, pp. 361–368, 2007.
- [301] M. De Vos, A. Vergult, L. De Lathauwer *et al.*, “Canonical decomposition of ictal scalp EEG reliably detects the seizure onset zone,” *NeuroImage*, vol. 37, no. 3, pp. 844–854, 2007.
- [302] M. Mørup, L. K. Hansen, C. S. Herrmann, J. Parnas, and S. M. Arnfred, “Parallel factor analysis as an exploratory tool for wavelet transformed event-related EEG,” *NeuroImage*, vol. 29, no. 3, pp. 938–947, 2006.
- [303] E. Acar, C. Aykut-Bingol, H. Bingol, R. Bro, and B. Yener, “Multiway analysis of epilepsy tensors,” *Bioinformatics*, vol. 23, no. 13, pp. i10–i18, 2007.
- [304] E. Acar, C. A. Bingol, H. Bingol, R. Bro, and B. Yener, “Seizure recognition on epilepsy feature tensor,” in *Engineering in Medicine and Biology Society, 2007. EMBS 2007. 29th Annual International Conference of the IEEE*. IEEE, 2007, pp. 4273–4276.
- [305] N. Liu, B. Zhang, J. Yan *et al.*, “Text representation: From vector to tensor,” in *Data Mining, Fifth IEEE International Conference on*. IEEE, 2005, pp. 4–pp.
- [306] T. G. Kolda, B. W. Bader, and J. P. Kenny, “Higher-order web link analysis using multilinear algebra,” in *Data Mining, Fifth IEEE International Conference on*. IEEE, 2005, pp. 8–pp.
- [307] B. W. Bader and T. G. Kolda, “Algorithm 862: MATLAB tensor classes for fast algorithm prototyping,” *ACM Transactions on Mathematical Software (TOMS)*, vol. 32, no. 4, pp. 635–653, 2006.
- [308] B. W. Bader, R. A. Harshman, and T. G. Kolda, “Temporal analysis of semantic graphs using ASALSAN,” in *Data Mining, 2007. ICDM 2007. Seventh IEEE International Conference on*. IEEE, 2007, pp. 33–42.
- [309] B. W. Bader, M. W. Berry, and M. Browne, “Discussion tracking in Enron email using PARAFAC,” in *Survey of Text Mining II*. Springer, 2008, pp. 147–163.
- [310] D. Vlasic, M. Brand, H. Pfister, and J. Popović, “Face transfer with multilinear models,” *ACM transactions on graphics (TOG)*, vol. 24, no. 3, pp. 426–433, 2005.
- [311] J. Sun, D. Tao, and C. Faloutsos, “Beyond streams and graphs: dynamic tensor analysis,” in *Proceedings of the 12th ACM SIGKDD international conference on Knowledge discovery and data mining*. ACM, 2006, pp. 374–383.

- [312] O. Duchenne, F. Bach, I.-S. Kweon, and J. Ponce, “A tensor-based algorithm for high-order graph matching,” *IEEE transactions on pattern analysis and machine intelligence*, vol. 33, no. 12, pp. 2383–2395, 2011.
- [313] M. A. O. Vasilescu and D. Terzopoulos, “Multilinear analysis of image ensembles: Tensorfaces,” in *European Conference on Computer Vision*. Springer, 2002, pp. 447–460.
- [314] M. A. O. Vasilescu and D. Terzopoulos, “Multilinear image analysis for facial recognition,” in *Pattern Recognition, 2002. Proceedings. 16th International Conference on*, vol. 2. IEEE, 2002, pp. 511–514.
- [315] M. A. O. Vasilescu and D. Terzopoulos, “Multilinear subspace analysis of image ensembles,” in *Computer Vision and Pattern Recognition, 2003. Proceedings. 2003 IEEE Computer Society Conference on*, vol. 2. IEEE, 2003, pp. II–93.
- [316] H. Wang *et al.*, “Facial expression decomposition,” in *Computer Vision, 2003. Proceedings. Ninth IEEE International Conference on*. IEEE, 2003, pp. 958–965.
- [317] B. Savas, “Analyses and tests of handwritten digit recognition algorithms,” *LiTH-MAT-EX-2003-01, Linköping University, Department of Mathematics*, 2003.
- [318] T. Hazan, S. Polak, and A. Shashua, “Sparse image coding using a 3D non-negative tensor factorization,” in *Computer Vision, 2005. ICCV 2005. Tenth IEEE International Conference on*, vol. 1. IEEE, 2005, pp. 50–57.
- [319] A. Shashua and T. Hazan, “Non-negative tensor factorization with applications to statistics and computer vision,” in *Proceedings of the 22nd international conference on Machine learning*. ACM, 2005, pp. 792–799.
- [320] A. Rajwade, A. Rangarajan, and A. Banerjee, “Image denoising using the higher order singular value decomposition,” *IEEE Transactions on Pattern Analysis and Machine Intelligence*, vol. 35, no. 4, pp. 849–862, 2013.
- [321] S. Leurgans and R. T. Ross, “Multilinear models: applications in spectroscopy,” *Statistical Science*, pp. 289–310, 1992.
- [322] C. A. Andersson and R. Henrion, “A general algorithm for obtaining simple structure of core arrays in N-way PCA with application to fluorometric data,” *Computational statistics & data analysis*, vol. 31, no. 3, pp. 255–278, 1999.
- [323] W. Hackbusch, B. N. Khoromskij, and E. E. Tyrtyshnikov, “Hierarchical Kronecker tensor-product approximations,” *Journal of Numerical Mathematics jnma*, vol. 13, no. 2, pp. 119–156, 2005.

- [324] J. Landsberg, “The border rank of the multiplication of  $2 \times 2$  matrices is seven,” *Journal of the American Mathematical Society*, vol. 19, no. 2, pp. 447–459, 2006.
- [325] W. Hackbusch and B. N. Khoromskij, “Tensor-product approximation to operators and functions in high dimensions,” *Journal of Complexity*, vol. 23, no. 4-6, pp. 697–714, 2007.
- [326] J. B. Kruskal, “Three-way arrays: rank and uniqueness of trilinear decompositions, with application to arithmetic complexity and statistics,” *Linear algebra and its applications*, vol. 18, no. 2, pp. 95–138, 1977.
- [327] V. S. Grigorascu and P. A. Regalia, “Tensor displacement structures and polyspectral matching,” in *Fast reliable algorithms for matrices with structure*. SIAM, 1999, pp. 245–276.
- [328] L. De Lathauwer, B. De Moor, and J. Vandewalle, “A multilinear singular value decomposition,” *SIAM journal on Matrix Analysis and Applications*, vol. 21, no. 4, pp. 1253–1278, 2000.
- [329] L. De Lathauwer, B. De Moor, and J. Vandewalle, “On the best rank-1 and rank- $(r_1, r_2, \dots, r_n)$  approximation of higher-order tensors,” *SIAM journal on Matrix Analysis and Applications*, vol. 21, no. 4, pp. 1324–1342, 2000.
- [330] T. Zhang and G. H. Golub, “Rank-one approximation to high order tensors,” *SIAM Journal on Matrix Analysis and Applications*, vol. 23, no. 2, pp. 534–550, 2001.
- [331] T. G. Kolda, “Orthogonal tensor decompositions,” *SIAM Journal on Matrix Analysis and Applications*, vol. 23, no. 1, pp. 243–255, 2001.
- [332] I. Ibraghimov, “Application of the three-way decomposition for matrix compression,” *Numerical linear algebra with applications*, vol. 9, no. 6-7, pp. 551–565, 2002.
- [333] L. De Lathauwer and J. Vandewalle, “Dimensionality reduction in higher-order signal processing and rank- $(R_1, R_2, \dots, R_N)$  reduction in multilinear algebra,” *Linear Algebra and its Applications*, vol. 391, pp. 31–55, 2004.
- [334] A. N. Langville and W. J. Stewart, “A kronecker product approximate preconditioner for SANs,” *Numerical Linear Algebra with Applications*, vol. 11, no. 8-9, pp. 723–752, 2004.
- [335] N. Vervliet, O. Debals, L. Sorber, M. Van Barel, and L. De Lathauwer, “Tensorlab 3.0, Mar. 2016,” URL <http://www.tensorlab.net> Available online, 2016.
- [336] B. Bader and T. Kolda, “Matlab tensor toolbox version 2.2, january 2007,” URL <http://csmr.ca.sandia.gov/tgkolda/TensorToolbox>, 2007.

- [337] B. W. Bader and T. G. Kolda, “Efficient MATLAB computations with sparse and factored tensors,” *SIAM Journal on Scientific Computing*, vol. 30, no. 1, pp. 205–231, 2007.
- [338] V. De Silva and L.-H. Lim, “Tensor rank and the ill-posedness of the best low-rank approximation problem,” *SIAM Journal on Matrix Analysis and Applications*, vol. 30, no. 3, pp. 1084–1127, 2008.
- [339] T. G. Kolda and B. W. Bader, “Tensor decompositions and applications,” *SIAM review*, vol. 51, no. 3, pp. 455–500, 2009.
- [340] L. Grasedyck, “Hierarchical singular value decomposition of tensors,” *SIAM Journal on Matrix Analysis and Applications*, vol. 31, no. 4, pp. 2029–2054, 2010.
- [341] L. Sorber, M. Van Barel, and L. De Lathauwer, “Optimization-based algorithms for tensor decompositions: Canonical polyadic decomposition, decomposition in rank- $(l_r, l_r, 1)$  terms, and a new generalization,” *SIAM Journal on Optimization*, vol. 23, no. 2, pp. 695–720, 2013.
- [342] I. Oseledets, “A new tensor decomposition,” in *Doklady Mathematics*, vol. 80, no. 1. Springer, 2009, pp. 495–496.
- [343] I. V. Oseledets, “Tensor-train decomposition,” *SIAM Journal on Scientific Computing*, vol. 33, no. 5, pp. 2295–2317, 2011.
- [344] I. Oseledets, S. Dolgov, V. Kazeev, O. Lebedeva, and T. Mach, “TT-toolbox 2.2,” *available online*, URL: <http://spring.inm.ras.ru/osel>, 2012.
- [345] B. N. Khoromskij, “Structured rank- $(r_1, \dots, r_d)$  decomposition of function-related tensors in  $R_D$ ,” *Computational Methods in Applied Mathematics Comput. Methods Appl. Math.*, vol. 6, no. 2, pp. 194–220, 2006.
- [346] B. Khoromskij and V. Khoromskaia, “Low rank Tucker-type tensor approximation to classical potentials,” *Open Mathematics*, vol. 5, no. 3, pp. 523–550, 2007.
- [347] B. N. Khoromskij and I. Oseledets, “Quantics-TT collocation approximation of parameter-dependent and stochastic elliptic pdes,” *Computational Methods in Applied Mathematics Comput. Methods Appl. Math.*, vol. 10, no. 4, pp. 376–394, 2010.
- [348] M. A. Turk and A. P. Pentland, “Face recognition using eigenfaces,” in *Proceedings. 1991 IEEE Computer Society Conference on Computer Vision and Pattern Recognition*. IEEE, 1991, pp. 586–591.
- [349] J. Håstad, “Tensor rank is NP-complete,” *Journal of Algorithms*, vol. 11, no. 4, pp. 644–654, 1990.

- [350] W. Hackbusch and S. Kühn, “A new scheme for the tensor representation,” *Journal of Fourier analysis and applications*, vol. 15, no. 5, pp. 706–722, 2009.
- [351] I. V. Oseledets, D. Savostianov, and E. E. Tyrtshnikov, “Tucker dimensionality reduction of three-dimensional arrays in linear time,” *SIAM Journal on Matrix Analysis and Applications*, vol. 30, no. 3, pp. 939–956, 2008.
- [352] M. Rakhuba and I. V. Oseledets, “Fast multidimensional convolution in low-rank tensor formats via cross approximation,” *SIAM Journal on Scientific Computing*, vol. 37, no. 2, pp. A565–A582, 2015.
- [353] G. Zhou, A. Cichocki, and S. Xie, “Decomposition of big tensors with low multilinear rank,” *arXiv preprint arXiv:1412.1885*, 2014.
- [354] V. Cevher, S. Becker, and M. Schmidt, “Convex optimization for big data: Scalable, randomized, and parallel algorithms for big data analytics,” *IEEE Signal Processing Magazine*, vol. 31, no. 5, pp. 32–43, 2014.
- [355] D. Kressner and L. Perisa, “Recompression of hadamard products of tensors in tucker format,” *SIAM Journal on Scientific Computing*, vol. 39, no. 5, pp. A1879–A1902, 2017.
- [356] A. G. Polimeridis, M. H. Reid, S. G. Johnson, J. K. White, and A. W. Rodriguez, “On the computation of power in volume integral equation formulations,” *IEEE Transactions on Antennas and Propagation*, vol. 63, no. 2, pp. 611–620, 2015.
- [357] C. M. Collins and Z. Wang, “Calculation of radiofrequency electromagnetic fields and their effects in MRI of human subjects,” *Magnetic resonance in medicine*, vol. 65, no. 5, pp. 1470–1482, 2011.
- [358] J. Hand, “Modelling the interaction of electromagnetic fields (10 MHz–10 GHz) with the human body: methods and applications,” *Physics in Medicine & Biology*, vol. 53, no. 16, p. R243, 2008.
- [359] E. Balidemaj, H. P. Kok, G. Schooneveldt *et al.*, “Hyperthermia treatment planning for cervical cancer patients based on electrical conductivity tissue properties acquired in vivo with EPT at 3 T MRI,” *International Journal of Hyperthermia*, vol. 32, no. 5, pp. 558–568, 2016.
- [360] M. M. de Oliveira, P. Wen, and T. Ahfock, “Bio-heat transfer model of electroconvulsive therapy: Effect of biological properties on induced temperature variation,” in *Engineering in Medicine and Biology Society (EMBC), 38th Annual International Conference of the IEEE*, 2016, pp. 3997–4000.

- [361] S. K. Hall, E. H. Ooi, and S. J. Payne, "Cell death, perfusion and electrical parameters are critical in models of hepatic radiofrequency ablation," *International Journal of Hyperthermia*, vol. 31, no. 5, pp. 538–550, 2015.
- [362] C. Rossmann and D. Haemmerich, "Review of temperature dependence of thermal properties, dielectric properties, and perfusion of biological tissues at hyperthermic and ablation temperatures," *Critical Reviews™ in Biomedical Engineering*, vol. 42, no. 6, 2014.
- [363] L. J. Gomez, A. C. Yücel, L. Hernandez-Garcia, S. F. Taylor, and E. Michielssen, "Uncertainty quantification in transcranial magnetic stimulation via high-dimensional model representation," *IEEE Transactions on Biomedical Engineering*, vol. 62, no. 1, pp. 361–372, 2015.
- [364] J. O. Nieminen, L. M. Koponen, and R. J. Ilmoniemi, "Experimental characterization of the electric field distribution induced by tms devices," *Brain Stimulation: Basic, Translational, and Clinical Research in Neuromodulation*, vol. 8, no. 3, pp. 582–589, 2015.
- [365] U. Katscher, T. Dorniok, C. Findelee, P. Vernickel, and K. Nehrke, "In vivo determination of electric conductivity and permittivity using a standard MR system," in *13th International Conference on Electrical Bioimpedance and the 8th Conference on Electrical Impedance Tomography*. Springer, 2007, pp. 508–511.
- [366] J. K. Seo, M.-O. Kim, J. Lee *et al.*, "Error analysis of nonconstant admittivity for mr-based electric property imaging," *IEEE transactions on medical imaging*, vol. 31, no. 2, pp. 430–437, 2012.
- [367] X. Zhang, P.-F. V. de Moortele, S. Schmitter, and B. He, "Complex B1 mapping and electrical properties imaging of the human brain using a 16-channel transceiver coil at 7T," *Magnetic resonance in medicine*, vol. 69, no. 5, pp. 1285–1296, 2013.
- [368] J. Liu, X. Zhang, P.-F. Van de Moortele, S. Schmitter, and B. He, "Determining electrical properties based on B1 fields measured in an MR scanner using a multi-channel transmit/receive coil: a general approach," *Physics in medicine and biology*, vol. 58, no. 13, p. 4395, 2013.
- [369] S. Y. Huang, L. Hou, and J. Wu, "MRI-based electrical property retrieval by applying the finite-element method (FEM)," *IEEE Transactions on Microwave Theory and Techniques*, vol. 63, no. 8, pp. 2482–2490, 2015.
- [370] A. L. Van Lier, D. O. Brunner, K. P. Pruessmann *et al.*, "B phase mapping at 7 T and its application for in vivo electrical conductivity mapping," *Magnetic Resonance in Medicine*, vol. 67, no. 2, pp. 552–561, 2012.

- [371] Y. Song and J. K. Seo, "Conductivity and permittivity image reconstruction at the Larmor frequency using MRI," *SIAM Journal on Applied Mathematics*, vol. 73, no. 6, pp. 2262–2280, 2013.
- [372] D. K. Sodickson, L. Alon, C. M. Deniz *et al.*, "Local Maxwell tomography using transmit-receive coil arrays for contact-free mapping of tissue electrical properties and determination of absolute RF phase," in *Proc. ISMRM*, 2012, p. 388.
- [373] Y. Wan, M. Negishi, and R. T. Constable, "2D magnetic resonance electrical property tomography based on B<sub>1</sub>-field mapping," in *Engineering in Medicine and Biology Society (EMBC), 2014 36th Annual International Conference of the IEEE*. IEEE, 2014, pp. 6060–6063.
- [374] J. Lee, J. Shin, and D.-H. Kim, "MR-based conductivity imaging using multiple receiver coils," *Magnetic resonance in medicine*, vol. 76, no. 2, pp. 530–539, 2016.
- [375] J. P. Marques, D. K. Sodickson, O. Ipek, C. M. Collins, and R. Gruetter, "Single acquisition electrical property mapping based on relative coil sensitivities: a proof-of-concept demonstration," *Magnetic resonance in medicine*, vol. 74, no. 1, pp. 185–195, 2015.
- [376] S.-K. Lee, S. Bulumulla, F. Wiesinger *et al.*, "Tissue electrical property mapping from zero echo-time magnetic resonance imaging," *IEEE transactions on medical imaging*, vol. 34, no. 2, pp. 541–550, 2015.
- [377] E. Michel, D. Hernandez, M. H. Cho, and S. Y. Lee, "Denoising of B<sub>1</sub>+ field maps for noise-robust image reconstruction in electrical properties tomography," *Medical physics*, vol. 41, no. 10, 2014.
- [378] L. Guo, J. Jin, C. Liu, F. Liu, and S. Crozier, "An efficient integral-based method for three-dimensional MR-EPT and the calculation of the RF-coil-induced B<sub>z</sub> field," *IEEE Transactions on Biomedical Engineering*, vol. 65, no. 2, pp. 282–293, 2018.
- [379] R. Schmidt and A. Webb, "A new approach for electrical properties estimation using a global integral equation and improvements using high permittivity materials," *Journal of Magnetic Resonance*, vol. 262, pp. 8–14, 2016.
- [380] R. Hong, S. Li, J. Zhang *et al.*, "3-D MRI-based electrical properties tomography using the volume integral equation method," *IEEE Trans. Microw. Theory Tech.*, no. 99, pp. 1–10, 2017.
- [381] J. E. C. Serrallés, E. Boeru, A. G. Polimeridis *et al.*, "Investigation of the feasibility of inverse scattering via Global Maxwell Tomography," in *International Conference on Electromagnetics in Advanced Applications*, 09 2017, p. 668.

- [382] J. E. C. Serrallés, I. Georgakis, A. G. Polimeridis *et al.*, “Volumetric reconstruction of tissue electrical properties from B1+ and MR signals using Global Maxwell Tomography: Theory and simulation results.” in *Proc. ISMRM*, 05 2017, p. 3647.
- [383] C. Zhu, R. H. Byrd, P. Lu, and J. Nocedal, “Algorithm 778: L-BFGS-B: Fortran subroutines for large-scale bound-constrained optimization,” *ACM Transactions on Mathematical Software (TOMS)*, vol. 23, no. 4, pp. 550–560, 1997.
- [384] Y. Wang, A. G. Yagola, C. Yang *et al.*, *Optimization and regularization for computational inverse problems and applications*. Springer, 2011.
- [385] K. Hammernik, T. Klatzer, E. Kobler *et al.*, “Learning a variational network for reconstruction of accelerated MRI data,” *Magnetic resonance in medicine*, vol. 79, no. 6, pp. 3055–3071, 2018.
- [386] S. Roth and M. J. Black, “Fields of experts: A framework for learning image priors,” in *2005 IEEE Computer Society Conference on Computer Vision and Pattern Recognition (CVPR’05)*, vol. 2. Citeseer, 2005, pp. 860–867.
- [387] C. K. Alexander and M. no Sadiku, “Electric circuits,” *Transformation*, vol. 135, pp. 4–5, 2000.
- [388] P. B. Roemer, W. A. Edelstein, C. E. Hayes, S. P. Souza, and O. M. Mueller, “The NMR phased array,” *Magnetic resonance in medicine*, vol. 16, no. 2, pp. 192–225, 1990.
- [389] Z. Mahmood, B. Guérin, E. Adalsteinsson, L. L. Wald, and L. Daniel, “An automated framework to decouple pTx arrays with many channels,” in *Proc. ISMRM*, 2013, p. 2722.
- [390] M. A. Cloos, F. Knoll, T. Zhao *et al.*, “Multiparametric imaging with heterogeneous radiofrequency fields,” *Nature communications*, vol. 7, p. 12445, 2016.
- [391] C. E. Hayes, W. A. Edelstein, J. F. Schenck, O. M. Mueller, and M. Eash, “An efficient, highly homogeneous radiofrequency coil for whole-body NMR imaging at 1.5 T” *Journal of Magnetic Resonance (1969)*, vol. 63, no. 3, pp. 622–628, 1985.
- [392] M. Huhndorf, C. Stehning, A. Rohr *et al.*, “Systematic brain tumor conductivity study with optimized EPT sequence and reconstruction algorithm,” in *Proc. ISMRM*, 2013, p. 3626.
- [393] D.-S. Yoo, “The dielectric properties of cancerous tissues in a nude mouse xenograft model,” *Bioelectromagnetics: Journal of the Bioelectromagnetics Society, The Society for Physical Regulation in Biology and Medicine, The European Bioelectromagnetics Association*, vol. 25, no. 7, pp. 492–497, 2004.
- [394] M. Just and M. Thelen, “Tissue characterization with T1, T2, and proton density values: results in 160 patients with brain tumors.” *Radiology*, vol. 169, no. 3, pp. 779–785, 1988.

- [395] I. Goodfellow, Y. Bengio, and A. Courville, *Deep learning*. MIT press, 2016.
- [396] T. N. Sainath, O. Vinyals, A. Senior, and H. Sak, “Convolutional, long short-term memory, fully connected deep neural networks,” in *2015 IEEE International Conference on Acoustics, Speech and Signal Processing (ICASSP)*. IEEE, 2015, pp. 4580–4584.
- [397] A. Krizhevsky, I. Sutskever, and G. E. Hinton, “Imagenet classification with deep convolutional neural networks,” in *Advances in neural information processing systems*, 2012, pp. 1097–1105.
- [398] Y. Kim, “Convolutional neural networks for sentence classification,” *arXiv preprint arXiv:1408.5882*, 2014.
- [399] P. Isola, J.-Y. Zhu, T. Zhou, and A. A. Efros, “Image-to-image translation with conditional adversarial networks,” in *Proceedings of the IEEE conference on computer vision and pattern recognition*, 2017, pp. 1125–1134.
- [400] Ö. Çiçek, A. Abdulkadir, S. S. Lienkamp, T. Brox, and O. Ronneberger, “3D U-Net: learning dense volumetric segmentation from sparse annotation,” in *International conference on medical image computing and computer-assisted intervention*. Springer, 2016, pp. 424–432.
- [401] A. Paszke, S. Gross, S. Chintala *et al.*, “Automatic differentiation in pytorch,” *NIPS Workshop Autodiff*, 2017.
- [402] M. Mirza and S. Osindero, “Conditional generative adversarial nets,” *arXiv preprint arXiv:1411.1784*, 2014.
- [403] I. Isaev and S. Dolenko, “Training with noise addition in neural network solution of inverse problems: Procedures for selection of the optimal network,” *Procedia computer science*, vol. 123, pp. 171–176, 2018.
- [404] G. G. Guryev, A. G. Polimeridis, L. Wald, E. Adalsteinsson, and J. K. White, “Fast field analysis for complex coils and metal implants in MARIE 2.0.” in *Proc. ISMRM*, 2019, p. 1035.
- [405] I. Sosnovik and I. Oseledets, “Neural networks for topology optimization,” *Russian Journal of Numerical Analysis and Mathematical Modelling*, vol. 34, no. 4, pp. 215–223, 2019.
- [406] C. L. Dumoulin, R. D. Watkins, I. E. T. Iben, S.-A. A. El-Hamamsy, and W. A. Edelstein, “Method to automatically tune mri rf coils,” Apr. 25 2000, uS Patent 6,054,858.
- [407] D. P. Chrissoulidis, “Introduction to scattering of electromagnetic waves,” (*in hellenic*), 2004.

- [408] J. A. Stratton, *Electromagnetic theory*. John Wiley & Sons, 2007.
- [409] H. C. Hulst and H. C. van de Hulst, *Light scattering by small particles*. Courier Corporation, 1957.
- [410] M. Born and E. Wolf, *Principles of optics: electromagnetic theory of propagation, interference and diffraction of light*. Elsevier, 2013.
- [411] C. F. Bohren and D. R. Huffman, *Absorption and scattering by a sphere*. Wiley Online Library, 1983.
- [412] H. Du, “Mie-scattering calculation,” *Applied Optics*, vol. 43, no. 9, pp. 1951–1956, 2004.
- [413] J. Dave, “Scattering of electromagnetic radiation by a large, absorbing sphere,” *IBM Journal of Research and Development*, vol. 13, no. 3, pp. 302–313, 1969.
- [414] G. A. Shah, “Numerical methods for Mie theory of scattering by a sphere,” *Kodalkanal Obs. Bull. Ser. A*, vol. 2, pp. 42–63, 1977.
- [415] **Giannakopoulos, Ilias I**, “MieScattering,” available online, URL: <https://github.com/GiannakopoulosIlias/MieScattering>, 2018.
- [416] J. W. rown *et al.*, *Complex variables and applications*. Boston: McGraw-Hill Higher Education, 2009.
- [417] W. R. LePage, *Complex variables and the Laplace transform for engineers*. Courier Corporation, 2012.
- [418] F. J. Flanigan, *Complex variables: harmonic and analytic functions*. Courier Corporation, 1972.
- [419] J. Mathews and R. Howell, *Complex analysis for mathematics and engineering*. Jones & Bartlett Publishers, 2012.
- [420] W. Wirtinger, “Zur formalen theorie der funktionen von mehr komplexen veränderlichen,” *Mathematische Annalen*, (in german), vol. 97, no. 1, pp. 357–375, 1927.
- [421] K. Kreutz-Delgado, “The complex gradient operator and the CR-calculus,” *arXiv preprint arXiv:0906.4835*, 2009.
- [422] Z. Nehari, *Introduction to complex analysis*. Allyn and Bacon Boston, MA, 1961, vol. 25.
- [423] R. Remmert, *Theory of complex functions*. Springer Science & Business Media, 2012, vol. 122.

- [424] D. Brandwood, "A complex gradient operator and its application in adaptive array theory," in *IEE Proceedings F-Communications, Radar and Signal Processing*, vol. 130, no. 1. IET, 1983, pp. 11–16.
- [425] G. Henkin and J. Leiterer, *Theory of functions on complex manifolds*. Springer, 1983.
- [426] L. Hormander, *An introduction to complex analysis in several variables*. Elsevier, 1973, vol. 7.
- [427] S. G. Krantz, *Function theory of several complex variables*. American Mathematical Soc., 2001, vol. 340.
- [428] B. Shabat, "Introduction to complex analysis, part II. Functions of several variables, transl. math," *Monographs, Amer. Math. Soc.*, vol. 110, 1992.
- [429] A. Van Den Bos, "Complex gradient and Hessian," *IEE Proceedings-Vision, Image and Signal Processing*, vol. 141, no. 6, pp. 380–382, 1994.
- [430] M. Bebendorf, "Approximation of boundary element matrices," *Numerische Mathematik*, vol. 86, no. 4, pp. 565–589, 2000.
- [431] S. Kurz, O. Rain, and S. Rjasanow, "The adaptive cross-approximation technique for the 3D boundary-element method," *IEEE transactions on Magnetics*, vol. 38, no. 2, pp. 421–424, 2002.
- [432] M. Bebendorf and S. Rjasanow, "Adaptive low-rank approximation of collocation matrices," *Computing*, vol. 70, no. 1, pp. 1–24, 2003.
- [433] E. Tyrtshnikov, "Mosaic-skeleton approximations," *Calcolo*, vol. 33, no. 1-2, pp. 47–57, 1996.
- [434] E. Tyrtshnikov, "Mosaic ranks and skeletons," in *International Workshop on Numerical Analysis and Its Applications*. Springer, 1996, pp. 505–516.
- [435] K. Zhao, M. Vouvakis, and J.-F. Lee, "Application of the multilevel adaptive cross-approximation on ground plane designs," in *Electromagnetic Compatibility, 2004. EMC 2004. 2004 International Symposium on*, vol. 1. IEEE, 2004, pp. 124–127.
- [436] K. Zhao, M. N. Vouvakis, and J.-F. Lee, "The adaptive cross approximation algorithm for accelerated method of moments computations of EMC problems," *IEEE transactions on electromagnetic compatibility*, vol. 47, no. 4, pp. 763–773, 2005.
- [437] S. A. Goreinov and E. E. Tyrtshnikov, "The maximal-volume concept in approximation by low-rank matrices," *Contemporary Mathematics*, vol. 280, pp. 47–52, 2001.

- [438] S. Goreinov, I. Oseledets, D. Savostyanov, E. Tyrtshnikov, and N. Zamarashkin, “How to find a good submatrix,” in *Matrix Methods: Theory, Algorithms And Applications: Dedicated to the Memory of Gene Golub*. World Scientific, 2010, pp. 247–256.
- [439] M. A. Woodbury, “Inverting modified matrices,” *Memorandum report*, vol. 42, no. 106, p. 336, 1950.
- [440] J. Sherman and W. J. Morrison, “Adjustment of an inverse matrix corresponding to a change in one element of a given matrix,” *The Annals of Mathematical Statistics*, vol. 21, no. 1, pp. 124–127, 1950.
- [441] K. K. Sabelfeld and I. Shalimopva, *Spherical means for PDEs*. Vsp, 1997.



# Appendix A

## MIE SCATTERING

---

In this appendix, we will provide a brief analysis of the Mie solution to Maxwell's equations for the scattering of a sphere, when a linear polarized plane wave irradiates it. The solution developed initially in [138] by Gustav Mie, takes the form of an infinite series expansion, with basis the vector spherical harmonics (wave functions). Modern formulations of the solution can be found in many textbooks in the literature like [407–414]. Finally, most of the following implementations are available as open-source software on GitHub [415].

### A.1 Debye's Potentials

The electromagnetic field can be expressed with the help of Debye's potentials (electric  $\pi_e$ , magnetic  $\pi_m$ ). We note that the Debye's potentials are connected to the well-known Hertz potential ( $\pi_h$ ) according to the following

$$\begin{aligned} r\pi_m &= j\omega\epsilon(\pi_h \cdot \hat{r}) \\ r\pi_e &= (\nabla \times \pi_h) \cdot \hat{r}, \end{aligned} \tag{A.1}$$

where  $\omega$  is the angular frequency,  $\epsilon$  is the permittivity of the dielectric medium and  $r$  is the distance in the Euclidean space. As a result, the electromagnetic field is written as follows

$$\begin{aligned} \mathbf{e} &= \nabla \times (\pi_e \mathbf{r}) + \frac{1}{i\omega\epsilon} \nabla \times \nabla \times (\pi_m \mathbf{r}) \\ \mathbf{h} &= -\frac{1}{i\omega\mu} \nabla \times \nabla \times (\pi_e \mathbf{r}) + \nabla \times (\pi_m \mathbf{r}). \end{aligned} \tag{A.2}$$

The first term of the right hand side of A.2 is a transverse electric (TE) wave and the second one is a transverse magnetic (TM) wave. Since our goal is to find the scattered electromagnetic field from a sphere, it makes more sense to use spherical coordinates from now on. Therefore, the

electromagnetic field can written as

$$\begin{aligned}
 e_r &= \frac{1}{i\omega\epsilon} \left( \frac{\partial^2}{\partial r^2} + k^2 \right) (r\pi_m), & h_r &= -\frac{1}{i\omega\mu} \left( \frac{\partial^2}{\partial r^2} + k^2 \right) (r\pi_e) \\
 e_\theta &= \frac{1}{i\omega\epsilon r} \frac{\partial^2(r\pi_m)}{\partial r\partial\theta} + \frac{1}{r\sin\theta} \frac{\partial(r\pi_e)}{\partial\phi}, & h_\theta &= -\frac{1}{i\omega\mu r} \frac{\partial^2(r\pi_e)}{\partial r\partial\theta} + \frac{1}{r\sin\theta} \frac{\partial(r\pi_m)}{\partial\phi} \\
 e_\phi &= \frac{1}{i\omega\epsilon r\sin\theta} \frac{\partial^2(r\pi_m)}{\partial r\partial\phi} - \frac{1}{r} \frac{\partial(r\pi_e)}{\partial\theta}, & h_\phi &= -\frac{1}{i\omega\mu r\sin\theta} \frac{\partial^2(r\pi_e)}{\partial r\partial\phi} - \frac{1}{r} \frac{\partial(r\pi_m)}{\partial\theta},
 \end{aligned} \tag{A.3}$$

where  $k$  is the wavenumber of the medium. By applying the Maxwell's equations on the TE wave, we will obtain the following differential equation

$$[(\nabla \times \nabla \times) - k^2]\pi_e \mathbf{r} = \nabla\psi, \tag{A.4}$$

where  $\psi$  is an arbitrary function. By considering the following identity for  $\mathbf{f}$

$$\nabla \times \nabla \times \mathbf{f} = \nabla(\nabla \cdot \mathbf{f}) - \nabla^2 \mathbf{f}, \tag{A.5}$$

the equation A.4 becomes

$$\nabla[\nabla \cdot (\pi_e \mathbf{r})] - (\nabla^2 + k^2)(\pi_e \mathbf{r}) = \nabla\psi. \tag{A.6}$$

Now, using the identities

$$\begin{aligned}
 \nabla(\phi \mathbf{f}) &= \phi \nabla \mathbf{f} + \mathbf{f} \nabla \phi \\
 \nabla^2(\phi \mathbf{f}) &= \phi \nabla^2 \mathbf{f} + \mathbf{f} \nabla^2 \phi + 2(\nabla \phi \cdot \nabla) \mathbf{f},
 \end{aligned} \tag{A.7}$$

and also that  $\nabla \mathbf{r} = 3$  and  $\nabla^2 \mathbf{r} = 0$ , the equation A.6 acquires the following form

$$\mathbf{r}(\nabla^2 + k^2)\pi_e = \nabla \left( \frac{\partial(r\pi_e)}{\partial r} - \psi \right). \tag{A.8}$$

Since,  $\psi$  is an arbitrary function, it can be equal to  $\partial(r\pi_e)/\partial r$ . Consequently, the equation A.8 becomes the homogeneous Helmholtz equation  $(\nabla^2 + k^2)\pi_e = 0$ . It is proven (following the same thinking) that  $\pi_m$  satisfies the same equation. Therefore, in order to find the electric and the magnetic field, we have to solve the Helmholtz equation, which, in spherical coordinates can be written as

$$\left( \frac{\partial^2}{\partial r^2} + \frac{2}{r} \frac{\partial}{\partial r} + \frac{1}{r^2} \frac{\partial^2}{\partial \theta^2} + \frac{\cot\theta}{r^2} \frac{\partial}{\partial \theta} + \frac{1}{r^2 \sin^2 \theta} \frac{\partial^2}{\partial \phi^2} + k^2 \right) \pi(r, \theta, \phi) = 0, \tag{A.9}$$

where  $\pi$  is either the electric or the magnetic Debye's potential. It is proven that the equation A.9 has a solution of the form  $\pi(r, \theta, \phi) = R(r)\Theta(\theta)\Phi(\phi)$ . For  $\Phi(\phi)$  the solution is

$$\begin{aligned}
 \Phi^e(\phi) &= \cos(m\phi) \\
 \Phi^o(\phi) &= \sin(m\phi),
 \end{aligned} \tag{A.10}$$

where  $m = -i\mu$  and  $\mu \in \mathbb{Z}$ . The marks e and o denote the even and the odd symmetry in respect to  $\hat{x}$  axis. The solutions  $\Theta(\theta)$  are the associate Legendre functions of the first and second kind  $P_n^m(\cos \theta)$ ,  $Q_n^m(\cos \theta)$  respectively. The second kind functions are not accepted as solutions because they are not blocked at  $\theta = 0$ ,  $\theta = \pi$  and  $\theta = -\pi$ . The functions of the first kind are connected with the Legendre polynomials with the following equation

$$P_n^m(x) = (-1)^m (1-x^2)^{\frac{m}{2}} \frac{d^m}{dx^m} P_n(x) \quad 0 < m \leq n. \quad (\text{A.11})$$

Some Legendre polynomials are portrayed in figure A.1.

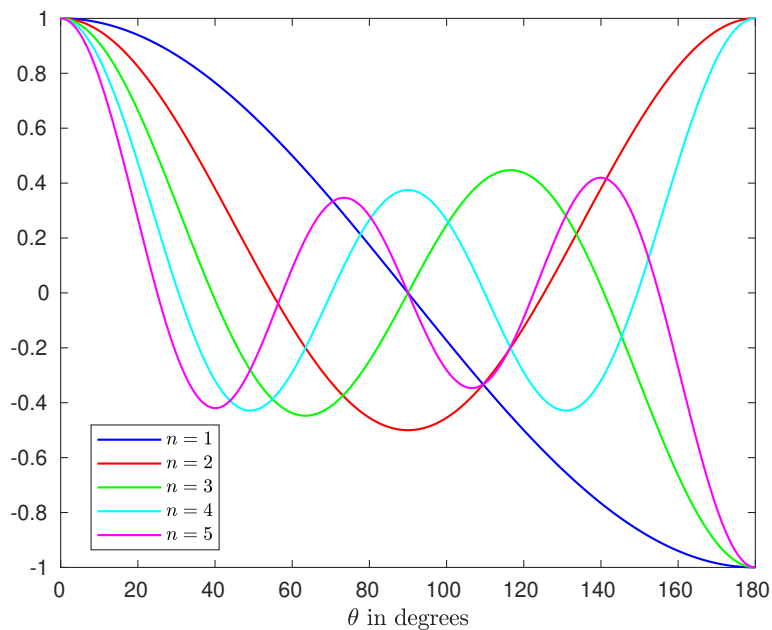


Figure A.1: Legendre polynomials.

Finally, the solutions of  $R(r)$  are the spherical Bessel functions of the first and second kind and the spherical Hankel functions of the first and second kind. Their general form is  $R(r) = z_n^{(i)}(kr)$ , where

$$\begin{aligned} z_n^{(1)}(kr) &= j_n(kr) \\ z_n^{(2)}(kr) &= y_n(kr) \\ z_n^{(3)}(kr) &= h_n^{(1)}(kr) \\ z_n^{(4)}(kr) &= h_n^{(2)}(kr). \end{aligned} \quad (\text{A.12})$$

All these functions are linear independent for every value of  $n \in \mathbb{N}$ . In the case of a standing wave, the solutions will contain the spherical Bessel functions of the first and second kind. Although if the solution must be finite in the point  $(0, 0, 0)$ , then we must reject the second kind functions since they tend to infinity when  $r \rightarrow 0$ . This behavior is illustrated in figure A.2. In the case of radiated waves, the solution will contain spherical Hankel functions of the first and second kind.

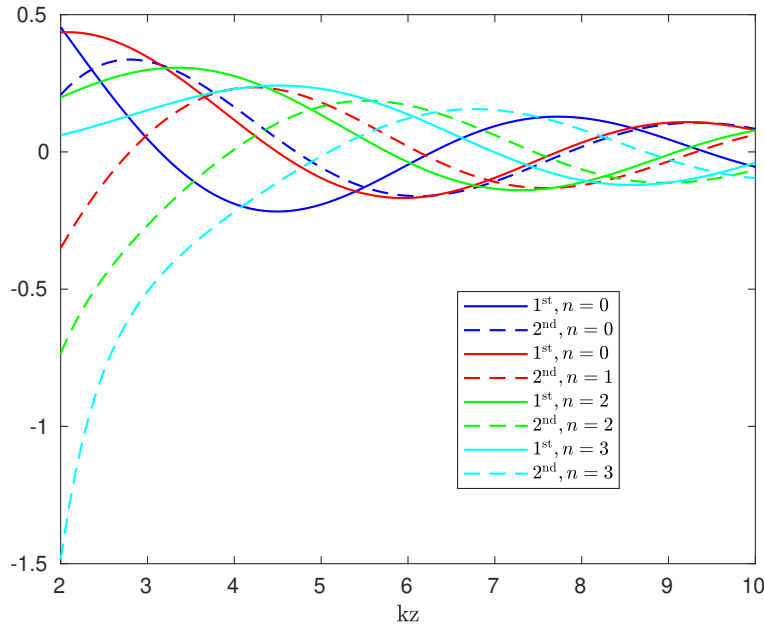


Figure A.2: Spherical Bessel functions of the first and second kind.

Furthermore, for  $kr \gg 1$  the approximations

$$\begin{aligned} h_n^{(1)}(kr) &\rightarrow (-i)^{n+1} \frac{e^{ikr}}{kr} \\ h_n^{(2)}(kr) &\rightarrow i^{n+1} \frac{e^{-ikr}}{kr}, \end{aligned} \quad (\text{A.13})$$

contain the factor  $e^{\pm ikr}/kr$ , which characterizes travelling spherical waves. Thus, if the dependence of the time is  $e^{-i\omega t}$ , we will use the first kind functions, but, if the dependence is  $e^{i\omega t}$ , then the second kind functions are used.

To conclude, the solution of A.9 has the following general forms

$$\begin{aligned} f_{mn}^{ie} &= z_n^{(i)}(kr) P_n^m(\cos \theta) \cos(m\phi) \\ f_{mn}^{io} &= z_n^{(i)}(kr) P_n^m(\cos \theta) \sin(m\phi), \end{aligned} \quad (\text{A.14})$$

which means that Debye's potentials can be written as

$$\pi_e = \sum_{n=0}^{\infty} \sum_{m=0}^n M_{mn} f_{mn}^{ie,o}, \quad \pi_m = \sum_{n=0}^{\infty} \sum_{m=0}^n N_{mn} f_{mn}^{ie,o}. \quad (\text{A.15})$$

The constants  $M_{mn}$  and  $N_{mn}$  depend from the sphere, and they can be identified with the application of the proper boundary conditions.

## A.2 Spherical Wave Functions

The electric and the magnetic field can be expressed with the help of Debye's potentials as

follows

$$\begin{aligned}\mathbf{E} &= \sum_{n=0}^{\infty} \sum_{m=0}^n \left( M_{mn} \mathbf{m}_{mn}^{ie,o} - i \sqrt{\frac{\mu}{\epsilon}} N_{mn} \mathbf{n}_{mn}^{ie,o} \right) \\ \mathbf{H} &= \sum_{n=0}^{\infty} \sum_{m=0}^n \left( N_{mn} \mathbf{m}_{mn}^{ie,o} - \frac{1}{i \sqrt{\frac{\mu}{\epsilon}}} M_{mn} \mathbf{n}_{mn}^{ie,o} \right),\end{aligned}\tag{A.16}$$

where

$$\begin{aligned}\mathbf{m}_{mn}^{ie,o} &= \nabla \times (f_{mn}^{ie,o} \mathbf{r}) \\ \mathbf{n}_{mn}^{ie,o} &= \frac{1}{k} \nabla \times \nabla \times (f_{mn}^{ie,o} \mathbf{r}),\end{aligned}\tag{A.17}$$

are the so-called *spherical wave functions*. One can easily note that these two functions are independent solutions of the homogeneous vector Helmholtz equation. They are both solenoidal and satisfy the following equations

$$\begin{aligned}\mathbf{m}_{mn}^{ie,o} &= \frac{1}{k} \nabla \times \mathbf{n}_{mn}^{ie,o} \\ \mathbf{n}_{mn}^{ie,o} &= \frac{1}{k} \nabla \times \mathbf{m}_{mn}^{ie,o},\end{aligned}\tag{A.18}$$

thus, they are orthogonal to each other. We will write the spherical wave functions analytically in the spherical coordinates system

$$\begin{aligned}\mathbf{m}_{mn}^{ie} &= -\hat{\theta} z_n^{(i)}(kr) \frac{P_n^m(\cos \theta)}{\sin \theta} m \sin(m\phi) \\ &\quad - \hat{\phi} z_n^{(i)}(kr) \frac{dP_n^m(\cos \theta)}{d\theta} \cos(m\phi) \\ \mathbf{m}_{mn}^{io} &= -\hat{\theta} z_n^{(i)}(kr) \frac{P_n^m(\cos \theta)}{\sin \theta} \cos(m\phi) \\ &\quad - \hat{\phi} z_n^{(i)}(kr) \frac{dP_n^m(\cos \theta)}{d\theta} \sin(m\phi) \\ \mathbf{n}_{mn}^{ie} &= \hat{r} n(n+1) \frac{z_n^{(i)}(kr)}{kr} P_n^m(\cos \theta) \cos(m\phi) \\ &\quad + \hat{\theta} \left[ \frac{z_n^{(i)}(kr)}{kr} \right]' \frac{dP_n^m(\cos \theta)}{d\theta} \cos(m\phi) \\ &\quad - \hat{\phi} \left[ \frac{z_n^{(i)}(kr)}{kr} \right]' \frac{P_n^m(\cos \theta)}{\sin \theta} m \sin(m\phi) \\ \mathbf{n}_{mn}^{io} &= \hat{r} n(n+1) \frac{z_n^{(i)}(kr)}{kr} P_n^m(\cos \theta) \sin(m\phi) \\ &\quad + \hat{\theta} \left[ \frac{z_n^{(i)}(kr)}{kr} \right]' \frac{dP_n^m(\cos \theta)}{d\theta} \sin(m\phi) \\ &\quad - \hat{\phi} \left[ \frac{z_n^{(i)}(kr)}{kr} \right]' \frac{P_n^m(\cos \theta)}{\sin \theta} m \cos(m\phi).\end{aligned}\tag{A.19}$$

where for convenience the symbol ' denotes derivation with respect to the argument. At this point we need to calculate the inner product of all the above possible cases, since we will need

it for the remaining of this Appendix. We note that the inner product of two spherical wave functions is defined as follows

$$\langle \mathbf{x}, \mathbf{y} \rangle = \int_{\phi=0}^{2\pi} \int_{\theta=0}^{\pi} \mathbf{x} \cdot \mathbf{y} \sin \theta d\theta d\phi. \quad (\text{A.20})$$

It is proven that  $(\mathbf{x}^e, \mathbf{y}^o) = 0$  and  $(\mathbf{x}_{mn}, \mathbf{y}_{m'n'}) = 0$ , where  $m' \neq m$  and  $n' \neq n$ . If  $m = m'$  and  $n = n'$  we end up to the following equations

$$\begin{aligned} \langle \mathbf{m}_{mn}^{ie,o}, \mathbf{m}_{mn}^{ie,o} \rangle &= \frac{4\pi}{\epsilon_m} \frac{n(n+1)}{(2n+1)} \frac{(n+m)!}{(n-m)!} \left[ z_n^{(i)}(kr) \right]^2 \\ \langle \mathbf{n}_{mn}^{ie,o}, \mathbf{n}_{mn}^{ie,o} \rangle &= \frac{4\pi}{\epsilon_m} \frac{n(n+1)}{(2n+1)^2} \frac{(n+m)!}{(n-m)!} \left\{ (n+1) \left[ z_{n-1}^{(i)}(kr) \right]^2 + n \left[ z_{n+1}^{(i)}(kr) \right]^2 \right\}, \end{aligned} \quad (\text{A.21})$$

with  $\epsilon_m$  being the Neumann constant.

### A.3 Incident Plane Wave

In figure A.3, we can see a sphere irradiated by a linear polarized plane wave ( $\mathbf{e}_{\text{inc}} \parallel \hat{x}$ ,  $\mathbf{h}_{\text{inc}} \parallel \hat{y}$ ). In this and the following sections, we will derive analytical solutions for the electromagnetic quantities for this simple case.

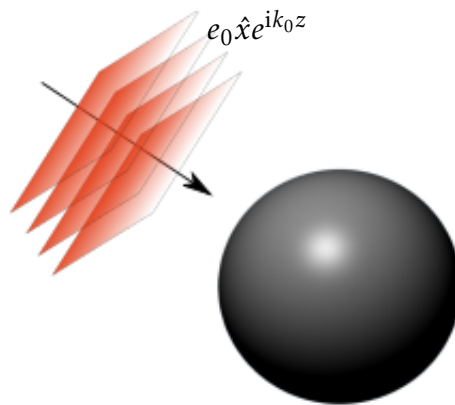


Figure A.3: Incident plane wave.

The incident electromagnetic wave in cartesian coordinates is

$$\begin{aligned} \mathbf{e}_{\text{inc}} &= e_0 \hat{x} e^{i(\omega t - k_0 z)} \\ \mathbf{h}_{\text{inc}} &= \frac{e_0}{\sqrt{\frac{\mu_0}{\epsilon_0}}} \hat{y} e^{i(\omega t - k_0 z)}. \end{aligned} \quad (\text{A.22})$$

We can skip the time-dependent term since we are dealing with time-harmonic problems. Furthermore, it is convenient to use spherical coordinates since we are dealing with spheres. The

incident fields are

$$\begin{aligned}\mathbf{e}_{\text{inc}} &= e_0(\hat{r} \sin \theta \cos \phi + \hat{\theta} \cos \theta \cos \phi - \hat{\phi} \sin \phi)e^{-ik_0 r \cos \theta} \\ \mathbf{e}_{\text{inc}} &= \frac{e_0}{\sqrt{\frac{\mu_0}{\epsilon_0}}}(\hat{r} \sin \theta \sin \phi + \hat{\theta} \cos \theta \sin \phi - \hat{\phi} \cos \phi)e^{-ik_0 r \cos \theta}.\end{aligned}\quad (\text{A.23})$$

Therefore, the Debye's potentials can be written as

$$\begin{aligned}\pi_e &= \sum_{n=1}^{\infty} M_n f_{1n}^{1o} \\ \pi_m &= \sum_{n=1}^{\infty} N_n f_{1n}^{1e},\end{aligned}\quad (\text{A.24})$$

where

$$f_{1n}^{1e} = j_n(k_0 r) P_n^1(\cos \theta) \cos \phi f_{1n}^{1o} = j_n(k_0 r) P_n^1(\cos \theta) \sin \phi. \quad (\text{A.25})$$

We are choosing  $i = 1$ , because the solutions must be definite for  $r \rightarrow 0$ . Therefore the incident field can be written with the help of spherical wave functions as follows

$$\begin{aligned}\mathbf{e}_{\text{inc}} &= \sum_{n=1}^{\infty} (M_n \mathbf{m}_{1n}^{1o} - i \sqrt{\frac{\mu_0}{\epsilon_0}} N_n \mathbf{n}_{1n}^{1e}) \\ \mathbf{e}_{\text{inc}} &= \sum_{n=1}^{\infty} (N_n \mathbf{m}_{1n}^{1e} - \frac{1}{i \sqrt{\frac{\mu_0}{\epsilon_0}}} M_n \mathbf{n}_{1n}^{1o}).\end{aligned}\quad (\text{A.26})$$

To define the coefficients  $M_n$  and  $N_n$  we have to calculate the inner product  $\langle \mathbf{e}^i, \mathbf{m}_{1n}^{1o} \rangle$

$$\langle \mathbf{e}_{\text{inc}}, \mathbf{m}_{1n}^{1o} \rangle = 2\pi \frac{n(n+1)(n+1)!}{(2n+1)(n-1)!} [j_n(k_0 r)]^2 M_n. \quad (\text{A.27})$$

Since the left hand side is equal to  $-2\pi e_0 (-j)^n n(n+1) [j_n(k_0 r)]^2$  the coefficients  $M_n$  and  $N_n$  are

$$\begin{aligned}M_n &= -e_0 (-i)^n \frac{2n+1}{n(n+1)} \\ N_n &= \frac{e_0}{\sqrt{\frac{\mu_0}{\epsilon_0}}} (-i)^n \frac{2n+1}{n(n+1)}.\end{aligned}\quad (\text{A.28})$$

The incident fields are

$$\begin{aligned}\mathbf{e}_{\text{inc}} &= -e_0 \sum_{n=1}^{\infty} (-i)^n \frac{2n+1}{n(n+1)} (\mathbf{m}_{1n}^{1o} + i \mathbf{n}_{1n}^{1e}) \\ \mathbf{h}_{\text{inc}} &= -\frac{e_0}{\sqrt{\frac{\mu_0}{\epsilon_0}}} \sum_{n=1}^{\infty} (-i)^n \frac{2n+1}{n(n+1)} (\mathbf{m}_{1n}^{1e} - i \mathbf{n}_{1n}^{1o}).\end{aligned}\quad (\text{A.29})$$

#### A.4 Scattered Wave

The scattered electric wave from a sphere is

$$\mathbf{e}_{\text{sca}} = e_0 \sum_{n=1}^{\infty} \sum_{m=0}^n (-i)^n \frac{2n+1}{n(n+1)} (A_{mn}^o \mathbf{m}_{mn}^{4o} + A_{mn}^e \mathbf{m}_{mn}^{4e} + i B_{mn}^o \mathbf{n}_{mn}^{4o} + j B_{mn}^e \mathbf{n}_{mn}^{4e}). \quad (\text{A.30})$$

In the case of a perfect electric conducting sphere with radius  $a$  we have to enforce the following boundary condition

$$\hat{r}(\mathbf{e}_{\text{inc}} + \mathbf{e}_{\text{sca}})|_{r=a} = 0. \quad (\text{A.31})$$

Thus, we can derive the following simple form

$$\mathbf{e}_{\text{sca}} = -e_0 \sum_{n=1}^{\infty} (-i)^n \frac{2n+1}{n(n+1)} (A_n \mathbf{m}_{1n}^{4o} + jB_n \mathbf{n}_{1n}^{4e}), \quad (\text{A.32})$$

where  $A_n$  and  $B_n$  are coefficients to be calculated. By applying the Maxwell's equation  $\nabla \times \mathbf{e}_{\text{sca}} = -i\omega\mu_0 \mathbf{h}_{\text{sca}}$  we derive the following

$$\mathbf{h}_{\text{sca}} = \frac{e_0}{\sqrt{\frac{\mu_0}{\epsilon_0}}} \sum_{n=1}^{\infty} (-i)^n \frac{2n+1}{n(n+1)} (B_n \mathbf{m}_{1n}^{4e} - jA_n \mathbf{n}_{1n}^{4o}). \quad (\text{A.33})$$

### A.5 Impenetrable Sphere

In the case of an impenetrable sphere (PEC), the boundary conditions to be satisfied are

$$\int_0^{2\pi} \int_0^{\pi} \left\{ [\hat{r} \times (\mathbf{e}_{\text{inc}} + \mathbf{e}_{\text{sca}})] \times \mathbf{m}_{1v}^1 \right\}_{r=a} \sin \theta d\theta d\phi = 0 \quad (\text{A.34})$$

$$\int_0^{2\pi} \int_0^{\pi} \left\{ [\hat{r} \times (\mathbf{e}_{\text{inc}} + \mathbf{e}_{\text{sca}})] \mathbf{m}_{1v}^{1e} \right\}_{r=a} \sin \theta d\theta d\phi = 0,$$

where  $v \in \mathbb{N}$ . After some calculations we can derive the coefficients  $A_n, B_n$  according to

$$A_n = -\frac{j_n(k_0 a)}{h_n^{(2)}(k_0 a)}$$

$$B_n = -\frac{[k_0 r j_n(k_0 r)]'}{[k_0 r h_n^{(2)}(k_0 r)]'} \Big|_{r=a}. \quad (\text{A.35})$$

For the far field calculations, the scattered electric field is a TEM waveform given by

$$\mathbf{e}_{\text{sca}} = (f_{\theta} \hat{\theta} + f_{\phi} \hat{\phi}) \frac{e^{i(\omega t - k_0 r)}}{r}, \quad (\text{A.36})$$

where

$$f_{\theta}(\theta, \phi) = -\frac{ie_0}{k_0} \cos \phi \sum_{n=1}^{\infty} \frac{2n+1}{n(n+1)} \left[ A_n \frac{P_n^1(\cos \theta)}{\sin \theta} + B_n \frac{dP_n^1(\cos \theta)}{d\theta} \right]$$

$$f_{\phi}(\theta, \phi) = \frac{ie_0}{k_0} \sin \phi \sum_{n=1}^{\infty} \frac{2n+1}{n(n+1)} \left[ A_n \frac{dP_n^1(\cos \theta)}{d\theta} + B_n \frac{P_n^1(\cos \theta)}{\sin \theta} \right]. \quad (\text{A.37})$$

We note that in the case of  $\theta = 0$ ,  $\theta = \pi$  or  $\theta = -\pi$ , we should consider the following

$$\frac{P_n^1(\cos \theta)}{\sin \theta} \Big|_{\theta=0} = \frac{dP_n^1(\cos \theta)}{d\theta} \Big|_{\theta=0} = -\frac{n(n+1)}{2}$$

$$\frac{P_n^1(\cos \theta)}{\sin \theta} \Big|_{\theta=\pm\pi} = -\frac{dP_n^1(\cos \theta)}{d\theta} \Big|_{\theta=\pm\pi} = (-1)^n \frac{n(n+1)}{2}. \quad (\text{A.38})$$

According to the above, the bistatic radar cross section (BRCS) is given from

$$\sigma_d = |\mathbf{f}(\theta, \phi)|^2 = |f_\theta|^2 + |f_\phi|^2. \quad (\text{A.39})$$

Moreover, the monostatic radar cross section (MRCS) will be

$$\frac{\sigma_{mo}}{\pi a^2} = \frac{1}{(k_0 a)^2} \left| \sum_{n=1}^{\infty} (-1)^n (2n+1) (A_n - B_n) \right|^2. \quad (\text{A.40})$$

Furthermore, The total radar cross section can be computed from the following integral

$$\sigma_s = \int_{4\pi} \sigma_d d\Omega = \int_0^{2\pi} \int_0^\pi |\mathbf{f}(\theta, \phi)|^2 \sin \theta d\theta d\phi. \quad (\text{A.41})$$

After some operations we can retrieve the following elegant form

$$\frac{\sigma_s}{\pi a^2} = \frac{2}{(k_0 a)^2} \sum_{n=1}^{\infty} (2n+1) (|A_n|^2 + |B_n|^2). \quad (\text{A.42})$$

Finally, the elimination section is given from the following equation

$$\frac{\sigma_e}{\pi a^2} = -\frac{2}{(k_0 a)^2} \sum_{n=1}^{\infty} (2n+1) \mathcal{R}e\{A_n + B_n\}. \quad (\text{A.43})$$

## A.6 Penetrable Sphere

In the case of a penetrable sphere (a dielectric sphere) with a refractive index  $n_s$ , the interior field is given from

$$\begin{aligned} \mathbf{e}_{\text{int}} &= -e_0 \sum_{n=1}^{\infty} (-i)^n \frac{2n+1}{n(n+1)} (C_n \mathbf{m}_{1n}^{1o} + jD_n \mathbf{n}_{1n}^{1e}) \\ \mathbf{h}_{\text{int}} &= \frac{e_0}{\sqrt{\frac{\mu_0}{\epsilon_0}}} \sum_{n=1}^{\infty} (-i)^n \frac{2n+1}{n(n+1)} (D_n \mathbf{m}_{1n}^{1e} - jC_n \mathbf{n}_{1n}^{1o}), \end{aligned} \quad (\text{A.44})$$

where  $C_n$  and  $D_n$  are the wave coefficients of the refracted wave. We note that the change of  $i$  from 4 to 1, is done, because the spherical Bessel function ( $j_n(n_s k_0 r)$ ) must be definite when  $r \rightarrow 0$ . Moreover. The boundary conditions on the surface of the sphere are

$$\begin{aligned} \hat{r} \times (\mathbf{e}_{\text{inc}} + \mathbf{e}_{\text{sca}})|_{r=a} &= \hat{r} \times \mathbf{e}_{\text{int}}|_{r=a} \\ \hat{r} \times (\mathbf{h}_{\text{inc}} + \mathbf{h}_{\text{sca}})|_{r=a} &= \hat{r} \times \mathbf{h}_{\text{int}}|_{r=a}, \end{aligned} \quad (\text{A.45})$$

and after some simple operations we can calculate the wave coefficients. We tabulate them in A.1.

In the case of a dielectric sphere, BRCS, MRCS, total, and extinction cross-sections are given from the same equations as in the case of the PEC sphere. However, for the dielectric spheres we

Table A.1: Mie scattering coefficients

$A_n$ (PEC)	$-\frac{j_n(k_0a)}{h_n^{(2)}(k_0a)}$
$B_n$ (PEC)	$-\frac{[k_0r j_n(k_0r)]'}{[k_0r h_n^{(2)}(k_0r)]'} \Big _{r=a}$
$A_n$ (Dielectric)	$-\frac{j_n(n_s k_0a) [k_0a j_n(k_0a)]' - j_n(k_0a) [n_s k_0a j_n(n_s k_0a)]'}{j_n(n_s k_0a) [k_0a h_n^{(2)}(k_0a)]' - h_n^{(2)}(k_0a) [n_s k_0a j_n(n_s k_0a)]'}$
$B_n$ (Dielectric)	$-\frac{j_n(k_0a) [n_s k_0a j_n(n_s k_0a)]' - n_s^2 j_n(n_s k_0a) [k_0a j_n(k_0a)]'}{h_n^{(2)}(k_0a) [n_s k_0a j_n(n_s k_0a)]' - n_s^2 j_n(n_s k_0a) [k_0a h_n^{(2)}(k_0a)]'}$
$C_n$ (Dielectric)	$-\frac{-j_n(k_0a) [k_0a h_n^{(2)}(k_0a)]' + h_n^{(2)}(k_0a) [k_0a j_n(k_0a)]'}{j_n(n_s k_0a) [k_0a h_n^{(2)}(k_0a)]' - h_n^{(2)}(k_0a) [n_s k_0a j_n(n_s k_0a)]'}$
$D_n$ (Dielectric)	$-n_s \frac{j_n(k_0a) [k_0a h_n^{(2)}(k_0a)]' - h_n^{(2)}(k_0a) [k_0a j_n(k_0a)]'}{h_n^{(2)}(k_0a) [n_s k_0a j_n(n_s k_0a)]' - n_s^2 j_n(n_s k_0a) [k_0a h_n^{(2)}(k_0a)]'}$

are dealing with the absorption cross-section  $\sigma_a = \sigma_e - \sigma_s$  as well, which was 0 for the PEC case, which means that the dielectric sphere presents losses.

### A.7 Extinction- and Scattering-Cross Sections

The scattered and extinction cross-sections from a sphere can be obtained from the following equations

$$c_{\text{sca}} = \frac{w_{\text{sca}}}{i_{\text{inc}}}, \quad c_{\text{ext}} = \frac{w_{\text{ext}}}{i_{\text{inc}}}, \quad i_{\text{inc}} = \frac{|\mathbf{e}_{\text{incl}}|^2}{2\sqrt{\frac{\mu_0}{\epsilon_0}}} \quad (\text{A.46})$$

where  $i_{\text{inc}}$  is the intensity incident of the sphere. The scattered  $w_{\text{sca}}$  and the extinction  $w_{\text{ext}}$  energies can be calculated by

$$\begin{aligned} w_{\text{sca}} &= \frac{1}{2} \mathcal{R}e \left\{ \int_0^{2\pi} \int_0^\pi (\mathbf{e}_{\text{sca}} \times \mathbf{h}_{\text{sca}}^*) r^2 \sin \theta d\theta d\phi \right\} = \frac{1}{2} \mathcal{R}e \left\{ \int_0^{2\pi} \int_0^\pi (\mathbf{e}_{\text{sca},\theta} \times \mathbf{h}_{\text{sca},\phi}^* - \mathbf{e}_{\text{sca},\phi} \times \mathbf{h}_{\text{sca},\theta}^*) r^2 \sin \theta d\theta d\phi \right\} \\ w_{\text{ext}} &= \frac{1}{2} \mathcal{R}e \left\{ \int_0^{2\pi} \int_0^\pi (\mathbf{e}_{\text{inc}} \times \mathbf{h}_{\text{sca}}^* + \mathbf{e}_{\text{sca}} \times \mathbf{h}_{\text{inc}}^*) r^2 \sin \theta d\theta d\phi \right\} = \\ &= \frac{1}{2} \mathcal{R}e \left\{ \int_0^{2\pi} \int_0^\pi (\mathbf{e}_{\text{inc},\phi} \times \mathbf{h}_{\text{sca},\theta}^* - \mathbf{e}_{\text{inc},\theta} \times \mathbf{h}_{\text{sca},\phi}^* - \mathbf{e}_{\text{sca},\theta} \times \mathbf{h}_{\text{inc},\phi}^* + \mathbf{e}_{\text{sca},\phi} \times \mathbf{h}_{\text{inc},\theta}^*) r^2 \sin \theta d\theta d\phi \right\}. \end{aligned} \quad (\text{A.47})$$

The absorbed energy relates with the scattered and extinction energies by  $w_{\text{abs}} = w_{\text{ext}} - w_{\text{sca}}$ .

Therefore, the scattering and the extinction cross-sections are

$$\begin{aligned}
C_{\text{sca}} &= \frac{2\pi}{k_0^2} \sum_{n=1}^{\infty} (2n+1)(A_n |H_{n,m}|^2 + B_n |F_{l,m}|^2) \\
C_{\text{ext}} &= \frac{2\pi}{k_0^2} \mathcal{Re} \left\{ \sum_{n=1}^{\infty} (2n+1)(A_n |H_{n,m}|^2 + B_n |F_{l,m}|^2) \right\}.
\end{aligned} \tag{A.48}$$

The functions  $F_{n,m}$  and  $H_{n,m}$  are given from the following formulas

$$\begin{aligned}
F_{n,m} &= \frac{2}{n(n+1)} \sum_{m=-n}^{m=n} \frac{(n-m)!}{(n+m)!} \left| \frac{m P_n^m}{\sin \theta} \right|^2 \\
H_{n,m} &= \frac{2}{n(n+1)} \sum_{m=-n}^{m=n} \frac{(n-m)!}{(n+m)!} \left| \frac{d P_n^m}{d \theta} \right|^2.
\end{aligned} \tag{A.49}$$

For the case of plane wave excitation where all terms vanish except for  $m = 1$  the cross-sections become

$$\begin{aligned}
C_{\text{sca}} &= \frac{2\pi}{k_0^2} \sum_{n=1}^{\infty} (2n+1)(|A_n|^2 + |B_n|^2) \\
C_{\text{ext}} &= \frac{2\pi}{k_0^2} \mathcal{Re} \left\{ \sum_{n=1}^{\infty} (2n+1)(A_n + B_n) \right\}.
\end{aligned} \tag{A.50}$$

One important term associated with cross-section is the dimensionless parameter commonly known as efficiency factor or Q-factor. The extinction and scattering efficiencies are given respectively by

$$Q_{\text{ext}} = \frac{C_{\text{ext}}}{g}, \quad Q_{\text{sca}} = \frac{C_{\text{sca}}}{g}. \tag{A.51}$$

where  $g$  is the geometrical cross-section and it is equal to  $\pi a^2$  for a sphere of radius  $a$ .



# Appendix B

## WIRTINGER CALCULUS

---

In the case of GMT and similar inverse problems, the real-valued cost function depends on the complex-valued variable  $\epsilon$ . Consequently, the cost function is not analytic in  $\epsilon$ . Thus, its partial derivatives or gradient cannot be calculated with the standard complex calculus sense [416–419]. This impasse is avoided if the *Wirtinger Calculus* [420] or  $\mathbb{C}\mathbb{R}$ -Calculus [421] is used. Additionally, in the tuning-matching-decoupling optimization process, the cost function was real-valued with real arguments (capacitance values); however, it can be easily generalized to complex impedances with the aid of  $\mathbb{C}\mathbb{R}$ -Calculus.

### B.1 Introduction to $\mathbb{C}\mathbb{R}$ -Calculus

In this section we will briefly provide the basic theory behind Wirtinger Calculus, for functions of single complex variables  $z = x + iy$ . More information on this topic can be found in [421–424]. First of all, we consider the function  $f(z)$

$$f(z) = u(x, y) + iv(x, y). \quad (\text{B.1})$$

$f(z)$  is holomorphic when the partial derivatives of  $u$  and  $v$  exist and also they satisfy the well-known Cauchy-Riemann conditions:

$$\frac{\partial u}{\partial x} = \frac{\partial v}{\partial y}, \quad \frac{\partial v}{\partial x} = -\frac{\partial u}{\partial y}. \quad (\text{B.2})$$

However, we can depict the real-valued function  $f(z)$  as a function of the real and the imaginary parts of  $z$ , meaning as a function over  $\mathbb{R}^2$

$$f(x, y) : \mathbb{R}^2 \rightarrow \mathbb{R}. \quad (\text{B.3})$$

Furthermore,  $f$  can be written as a function of  $(z, z^*)$ , which means that it is holomorphic in  $z$  ( $z^*$ ) for fixed  $z^*$  ( $z$ ), if and only if the partial derivatives of  $u$  and  $v$  exist. At this point we consider a new set of coordinates, called *conjugate coordinates* that exploit the representation of  $f$  as a function of  $\mathbb{R}^2$

$$c \triangleq (z, z^*)^T \in \mathbb{C} \times \mathbb{C}, \quad z = x + iy, \quad z^* = x - iy. \quad (\text{B.4})$$

By using the conjugate coordinates, we can define the following set of partial derivatives for any function  $f(c)$  (complex or real-valued)

$$\begin{aligned}\mathbb{R}\text{-Derivative of } f(c) &\triangleq \frac{\partial f(z, z^*)}{\partial z} \\ \text{Conjugate } \mathbb{R}\text{-Derivative of } f(c) &\triangleq \frac{\partial f(z, z^*)}{\partial z^*},\end{aligned}\tag{B.5}$$

or equivalently we can write

$$\frac{\partial f(z, z^*)}{\partial z} = \frac{1}{2} \left( \frac{\partial f}{\partial x} - i \frac{\partial f}{\partial y} \right), \quad \frac{\partial f(z, z^*)}{\partial z^*} = \frac{1}{2} \left( \frac{\partial f}{\partial x} + i \frac{\partial f}{\partial y} \right).\tag{B.6}$$

Subsequently, an  $\mathbb{R}$ -differentiable function  $f$  is holomorphic if and only if it depends only from  $z$ , thus it should satisfy the following *new Cauchy-Riemann condition*

$$\frac{\partial f}{\partial z^*} = 0.\tag{B.7}$$

For completeness we mention some properties and identities of such complex derivatives.

- $\mathbb{R}$ - and  $\mathbb{R}^*$ -derivatives are linear operators.
- *Differential Rule*:  $\partial f = \frac{\partial f}{\partial z} dz + \frac{\partial f}{\partial z^*} dz^*$ .
- *Chain Rule I*:  $\frac{\partial h(g)}{\partial z} = \frac{\partial h}{\partial g} \frac{\partial g}{\partial z} + \frac{\partial h}{\partial g^*} \frac{\partial g^*}{\partial z}$ .
- *Chain Rule II*:  $\frac{\partial h(g)}{\partial z^*} = \frac{\partial h}{\partial g} \frac{\partial g}{\partial z^*} + \frac{\partial h}{\partial g^*} \frac{\partial g^*}{\partial z^*}$ .
- $\frac{\partial f^*}{\partial z^*} = \overline{\left( \frac{\partial f}{\partial z} \right)}$ ,  $\frac{\partial f^*}{\partial z} = \left( \frac{\partial f}{\partial z^*} \right)^*$ .
- $f(z) \in \mathbb{R} \Rightarrow \left( \frac{\partial f}{\partial z} \right)^* = \frac{\partial f}{\partial z^*}$ .

Finally, a real-valued function  $f(z)$  has a stationary point  $r_0 \triangleq (x_0, y_0)^T$ , if its  $\mathbb{R}^*$ -derivative vanishes at this point, or equivalently, its  $\mathbb{R}$ -derivative vanishes at this point.

## B.2 $\mathbb{C}\mathbb{R}$ -Calculus of Multiple Variables

In this section we will provide basic definitions of the multivariate  $\mathbb{C}\mathbb{R}$ -Calculus, originally developed in [421, 424–429]. We initiate our analysis by defining the  $n$ -dimensional complex vector  $\mathbf{z}$

$$\mathbf{z} = (z_1, \dots, z_n)^T \in \mathbb{C}^n, \quad \mathbf{z} = \mathbf{x} + i\mathbf{y}, \quad \mathbf{x} = (x_1, \dots, x_n)^T, \quad \mathbf{y} = (y_1, \dots, y_n)^T.\tag{B.8}$$

The space  $\mathbb{C}^n$  is a vector space over complex numbers, with standard definitions for vector addition and scalar-vector multiplications. Moreover, we can compare this space with a space of real numbers as follows

$$\mathbf{z} \in \mathbb{C}^n \Leftrightarrow (\mathbf{x}, \mathbf{y})^T \in \mathbb{R}^{2n} = \mathbb{R}^n \times \mathbb{R}^n. \quad (\text{B.9})$$

The conjugate of  $\mathbf{z}$  is defined as follows

$$\mathbf{z}^* = (z_1^*, \dots, z_n^*)^T \in \mathbb{C}^n. \quad (\text{B.10})$$

In a similar way as in B.4 we can define the conjugate coordinate vectors as follows

$$\mathbf{c} = (\mathbf{z}, \mathbf{z}^*)^T \in \mathbb{C}^{2n} = \mathbb{C}^n \times \mathbb{C}^n. \quad (\text{B.11})$$

For the vector  $\mathbf{z}$  we define the *cogradient*  $\partial/\partial\mathbf{z}$  ( $\mathbf{z}^*$  treated as constant) and the *conjugate cogradient*  $\partial/\partial\mathbf{z}^*$  ( $\mathbf{z}$  treated as constant) operators as follows

$$\frac{\partial}{\partial\mathbf{z}} \triangleq \left( \frac{\partial}{\partial z_1}, \dots, \frac{\partial}{\partial z_n} \right), \quad \frac{\partial}{\partial\mathbf{z}^*} \triangleq \left( \frac{\partial}{\partial z_1^*}, \dots, \frac{\partial}{\partial z_n^*} \right), \quad (\text{B.12})$$

where each of the above components can be calculated with B.6, thus, the following equivalent notation is preferred

$$\frac{\partial}{\partial\mathbf{z}} = \frac{1}{2} \left( \frac{\partial}{\partial\mathbf{x}} - i \frac{\partial}{\partial\mathbf{y}} \right), \quad \frac{\partial}{\partial\mathbf{z}^*} = \frac{1}{2} \left( \frac{\partial}{\partial\mathbf{x}} + i \frac{\partial}{\partial\mathbf{y}} \right). \quad (\text{B.13})$$

Let us consider a mapping  $\mathbf{f}(\mathbf{c}) = \mathbf{f}(\mathbf{z}, \mathbf{z}^*) : \mathbb{C}^n \rightarrow \mathbb{C}^m$ . The differential rule, in the case of multiple variables, can be written as follows

$$d\mathbf{f}(\mathbf{c}) = \frac{\partial\mathbf{f}(\mathbf{c})}{\partial\mathbf{z}} d\mathbf{z} + \frac{\partial\mathbf{f}(\mathbf{c})}{\partial\mathbf{z}^*} d\mathbf{z}^*, \quad (\text{B.14})$$

where the  $J_{\mathbf{f}}(\mathbf{c}) = \partial\mathbf{f}(\mathbf{c})/\partial\mathbf{z}$  is the *Jacobian matrix*, while the  $J_{\mathbf{f}}^c(\mathbf{c}) = \partial\mathbf{f}(\mathbf{c})/\partial\mathbf{z}^*$  is the *conjugate Jacobian matrix* of  $\mathbf{f}$ . They can be calculated as follows

$$J_{\mathbf{f}}(\mathbf{c}) = \begin{bmatrix} \frac{\partial f_1(\mathbf{c})}{\partial z_1} & \dots & \frac{\partial f_1(\mathbf{c})}{\partial z_n} \\ \dots & \dots & \dots \\ \frac{\partial f_m(\mathbf{c})}{\partial z_1} & \dots & \frac{\partial f_m(\mathbf{c})}{\partial z_n} \end{bmatrix} \in \mathbb{C}^{m \times n}, \quad J_{\mathbf{f}}^c(\mathbf{c}) = \begin{bmatrix} \frac{\partial f_1(\mathbf{c})}{\partial z_1^*} & \dots & \frac{\partial f_1(\mathbf{c})}{\partial z_n^*} \\ \dots & \dots & \dots \\ \frac{\partial f_m(\mathbf{c})}{\partial z_1^*} & \dots & \frac{\partial f_m(\mathbf{c})}{\partial z_n^*} \end{bmatrix} \in \mathbb{C}^{m \times n}. \quad (\text{B.15})$$

In the case of  $\mathbf{f}(\mathbf{c}) \in \mathbb{R}^m$  the following identity holds true

$$J_{\mathbf{f}}^*(\mathbf{c}) = \overline{\left( \frac{\partial\mathbf{f}(\mathbf{c})}{\partial\mathbf{z}} \right)} = \frac{\partial\mathbf{f}(\mathbf{c})}{\partial\mathbf{z}^*} = J_{\mathbf{f}}^c(\mathbf{c}). \quad (\text{B.16})$$

Thus, the differential rule obtains the following elegant form

$$d\mathbf{f}(\mathbf{c}) = J_{\mathbf{f}}(\mathbf{c})d\mathbf{z} + J_{\mathbf{f}}^c(\mathbf{c})d\mathbf{z}^* = 2\mathcal{R}e \{J_{\mathbf{f}}(\mathbf{c})d\mathbf{z}\}. \quad (\text{B.17})$$

In addition the chain rule for the composition  $\mathbf{h} \circ \mathbf{g} : \mathbb{C}^k \rightarrow \mathbb{C}^m$  of two mappings  $\mathbf{h} : \mathbb{C}^n \rightarrow \mathbb{C}^m$ ,  $\mathbf{g} : \mathbb{C}^k \rightarrow \mathbb{C}^n$ , obtains the following generalized form

$$\text{I: } \frac{\partial \mathbf{h}(\mathbf{g})}{\partial \mathbf{z}} = \frac{\partial \mathbf{h}}{\partial \mathbf{g}} \frac{\partial \mathbf{g}^*}{\partial \mathbf{z}} + \frac{\partial \mathbf{h}}{\partial \mathbf{g}^*} \frac{\partial \mathbf{g}^*}{\partial \mathbf{z}}, \quad \text{II: } \frac{\partial \mathbf{h}(\mathbf{g})}{\partial \mathbf{z}^*} = \frac{\partial \mathbf{h}}{\partial \mathbf{g}} \frac{\partial \mathbf{g}}{\partial \mathbf{z}^*} + \frac{\partial \mathbf{h}}{\partial \mathbf{g}^*} \frac{\partial \mathbf{g}^*}{\partial \mathbf{z}^*}, \quad (\text{B.18})$$

or

$$J_{\mathbf{h} \circ \mathbf{g}} = J_{\mathbf{h}} J_{\mathbf{g}} + J_{\mathbf{h}}^c (J_{\mathbf{g}}^c)^*, \quad J_{\mathbf{h} \circ \mathbf{g}}^c = J_{\mathbf{h}} J_{\mathbf{g}}^c + J_{\mathbf{h}}^c J_{\mathbf{g}}^*. \quad (\text{B.19})$$

A vector-valued function  $\mathbf{f}(\mathbf{z})$  is holomorphic in  $\mathbf{z}$  if and only if all of its components  $f_i(\mathbf{z}, \mathbf{z}^*)$ ,  $i = 1, \dots, m$  are holomorphic separately on each  $z_j$ ,  $j = 1, \dots, n$  or it is a function only of  $\mathbf{z}$  or if it satisfies the *matrix Cauchy-Riemann condition*

$$J_{\mathbf{f}}^c = \frac{\partial \mathbf{f}}{\partial \mathbf{z}^*} = 0. \quad (\text{B.20})$$

Therefore, in an analogous way as in B.7, a scalar real-valued function from  $\mathbb{C}^n$  to  $\mathbb{R}$  has a stationary point at  $(\mathbf{z}_0, \mathbf{z}_0^*)$  if the equivalent following conditions are satisfied

$$\frac{\partial f(\mathbf{z}_0, \mathbf{z}_0^*)}{\partial \mathbf{z}} = 0, \quad \frac{\partial f(\mathbf{z}_0, \mathbf{z}_0^*)}{\partial \mathbf{z}^*} = 0. \quad (\text{B.21})$$

This page is intentionally left blank.



# Appendix C

## NUMERICAL LINEAR ALGEBRA

---

### C.1 Definitions

**Definition C.1.** The Frobenius norm of a tensor  $\mathcal{A} \in \mathbb{C}^{n_1 \times n_2 \times n_3}$  is defined as follows

$$\|\mathcal{A}\|_F \triangleq \left( \sum_{i=1}^{n_1} \sum_{j=1}^{n_2} \sum_{k=1}^{n_3} |\mathcal{A}_{ijk}|^2 \right)^{\frac{1}{2}}. \quad (\text{C.1})$$

**Definition C.2.** The Chebyshev norm of a tensor  $\mathcal{A} \in \mathbb{C}^{n_1 \times n_2 \times n_3}$  is defined as follows

$$\|\mathcal{A}\|_C \triangleq \max_{ijk} |\mathcal{A}_{ijk}|, \quad i = 1, \dots, n_1, j = 1, \dots, n_2, k = 1, \dots, n_3. \quad (\text{C.2})$$

**Definition C.3.** The  $L_2$  inner product  $\langle \cdot \rangle_V$  between two vectors  $\mathbf{u}, \mathbf{v} \in \mathbb{C}^n$ , over  $V$ , is defined as follows

$$\langle \mathbf{u}, \mathbf{v} \rangle_V = \int_V \mathbf{u}^* \mathbf{v} dV. \quad (\text{C.3})$$

**Definition C.4.** The  $n$ -mode product between a tensor  $\mathcal{A} \in \mathbb{C}^{m_1 \times m_2 \times m_3}$  with a matrix  $U^n \in \mathbb{C}^{q_n \times m_n}$ ,  $n = 1, 2, 3$  results to a new tensor  $\mathcal{B}^n$  obtained by the convolution over the  $n$  axis, i.e., for  $\mathcal{B}^1 \in \mathbb{C}^{q_1 \times m_2 \times m_3}$ :

$$\mathcal{B}^1 = \mathcal{A} \times_1 U^1, \quad \mathcal{B}_{ijk} = \sum_{t=1}^{m_1} \mathcal{A}_{tjk} U_{it}^1. \quad (\text{C.4})$$

**Definition C.5.** The outer product  $\odot$  between two multidimensional arrays  $A \in \mathbb{C}^{n_1 \times \dots \times n_N}$ ,  $B \in \mathbb{C}^{m_1 \times \dots \times m_M}$  is defined as follows

$$(A \odot B)_{i_1, \dots, i_N, j_1, \dots, j_M} = A_{i_1, \dots, i_N} \cdot B_{j_1, \dots, j_M}. \quad (\text{C.5})$$

**Definition C.6.** The Kronecker product  $\otimes$  between two matrices  $A \in \mathbb{C}^{n_1 \times n_2}$ ,  $B \in \mathbb{C}^{m_1 \times m_2}$  is an  $n_1 m_1 \times n_2 m_2$  matrix, defined as follows

$$A \otimes B = \begin{bmatrix} A_{11}B & \cdots & A_{1n_2}B \\ \cdots & \cdots & \cdots \\ A_{n_1 1}B & \cdots & A_{n_1 n_2}B \end{bmatrix}. \quad (\text{C.6})$$

**Definition C.7.** The Khatri-Rao product  $\otimes$  between two matrices  $A \in \mathbb{C}^{n \times q}, B \in \mathbb{C}^{m \times q}$  is an  $nm \times q$  matrix, defined as follows

$$A \otimes B = [A_{:1} \otimes B_{:1} \cdots A_{:q} \otimes B_{:q}]. \quad (\text{C.7})$$

**Definition C.8.** The elementwise product (or entrywise product)  $\circ$  between two arrays  $A \in \mathbb{C}^{n_1 \times n_2 \times \cdots \times n_m}, B \in \mathbb{C}^{n_1 \times n_2 \times \cdots \times n_m}$  is an  $n_1 \times n_2 \times \cdots \times n_m$  array, with elements given from

$$(A \circ B)_{i_1 i_2 \cdots i_m} = A_{i_1 i_2 \cdots i_m} B_{i_1 i_2 \cdots i_m}. \quad (\text{C.8})$$

In the case of matrices, the elementwise product is called Hadamard product.

## C.2 Adaptive Cross Approximation

The adaptive cross approximation (ACA) [430–432], is an algorithm used for the application of skeleton decomposition [433, 434]. The method aims to approximate a low-rank matrix only by using some rows and columns of it, an advantage in the operation and memory complexities over the classic SVD method. In this section, the analysis of the algorithm is presented in a similar way as in [435, 436], where the ACA is used to compress the off-diagonal blocks of the EFIE MoM matrix.

Let us consider a matrix  $A \in \mathbb{C}^{m \times n}$  with effective (numerical) rank  $r$ . According to skeleton decomposition theory the matrix can be approximated as follows

$$Z \approx \tilde{Z} = UV = \sum_{i=1}^r U_{:i} V_{i:}. \quad (\text{C.9})$$

where  $U \in \mathbb{C}^{m \times r}$  and  $V \in \mathbb{C}^{r \times n}$ . This cross approximation achieves an error defined by the matrix  $R$  as follows

$$\|R\|_F = \|Z - \tilde{Z}\|_F \leq \epsilon \|Z\|_F. \quad (\text{C.10})$$

where  $\epsilon$  is the setted tolerance. The ACA algorithm is provided below.

---

### Algorithm 6 Adaptive Cross Approximation Algorithm

---

- 1:  $\tilde{Z} = 0$
- 2:  $\tilde{R}_1 = \tilde{Z}_1$
- 3: Find  $j$  such as  $|\tilde{R}_{1j}| = \max(|R_{1:}|)$
- 4:  $V_{1:} = \tilde{R}_1 / \tilde{R}_{1j}$
- 5:  $\tilde{R}_{:j} = Z_{:j}$
- 6:  $U_{:1} = \tilde{R}_{:j}$
- 7:  $\|\tilde{Z}\|_F^2 = \|\tilde{Z}\|_F^2 + \|U_{:1}\|_F^2 \|V_{1:}\|_F^2$
- 8:  $p = 2$

9: **loop**

- 10: Find  $i$  such as  $\tilde{R}_{ij} = \max(|R_{:,j}|)$ ,  $i \neq$  already used rows
- 11:  $\tilde{R}_{i,:} = Z_{i,:} - \sum_{l=1}^{p-1} U_{il} V_l$
- 12: Find  $j$  such as  $|\tilde{R}_{ij}| = \max(|\tilde{R}_{i,:}|)$ ,  $j \neq$  already used columns
- 13:  $V_p = \tilde{R}_{i,:} / \tilde{R}_{ij}$
- 14:  $\tilde{R}_{:,j} = Z_{:,j} - \sum_{l=1}^{p-1} V_{jl} U_{:,l}$
- 15:  $U_{:,p} = \tilde{R}_{:,j}$
- 16:  $\|\tilde{Z}\|_F^2 = \|\tilde{Z}\|_F^2 + 2 \sum_{l=1}^{p-1} (|U_{:,l}^T U_{:,p}| |V_{l,:}^T V_{p,:}|) + \|U_{:,p}\|_F^2 \|V_{p,:}\|_F^2$
- 17: **if**  $\|U_{:,p}\| \|V_{p,:}\| > \epsilon \|\tilde{Z}\|$  **then**  $p = p + 1$
- 18: **else return**  $U, V$
- 

Only  $\mathcal{O}(rn + rm)$  entries need to be stored. The complexity of the ACA algorithm is  $\mathcal{O}(r^2 n + r^2 m)$ .

### C.3 Maxvol Algorithm

Cross approximation method often requires the evaluation of a sufficiently good submatrix of the initial array. Usually, the well-conditioning of this submatrix is measured via the absolute value of its determinant (volume of the matrix) [437, 438]. In this section, we will provide the algorithm, dubbed MaxVol, that is used in order to approximate such submatrix. The method finds many applications, especially in tensor and matrix cross approximations, and in the fast evaluation of the maximum element of matrices.

Let us consider a matrix  $A \in \mathbb{C}^{m \times n}$  with rank  $r$ . For some set of rows  $\mathbf{i}$  and columns  $\mathbf{j}$ , of length  $r$  with element values between  $1, \dots, n$  and  $1, \dots, m$  respectively, the following equations holds true

$$A = A_{:,j} A_{ij}^{-1} A_{i,:}, \quad (\text{C.11})$$

where the matrix  $A_{ij} = \hat{A}$  is non-singular. In the approximate case, this submatrix is required to have the maximum volume over all other submatrices of  $A$  with dimensions  $r \times r$ . A practical algorithm for finding a good submatrix is provided below.

---

#### Algorithm 7 MaxVol algorithm

---

- 1:  $A \in \mathbb{C}^{n \times r}$
- 2: Arbitrary non-singular submatrix  $\hat{A} \in \mathbb{C}^{r \times r}$
- 3: Reorder rows of  $A$  so  $\hat{A}$  will occupy the first  $r$  rows
- 4: Compute  $A \hat{A}^{-1} = B$
- 5: Find maximum absolute value element  $b_{ij}$  of  $B$

---

```

6: loop
7:   if  $|b_{ij}| > 1 + \delta$  then swap the rows  $i$  and  $j$  in  $B$ 
8:   else return  $\hat{A}$ 

```

---

In step 7 the reordering of the rows leads to the increasment of the volume of  $\hat{A}$ . The parameter  $\delta$  is  $\sim 10^{-2}$  and it is used to reduce the number of the required iterations in order to retrieve the maximum volume submatrix. In addition, since in every iteration  $\hat{A}$  receives rank-one modifications we can calculate its inverse with Sherman-Woodbury-Morrisson formula [439, 440], resulting to  $\mathcal{O}(2c(nr - r^2))$  complexity, where  $c$  is the number of iterations.

Let us consider a low-rank matrix  $A \in \mathbb{C}^{n \times n}$  with rank  $r$  to which we want to find its maximum element, but with linear complexity (over the classic  $\mathcal{O}(n^2)$  comparisons). By applying a cross approximation method we have

$$A = BC^T, \tag{C.12}$$

where  $B, C \in \mathbb{C}^{n \times r}$ . In addition, let us consider a submatrix of maximum volume of  $A$ ,  $\hat{A}$ . The following inequality holds true

$$\|\hat{A}\|_C \geq \frac{\|A\|_C}{r}. \tag{C.13}$$

Hence, the maximum element of  $\hat{A}$  is more or less similar to the maximum element of  $A$ , and to define it we need only  $\mathcal{O}(r^2)$  comparisons. To find  $\hat{A}$  we need to apply the MaxVol on either  $B$  or  $C$ .

This page is intentionally left blank.



# Appendix D

## INTEGRATION BACKGROUND

---

### D.1 Simplex Coordinates

Usually, the surface integral equation formulations are discretized over triangular meshes, in order to exploit the superior properties of RWG (or BC) basis functions. Thus, we prefer to express these functions on the local simplex or barycentric coordinates because they transform any triangle to a right-angled one, where the integration with a Gauss quadrature rule is trivial. Let us consider the following triangle  $\mathcal{T}$  on the two-dimensional Euclidean space.

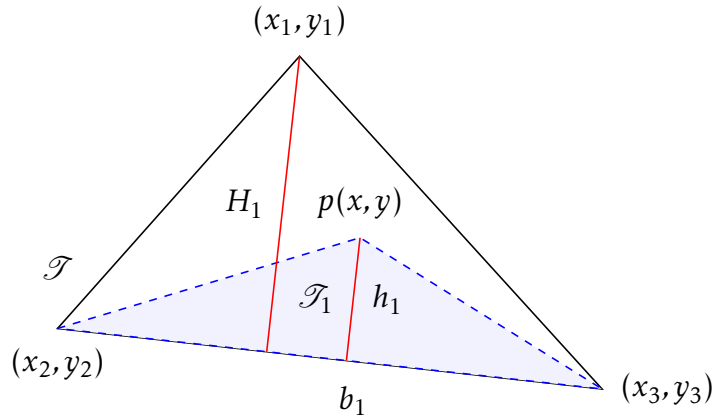


Figure D.1: Triangular Element - Simplex Coordinates.

The barycentric coordinates of a point  $p(x, y) \in \mathcal{T}$  are defined as follows

$$\zeta_i = \frac{h_i}{H_i}, \quad i = 1, 2, 3, \quad (\text{D.1})$$

where  $H_i$  is the height from the node  $(x_i, y_i)$  and  $h_i$  is the vertical distance from  $p$  to the opposite edge of the node  $(x_i, y_i)$ . Thus, the following property holds true

$$\zeta_i = \begin{cases} 1 & \text{at node } i \\ 0 & \text{at other nodes} \end{cases}. \quad (\text{D.2})$$

Moreover, the simplex coordinates satisfy the following equation

$$\zeta_i = \frac{h_i}{H_i} = \frac{T_i}{T}, \quad (\text{D.3})$$

where  $T$  is the area of  $\mathcal{T}$ , and  $T_i$  is the area of the respective sub-triangle, portrayed with blue color in D.1. The following property applies

$$\zeta_1 + \zeta_2 + \zeta_3 = \frac{T_1 + T_2 + T_3}{T} = 1. \quad (\text{D.4})$$

From the aforementioned, one can write the barycentric coordinates as a function of the Cartesian ones as follows

$$\begin{aligned} \zeta_1(x, y) &= \frac{x_2 y_3 - x_3 y_2}{2T} + \frac{y_2 - y_3}{2T}x + \frac{x_3 - x_2}{2T}y \\ \zeta_2(x, y) &= \frac{x_3 y_1 - x_1 y_3}{2T} + \frac{y_3 - y_1}{2T}x + \frac{x_1 - x_3}{2T}y \\ \zeta_3(x, y) &= \frac{x_1 y_2 - x_2 y_1}{2T} + \frac{y_1 - y_2}{2T}x + \frac{x_2 - x_1}{2T}y. \end{aligned} \quad (\text{D.5})$$

Finally, the gradients of the simplex coordinates are

$$\begin{aligned} \nabla \zeta_1 &= b_1 \hat{x} + c_1 \hat{y} \\ \nabla \zeta_2 &= b_2 \hat{x} + c_2 \hat{y} \\ \nabla \zeta_3 &= b_3 \hat{x} + c_3 \hat{y}. \end{aligned} \quad (\text{D.6})$$

## D.2 Gauss Quadrature Rules

In order to accurately approximate the arising definite integrals in SIE or VIE formulations, we can use a variety of algorithms for numerical integrations. Specifically in the current thesis we use the *Gauss-Legendre quadrature rule*. This algorithm approximates the integral as a weighted sum of function values at specified predefined points, within the domain of the integration. We note that the  $n$ -point Gaussian quadrature rule will yield an exact result for the integration of polynomials of degree  $2n-1$  or less, for a suitable choice of points  $x_i$  and weights  $w_i$ ,  $i = 1, \dots, n$ . The rule for the integration of a function  $f$ , for the conventionally chosen domain of integration  $[-1, 1]$ , is stated as

$$\int_{-1}^1 f(x) dx \approx \sum_{i=1}^n w_i f(x_i), \quad (\text{D.7})$$

where the weights  $w_i$  are functions of the derivatives of the Legendre polynomials

$$w_i = \frac{2}{(1 - x_i^2)[P'_n(x_i)]^2}, \quad (\text{D.8})$$

and  $x_i$  are the roots of the Legendre polynomials  $P_n(x_i) = 0$ . In addition, for integration over a different domain we have

$$\int_a^b f(x) dx \approx \frac{b-a}{2} \sum_{i=1}^n w_i f\left(\frac{b-a}{2}x_i + \frac{a+b}{2}\right). \quad (\text{D.9})$$

### D.2.1 Gauss Quadrature Rule for Rectangles

If we are interested in 2D integrations, for example over a rectangle  $\mathcal{R} = [-1, 1]^2$ , we need to calculate the following integral

$$I = \iint_{\mathcal{R}} g(\xi, \eta) d\xi d\eta = \int_{-1}^1 \int_{-1}^1 g(\xi, \eta) d\xi d\eta. \quad (\text{D.10})$$

To implement such integration, we implement two 1D rules for each of the integrals, thus we have

$$I \approx \sum_{i=1}^M \sum_{j=1}^N \hat{w}_j w_i g(\xi_i, \eta_j), \quad (\text{D.11})$$

where  $\xi_i, w_i$  are the points and the weights of order of  $M$  over  $\xi$ , and  $\eta_j, \hat{w}_j$  are the points and the weights of order  $N$  over  $\eta$ . Usually we choose  $M = N$  in order to have  $\eta_i = \xi_i$  and  $w_i = \hat{w}_i$ . Thus, the final formula of the integration is

$$\int_{-1}^1 \int_{-1}^1 g(\xi, \eta) d\xi d\eta \approx \sum_{i=1}^N \sum_{j=1}^N w_j w_i g(\xi_i, \xi_j). \quad (\text{D.12})$$

### D.2.2 Gauss Quadrature Rule for Right-Angle Triangles

In order to calculate the quadrature rule over an arbitrary triangle, we have to transform it first to a right-angle triangle  $\mathcal{T}$ , then to a rectangle  $\mathcal{R}$  and finally apply the rule as in the previous subsection. According to the axis defined in D.2, the transformation is defined as follows

$$\begin{cases} \xi = \frac{(1+a)(1-b)}{4} \\ \eta = \frac{(1+b)}{2} \end{cases}, \text{ or } \begin{cases} a = \frac{2\xi}{1-\eta} - 1 \\ b = 2\eta - 1 \end{cases}. \quad (\text{D.13})$$

The Jacobian of the transformation is given from

$$J(a, b) = \det \left( \frac{\partial(\xi, \eta)}{\partial(a, b)} \right) = \frac{1-b}{8} = \frac{1-\eta}{4}, \quad (\text{D.14})$$

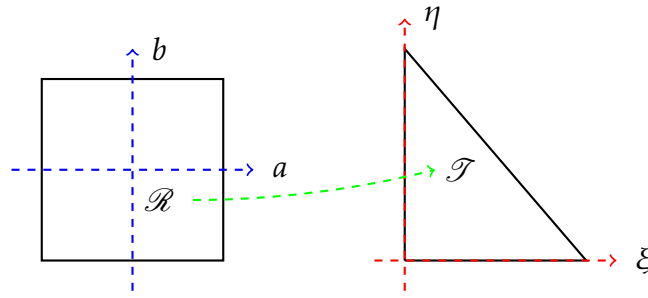
and the rule takes the following final form

$$I = \iint_{\mathcal{T}} g(\xi, \eta) d\xi d\eta = \iint_{\mathcal{R}} g(\xi(a, b), \eta(a, b)) |J(a, b)| da db. \quad (\text{D.15})$$

### D.2.3 Gauss Quadrature Rule for Cubes

For 3D integrations over a cube (voxel),  $\mathcal{R} = [-1, 1]^3$ , the following integral

$$I = \iiint_{\mathcal{R}} g(\xi, \eta, \zeta) d\xi d\eta d\zeta = \int_{-1}^1 \int_{-1}^1 \int_{-1}^1 g(\xi, \eta, \zeta) d\xi d\eta d\zeta, \quad (\text{D.16})$$


 Figure D.2: Transformation between  $\mathcal{R}$  and  $\mathcal{T}$ .

can be solved with Gauss-Legendre rule, if we implement three 1D rules for each integral as follows

$$I \approx \sum_{i=1}^M \sum_{j=1}^N \sum_{k=1}^L \hat{w}_k \hat{w}_j w_i g(\xi_i, \eta_j, \zeta_k), \quad (\text{D.17})$$

where  $(\xi_i, w_i), (\eta_j, \hat{w}_j), (\zeta_k, \hat{w}_k)$  are the points and the weights of order of  $N, M, L$  over  $\xi, \eta, \zeta$  respectively. For  $N = M = L$  the integral acquires the following symmetric form

$$\int_{-1}^1 \int_{-1}^1 \int_{-1}^1 g(\xi, \eta, \zeta) d\xi d\eta d\zeta \approx \sum_{i=1}^N \sum_{j=1}^N \sum_{k=1}^N w_k w_j w_i g(\xi_i, \xi_j, \xi_k). \quad (\text{D.18})$$

### D.3 Spherical Mean

The spherical mean [441] of a function around a point  $x$ , is the average of all its values on a sphere of a given radius centered at that point. Specifically, considering an open set  $\mathbb{X} \subseteq \mathbb{R}^n$ , a continuous function  $f(y) : \mathbb{X} \rightarrow \mathbb{C}^n$ , a radius  $r > 0$  and a point  $x \in \mathbb{X}$  such as the *closed ball*  $\mathbb{B}(x, r) \subseteq \mathbb{X}$ , the spherical mean over the sphere of radius  $r$  and center  $x$  is defined as follows

$$[f](r) = \frac{1}{\omega_{n-1}(r)} \int_{\partial \mathbb{B}(x, r)} f(y) dS(y), \quad (\text{D.19})$$

where,  $\partial \mathbb{B}(x, r)$  is the boundary of  $\mathbb{B}(x, r)$ ,  $dS$  denotes the integration with respect to *spherical measure* and  $\omega_{n-1}(r)$  is the *surface area* of the  $(n - 1)$  unit sphere.

This page is intentionally left blank.



# Appendix E

## GRADIENT CALCULATION

---

The cost function of the tuning-matching-decoupling optimization process is the following

$$f(C) = \frac{1}{2} \|W \circ S_m(C)\|_{\text{fro}}^2. \quad (\text{E.1})$$

Here,  $W$  is a constant matrix with various entries, depending on what values we want to prioritize for the minimization. For the calculation of this gradient, we will consider  $n-m$  tuning capacitors attached to the ports of indices  $l$  and  $m$  feeding ports with indices  $p$ . Also, we consider a matching network of one parallel and one in series capacitor in each port. This approach is simple, yet very informative since it includes all the possible attachments of lumped elements. Finally, the tuning capacitors are denoted as  $C_t$ , the matching parallel capacitors as  $C_p$  and the matching series capacitors as  $C_s$ .

The  $S_m$  parameters are related to the  $Z_m$  parameters as follows

$$S_m(C_t, C_p, C_s) = \left( Z_m(C_t, C_p, C_s) + z_0 I \right)^{-1} \left( Z_m(C_t, C_p, C_s) - z_0 I \right), \quad (\text{E.2})$$

where  $z_0$  is the impedance of the feeding cable (usually  $50\Omega$ ) and  $I$  is the identity matrix. The  $Z_m$  parameters are related to the  $Y_m$  parameters as follows

$$Z_m(C_t, C_p, C_s) = Y_m^{-1}(C_t, C_p) + \text{diag}\left(\frac{1}{i\omega C_s}\right), \quad (\text{E.3})$$

where  $\omega$  is the angular frequency. Finally the  $Y_m$  parameters are related to the  $Y_n$  parameters (MARIE's output) as follows

$$\begin{aligned} Y_m(C_t, C_p) &= Y_n^{pp} + \text{diag}(i\omega C_p) - Y_n^{pl} Y_L^{-1} Y_n^{lp} \\ Y_L &= \left( Y_n^{ll} + \text{diag}(i\omega C_t) \right). \end{aligned} \quad (\text{E.4})$$

For the computation of the cost function's gradient concerning a capacitor  $c \in \{C_t, C_p, C_s\}$  we calculate the following partial derivative of  $f$ :

$$\frac{\partial f}{\partial c} = \frac{1}{2} \text{trace}\left( \left( W \circ \frac{\partial S_m}{\partial c} \right)^* (W \circ S_m) + (W \circ S_m)^* \left( W \circ \frac{\partial S_m}{\partial c} \right) \right). \quad (\text{E.5})$$

We continue by calculating the partial derivative of  $S_m$  over  $c$ .

$$\frac{\partial S_m}{\partial c} = -(Z_m + z_0 I)^{-1} \frac{\partial Z_m}{\partial c} (Z_m + z_0 I)^{-1} (Z_m - z_0 I) + (Z_m + z_0 I)^{-1} \frac{\partial Z_m}{\partial c}, \quad (\text{E.6})$$

where we used the identity  $\partial A^{-1} = -A^{-1} \partial A A^{-1}$ . The derivative of  $Z_m$  varies depending the set where  $c$  belongs to. If  $c \in C_s$ , then  $\partial Z_m / \partial c$  is a matrix with all vaules equal to zero except one element  $\{i, i\}, i \in p$  corresponding to the feeding port equipped with the matching capacitor in series:

$$\frac{\partial Z_m}{\partial c} \Big|_{ii} = -\frac{1}{i\omega c^2}, \quad (\text{E.7})$$

and this concludes the computation of the gradient. If  $c \in \{C_p, C_t\}$  then

$$\frac{\partial Z_m}{\partial c} = -Y_m^{-1} \frac{\partial Y_m}{\partial c} Y_m^{-1}. \quad (\text{E.8})$$

If  $c \in C_p$  then  $\partial Y_m / \partial c$  is a matrix with all vaules equal to zero similarly as before, except one element  $\{i, i\}, i \in p$  corresponding to the feeding port equipped with the parallel matching capacitor:

$$\frac{\partial Y_m}{\partial c} \Big|_{ii} = i\omega, \quad (\text{E.9})$$

thus the gradient is computed. In the last case where  $c \in C_t$  the derivative is

$$\frac{\partial Y_m}{\partial c} = Y_n^{pl} Y_L^{-1} \left( \frac{\partial Y_L}{\partial c} \right) Y_L^{-1} Y_n^{lp}. \quad (\text{E.10})$$

The final derivative  $\partial Y_L / \partial c$  is a matrix with all the elements equal to zero except the element  $\{i, i\}, i \in l$  corresponding to the lumped elements port equipped with the tuning capacitor:

$$\frac{\partial Y_L}{\partial c} \Big|_{ii} = i\omega. \quad (\text{E.11})$$

This concludes the calculation of the gradient for all cases.





2020